

Columnlike free-interface flows: symmetry breaking and linear instability

Présentée le 24 mars 2023

Faculté des sciences et techniques de l'ingénieur
Laboratoire de mécanique des fluides et instabilités
Programme doctoral en mécanique

pour l'obtention du grade de Docteur ès Sciences

par

Shahab EGHBALI

Acceptée sur proposition du jury

Prof. F. Porté Agel, président du jury
Prof. F. Gallaire, directeur de thèse
Prof. C. Duprat, rapporteuse
Prof. L. Zhu, rapporteur
Prof. J. Kolinski, rapporteur

To my family

Acknowledgements

I view this work and my Ph.D. life as a journey that began with curiosity, and motivation for learning and trying, and completed with deeper curiosity and thirst for learning and trying. But harking back to the first days, I humbly feel the growth in my attitude and vision. For the progress and pleasure of this journey, I owe several people for their presence and honest support. The long list commences with François who supervised my work. I am unable to express my gratitude in words for the trust you gave me to join LFMI, for the liberty, inspiration, and advice you gave me along the way, for your patience, and for all the moral support you carried for me in hardships. Not only does your contagious enthusiasm for science fuel the passion in each work, but also your wisdom, strong humanity, and benevolence make you an exceptional leader and a priceless friend.

I am very thankful to Prof. Camille Duprat, Prof. Lailai Zhu, and Prof. John Martin Kolinski for having accepted to evaluate this work. I deeply appreciated the constructive discussion during the thesis defense and what I learned from your viewpoints. My gratitude also goes to Prof. Fernando Porté-Agel for kindly accepting to preside over the jury. I am grateful for what I learned from your courses and the support you had for me for many years since when I was a master's student, and for your wise advice when I decided to step on this path.

I would like to thank the members of the powder focusing project: Prof. Patrik Hoffmann and Prof. Sebastien Vaucher from EMPA, Prof. Manuel Pouchon and Choi Kwanghoon from PSI, Prof. Dimos Poulikakos, Prof. Jürg Dual, Patrik Rohner and Michael Gerlt from ETHZ.

Without further saying, I must thank every and each member of the LFMI family and recall firstly Petra Bendel; the peaceful and caring environment of the lab is undoubtedly thanks to your maternal care for each of us, and the smooth organisation of the administrations is not possible without your precision. Next, I was lucky to have shared these years with talented colleagues, from whom I gained continuous support and enriched my thoughts and ideas directly and indirectly. Thank you, Giacomo Gallino, and Gioele Balestra for being models in my first year of this adventure, I learned a lot from you, especially during my master's courses. My special thanks to Simon Pasche and Lorenzo Siconolfi who guided me through the technical challenges in the beginning of this work, to Eunok Yim who always listened openly to my doubts and helped me with my "silly questions", and to Isha Shukla who supported me morally at frustrations. Thank you Mathias Bechert for nicely introducing me to COMSOL MultiphysicsTM and for sharing your exemplary models that inspired me for future model developments. Thank you Hervé Elettro, Gaétan Lerisson, and Martin Coux for the nice time we spent together, your energy, brilliant ideas, and stimulating insights about physical

Acknowledgements

interpretations. I am indebted to you Ludovic Keiser, for the fascination that you awakened inside me with the whirling structures, for your nice encouragement to analyse them, for leading me in developing the experiments, and for your bright intuitions. You opened a new window to my work and way of thinking that reformed this thesis. Also, thank you for being such a lovely office mate, I miss your delicate humour since you left LFMI. Thank you Edouard Boujo, my former master's thesis referee and a colleague and friend of today. I learned a lot from discussing with you, from your precision in research and care for details. Thank you Giuseppe Zampogna for your support in developing my numerical model. I am impressed by your detective eyes and magical touch on numerics.

It was a great pleasure Pierre Giuseppe Ledda, Alessandro Bongarzone, and Yves-Marie Ducimetière to have shared this adventure called Ph.D. together. I am impressed by your courage and pragmatism P.G., and I always remember your warm hospitality while discovering Bosa. Thank you, Alessandro and Y.-M. for your rigour, theoretical and technical support, for being ears for my ideas and stories, and for the countless moments we spent together. Your presence meant a lot to me. Thank you Kevin Wittkowski for sharing the office with me during these last months, our nice discussions, and your tasty olive oil. Thank you Simeon Djambov for your nice presence, calming humour, and smart ideas. Also, I wish I had more time to brainstorm and collaborate with you. Thank you Alice Marcotte and Jesus Sanchez for bringing your lovely energy and vibes to the group. It was adorable to spend time with you. I wish you a wonderful and successful Ph.D. adventure, Timothée Salamon.

Thank you Amin Kaboli and Ramin Kaviani for your practical tips, unique attitudes, and philosophical discussions. They were precious feeds of thoughts, and indeed, I will always remember your words of wisdom. I should also thank our neighbours in EMSI, Albert Taureg, Youssef Eddebbbarh, Lebo Molefe, Xinyue Wei, and in ECPS, Prof. Tobias Schneider, Alessia Ferraro, Emilio Lozano, Omid Ashtari, Sajjad Azimi, for our great moments during gatherings, and especially Christmas dinners.

I shall express my sincere appreciation for many other friends all around Switzerland, who were big moral assets for me on this journey. Thank you Yasaman I., Mohammad A., Ali A., Narges K., Shekoofeh Y., Ali F., Mehrshad F., Shiva M., Fatemeh Gh., Mohsen H., Amirsavosh B., Dorsa A., Nima M., Mohadese R., Pasha P., Mahshid M., Alireza G., Niloofar G., Mehrak A., Mohammadreza S., Caio V., Patrick S., Fleur B., Marielle B., Mathieu C. and many other friends that I did not list here. Thank you Dara V. and Soroosh S. for all you did for me these years and your eternal support at any moment I needed. Your friendship is of the most significant assets I have gained in my life.

I thank you Shamim for all the patience you had when we were far apart, all the love and care you carry for me, and the warmth of love and hope that you sustain in my heart. Last, but not least, I would like to express my deepest gratitude to my parents, for their self-abnegation, the infinite love and support they gave me at every single moment of my life, the tranquillity they gifted to me with their smiles, and the trust they gave me to pursue what I love in this journey.

Lausanne, January 19, 2023

S. E.

Abstract

This thesis is dedicated to the analysis of a subclass of interfacial flows, columnlike free-interface flows, from two view angles: (i) the symmetry breaking under geometry-induced or external forces, (ii) their stability against infinitesimal disturbances. We employ the domain perturbation method to address three flow types by means of linear stability analysis. First, we examine the flow down an eccentric vertical fibre: the non-axisymmetric base flow brings interfacial shear into play to deform the capillary-driven Rayleigh-Plateau modes. A large enough eccentricity destabilises extra whirl modes despite the surface energy barrier to coil the interface. The linear analysis concludes according with our experiments that the combination of a thin fibre (with respect to the liquid column), a large Bond number (Bo , that compares gravitational forces with surface tension), and large eccentricity leads to the destabilisation and dominance of the whirl mode. We secondly study numerically and theoretically the draining liquid film coating the inside of a horizontal tube at moderate Bo . The buoyancy-driven rising interface deforms as Bo increases, and a large enough deformation can suppress the Rayleigh-Plateau instability at large times. The linear analysis seconds pre-existing experiments in the literature, showing that the critical stabilising Bo increases with the average film thickness, irrespective of finite inertia and transient growth of the perturbations. Thirdly, we explore the draining film down a horizontal cylinder, a configuration suitable for the co-existence of the Rayleigh-Plateau and Rayleigh-Taylor instabilities. The base flow either reaches a quasi-static pendant equilibrium or keeps falling until a two-dimensional rupture occurs. Nonlinear simulations suggest that the critical Bo to maintain a pendant curtain scales inversely with mean film thickness. The resulting quasi-static state is linearly unstable and the collective action of capillary and gravitational effects can form two distinct patterns: (i) pearls enveloping the cylinder when surface tension dominates, (ii) vertical fingers underneath the cylinder when gravity dominates. The most linearly amplified mode will either form an array of pendant drops or result in a three-dimensional rupture, a threshold found unaffected by the transient growth of the perturbations. Lastly, we inspect numerically an electrified liquid jet falling vertically from a nozzle by coupling the flow and electric field equations. When electrical forces dominate surface tension (at large electric Bond number), the interface smoothly transitions to a conical meniscus at the nozzle tip emitting a fine jet downstream. This is due to the tangential electrical stress at the interface that folds the streamlines in the vicinity of the nozzle tip. Further raising the electrical Bond number reinforces the thinning, increases the cone half-angle, and sets in a recirculating cell at the nozzle tip to conserve the flow rate.

Keywords: symmetry breaking, free-interface, stability analysis, pattern formation, meniscus

Résumé

Cette thèse est consacré à l'analyse d'un type d'écoulements interfaciaux, plus précisément d'écoulements à interface libre adoptant une géométrie "en colonne". Notre analyse se concentre sur la caractérisation (i) de la possible brisure de symétrie induite par des forces géométriques ou externes et (ii) de leur stabilité en réponse à des perturbations infinitésimales, par une méthode basée sur la perturbation du domaine combinée à une analyse de stabilité linéaire, pour traiter trois types d'écoulement. En premier lieu, nous examinons l'écoulement le long d'une fibre verticale excentrée. L'écoulement non-axi-symétrique de base introduit un cisaillement interfacial déformant les modes classiques de Rayleigh-Plateau gouvernés par effets capillaires. Une excentricité assez grande conduit à l'enroulement hélicoïdal de l'interface, malgré la barrière énergétique de surface du système. L'analyse montre que la combinaison d'une fibre fine (par rapport à la colonne liquide), d'un nombre élevé de Bond (Bo , paramètre qui compare les forces gravitationnelles et la tension superficielle) et d'une grande excentricité induit la déstabilisation de l'écoulement alors dominé par les modes de vorticit . Dans un second temps, le film liquide drainant recouvrant l'int rieur d'un tube horizontal est  tudi    valeurs mod r es de Bo . L'interface montant sous l'effet de la flottabilit  se d forme   mesure que Bo augmente. Une d formation suffisamment importante peut conduire   la suppression de l'instabilit  de Rayleigh-Plateau pendant une longue p riode. L'analyse lin aire suit les exp riences rapport es dans la litt rature et montre que le Bo critique pour la d stabilisation augmente avec l' paisseur moyenne du film, ind pendamment de l'inertie et de la croissance transitoire des perturbations. Dans un troisi me temps, nous observons le film drainant le long d'un cylindre horizontal, configuration adapt e   la co-existence des instabilit s de Rayleigh-Plateau et de Rayleigh-Taylor. L' coulement de base atteint soit un  quilibre de type pendule quasi-statique, soit se poursuit jusqu'  la rupture bidimensionnelle. Les simulations non lin aires sugg rent une valeur critique de Bo pour maintenir l' quilibre susmentionn  inversement proportionnelle   l' paisseur moyenne du film. L' tat quasi-statique qui en r sulte est lin airement instable, et l'action collective des effets capillaires et gravitationnels peut produire deux situations distinctes : (i) des "perles" recouvrant le cylindre lorsque la tension superficielle domine ou (ii) des structures verticales digitiformes lorsque la gravit  domine. Le mode le plus amplifi  formera une s rie de gouttes pendantes ou conduira   une rupture de sym trie tridimensionnelle ult rieure, dont le seuil n'est pas affect  par la croissance transitoire des perturbations. Enfin, nous  tudions la dynamique d'un jet de liquide  lectrifi  tombant verticalement d'une buse, par une approche couplant  quations de l' coulement et du champ  lectrique. Lorsque les forces  lectriques

Résumé

dominant la tension superficielle, l'interface se transforme lentement en un ménisque conique à l'extrémité de la buse. par la tension électrique tangentielle à l'interface qui déforme les lignes de courant près de la buse. En augmentant encore le nombre de Bond électrique, on observe un amincissement du jet, une augmentation du demi-angle du cône et l'apparition d'une zone de recirculation au niveau de la buse visant à préserver le débit.

Mots clés : brisure de symétrie, interface libre, analyse de stabilité linéaire, formation de motifs, ménisque

Riassunto

La tesi è dedicata all'analisi di flussi con interfaccia libera di tipo colonnare. L'analisi è incentrata sulla caratterizzazione (i) di possibili rotture di simmetria causate da forze geometriche o esterne e (ii) della loro stabilità rispetto a disturbi infinitesimali. Tre tipi di flusso sono analizzati con un metodo basato sulla perturbazione del dominio combinato con la stabilità lineare. In primo luogo, esaminiamo il flusso lungo una fibra verticale eccentrica: il flusso base, non assialsimmetrico, ha sforzi di taglio interfacciali che deformano i modi di Rayleigh-Plateau classici, governati da effetti capillari. Un grande eccentricità di fibra destabilizza i modi vorticosi che portano ad un avvolgimento elicoidale dell'interfaccia intorno alla fibra nella direzione del flusso. Il sistema si oppone a tali deformazioni grazie a barriera energetica associata alle deformazioni interfaccia. L'analisi lineare e i nostri esperimenti mostrano che la combinazione di una fibra sottile (rispetto alla colonna di liquido) con un alto numero di Bond (Bo , che mette a confronto forze gravitazionali e tensione superficiale) e una grande eccentricità di fibra induce la destabilizzazione del flusso, guidato dai modi vorticosi. In secondo luogo, la dinamica di un film liquido sull'interno di un cilindro orizzontale viene studiata da un punto di vista numerico e teorico per valori di Bo moderati. In tale configurazione, si crea un'interfaccia di risalita guidata dal galleggiamento, che si deforma all'aumentare di Bo , fino alla soppressione dell'instabilità di Rayleigh-Plateau per tempi lunghi. L'analisi lineare conferma esperimenti presenti in letteratura e mostra che il Bo critico per la stabilizzazione aumenta con lo spessore medio del film, indipendentemente da valori finiti di inerzia e dalla crescita transitoria delle perturbazioni. In terzo luogo, esploriamo la dinamica di un film sull'esterno di un cilindro orizzontale. Le instabilità di Rayleigh-Plateau e Rayleigh-Taylor coesistono. Il flusso base raggiunge un equilibrio di tipo pendolo quasi-statico, o continua a valle fino alla rottura della simmetria che lo rende bidimensionale. Simulazioni non lineari mostrano che il valore critico di Bo per mantenere l'equilibrio sopra citato scala inversamente allo spessore medio del film. L'azione di effetti capillari e gravitazionali può produrre due stati quasi-statici linearmente instabili: (i) "perle" che ricoprono il cilindro quando la tensione superficiale domina o (ii) strutture verticali digitiformi orientate verso il fondo del cilindro quando la gravità domina. Il modo linearmente più amplificato forma una serie di gocce pendenti con una successiva rottura di simmetria, in questo caso tridimensionale, la cui soglia non è influenzata dalla crescita transitoria di eventuali perturbazioni. Infine, investighiamo la dinamica di un getto liquido elettrificato che fuoriesce verticalmente da un ugello. Le equazioni del flusso e del campo elettrico sono accoppiate numericamente. Quando le forze elettriche dominano sulla tensione superficiale (ad alti Bo elettrici), l'interfaccia è un menisco

Riassunto

conico all'estremità dell'ugello che emette un getto sottile. Ciò è dovuto alla tensione elettrica tangenziale all'interfaccia che deforma le linee di flusso in prossimità della punta dell'ugello. L'aumento del Bo elettrico rafforza l'assottigliamento, aumenta il semi-angolo del cono e crea un ricircolo in corrispondenza dell'ugello che conserva la portata.

Parole chiave: rotture di simmetria, interfaccia libera, linearmente instabili, formazione di motivi, menisco

Contents

Acknowledgements	i
Abstract (English/Français/Italiano)	iii
1 Introduction	1
1.1 Instabilities of interfacial flows	3
1.1.1 Stability analysis	3
1.1.2 Rayleigh-Plateau instability	6
1.1.3 Rayleigh-Taylor instability	8
1.2 In this thesis	10
1.3 Thesis outline	10
2 A versatile formulation for the linear analysis of perturbed columnlike interfaces	13
2.1 Some special geometries	18
2.1.1 Axially-invariant interface	18
2.1.2 Cylindrical interface	20
2.1.3 Axially varying interface with circular cross-section	21
2.2 Numerical implementation in COMSOL Multiphysics TM	23
2.2.1 Variable operator versus finite element space	24
2.2.2 Proposed numerical model	26
2.2.3 Method validation	28
2.3 Method limitations and future perspective	28
3 Whirling instability of an eccentric coated fibre	33
3.1 Introduction	34
3.2 Governing equations and methods	35
3.2.1 Problem formulation	35
3.2.2 Base Flow	37
3.2.3 Linear stability analysis	39
3.2.4 Numerical method	40
3.3 Results	41
3.3.1 Effect of the fibre eccentricity (R_{ec})	41
3.3.2 Bo and α effects	43
3.3.3 Phase diagrams	43

3.3.4	Energy analysis	45
3.3.5	Experimental observations	48
3.4	Summary and conclusion	51
3.5	Appendix	53
3.5.1	Derivation of the interface boundary conditions	53
3.5.2	Variational formulation of problem and implementation of boundary conditions	53
3.5.3	Validation of numerical model	56
3.5.4	Derivation of the energy equation	58
3.5.5	Image analysis of the experiments	60
4	On the liquid film instability of an internally coated horizontal tube	63
4.1	Introduction	64
4.2	Governing equations and methods	66
4.2.1	Problem formulation	66
4.2.2	Base flow	67
4.2.3	Linear stability analysis	69
4.2.4	Transient growth analysis	70
4.2.5	Numerical method	72
4.3	Stability analysis results	73
4.3.1	Stability of draining film at different instants of its evolution	73
4.3.2	Effect of the Bond (Bo) number	74
4.3.3	Effect of the Ohnesorge (Oh) number	76
4.3.4	Asymptotic linear stability diagram	77
4.3.5	Why does increasing Bond number stabilise the flow?	78
4.3.6	Maximal unstable wavenumber	81
4.3.7	Validity of the frozen frame assumption	81
4.3.8	Transient growth analysis	83
4.4	Summary and conclusion	85
4.5	Appendix	87
4.5.1	Derivation of the interface boundary conditions	87
4.5.2	Variational formulation of the linear stability analysis and implementation of boundary conditions	88
4.5.3	Characterization of an arbitrary interface	89
4.5.4	Derivation of a simplified expression for the energy density of the transient response.	92
4.5.5	Validation of the numerical model	93
5	Stability of liquid film coating a horizontal cylinder: capillary and potential interplay	97
5.1	Introduction	98
5.2	Governing equations and methods	100
5.2.1	Problem formulation	100

5.2.2	Base flow	102
5.2.3	Linear stability analysis of the pendant curtain	104
5.2.4	Transient growth analysis	106
5.2.5	Numerical method	108
5.3	Results	109
5.3.1	Linear stability of the pendant curtain	109
5.3.2	Energy analysis	111
5.3.3	Linear prediction: pattern formation and three-dimensional pinch-off	115
5.3.4	Transient growth analysis	117
5.4	Summary and conclusion	118
5.5	Appendix	121
5.5.1	Derivation of the interface boundary conditions	121
5.5.2	Variational formulation of the linear stability analysis and implementation of its boundary conditions	122
5.5.3	Derivation of a simplified expression for the energy density of the transient response.	122
5.5.4	Validation of the numerical model	123
5.5.5	Derivation of the energy equation	126
6	Modeling melt electrowriting beam	129
6.1	Introduction	129
6.2	Governing equations and methods	131
6.2.1	Problem formulation	131
6.2.2	Numerical method	133
6.3	Results	137
6.3.1	Influence of the electrical Bond number (χ)	137
6.3.2	Jet interface	139
6.3.3	Effect of the gravity	141
6.4	Summary and perspective	142
6.5	Appendix	144
6.5.1	Surface divergence in the cylindrical coordinates	144
6.5.2	Validation of the numerical model	144
7	Conclusions and perspectives	149
7.1	Conclusions	149
7.2	Perspectives	152
7.2.1	Methodological perspectives	152
7.2.2	Theoretical, numerical and experimental perspectives	152
	Bibliography	159
	Curriculum Vitae	175

1 Introduction

The study of interfacial flow, that is, of the flow of immiscible fluids in contact with each other and separated by physical interfaces, is one of the classical branches of fluid mechanics. These flows are omnipresent in nature, have captured the attention of human beings, and have challenged scientists for centuries. Sometimes constructive, as in the exchange of mass, heat, and gas on the ocean surface, or sometimes devastating, as in tsunamis, interfacial flows play a significant role in life on our planet and span a wide variety of scales, from nanopores (Hibara et al., 2016; Zhang et al., 2019) up to kilometer scale of oceans (Garvine, 1974; Eames and Flor, 2011; Kneller et al., 2016). Countless natural observations inspired humans for take advantage of the interfacial flow phenomena, not only for applied engineering purposes but also for joy and aesthetics. In our childhood, we enjoyed splashing water in the bathtub and chasing soap bubbles, and in our adult lives, we refresh our moods while relishing hot summer days on water slides and challenging our artistic creativity while drawing schemes layer-by-layer with oil paint on canvas. None of these pleasures are possible without interfacial flows.

Besides, innumerable examples can be thought of in our technology-based today life where fundamental interfacial phenomena are entangled. Particularly, the laminar flows in the small characteristic length scales, from microns up to a few centimeters are of great interest as the fluid motion is smooth and one may represent and control it thanks to analytical solutions of the flow equations or their high-resolution numerical counterparts (Smith, 1982; Schrauf, 2005). Examples of using laminar interfacial flows of small length scale in industries include continuous casting (Santos et al., 2001; Mohammad Karim, 2022), substrate coating (De Meijer, 2004; Buerkin et al., 2017), lubricant cooling (Barbosa and Jader, 2018; Chen et al., 2021), liquid atomisation (Eggers and Villermaux, 2008), fuel cells (Mousavi Shaegh et al., 2011), oil extraction and transfer (Shah, 2012; Joseph and Renardy, 2013a,b), cell cultivating and pharmaceutical industry (Chen et al., 2012; Zhu et al., 2017b,a), soft tissue printing (Zhou et al., 2020), and powder focusing 3D printing (Hoffmann, 2017) to name a few.

When interfacial laminar flow is incorporated into processes, flow instabilities are a common concern. Let us first describe a stable flow before explaining what flow instability means. Here is a quote from James Clerk Maxwell, a renowned mathematician and scientist of the 18th

century, who demonstrated the qualitative concept of stable and unstable flows:

"When an infinitely small variation of the present state will alter only by an infinitely small quantity the state at some future time, the condition of the system, whether at rest or in motion, is said to be stable but when an infinitely small variation in the present state may bring about a finite difference in the state of the system in a finite time, the system is said to be unstable." (Drazin, 2002)

Pursuing this description, instability implies a finite transition in time between two states of the flow that occur under a small variation, hereafter referred to as the *perturbation* or *disturbance*. In classical fluid dynamics, and in the absence of heat and mass transfer, the state of a flow is merely described by the velocity and pressure fields within the fluid domain and its boundaries which we choose to describe using the following notations.

Throughout this thesis, time is denoted by $t[s]$, the three-dimensional spatial coordinates are denoted by $\mathbf{x} = (x_1, x_2, x_3)^T$ where $x_j[m]$ are independent orthogonal spatial coordinates, the three-dimensional velocity field is denoted by the velocity vector $\mathbf{u}[m/s]$, pressure is denoted by the scalar $p[Pa]$, and the coordinates of the fluid domain boundary is denoted by \mathbf{x}_b . Unless otherwise noted in this chapter, the quantities are introduced in their dimensional form whose dimension is presented in the brackets. These values are referred to also as the *state variables*. The state of a flow is denoted thus by the *state vector* $\mathbf{q}(t, \mathbf{x}) = (\mathbf{u}, p, \mathbf{x}_b)^T$, which is a vector including all state variables. The state vector of any continuum fluidic medium is fundamentally governed by the conservation of mass and momentum, that is, the differential representation of second Newton's law expressing the force balance on fluid elements. These governing equations in differential form, respectively, can be expressed for an incompressible fluid as

$$\nabla \cdot \mathbf{u} = 0, \quad (1.1)$$

$$\rho (\partial_t + \mathbf{u} \cdot \nabla) \mathbf{u} = \nabla \cdot \underline{\underline{\tau}} + \mathbf{f}, \quad (1.2)$$

where $\rho[kg/m^3]$ denotes the fluid density, ∂_i denotes the partial derivative with respect to the quantity i (not to be mixed with the imaginary part of a complex-valued quantity), ∇ denotes the gradient operator, $\underline{\underline{\tau}}[Pa]$ denotes the stress tensor, and $\mathbf{f}[N/m^3]$ denotes body force field per unit volume. In the context of the present thesis, $\mathbf{f} = \rho \mathbf{g}$, where $\mathbf{g}[m/s^2]$ denotes the gravitational acceleration. For a Newtonian fluid of constant dynamic viscosity $\mu[Pa.s]$, a particular limit of media of interest in the present thesis, the stress tensor can be expressed as

$$\underline{\underline{\tau}} = -p\mathbf{I} + \mu(\nabla \mathbf{u} + \nabla \mathbf{u}^T). \quad (1.3)$$

Relation (1.1) is referred to as the continuity or incompressibility equation, and the vectorial equation (1.2) is referred to hereafter as the momentum equation. Further simplification of the momentum equation (1.2) using the incompressibility (1.1), gives the Navier-Stokes

equations as follows:

$$\nabla \cdot \mathbf{u} = 0, \quad (1.4)$$

$$\rho (\partial_t + \mathbf{u} \cdot \nabla) \mathbf{u} = -\nabla p + \nabla^2 \mathbf{u} + \mathbf{f}, \quad (1.5)$$

where $\nabla^2 = \nabla \cdot \nabla$ is the Laplacian of a vector field. From the mathematical point of view, the Navier-Stokes equations form a system of deterministic non-linear partial differential equations, second order in velocity and first order in pressure. Solving this system of equations requires a proper set of *boundary conditions* and an *initial condition*. A thorough summary of classical boundary conditions can be found in (Batchelor, 2000) or other fluid mechanics references. In each chapter of the present thesis, we will recall the proper set of boundary conditions that are relevant to the associated flow. The solution of the governing equations describes the state of a flow at any time. Knowing the state at each instance, one can follow systematic approaches, inspired by the description of the flow instability which was previously introduced qualitatively in this section, to determine the effect of disturbances on the flow stability. In §1.1 we present some of these systematic approaches employed in the present thesis, entitled *linear stability analysis*, and we shed light on some classical instabilities of interfacial flows, that are relevant in the context of this work.

1.1 Instabilities of interfacial flows

When the fluid properties are constant and in absence of any external forcing (like magnetic or electric excitation), surface tension, gravity, shear, and inertia may cause six major families of interfacial instabilities, depending on the possible existence of a fluid-solid contact, flow and/or interface geometry, relative flow at two sides of the interface, and the orientation of gravity with respect to the fluid interface. (See Gallaire and Brun (2017) for a review of these instabilities.) These instabilities are the capillarity-driven Rayleigh-Plateau instability, gravity-driven Rayleigh-Taylor instability, shear-driven Kelvin-Helmholtz instability, mobility-driven Saffman-Taylor instability, inertia-driven Kapitza instabilities, and contact line-driven instabilities. Hereafter we focus on the first two types of instabilities, namely the Rayleigh-Plateau and Rayleigh-Taylor instabilities.

1.1.1 Stability analysis

A classical approach for theoretically studying fluid flow stability is based on the dynamics of the small amplitude perturbations using the perturbation theory (for more details about the perturbation theory, see Bender et al. (1999)). Accordingly, the superposition of an unperturbed state \mathbf{q}^0 by small perturbation $\epsilon \mathbf{q}^1$ where $\epsilon \ll 1$, and casting it to the governing equations of the flow yields a natural separation of orders where the first two leading orders correspond to the unperturbed flow evolution and the linear spatio-temporal evolution of the perturbations, respectively.

Introduction

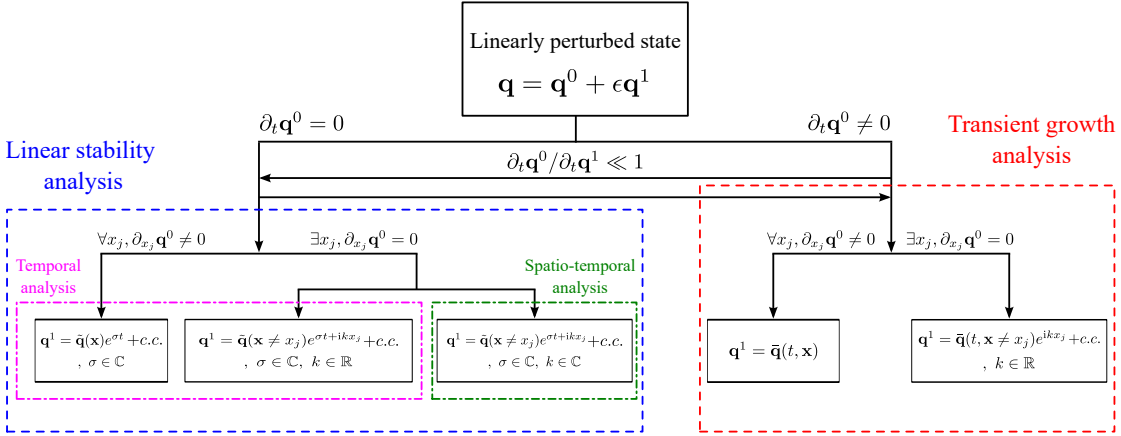
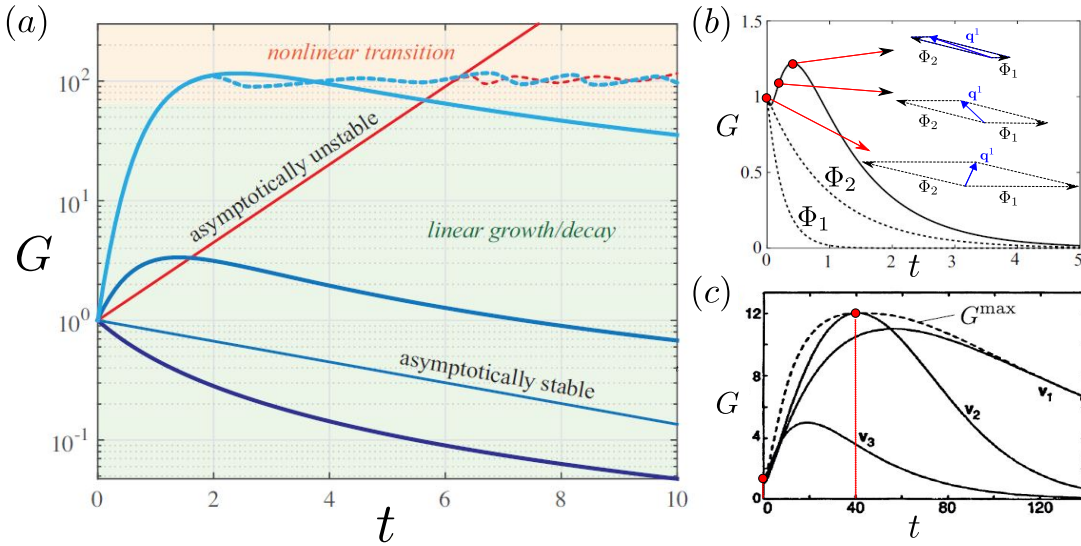


Figure 1.1: Summary of the classical small perturbation stability analyses, where $\epsilon \ll 1$; the state vector is denoted by \mathbf{q} , and spacial coordinate vector is denoted by $\mathbf{x} = (x_1, x_2, x_3)^T$.



A vast number of analyses investigate the unperturbed flows, hereafter *base flow*, which are time- or space-invariant. In such a case, the linearity of the mathematical system for small perturbations allows one to decompose them as a sum of Fourier modes, and investigate the evolution of each mode individually, thus conducting a *modal analysis*. Decomposition of the perturbations is plausible for each dimension from which the base flow is independent. For a steady-state base flow, the complex temporal Fourier mode of the so-called *normal-mode ansatz* $\mathbf{q}^1 = \tilde{\mathbf{q}}(\mathbf{x}) \exp(\sigma t) + c.c.$, where *c.c.* denotes the complex conjugate of a complex number is relevant, $\Re(\sigma)$ represents the growth rate of perturbations, and $\Im(\sigma)$ represents their frequency of oscillations, and the analysis is entitled to the *linear stability analysis*. For spatially-invariant base flows in the x_j direction, Fourier modes of the form $\exp(ik_j x) + c.c.$ are relevant. A complex temporal and spatial decomposition of the form $\mathbf{q}^1 = \tilde{\mathbf{q}}(\mathbf{x} \neq x_j) \exp(\sigma t + ik_j x_j) + c.c.$ leads to a spatio-temporal analysis of perturbations, whereas attributing the complex modes only to time, results in their temporal analysis. In the latter case, if the base flow is zero in the invariant spatial direction, the study is referred to as a *local stability analysis*, otherwise, a *global stability analysis*. This classification is summarised in figure 1.1. Figure 1.2(a) depicts different possibilities for the evolution of the perturbations. In any of the above-mentioned decompositions with a steady base flow, the ansatz allows the transformation of the linear problem into a generalised eigenvalue problem where $\Re(\sigma) > 0$ (resp. $\Re(\sigma) < 0$) indicates an asymptotically unstable (resp. stable) behaviour, sketched with red-thin (resp. blue-thin) line in figure 1.2(a).

In spite of the asymptotic insight gained from the spatio-temporal analysis of the perturbations when $t \rightarrow \infty$, it cannot guarantee the identical behaviour of the linear perturbations in the short term (cf. figure 1.2(a)). This approach ignores the interaction between modes at all times. Nevertheless, when the linear operator associated with the linear system is non-normal (Schmid et al., 2002), meaning that the eigenvector basis is non-orthogonal, the short-term interaction between the modes can result in a transient gain in the energy of the perturbations (cf. figure 1.2(b)). Consequently, the perturbations' energy coming from the small external noises (inevitable in any flow) may be amplified by several orders, triggering non-linearities for a different fate than is predicted by linear stability analysis. Notably, linear stability analysis has failed in providing the proper comprehension of the mechanism underlying the laminar-to-turbulence transition in several wall-bounded shear flows (Schmid, 2007). As an example, in the pipe flow and Couette flow, all eigenmodes are predicted to be linearly stable, thus decaying monotonously in time. Nevertheless, due to the non-normality of these systems, the transient interaction between the linearly stable modes at large Reynolds number exhibits a large energy gain (cf. figure 1.2(c)), referred hereafter to a *transient growth* of the perturbations before decaying at large times, thus destabilisation of the laminar flow and transition to turbulent flow (Trefethen et al., 1993; Schmid and Henningson, 2001). Several free-interface flows also present significant transient growth, as a rising drop at low Reynolds number (Gallino et al., 2016), or the driven contact-line fingering instability (Bertozzi and Brenner, 1997; Balestra et al., 2019).

Additionally, the dynamics of the perturbations applied to time-dependent base flows cannot

be studied by employing the linear stability analysis. In the limit of a slowly varying base flow, one remedy is to approximate the base state at each time with a quasi-steady-state, so-called a *frozen frame*. Then, it is possible to apply the modal linear stability analysis to each frozen frame, sequentially. The key assumption in the linear stability analysis of the frozen frames is that perturbations grow considerably faster than the base flow evolves itself. This assumption cannot be verified before conducting the analysis, thus the validity of the frozen frame approximation must be investigated *a posteriori*. This method was successfully applied for instance in the early study of Tan and Homsy (1986) on the miscible viscous fingering instability in porous media, where comparison of results with initial value solutions of the full governing equations suggests that frozen frame linear stability analysis gives a good prediction for the most unstable wavelengths, except for short times. Even though the frozen frame assumption is beneficial to shed light on the asymptotic behaviour of the slowly varying time-dependent flows, the short-term dynamics of small perturbations can merely be demonstrated rigorously by a transient growth analysis. Taking the time-varying thin film flow coatings on the underside of some curved substrates, for example, the drainage solution is found asymptotically linearly stable, although droplets often form in reality. Generalising the experimental and theoretical observations of Trinh et al. (2014), Balestra et al. (2016, 2018a,b) showed that transient growth of small perturbations can cause dripping or formation of rivulets that span in the transversal direction. Their results agree favourably with the non-linear simulations. Thus, transient growth analysis can be used to analyse perturbation evolutions at short time scales, as well as to take time-dependent flows into account that cannot be fully addressed with modal analysis (Schmid, 2007).

In the following section, we demonstrate two key instabilities associated with interfacial flows of the columnlike interfaces. Such interfaces are materialised in divers moving and stagnant flows of various interests, like in curved liquid sheets, jets, threads, co-flows, and bubbles.

1.1.2 Rayleigh-Plateau instability

The Rayleigh-Plateau instability is the principal mechanism underlying the bubble and drop formation emerging from columnlike interfaces (cf. figure 1.3). Long round interfaces of various configurations, like free jets, and liquid film coating the exterior or interior side of a cylindrical wall among many, are subject to this instability under which they break up into droplets, beads, and plugs, respectively (cf. figure 1.3(a), see Gallaire and Brun (2017) for a review on their similarities in pattern formation).

The first evidence of investigating the Rayleigh-Plateau instability dates back to the early study of fluid jets by Savart (1833). It took some decades until Plateau (1873) and Rayleigh (1878, 1879) quantified this phenomenon independently for round liquid jets and threads, stating that such a transition is in favour of surface energy minimisation (see Eggers and Villermaux (2008) for a review). Plateau (1873) showed that when the length of a liquid column is larger than its cross-sectional periphery, the transition to droplets occurs. Rayleigh (1878) followed a

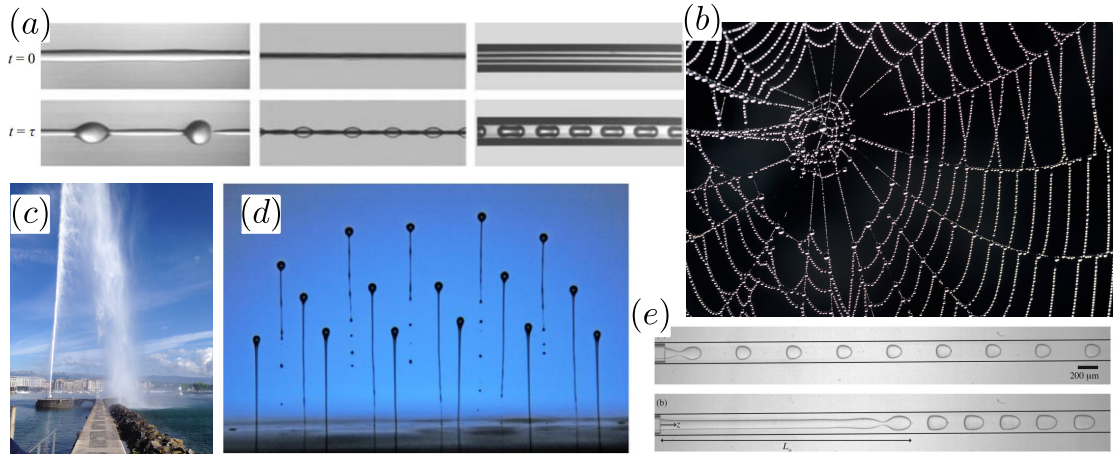


Figure 1.3: Examples of the Rayleigh-Plateau instability: (a) Three variants of the instability before (top row) and after (bottom row) occurrence: liquid jet (left); liquid column coating a fibre (middle); liquid film coating inside a tube (right), reprinted from Duclaux et al. (2006); (b) Drop formation on wet spider silk; reprinted from (<https://news.mit.edu/2012/spider-web-strength-0202>); (c) Segregation of the Geneva water fountain (140 m height) into tiny clusters of droplets; reprinted from (https://commons.wikimedia.org/wiki/File:Le_jet_d-eau_de_Gen%C3%A8ve.jpg); (d) Micrometer size drops emerging from a bank of ink-jet nozzles; reprinted from (<https://www.in-fuseon.com/>); (e) Co-axial two-phase flow in a micro-channel; reprinted from Cordero et al. (2011).

classical linear stability approach for an infinitely long inviscid liquid jet in air and illustrated that the threshold for the interface destabilisation depends only on the geometry, identical to that obtained by Plateau (1873). His analysis suggests that this threshold is due to the dual role of the interface curvature while being undulated in the streamwise direction. The axial curvature has a stabilising effect, whereas cross-sectional curvature has a destabilising effect, thus the above-mentioned threshold for column instability. Furthermore, his linear analysis proposed, in very good agreement with experiments of Savart (1833), for an inviscid jet the most amplification for the perturbations with a wavelength of $2\sqrt{2}\pi$ times the jet radius. Viscosity does not alter the instability threshold but pushes the most amplified perturbation to longer wavelengths, i.e. smaller wavenumbers (Rayleigh, 1892; Chandrasekhar, 2013; Augello, 2015; Pekker, 2018). On top of that, Rayleigh (1879) showed that the modification to the surface of a linearly perturbed cylinder is proportional to its increment of local curvature, which decreases only for axisymmetric perturbations. Thus all non-axisymmetric perturbations increase the surface energy and should be damped.

As mentioned earlier, the liquid film coating on a vertical fibre or inside tube experiences a similar capillary instability as the liquid jet, hence can be classified as the variants of the Rayleigh-Plateau instability. Craster and Matar (2006) and Camassa et al. (2014) followed a similar approach as Rayleigh (1878, 1879) and addressed analytically the linear stability of these variants, respectively. The Rayleigh-Plateau instability is ubiquitous in nature (cf. figure 1.3(b,c)) and has multiple practical applications from the micrometer-scale, in several

printing (cf. figure 1.3(d)), medical and microfluidic devices (Rodriguez-Rodriguez et al., 2015)(cf. figure 1.3(e)), up to the meter-scale in jets (Eggers and Villermaux, 2008)(cf. figure 1.3(c)), and heat exchanging systems (Zeng et al., 2018).

Rayleigh-Plateau instability is pertinent in many applications, like in the jet flow, annular co-flow, and liquid film coating on different sides of the conduits. These flows are involved in a multitude of processes, e.g. in oil transport (Joseph et al., 1997) and two-phase heat exchangers (Zeng et al., 2018; O'Neill and Mudawar, 2020b), gas exchange and purification processes (Zeng et al., 2019), and biological processes in the human airways (Camassa et al., 2014), among many. In all examples, this flow instability can affect the process in a desirable or undesirable fashion. While it can be favourable in altering the effective heat exchange surface when cooling the exterior side of the pipes, it can be destructive by lowering the heat exchanging efficiency in the condensers (Dobson and Chato, 1998; Teng et al., 1999). Also in the human body, when it happens to the mucous covering the human airways, it can be dangerous as it can cause airway closure (Heil et al., 2008; Levy et al., 2014).

1.1.3 Rayleigh-Taylor instability

When a heavier fluid is placed on top of lighter fluid with gravity pointing downward, toward the lighter one, the interface separating two fluids is subjected to the Rayleigh-Taylor instability (Rayleigh, 1882; Taylor, 1950), thus the formation of fingers (Lewis, 1950; Sharp, 1984) (cf. figure 1.4). More precisely, an immiscible liquid-gas/liquid-liquid interface transforms under capillary forces into advancing fingers, forming under non-linearities pendant droplets (Pitts, 1973; Yiantsios and Higgins, 1989) (cf. figure 1.4(a,d)), or rivulets (Charogiannis et al., 2018; Balestra et al., 2018a) depending on the geometrical conditions which may or may not pinch-off (Ledda and Gallaire, 2021; Jambon-Puillet et al., 2021) (cf. figure 1.4(a,b)), whereas, in the case of miscible fluids, the upper fluid sinks, and the lower one rises as a result of buoyancy (cf. figure 1.4(c)).

Early studies of this instability are devoted to two semi-infinite planar domains of inviscid fluids of different densities in contact with each other, whose detailed description is available in Charru (2011) and Chandrasekhar (2013). Such studies considered in the framework of the linear stability analysis of the small uni-directional interface undulations spanning along the interface. They illustrated that perturbations with a wavelength larger than $2\pi \approx 6.28$ times the capillary length are linearly unstable, that is the instability cut-off. Smaller wavelengths create too much surface energy and cannot overcome the energy barrier to grow. Furthermore, the linear analysis suggests that a perturbation of wavelength $3.33\pi \approx 10.47$ times the capillary length should grow the fastest, which agrees well with early experiments of Lewis (1950). Even though the instability threshold remains the same regardless of the viscosity, the presence of a wall and the domains' depth, the fastest-growing wavelength and emerging patterns are affected (see Gallaire and Brun (2017) for further details). For instance, for a thin liquid film on top of light air under a flat horizontal substrate, the highest amplification rate is associated

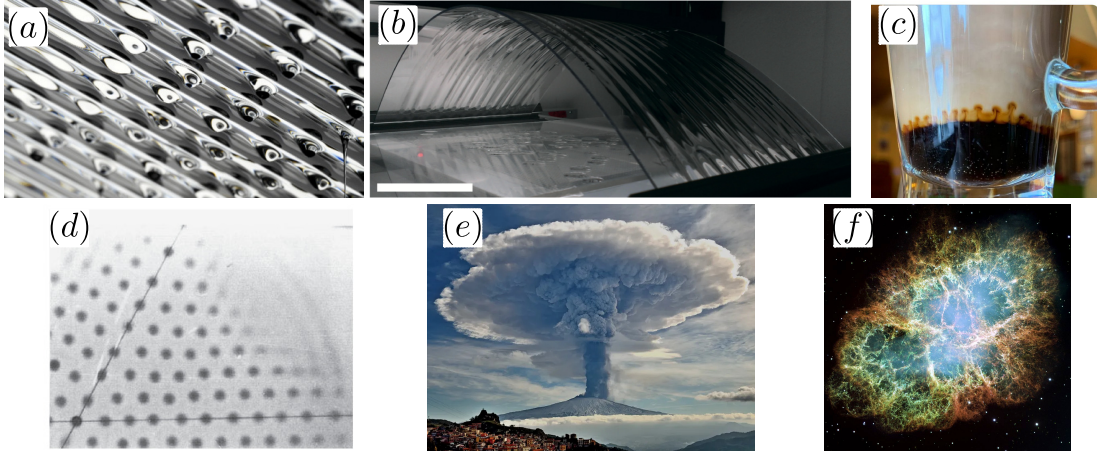


Figure 1.4: Examples of the Rayleigh-Taylor instability: (a) Lenses forming/dripping from the rivulets flowing under an inclined flat plate, reprinted from Lerisson et al. (2019); (b) Transversal rivulets under a curved substrate; reprinted from Balestra et al. (2018a); (c) Fingers at the miscible interface of milk (cold) and coffee (hot); (d) Regular pattern of pendant droplets under a horizontal flat plate; reprinted from Limat et al. (1992); (e) Paroxysm plume from Mount Etna's Voragine crater, Italy, 4 Dec. 2015; Credit: G. Famiani reprinted from (<https://eos.org/research-spotlights/can-we-predict-how-volcanic-ash-disperses-after-an-eruption>); (f) Filaments of the Crab Nebula; Credit: J. Hester and A. Loll; reprinted from (<https://hubblesite.org/resource-gallery/images>).

with the wavelength of $2\sqrt{2}\pi \approx 8.89$ times the capillary length (Limat, 1993).

Numerous recent studies have investigated the effect of geometrical parameters on Rayleigh-Taylor instability, such as the inclination of flat substrates and the finite curvature of the substrate whose underside is covered by fluid film. The geometrical parameters, also relevant in the context of the present manuscript, can give rise to spanwise instabilities (Scheid, 2013; Rietz et al., 2017; Chandrasekhar, 2013; Charogiannis et al., 2018), stable or unstable rivulets (Lerisson et al., 2019; Jambon-Puillet et al., 2021), secondary instabilities (Ledda and Gallaire, 2021), or suppression of the instability (Trinh et al., 2014; Balestra et al., 2016, 2018a).

Many familiar eye-catching fingering patterns, even though not all of them, are formed due to the Rayleigh-Taylor instability. Multiple examples can be found from the millimeter scale droplets formed under painted ceilings or under the ceiling of hammams, up to the kilometer scale plume mushrooms over volcanic areas (cf. figure 1.4(e)), and to the light year scale filaments of the Crab Nebula (Schmidt, 2006; Hester, 2008) (cf. figure 1.4(f)). This instability is substantial in wall cooling in nuclear fusion reactors, and in coating industries, amidst many other applications. In the case of fusion reactors, droplets dripping from the coating liquid, inside the tokamak walls, into the plasma can cause severe incidents (Majeski et al., 2010; Kaita et al., 2010). It can also reduce the quality of painting if fingers drain on a painted surface.

1.2 In this thesis

The dynamics and instabilities of laminar interfacial flows have been studied extensively in the past. The big majority of the previous studies employed averaged models and asymptotical limits of the governing equations, e.g. long-wavelength description for investigating the slender interfaces prone to longitudinal perturbations (Eggers and Dupont, 1994), and thin-film equation for analysing the coating flow on substrates with dimensions considerably larger than the liquid film (Oron et al., 1997). These models, originating from the idea of the lubrication approximation by Reynolds (1886), have achieved remarkable success when the full resolution of the flow is prohibitively expensive, yet the variation in flow quantities is negligible in one spatial direction compared to the others (Eggers and Villerraux, 2008). In spite of their accomplishments, existing asymptotical models are not capable of quantitatively capturing the phenomena whose underlying mechanisms lie in the details of the fully resolved flow. Flow details are typically filtered out if only the averaged flow is considered (Ruyer-Quil and Manneville, 2000; Augello, 2015; Tian et al., 2020). Even though some remedies can be considered to improve these limitations, most of the proposed treatments are useful only when the deviation from the asymptotical or averaged behaviour is still weak so that it can be addressed by considering further orders of magnitude into the asymptotical equations (Ruyer-Quil and Manneville, 2000; Amaouche et al., 2007). As a result, many of these phenomena, which have paramount fundamental importance and technical applications, are missed or not well understood (Duclaux et al., 2006; Gabbard and Bostwick, 2021).

Throughout this thesis, we will employ the classical temporal hydrodynamic instability approaches as well as more modern approaches, to help explain the appearance of patterns for steady and time-varying free-interface flows with columnlike interfaces. Free-interface flows are in essence a subclass of the interfacial flow family where a liquid medium is in contact with air. Recently, and in continuation of the classical studies, several examples (Gallino, 2018; Balestra, 2018; Shukla, 2019; Ledda, 2022) exhibited successfully the link between the dynamics of small perturbations and geometrical characteristics of the patterns emerging after destabilisation of interfacial flows. Our work comprises modal temporal analyses of steady-state and quasi-steady-state flows using their full-flow description, as well as non-modal analysis when there is any time dependence in the flows. Here, external forces exerted on a flow of fixed fluid quantities break temporal invariance, while the geometry of the interface or solid surfaces breaks the spatial invariance.

1.3 Thesis outline

The graphical schematic of the chapters is sketched in figure 1.5. We start in **chapter 2** with the development of a formulation to describe the hydrodynamic boundary conditions at generic columnlike fluid-fluid interfaces. Our formulation lies on the domain perturbation method (Séro-Guillaume and Er-Riani, 1999; Daners, 2008), an extension of the perturbation theory (Bender et al., 1999), and it is suitable for the spatio-temporal analysis of small dis-

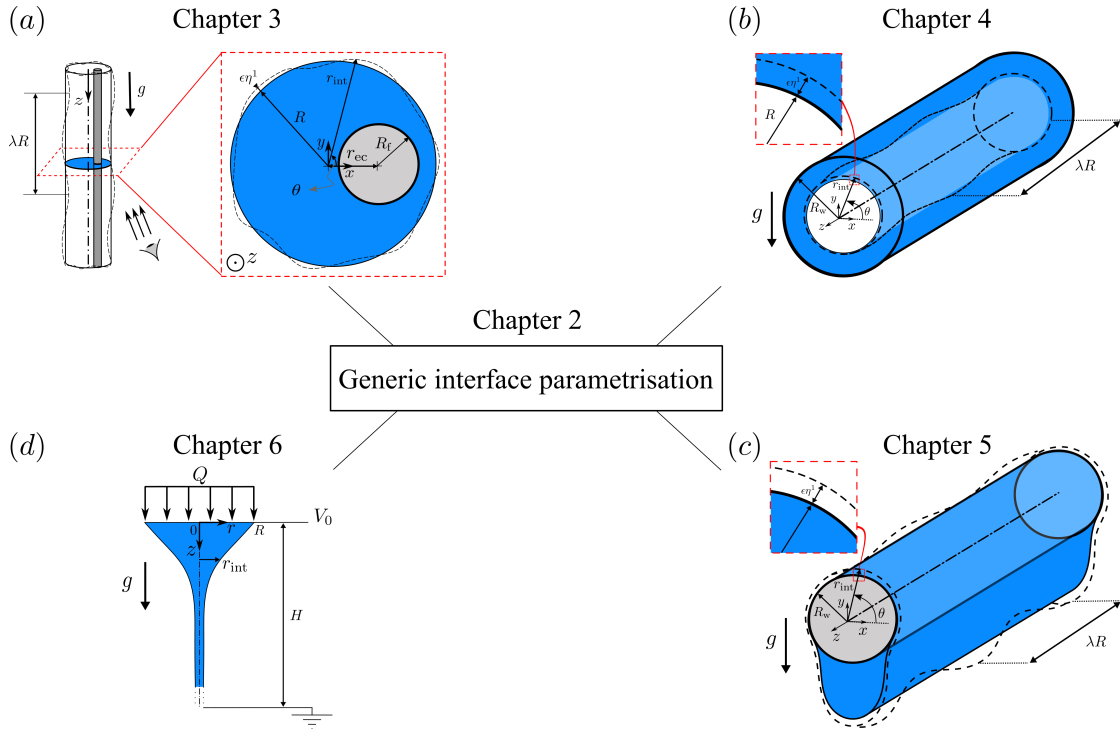


Figure 1.5: Schematic the thesis chapters.

turbances to the flow and its boundaries. After presenting the simplified formulations for several canonical columnlike geometries, and proposing a numerical implementation of the developed formulation, the limits of the method are discussed. This numerical model will be utilised in the following chapters of this thesis.

In **chapter 3** we examine numerically and experimentally the gravity-driven cylindrical liquid column flowing down an eccentric vertical fibre in the inertialess regime (cf. figure 1.5(a)). Here, the symmetry of the base flow is broken due to the fibre displacement. Linearly unstable modes and their thresholds are explored, characterised, and contrasted with the classical Rayleigh-Plateau mode, known for such flows with concentric fibre. Stability diagrams are provided for a wide range of involving dimensionless parameters, and the role of physical mechanisms in flow instability is elucidated.

In **chapter 4** we account for the symmetry breaking in the unperturbed domain, and investigate numerically the gravity-driven flow of thick liquid films coating the interior wall of a long horizontal tube (cf. figure 1.5(b)). After demonstrating the temporal symmetry breaking of the unperturbed flow, the linear stability of the frozen frames and transient growth of the perturbations are analysed and contrasted with the classical Rayleigh-Plateau instability. The good agreement of the results from the full flow equation analysis with the existing experimental data in the literature is discussed.

In **chapter 5** we study numerically the coexisting Rayleigh-Plateau and Rayleigh-Taylor insta-

	Flow axisymmetry	Interface axisymmetry	Axial flow	Axial invariance	Time invariance	Inertia
Chapter 3	×	✓	✓	✓	✓	×
Chapter 4	×	×	×	✓	×	✓
Chapter 5	×	×	×	✓	×	×
Chapter 6	✓	✓	✓	×	×	✓

Table 1.1: Base flow properties for the flows studied in this thesis

bilities during the gravity-driven drainage of a liquid film coating outside a long horizontal cylinder (cf. figure 1.5(c)). As in **chapter 3**, the temporal symmetry breaking of the unperturbed flow is demonstrated. Moreover, linear stability and transient growth analyses are used to characterise emerging two-dimensional patterns. The contributions of different flow instabilities and the most amplified perturbations are evaluated in the resulting patterns along with a prediction of the final three-dimensional structure.

In **chapter 6** we modestly visit numerically the flow of an electrified jet where ionising two fluids in contact induces an extra interfacial stress, so called Maxwell stress, which affects the free-interface. Electrified flows are of notable interest in several applications thanks to their capability for fine jet formation and high throughput drop production (Gañán-Calvo et al., 2018a). The influences of electrical excitement strength on the flow and interface are examined by solving the fully-resolved coupled fluid and electrical field equations.

(In each chapter of this thesis, time-dependence of the flow, spacial variations of the flow field, and non-linear mechanisms induced by interface geometry and inertia play important roles in the symmetry breaking and flow instability. The key features associated to the base flows considered in this thesis are summarised in table 1.1.)

Lastly, in **chapter 7** we conclude this thesis and draw the future perspectives.

This work was financed by the Strategic Focus Area (SFA) Advanced Manufacturing, under the project "Powder focusing for beam induced laser 3D printing" (Hoffmann, 2017).

2 A versatile formulation for the linear analysis of perturbed columnlike interfaces

In this chapter, the parametrisation of an arbitrary interface and the procedure for the numerical implementation of this parametrisation is outlined. Such a parametrisation is essential for imposing the interface boundary conditions while conducting the linear stability analysis and solving linearised Navier-Stokes equations for interfacial flows. Some numerical studies (Augello, 2015; Gallino, 2018) have employed level-set function and boundary integral techniques for this purpose, however, both of these methods have shown their limited applications for a rigorous analysis of curved liquid-liquid and liquid-gas interfaces. More specifically, level-set function is difficult to be linearly perturbed and the boundary integral method is only suitable for zero Reynolds number limit, i.e. in absence of inertia. Many of the existing studies take advantage of the specific geometrical properties of the interface or of depth-averaging methods enabling dimensional reduction like the lubrication for thin coating films (Oron et al., 1997) or the slender jet/thread approximation (Eggers and Dupont, 1994). In addition, geometries with specific symmetries (planes, cylinders, spheres, etc.) are often preferred. Although these limits are sometimes beneficial for linear and non-linear flow analyses, they lose the generality or practicality for a broader range of studies.

For instance, in the case of the temporal evolution of a thick film coating an arbitrary substrate, applying linear perturbation analysis needs a more general formulation that accounts for the instantaneous interface position. In a recent study, Ledda et al. (2022) employed a differential geometry approach to investigate the film thickness in the gravity-driven coating flows on (almost) arbitrarily curved substrates in the thin film limit. They obtained analytical and asymptotical solutions for the film thickness on some generic substrate geometries like ellipsoids or tori. In another interesting study, Bostwick and Steen (2018) followed a similar differential formulation proposed by Kreyszig (2013) to parametrise the interface of a static rivulet on a substrate, followed by its linear stability analysis. Despite the success of the two last-mentioned works with their respective interface geometries, they cannot be readily extended to study the perturbations of an arbitrarily developing interface with an unknown shape *a priori*. For this reason, in the following, we propose an interface parametrisation

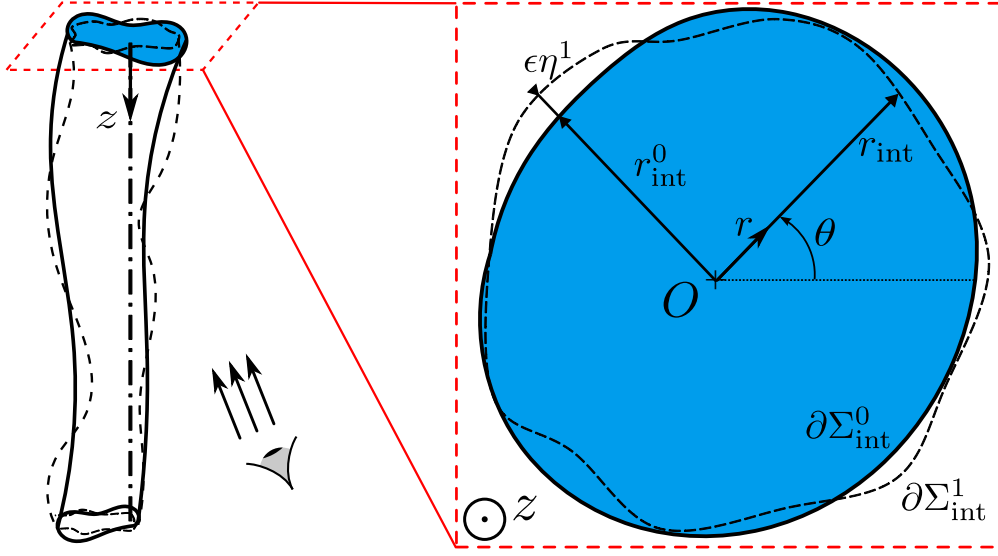


Figure 2.1: Schematic of the interface and geometrical parameters. The right panel shows a planar cross-section of the interface. The solid line shows the unperturbed interface, $\partial\Sigma_{\text{int}}^0$, and the dashed line shows the perturbed interface, $\partial\Sigma_{\text{int}}^1$.

suitable for the linear perturbation analysis of an evolving interface without any particular symmetry assumption. From the perspective of numerical implementation, this method is aimed to be simpler than the differential geometry approach (Kreyszig, 2013) since it does not involve any calculations of the metric tensor, and covariance and contravariance vectors, but it remains versatile enough to be applied on a wide range of interfacial flows.

Consider an arbitrary three-dimensional interface shown schematically in figure 2.1. Inspired by the interfacial flows subject to capillarity stress, we restrict the focus of this analysis to a family of smooth manifolds that can be parameterised by the cylindrical coordinates (r, θ, z) as $\mathcal{F} : r - r_{\text{int}}(t, \theta, z) = 0$ for a well-chosen origin O and axis Oz ; a condition we postulate, hereafter referred to as *explicit radial representation condition*. This condition is quite generic and permits multiple plausible choices of axis Oz inside or outside the liquid bulk as long as r_{int} remains single-valued. Some examples where this condition is violated are discussed in §2.3. As $\mathcal{F} = 0$ defines the material interface, the interface kinematic condition can be obtained from $(\partial_t + \mathbf{u} \cdot \nabla)\mathcal{F} = 0$ which implies

$$\partial_t r_{\text{int}} + \mathbf{u} \cdot \nabla r_{\text{int}} = \mathbf{u} \cdot \mathbf{e}_r \quad \text{at } r = r_{\text{int}}, \quad (2.1)$$

where \mathbf{e}_r denotes the unit radial vector, and the gradient vector in the cylindrical coordinates can be expressed as $\nabla = (\partial_r, 1/r \partial_\theta, \partial_z)^T$. To avoid any singularities of the kinematic condition (2.1), we should exclude from this analysis the interfaces such that $1/r_{\text{int}}^0 \rightarrow \infty$ or $\partial_z r_{\text{int}}^0 \rightarrow \infty$. While the former can be remedied in most cases by a proper choice of axis Oz not intersecting with the base interface, avoiding $r_{\text{int}}^0 = 0$ at any point, the latter restricts the present study to the axially open-ended interfaces. Such an interface is referred to hereafter as *columnlike* interface.

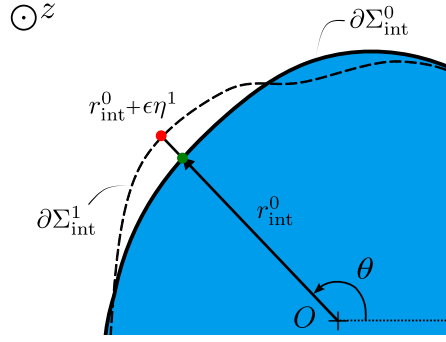


Figure 2.2: Schematic of the flattening: any quantity at the red point on the perturbed interface $\partial\Sigma_{\text{int}}^1$ is expressed as a Taylor series expanded around the same quantity at the green point on the base interface $\partial\Sigma_{\text{int}}^0$.

A columnlike interface can, intuitively, be mapped on at least one cylinder of non-zero radius, employing a one-to-one mapping.

We recall that the dynamic condition at the interface writes

$$\left(\underline{\tau} \mathbf{n}\right)_{\text{in}}^{\text{out}} = -\gamma \kappa \mathbf{n} \quad \text{at } r = r_{\text{int}},^1 \quad (2.2)$$

where $\underline{\tau}$ denotes the stress tensor, $\mathbf{n} = \nabla \mathcal{F} / \|\nabla \mathcal{F}\|$, denotes the interface unit normal vector pointing outward from the origin of the coordinates system O , $\|\cdot\|$ denotes the Euclidean norm, γ denotes surface tension and $\kappa = \nabla \cdot \mathbf{n}$ denotes the mean curvature of the interface. Directions "out" and "in" are measured with respect to O . The body at the same (respectively opposite) side of the interface as O is labeled as "in" (respectively "out").

Following the same formalism, let us now apply infinitesimal perturbations of the form $\epsilon\eta^1$ to a base columnlike interface r_{int}^0 , where $\epsilon \ll 1$. The base interface is marked as $\partial\Sigma_{\text{int}}^0$ in figure 2.1, where the perturbed interface is sketched in an exaggerated manner and marked as $\partial\Sigma_{\text{int}}^1$. Such an interface yields $\mathcal{F} = r - r_{\text{int}}^0(t, \theta, z) - \epsilon\eta^1(t, \theta, z) = 0$. Any quantity of interest f at the perturbed interface $\partial\Sigma_{\text{int}}^1$ can be linearised as $f = f^0 + \epsilon f^1$. Yet, for a typical perturbation analysis, η^1 is an unknown of the problem, hence $\partial\Sigma_{\text{int}}^1$ is not known *a priori* and one cannot readily apply the interface boundary conditions on it. To remedy the unknown perturbed boundaries, we here employ the domain perturbation technique (Séro-Guillaume and Er-Riani, 1999; Daners, 2008) as follows: Since the boundary perturbations occur in the linear order, we can benefit from knowing the base interface and express any quantity on the perturbed boundary as a Taylor series expanded around the base interface $\partial\Sigma_{\text{int}}^0$. This process is schematically sketched in figure 2.2 and is hereafter referred to as *flattening*. To express such Taylor series, we expand at time t , each quantity f from any point $(r = r_{\text{int}}^0 + \epsilon\eta^1, \theta, z)$ (red point in figure 2.2) on the perturbed interface $\partial\Sigma_{\text{int}}^1$ around its corresponding point on $\partial\Sigma_{\text{int}}^0$ of coordinates $(r = r_{\text{int}}^0, \theta, z)$ (green point in figure 2.2). Accordingly, any flow quantity $f(r, \theta, z, t)$

¹In the tensor notation, the left-hand side of the equation writes $(\mathbf{n} \cdot \underline{\tau})_{\text{in}}^{\text{out}}$. However, throughout this thesis, we follow the linear algebra notation as expressed in (2.2).

at the perturbed interface can be readily approximated as

$$f|_{(r=r_{\text{int}}^0+\epsilon\eta^1,\theta,z,t)} = f|_{(r=r_{\text{int}}^0,\theta,z,t)} + \epsilon\eta^1 \partial_r f|_{(r=r_{\text{int}}^0,\theta,z,t)} + \mathcal{O}(\epsilon^2), \quad (2.3)$$

and then, this quantity can be perturbed as $f = f^0 + \epsilon f^1$.

The kinematic condition (2.1) for the linearly perturbed flow field $\mathbf{u} = \mathbf{u}^0 + \epsilon\mathbf{u}^1$ implies

$$\partial_t (r_{\text{int}}^0 + \epsilon\eta^1) + (\mathbf{u}^0 + \epsilon\mathbf{u}^1) \cdot \nabla (r_{\text{int}}^0 + \epsilon\eta^1) = (\mathbf{u}^0 + \epsilon\mathbf{u}^1) \cdot \mathbf{e}_r \quad \text{at } \partial\Sigma_{\text{int}}^1. \quad (2.4)$$

Flattening and applying further simplifications result in a separation of orders, where in the framework of linear analysis, we are interested in the two leading orders as

ϵ^0 order:

$$\partial_t r_{\text{int}}^0 + \mathbf{u}^0 \cdot \nabla r_{\text{int}}^0 - u_r^0 = 0, \quad \text{at } \partial\Sigma_{\text{int}}^0$$

ϵ^1 order:

$$\begin{aligned} & \partial_t \eta^1 - u_r^1 + u_\theta^1 \frac{\partial_\theta r_{\text{int}}^0}{r_{\text{int}}^0} + u_z^1 \partial_z r_{\text{int}}^0 + \dots \\ & + \eta^1 \left[-\partial_r u_r^0 + \frac{\partial_r u_\theta^0 \partial_\theta r_{\text{int}}^0}{r_{\text{int}}^0} + \partial_r u_z^0 \partial_z r_{\text{int}}^0 - \frac{u_\theta^0 \partial_\theta r_{\text{int}}^0}{(r_{\text{int}}^0)^2} \right] + \dots \\ & + \partial_\theta \eta^1 \frac{u_\theta^0}{r_{\text{int}}^0} + u_z^0 \partial_z \eta^1 = 0, \quad \text{at } \partial\Sigma_{\text{int}}^0. \end{aligned} \quad (2.5)$$

Similarly, the dynamic condition (2.2) on the perturbed interface implies

$$\left[\left(\underline{\tau}^0 + \epsilon \underline{\tau}^1 \right) (\mathbf{n}^0 + \epsilon \mathbf{n}^1) \right]_{\text{in}}^{\text{out}} = -\gamma (\kappa^0 + \epsilon \kappa^1) (\mathbf{n}^0 + \epsilon \mathbf{n}^1) \quad \text{at } \partial\Sigma_{\text{int}}^1. \quad (2.6)$$

After flattening, the two leading orders of the linearised dynamic condition imply

ϵ^0 order:

$$\left(\underline{\tau}^0 \mathbf{n}^0 \right)_{\text{in}}^{\text{out}} + \gamma \kappa^0 \mathbf{n}^0 = 0, \quad \text{at } \partial\Sigma_{\text{int}}^0,$$

ϵ^1 order:

$$\left(\underline{\tau}^0 \mathbf{n}^1 + \eta^1 \partial_r \underline{\tau}^0 \mathbf{n}^0 + \underline{\tau}^1 \mathbf{n}^0 \right)_{\text{in}}^{\text{out}} + \gamma (\kappa^0 \mathbf{n}^1 + \kappa^1 \mathbf{n}^0) = 0, \quad \text{at } \partial\Sigma_{\text{int}}^0. \quad (2.7)$$

Relations (2.5) and (2.7) contain the normal vector and the curvature of the interface at the two leading orders. We can show that the unit normal vector of a linearly perturbed interface

can be decomposed as $\mathbf{n} = \mathbf{n}^0 + \epsilon \mathbf{n}^1$ which reads

ϵ^0 order:

$$\mathbf{n}^0 = \begin{pmatrix} n_r^0 \\ n_\theta^0 \\ n_z^0 \end{pmatrix} = A^{-1/2} \begin{pmatrix} 1 \\ -\frac{1}{r_{\text{int}}^0} \partial_\theta r_{\text{int}}^0 \\ \partial_z r_{\text{int}}^0 \end{pmatrix},$$

ϵ^1 order:

$$\mathbf{n}^1 = \begin{pmatrix} n_r^1 \\ n_\theta^1 \\ n_z^1 \end{pmatrix} = \begin{pmatrix} B_r \eta^1 + C_r \partial_\theta \eta^1 + D_r \partial_z \eta^1 \\ B_\theta \eta^1 + C_\theta \partial_\theta \eta^1 + D_\theta \partial_z \eta^1 \\ B_z \eta^1 + C_z \partial_\theta \eta^1 + D_z \partial_z \eta^1 \end{pmatrix}, \quad (2.8)$$

where

$$\begin{aligned} A &= 1 + \left(\frac{1}{r_{\text{int}}^0} \partial_\theta r_{\text{int}}^0 \right)^2 + (\partial_z r_{\text{int}}^0)^2, & B_r &= \frac{A^{-3/2}}{(r_{\text{int}}^0)^3} (\partial_\theta r_{\text{int}}^0)^2, \\ B_\theta &= A^{-3/2} \left(-\frac{1}{(r_{\text{int}}^0)^4} (\partial_\theta r_{\text{int}}^0)^3 + \frac{A}{(r_{\text{int}}^0)^2} \partial_\theta r_{\text{int}}^0 \right), & B_z &= -\frac{A^{-3/2}}{(r_{\text{int}}^0)^3} (\partial_\theta r_{\text{int}}^0)^2 \partial_z r_{\text{int}}^0, \\ C_r &= -\frac{A^{-3/2}}{(r_{\text{int}}^0)^2} \partial_\theta r_{\text{int}}^0, & C_\theta &= -\frac{A^{-3/2}}{r_{\text{int}}^0} \left(1 + (\partial_z r_{\text{int}}^0)^2 \right), & C_z &= \frac{A^{-3/2}}{(r_{\text{int}}^0)^2} \partial_\theta r_{\text{int}}^0 \partial_z r_{\text{int}}^0, \\ D_r &= -A^{-3/2} \partial_z r_{\text{int}}^0, & D_\theta &= \frac{A^{-3/2}}{r_{\text{int}}^0} \partial_z r_{\text{int}}^0 \partial_\theta r_{\text{int}}^0, & D_z &= A^{-3/2} \left((\partial_z r_{\text{int}}^0)^2 - A \right). \end{aligned} \quad (2.9)$$

We can also show that the local curvature of a linearly perturbed interface can be decomposed as $\kappa = \kappa^0 + \epsilon \kappa^1$ which reads

ϵ^0 order:

$$\kappa^0 = \frac{1}{r_{\text{int}}^0} (n_r^0 + \partial_\theta n_\theta^0) + \partial_z n_z^0,$$

ϵ^1 order:

$$\kappa^1 = E \eta^1 + F \partial_\theta \eta^1 + G \partial_z \eta^1 + D_z \partial_{zz} \eta^1 + \frac{C_\theta}{r_{\text{int}}^0} \partial_{\theta\theta} \eta^1, \quad (2.10)$$

where

$$\begin{aligned} E &= \frac{1}{r_{\text{int}}^0} (B_r + \partial_\theta B_\theta) - \frac{1}{(r_{\text{int}}^0)^2} (n_r^0 + \partial_\theta n_\theta^0) + \partial_z B_z, \\ F &= \frac{1}{r_{\text{int}}^0} (C_r + \partial_\theta C_\theta + B_\theta + D_\theta \partial_z) + \partial_z C_z + C_z \partial_z, \\ G &= B_z + \partial_z D_z. \end{aligned} \quad (2.11)$$

Note that the subscript r in (2.8)-(2.11) does not imply the real part of a complex number but rather indicates the prefactors in the radial component of the normal vector. In the following, we illustrate the presented formalism applied to some classical limits of interfacial shapes.

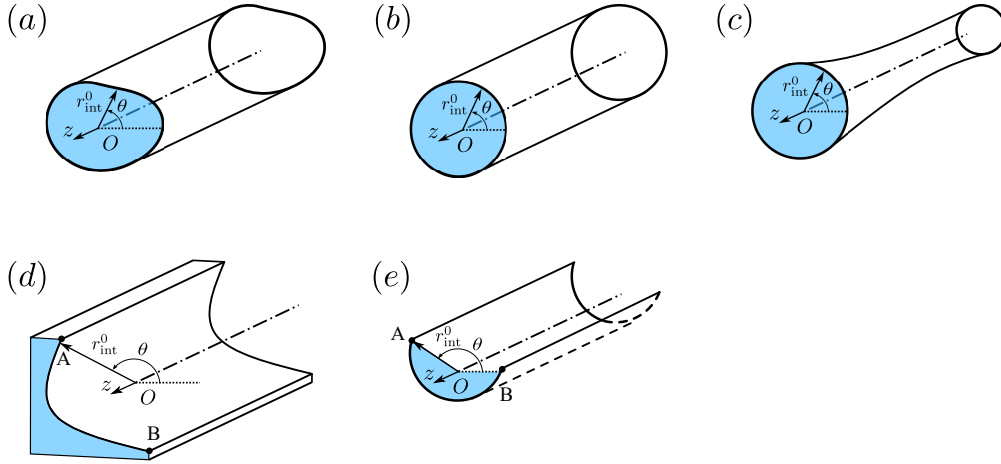


Figure 2.3: Examples of the geometries presented in §2.1. (a,d) Axially-invariant interface (cf. §2.1.1); (b,e) Cylindrical interface (cf. §2.1.2); (c) Axially varying interface with circular cross-section (cf. §2.1.3). The blue cuts shade the liquid cross-section.

2.1 Some special geometries

2.1.1 Axially-invariant interface

The first limit that we consider in this study is when the base interface has no dependence on the axial coordinate z (cf. figure 2.3(a,d)). In this case, $r_{\text{int}}^0 = r_{\text{int}}^0(t, \theta)$ for which the kinematic

condition (2.5) implies

ϵ^0 order:

$$\partial_t r_{\text{int}}^0 + \frac{u_\theta^0}{r_{\text{int}}^0} \partial_\theta r_{\text{int}}^0 - u_r^0 = 0, \text{ at } \partial \Sigma_{\text{int}}^0$$

ϵ^1 order:

$$\begin{aligned} & \partial_t \eta^1 - u_r^1 + u_\theta^1 \frac{\partial_\theta r_{\text{int}}^0}{r_{\text{int}}^0} + \dots \\ & + \eta^1 \left[-\partial_r u_r^0 + \frac{\partial_r u_\theta^0 \partial_\theta r_{\text{int}}^0}{r_{\text{int}}^0} - \frac{u_\theta^0 \partial_\theta r_{\text{int}}^0}{(r_{\text{int}}^0)^2} \right] + \dots \\ & + \partial_\theta \eta^1 \frac{u_\theta^0}{r_{\text{int}}^0} + u_z^0 \partial_z \eta^1 = 0, \text{ at } \partial \Sigma_{\text{int}}^0. \end{aligned} \quad (2.12)$$

The dynamic condition is readily given by (2.7) where the normal vector can be expressed as

ϵ^0 order:

$$\mathbf{n}^0 = \begin{pmatrix} n_r^0 \\ n_\theta^0 \\ n_z^0 \end{pmatrix} = A^{-1/2} \begin{pmatrix} 1 \\ -\frac{1}{r_{\text{int}}^0} \partial_\theta r_{\text{int}}^0 \\ 0 \end{pmatrix},$$

ϵ^1 order:

$$\mathbf{n}^1 = \begin{pmatrix} n_r^1 \\ n_\theta^1 \\ n_z^1 \end{pmatrix} = \begin{pmatrix} B_r \eta^1 + C_r \partial_\theta \eta^1 \\ B_\theta \eta^1 + C_\theta \partial_\theta \eta^1 \\ D_z \partial_z \eta^1 \end{pmatrix}, \quad (2.13)$$

where

$$\begin{aligned} A &= 1 + \left(\frac{1}{r_{\text{int}}^0} \partial_\theta r_{\text{int}}^0 \right)^2, & B_r &= \frac{A^{-3/2}}{(r_{\text{int}}^0)^3} (\partial_\theta r_{\text{int}}^0)^2, \\ B_\theta &= A^{-3/2} \left(-\frac{1}{(r_{\text{int}}^0)^4} (\partial_\theta r_{\text{int}}^0)^3 + \frac{A}{(r_{\text{int}}^0)^2} \partial_\theta r_{\text{int}}^0 \right), & C_r &= -\frac{A^{-3/2}}{(r_{\text{int}}^0)^2} \partial_\theta r_{\text{int}}^0, \\ C_\theta &= -\frac{A^{-3/2}}{r_{\text{int}}^0}, & D_z &= -A^{-1/2}. \end{aligned} \quad (2.14)$$

Similarly, the interface curvature writes

ϵ^0 order:

$$\kappa^0 = \frac{1}{r_{\text{int}}^0} (n_r^0 + \partial_\theta n_\theta^0),$$

ϵ^1 order:

$$\kappa^1 = E\eta^1 + F\partial_\theta\eta^1 + D_z\partial_{zz}\eta^1 + \frac{C_\theta}{r_{\text{int}}^0}\partial_{\theta\theta}\eta^1, \quad (2.15)$$

where

$$E = \frac{1}{r_{\text{int}}^0} (B_r + \partial_\theta B_\theta) - \frac{1}{(r_{\text{int}}^0)^2} (n_r^0 + \partial_\theta n_\theta^0), \quad F = \frac{1}{r_{\text{int}}^0} (C_r + \partial_\theta C_\theta + B_\theta). \quad (2.16)$$

In the present thesis, the main focus is dedicated to this geometrical limit. The linear stability analysis of an axially invariant interface is addressed for different configurations in **chapters 3,4,5**.

2.1.2 Cylindrical interface

A particularly interesting limit of the axially invariant interface is the cylindrical interface, where $r_{\text{int}}^0 = r_{\text{int}}^0(t)$ (cf. figure 2.3(b,e)). In this limit, the kinematic condition (2.12) further simplifies as

ϵ^0 order:

$$\partial_t r_{\text{int}}^0 - u_r^0 = 0, \text{ at } \partial\Sigma_{\text{int}}^0$$

ϵ^1 order:

$$\begin{aligned} & \partial_t \eta^1 - u_r^1 - \partial_r u_r^0 \eta^1 + \dots \\ & + \partial_\theta \eta^1 \frac{u_\theta^0}{r_{\text{int}}^0} + u_z^0 \partial_z \eta^1 = 0, \text{ at } \partial\Sigma_{\text{int}}^0. \end{aligned} \quad (2.17)$$

We recall that the dynamic condition is readily given by (2.7) where the normal vector presented in relation (2.13) simplifies further as

ϵ^0 order:

$$\mathbf{n}^0 = \begin{pmatrix} n_r^0 \\ n_\theta^0 \\ n_z^0 \end{pmatrix} = \begin{pmatrix} 1 \\ 0 \\ 0 \end{pmatrix},$$

ϵ^1 order:

$$\mathbf{n}^1 = \begin{pmatrix} n_r^1 \\ n_\theta^1 \\ n_z^1 \end{pmatrix} = \begin{pmatrix} 0 \\ \frac{-1}{r_{\text{int}}^0} \partial_\theta \eta^1 \\ -\partial_z \eta^1 \end{pmatrix}, \quad (2.18)$$

Additionally, relation (2.15) simplifies as

ϵ^0 order:

$$\kappa^0 = \frac{1}{r_{\text{int}}^0},$$

ϵ^1 order:

$$\kappa^1 = \frac{-1}{(r_{\text{int}}^0)^2} (\eta^1 + \partial_{\theta\theta} \eta^1) - \partial_{zz} \eta^1, \quad (2.19)$$

The linear stability analysis of a cylindrical interface is addressed in **chapter 3**. Note that a cylindrical interface does not necessarily indicate an axisymmetric flow. As will be presented in **chapter 3**, a non-axisymmetric axial flow can be reached inside a cylindrical liquid column.

2.1.3 Axially varying interface with circular cross-section

Another particularly interesting limit is when the interface varies along the axial direction with a circular cross-section at any z (cf. figure 2.3(c)). In other words, $r_{\text{int}}^0 = r_{\text{int}}^0(t, z)$. This limit is of interest for investigating annular co-flows or elongated open-ended bubbles. In this limit, the kinematic condition (2.5) implies

ϵ^0 order:

$$\partial_t r_{\text{int}}^0 + u_z^0 \partial_z r_{\text{int}}^0 - u_r^0 = 0, \text{ at } \partial \Sigma_{\text{int}}^0$$

ϵ^1 order:

$$\begin{aligned} & \partial_t \eta^1 - u_r^1 + u_z^1 \partial_z r_{\text{int}}^0 + \eta^1 (-\partial_r u_r^0 + \partial_r u_z^0 \partial_z r_{\text{int}}^0) + \dots \\ & + \partial_\theta \eta^1 \frac{u_\theta^0}{r_{\text{int}}^0} + u_z^0 \partial_z \eta^1 = 0, \text{ at } \partial \Sigma_{\text{int}}^0. \end{aligned} \quad (2.20)$$

The dynamic condition is readily given by (2.7) where the normal vector implies

ϵ^0 order:

$$\mathbf{n}^0 = \begin{pmatrix} n_r^0 \\ n_\theta^0 \\ n_z^0 \end{pmatrix} = A^{-1/2} \begin{pmatrix} 1 \\ 0 \\ \partial_z r_{\text{int}}^0 \end{pmatrix},$$

ϵ^1 order:

$$\mathbf{n}^1 = \begin{pmatrix} n_r^1 \\ n_\theta^1 \\ n_z^1 \end{pmatrix} = \begin{pmatrix} D_r \partial_z \eta^1 \\ C_\theta \partial_\theta \eta^1 \\ D_z \partial_z \eta^1 \end{pmatrix}, \quad (2.21)$$

where

$$\begin{aligned} A &= 1 + (\partial_z r_{\text{int}}^0)^2, & C_\theta &= -\frac{A^{-3/2}}{r_{\text{int}}^0} \left(1 + (\partial_z r_{\text{int}}^0)^2 \right), \\ D_r &= -A^{-3/2} \partial_z r_{\text{int}}^0, & D_z &= A^{-3/2} \left((\partial_z r_{\text{int}}^0)^2 - A \right). \end{aligned} \quad (2.22)$$

Similarly, the interface curvature implies

ϵ^0 order:

$$\kappa^0 = \frac{n_r^0}{r_{\text{int}}^0} + \partial_z n_z^0,$$

ϵ^1 order:

$$\kappa^1 = E \eta^1 + G \partial_z \eta^1 + D_z \partial_{zz} \eta^1 + \frac{C_\theta}{r_{\text{int}}^0} \partial_{\theta\theta} \eta^1, \quad (2.23)$$

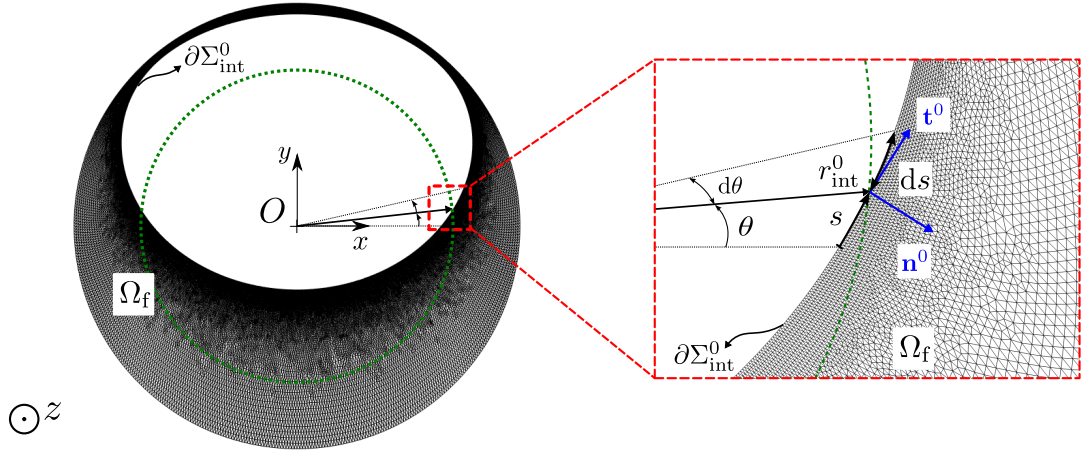


Figure 2.4: An exemplary numerical domain associated with a thick film coating the inner wall of a cylindrical tube; the meshed region is the liquid, denoted by Ω_f , separated through an interface, denoted by $\partial\Sigma_{\text{int}}^0$, from the surrounded air, the white region. The right panel shows a zoom at the interface and the arc length s ; the green dotted line shows a circle of constant radius at the zoomed point whose normal (\mathbf{n}^0) and tangent (\mathbf{t}^0) vectors are sketched in blue.

where

$$E = -\frac{n_r^0}{(r_{\text{int}}^0)^2}, \quad G = \partial_z D_z. \quad (2.24)$$

Even though the stability analysis of this class of geometry is not investigated in the present thesis (though such base states are calculated in **chapter 6**), one can confirm after a little bit of manipulation that relations (2.21)-(2.23) are identical to that presented in chapter 3 in Augello (2015).

2.2 Numerical implementation in COMSOL Multiphysics™

In this section, a numerical procedure is proposed to apply the method explained earlier. This procedure is implemented in the finite elements solver COMSOL Multiphysics™, and employed in the present thesis for some axially invariant flows with Cartesian (x, y) description of the flow in the cross-section. Indeed, a variety of numerical implementations may be considered for this method, however, in the present procedure, we try to keep it as general and versatile as possible. We anticipate the unperturbed numerical domain from **chapter 4**, shown in figure 2.4 to visually support the procedure as illustration.

We recall that the following procedure aims at calculating different terms in expressions (2.5)-(2.11) and impose these conditions at the interface. While some of the flow quantities like velocity and pressure are defined both in the fluid bulk, Ω_f , and at the interface, $\partial\Sigma_{\text{int}}^0$, some

others like the surface normal vector \mathbf{n}^0 and r_{int}^0 are only defined at the interface. The bulk values can be treated in a standard manner while differentiating, whereas derivating the quantities defined only at the interface requires further attention from a numerical point of view. Figure 2.4 shows the $z = 0$ cross-section of an exemplary base interface. This interface can be represented by a single-valued function $r_{\text{int}}^0(\theta, z = 0)$. However, as this quantity is defined along the curvilinear abscissa s in the numerical framework, $\partial_\theta r_{\text{int}}^0$ is not readily defined (neither $\partial_x r_{\text{int}}^0$ nor $\partial_y r_{\text{int}}^0$). Hence, we should firstly compute the derivative along s , and then employ the chain rule as $\partial_s r_{\text{int}}^0 = (\partial_\theta r_{\text{int}}^0) (\partial_s \theta)$. In COMSOL MultiphysicsTM, derivative along the curvilinear abscissa can be obtained as $\partial_s = \mathbf{t}^0 \cdot \nabla_s$, where \mathbf{t}^0 denotes the unit tangent vector along s , and $\nabla_s = \nabla - \mathbf{n}^0 (\mathbf{n}^0 \cdot \nabla)$ is the tangential gradient operator on the same boundary. Therefore, for r_{int}^0 and any other quantity defined only at the boundary with reference to a curvilinear abscissa s ,

$$\partial_\theta = \frac{\mathbf{t}^0 \cdot \nabla_s}{\mathbf{t}^0 \cdot \nabla_s \theta}, \quad \text{at } \partial \Sigma_{\text{int}}^0. \quad (2.25)$$

Note that the base interface in figure 2.4 is axially invariant. A general columnlike interface can have axial variations. Differentiating in the z direction can be similarly expressed as

$$\partial_z = \frac{\mathbf{t}^0 \cdot \nabla_s}{\mathbf{t}^0 \cdot \nabla_s z}, \quad \text{at } \partial \Sigma_{\text{int}}^0. \quad (2.26)$$

Since the performance of the numerical scheme is sensitive to how one exploits the available functions in the numerical set-up, in the following we shed light on different possible manners of defining quantities in COMSOL MultiphysicsTM.

2.2.1 Variable operator versus finite element space

One should distinguish between defining a quantity via variable operator, hereafter variable, or in the finite element space in COMSOL MultiphysicsTM. A variable evaluates a user-defined "strong" point-wise expression (as opposed to its weak or variational form). On the other hand, a quantity belonging to the finite element space should be defined in the software by means of a weak or strong equation. The value of this quantity is then evaluated by solving numerically its descriptive equation. Note that regardless of expressing such an equation in weak or strong form in the graphical panel of COMSOL MultiphysicsTM, it is automatically transformed to a weak expression.

Suppose that an arbitrary space- and/or time-dependent quantity $a(t, \mathbf{x})$ is the solution of an equation $f = f(a) = 0$, subject to a proper set of initial and boundary conditions.

1. To define a as a variable, it suffices to add it as a variable in the model tree in COMSOL MultiphysicsTM.
2. To define a in the finite element space using a weak expression, one must add a weak

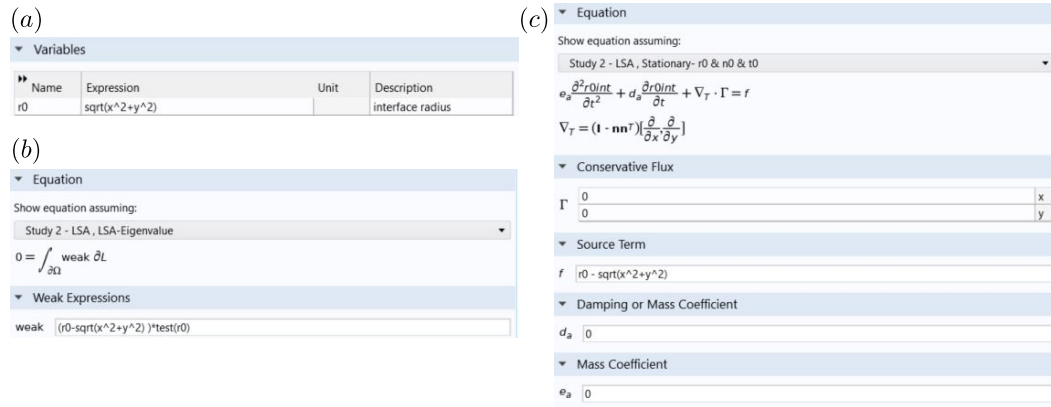


Figure 2.5: Defining a quantity $r0$, representing the base interface, as (a) a variable, and in the finite elements space through (b) weak form and (c) strong form equations.

form-based physics from the "Mathematics" module to the model tree in COMSOL Multiphysics™, set a as its dependent variable and prescribe the weak form equation $f = 0$, as $\int f \psi_a = 0$, along with the proper initial/boundary conditions on its domain/boundary of existence, where ψ_a is the corresponding test function.

3. To define a in the finite element space using a strong expression, one must add a strong form-based physics from the "Mathematics" module to the model tree in COMSOL Multiphysics™, set a as its dependent variable and prescribe the strong form equation $f = 0$, directly on its domain/boundary of existence along with the proper initial/boundary conditions. We recall that COMSOL Multiphysics™ converts this strong form to the same weak form as in step 2 before solving.

Example: In the framework of the following numerical model, let us take the base interface radius in the $x-y$ cross-section, then $a = r_{\text{int}}^0 = \sqrt{x^2 + y^2}$, and $f = r_{\text{int}}^0 - \sqrt{x^2 + y^2} = 0$. Figure 2.5 presents three different manners of defining this quantity.

In some certain cases, as will be addressed in §2.2.2, a specific way of defining a quantity is more desirable than the other. More specifically, defining a quantity as a variable is computationally inexpensive, whereas defining it in the finite element space can be beneficial to achieve smooth numerical values when high-order derivations of the quantity are needed, or when the quantity includes differentiated components itself. To clarify this point, let us take as an example the curvature of a cylindrical base interface of unit radius. We know from relation (2.19) that in this case, the base curvature is unity. Figure 2.6 presents an example of calculating the interface curvature κ^0 , using (2.10), once with the model proposed as in §2.2.2 (blue), and once by computing all of its contributing terms as variables (red). The variable-based evaluation results in small numerical oscillations. If the computed value is needed to be further differentiated, such oscillations become problematic. This is briefly because the weak expression results in an integral equation that ensures the smoothness of the solution.

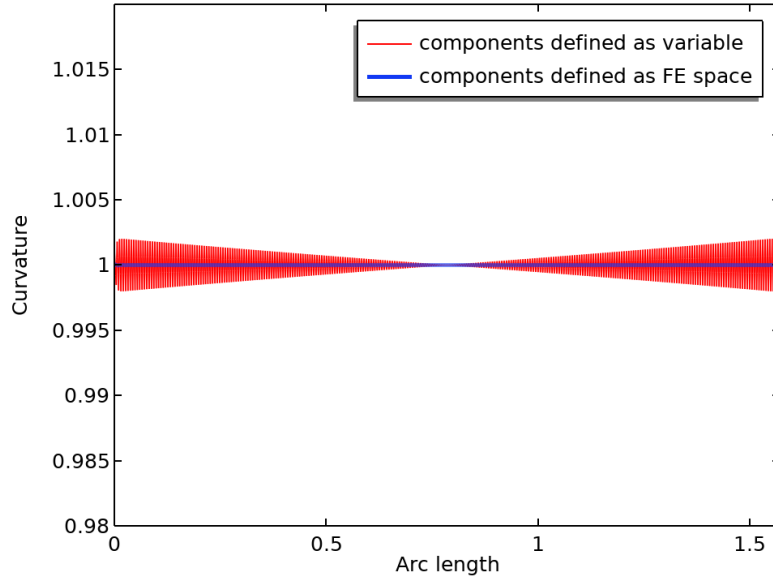


Figure 2.6: The curvature of a cylindrical interface of unite radius, computed from (2.10).

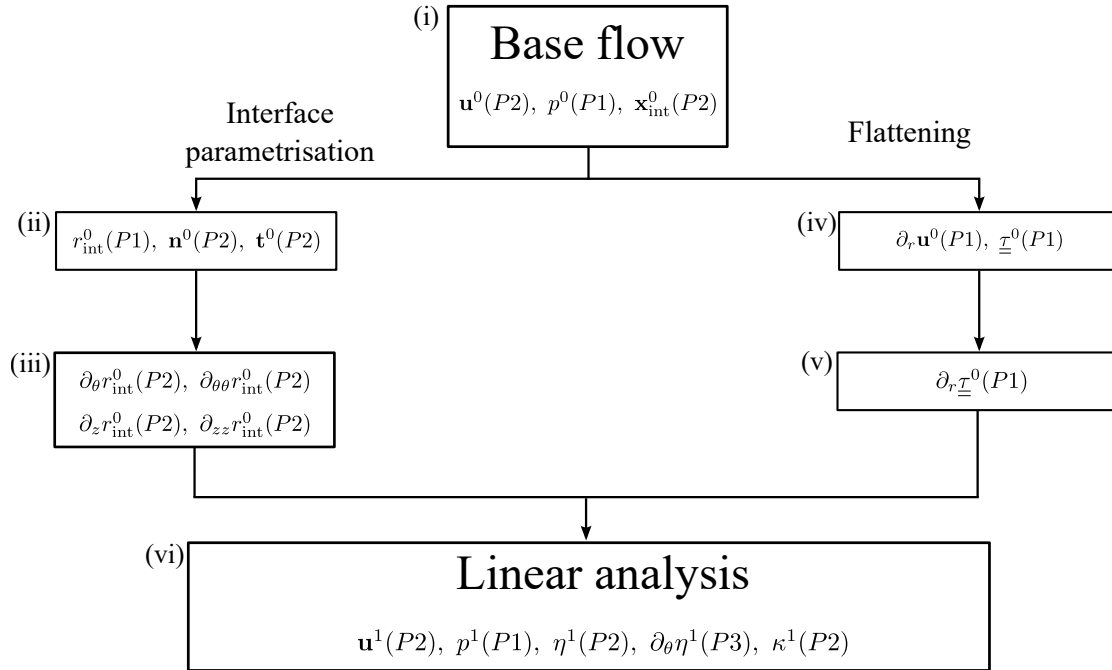


Figure 2.7: Schematic of the implemented method. Each step is shown with a box encapsulating the corresponding calculated finite element spaces. The shape function of each space is shown in parentheses.

2.2.2 Proposed numerical model

The schematic of the numerical procedure is shown in figure 2.7 and the steps are as follows:

- i. The first step is to solve the base flow. Upon the nature of the problem, a time-dependent solver or steady one may suit. To maintain the generality for both modal and nonmodal analyses, we continue the procedure by considering a temporally evolving flow coupled with a moving mesh module. In such a case, the geometrical shape function should crucially be quadratic Lagrange polynomial.
- ii. The second step is to extract the geometrical characteristics of the flow numerically. To this aim, the values of $\{r_{\text{int}}^0, \mathbf{n}^0, \mathbf{t}^0\}$ are computed through mathematical equation-based solvers only at the interface $\partial\Sigma_{\text{int}}^0$, defined in the finite element space of quadratic shape functions. In the $z = \text{const.}$ cross-section, the radial coordinate is defined by $r = \sqrt{x^2 + y^2}$, where (x, y) are the in-plane Cartesian coordinates. The interface unit normal and tangent vectors are defined using the built-in operators of COMSOL Multiphysics™. In addition, the polar angle θ is defined by $\theta = \arctan(y/x)$ as a parameter in the whole domain.

Note: Defining the \mathbf{n}^0 and \mathbf{t}^0 in the finite element space of the specified shape functions, as opposed to variable, is essential to avoid numerical oscillations, because they have to be differentiated on the interface in the next steps.

- iii. Next, $\{\partial_\theta r_{\text{int}}^0, \partial_{\theta\theta} r_{\text{int}}^0, \partial_z r_{\text{int}}^0, \partial_{zz} r_{\text{int}}^0\}$ are defined in the finite element space of quadratic shape functions only at $\partial\Sigma_{\text{int}}^0$. This step should be crucially done after step (ii.) to avoid a singular matrix error where value initialisation in COMSOL Multiphysics™ results in division by zero.
- iv. The values of $\{\partial_r \mathbf{u}^0, \underline{\underline{\tau}}^0\}$ are calculated in the finite element space of linear shape functions in the bulk Ω_f , where $\partial_r = \cos\theta \partial_x + \sin\theta \partial_y$.
- v. The value of $\partial_r \underline{\underline{\tau}}^0$ is calculated in the finite element space of linear shape function at $\partial\Sigma_{\text{int}}^0$. As $\underline{\underline{\tau}}^0$ is defined also in the bulk, a standard differentiation as in step (iv.) can be employed to compute the radial derivative at the interface. This step should be done after step (iv.) to avoid a singular matrix error.

Note: Defining the above-mentioned quantities in the finite element spaces is essential to avoid numerical oscillation in the values. In the case of a time-dependent base flow, steps (ii.)-(v.) can be computed and stored for each time step through a time-dependent solver. Following these steps, the quantities and coefficients contributing to the linear order of the normal vector and curvature, presented in relations (2.7)-(2.11), are computed as variable in COMSOL Multiphysics™.

- vi. Now, all of the constants and derived values from the base flow are readily in hand for further computations. Depending on the purpose of the study, the final step may be conducting the linear stability analysis of the linearised Navier-Stokes equations or following the temporal evolution of the linear perturbations, as needed for the transient growth analysis. In either case, $\{\mathbf{u}^1, p^1, \eta^1, \partial_\theta \eta^1, \partial_z \eta^1, \kappa^1\}$ are solved simultaneously in the finite element space. The Navier-Stokes equations (the momentum and continuity equations) are employed to define $\{\mathbf{u}^1, p^1\}$ with the quadratic and linear shape functions,

respectively. The dynamic interface condition (2.7) is applied by means of Lagrange multipliers of quadratic shape function. The kinematic condition (2.5) and relation (2.10) are used to define $\{\eta^1, \kappa^1\}$, respectively, with the quadratic shape functions. Both $\partial_\theta \eta^1$ and $\partial_z \eta^1$ are defined in the finite element space following (2.25) and (2.26), respectively, using cubic shape functions, and are similarly differentiated to compute $\partial_{\theta\theta} \eta^1$ and $\partial_{zz} \eta^1$ in (2.10). The choice of cubic shape function is somewhat peculiar, however, it was observed as the only choice that results in the validation of the model. A rigorous reason remains unsettled.

Note: The steps (ii.) and (iv.) can be done in parallel, as shown in figure 2.7. However, here they are presented in the same order as implemented in the COMSOL MultiphysicsTM model.

2.2.3 Method validation

The procedure presented in §2.2 is readily implemented and validated for an axially invariant flow with an asymmetric cross-sectional flow in the finite elements solver COMSOL MultiphysicsTM. In the scope of the present thesis, even though the equations can be simplified according to §2.1.1, in the COMSOL MultiphysicsTM model, each term is implemented without any simplification. For further details on the model validation and results, see appendix 4.5.5. The used benchmark takes into account the interface asymmetry as well as non-zero axial base flow gradients.

2.3 Method limitations and future perspective

The interface formulation introduced earlier in this chapter is a powerful tool to address a large variety of problems, where a liquid-liquid or liquid-air interface is perturbed with infinitesimal perturbations. Apart from its robustness and accuracy in the numerical framework, one of its major strong points is its numerical simplicity and modular implementation which makes this model a versatile tool to be employed readily for several interfacial flow analyses. This method has been already applied successfully to different examples that are presented in the following chapters of the present thesis. However, some limitations can be considered for this formulation, which keeps the interest for further improvement in the future. These limitations are elaborated on in the following

1. We recall that the key assumption behind the selection of the cylindrical parametrisation for the interface is the explicit radial representation condition. Even though this assumption holds for open-ended columnlike interfaces, it is not comprehensive. In some flows, one may find it difficult to spot an axis Oz to ensure the explicit radial representation condition for all times of the flow evolution. For instance, in the problem of a thick liquid film coating the inside of a horizontal tube, to be presented in **chapter 4**, if $R < R_w/3$, the displacement of the interface particles can be larger than the diameter

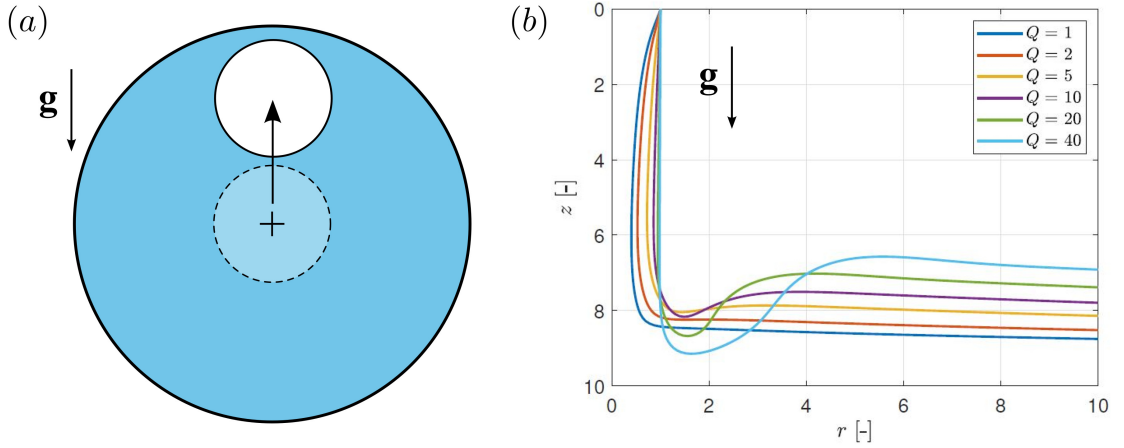


Figure 2.8: (a) Two schematic frames form a draining film coating the inside of a tube; the liquid is shown in blue, ; air is shown in white; the tube wall is shown by the thick solid line, the initial interface is shown with the dotted line and a later frame of the interface is shown in the thin solid line; (b) Interface of a laminar axisymmetric jet impinging a flat plate as a function of the flow rate Q (reprinted from Scherz (2022)).

of the initial cylindrical interface (cf. figure 2.8(a)). Starting from the initially concentric film of a uniform thickness, any axis Oz within the gaseous core and parallel to the tube centreline can be selected. However, as the interface rises, any selected axis eventually crosses the interface, violating $r_{\text{int}}^0 \neq 0$. Hence, our model cannot automatically follow the parametrisation of the interface, from its initial state until the quasi-static state approaching the upper tube wall. In this particular problem, a simple remedy could be to stop the simulation before the axis Oz crosses the interface, then continue the simulation with a new axis inside the displaced interface. Yet, an automatised solver is desirable.

2. Another example of violating explicit radial representation condition is when the interface exhibits axial overturning. For instance, when a laminar liquid jet impinges a flat plate at a high flow rate, the liquid may expand radially following a hydraulic jump at the interface (cf. figure 2.8(b)). The jump disables the radial representation of the interface as a single-valued function, thus failing the present formulation for studying the linear perturbations of such a flow.
3. The present model necessitates the columnlike interface to be open-ended along the axis. In the case of a closed-ended interface, like a drop or bubble, there exists at least one point where $\partial_z r_{\text{int}}^0 \rightarrow \infty$, preventing thus the applicability of the present formulation in imposing the interface conditions (2.5)-(2.7).
4. In general, the interface between two fluids may be perturbed in the normal direction to the interface at each point. We recall that the radial mapping applied while flattening (2.3) holds only if the unperturbed and perturbed interfaces are defined over the same ranges of (θ, z) . Such a flattening applies to any columnlike interface that forms a closed

curve in the $z = \text{const.}$ cross-section and satisfies the explicit radial representation condition. Nevertheless, when the interface forms an open-ended curve in the $z = \text{const.}$ cross-section, the choice of a proper axis Oz may not be easy. An example of such an interface is given in Bostwick and Steen (2018) where the linear stability of a static rivulet on top of a substrate is studied. In many other problems where the base flow with a closed interface at $z = \text{const.}$ cross-section benefits from some geometrical symmetries, one may study a cut of the interface under some symmetry conditions. In order for the flattening (2.3) to account for an open interface (cf. figure 2.3(d,e)) perturbed in the normal direction at all points, the axis Oz must strictly lie on the intersection of the normal vectors at the two endpoints of the interface (cf. points A, B in figure 2.3(d,e)). For such a choice of Oz , the range of (θ, z) for the base interface is the same as that of the perturbed one. As an example, we revisit the Rayleigh-Plateau instability for a viscous jet. The numerical domain, shown in figure 2.9(a), is a half-cut of a unit circle at $z = \text{const.}$ plane. Symmetry condition is applied to the flow with respect to its vertical diameter, $\partial\Sigma_{\text{sym}}^0$. The center of the circle is displaced away from the origin O in the x and y directions. Figure 2.9(b) presents the effect of axis position on the obtained dispersion curve for the axisymmetric perturbation, where several positions of O are considered for in the $z = \text{const.}$ cross-section. It can be seen that moving the center of the circle in the x direction results in a dispersion curve different from the correct one, whereas moving it only in the y direction inside the liquid bulk (keeping point O on $\partial\Sigma_{\text{sym}}^0$, the conjunction of the interface normal vectors at the endpoints) results in the correct growth rate. In this example, we had multiple choices of proper axis Oz along $\partial\Sigma_{\text{sym}}^0$. Let us now consider another example, which is the linear stability analysis of the Rayleigh-Taylor instability which occurs when a liquid film of constant thickness covers the underside of a horizontal flat plate. For such a flow, the base interface is a flat surface whose normal vectors are parallel at any point. Therefore, no proper position for Oz can be set and the radial formulation presented in this chapter fails.

5. In the case of a columnlike interface that satisfies all of the present formulation conditions, the limit where $r_{\text{int}}^0 \rightarrow \infty$ may cause numerical problems. Therefore, it is preferential to set the axis Oz such that this limit is avoided.

With the given overview of the developed interface parametrisation and its limitations, one can naturally draw a future perspective to complement the present method and address the abovementioned restrictions. A proper proposition is to develop a differential formulation, inspired by the work of Ledda et al. (2022), for the base and perturbed interfaces in the intrinsic normal-tangent coordinates. Such a local parametrisation of the perturbed interface can resolve the limitations of the present method, relax the explicit radial representation condition, and can open the door for the linear analysis of any arbitrary fluid-fluid interface perturbation. After this will be achieved, the extension of the local method to the perturbations of higher order can facilitate conducting the non-linear analysis of generic interfacial flows.

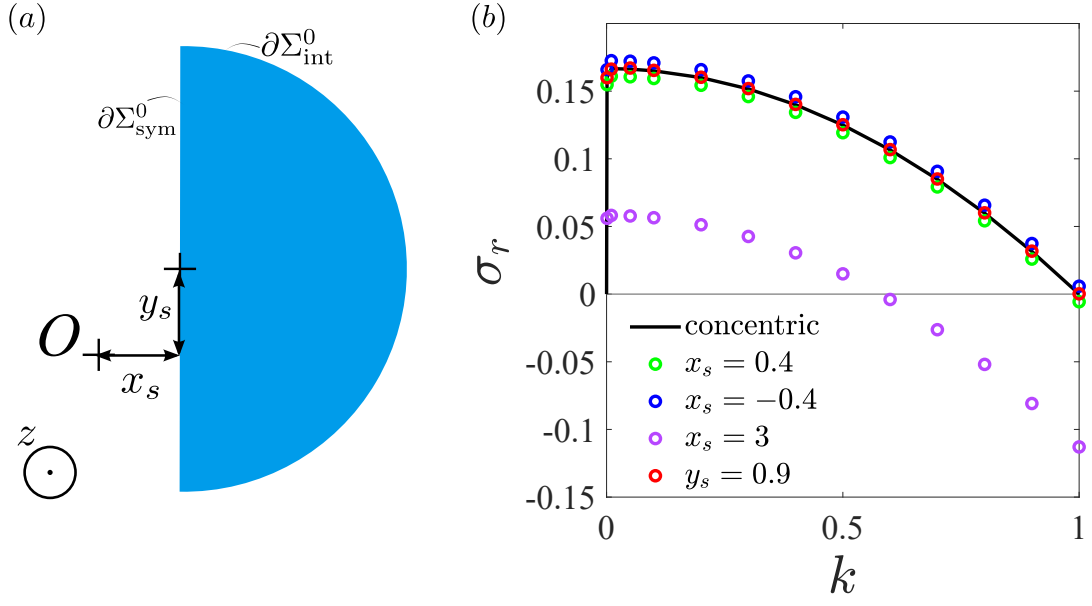


Figure 2.9: (a) Numerical domain for the Rayleigh-Plateau instability, computed on half-cylinder whose axis is located at (x_s, y_s) with respect to the axis Oz . Here, $\partial\Sigma_{\text{int}}^0$ marks the unperturbed interface, and $\partial\Sigma_{\text{sym}}^0$ marks the axis of symmetry. (b) The effect of positioning axis Oz on the dispersion curve of the axisymmetric mode; for each case, only one of x_s or y_s is varied.

3 Whirling instability of an eccentric coated fibre

Remark This chapter is largely inspired by the publications of the same name

Shahab Eghbali[†], L. Keiser², E. Boujo¹ and F. Gallaire¹

¹ Laboratory of Fluid Mechanics and Instabilities, École Polytechnique Fédérale de Lausanne, Lausanne CH-1015, Switzerland

² Université Côte d'Azur, CNRS, INPHYNI, Nice, 06000, France

Journal of Fluid Mechanics

Authors' contributions S.E. and L.K. conceived the project. S.E. performed, together with E.B., the stability analysis. S.E. and L.K. prepared the experimental set-up and carried out the experiments, S.E. conducted the analysis of the experimental data. All authors actively participated to the theoretical developments, analysis and interpretation of the results. S.E. wrote the manuscript and L.K. and E.B. edited it, guided by F.G..

We study a gravity-driven viscous flow coating a vertical cylindrical fibre. The destabilisation of a draining liquid column into a downward moving train of beads has been linked to the conjunction of the Rayleigh-Plateau and Kapitza instabilities in the limit of small Bond numbers Bo . Here, we focus on quasi-inertialess flows (large Ohnesorge number Oh) and conduct a linear stability analysis on a unidirectional flow along a rigid eccentric fibre for intermediate to large Bo . We show the existence of two unstable modes, pearl and whirl modes. The pearl mode depicts asymmetric beads, similar to that of the Rayleigh-Plateau instability, whereas a single helix forms along the axis in the whirl mode instability. The geometric and hydrodynamic thresholds of the whirl mode instability are investigated, and phase diagrams showing the transition thresholds between different regimes are presented. Additionally, an energy analysis is carried out to elucidate the whirl formation mechanism. This analysis reveals that despite the unfavourable capillary energy cost, the asymmetric interface shear distribution, caused by the fibre eccentricity, has the potential to sustain a whirling interface. In general, small fibre radius and large eccentricity tend to foster the whirl mode instability, while reducing Bo tends to favour the dominance of the pearl mode instability. Finally, we compare the predictions of our model with the results of some illustrative experiments, using

highly viscous silicone oils flowing down fibres. Whirling structures are observed for the first time, and the measured wavenumbers match our stability analysis prediction.

keywords: coating, drainage, Rayleigh-Plateau instability, surface tension, linear stability analysis, energy analysis, whirl, interface

3.1 Introduction

Initially long liquid columns always break apart into many droplets so as to minimise their surface energy. This phenomenon, referred to as Rayleigh-Plateau instability, has been well-known since the studies of Plateau (1873); Rayleigh (1878). This instability, originally described for liquid jets, can be observed under various conditions such as liquid film coating a fibre (Duprat, 2009) or inside a tube (Duclaux et al., 2006), which gives rise to the formation of similar interfacial patterns and represents a class of hydrodynamic instability under the same name, reviewed in further detail in the works of Eggers and Villermaux (2008); Gallaire and Brun (2017). One particularly interesting variant of the Rayleigh-Plateau instability is the destabilisation of a viscous fluid draining vertically down a rigid fibre under the influence of gravity, which leads to the formation of moving beads along the fibre. This flow has been attracting attention for decades as a result of its numerous applications and rich dynamics. Some direct applications are seen in coating technologies, optical coating and in drawing fibres into/from liquid baths (Quéré, 1999; Shen et al., 2002; Duprat et al., 2007). Furthermore, emerging patterns are characterised mainly by a high surface area to volume ratio, which is appealing for numerous applications that involve mass and heat transfer across the liquid-gas interfaces, e.g. microfluidics (Gilet et al., 2009), heat exchangers (Zeng et al., 2017, 2018), vapor absorption (Chinju et al., 2000; Grünig et al., 2012; Hosseini et al., 2014) and desalination (Sadeghpour et al., 2019). Predictability and control of the destabilised patterns are crucial in many of these applications.

Numerous theoretical and experimental studies have examined the flow down rigid fibres. Remarkably, Kliakhandler et al. (2001) reported experimentally three distinct unstable regimes: (i) isolated beads, (ii) regularly distanced beads train, and (iii) irregularly distanced beads train. Transition from the absolute to convective regimes occurs when the film thickness exceeds a critical value, for which the corresponding thresholds are discussed widely in the works of Chang and Demekhin (1999); Duprat et al. (2007). Besides secondary instabilities and non-linear phenomena that may be observed as beads grow, solitary waves may appear along the fibre in the non-zero inertia limit, reminiscent of the capillary Kapitza waves (Kapitza, 1949; Duprat, 2009). Several theoretical and numerical models have been proposed to elucidate the dynamics of the growth and motion of the emergent unstable patterns in the linear and non-linear regimes in the limits of thin films (Frenkel, 1992; Ruyer-Quil et al., 2008; Ruyer-Quil and Kalliadasis, 2012; Yu and Hinch, 2013) and thick films (Craster and Matar, 2006; Liu and Ding, 2021). Each of these models captures some features of the destabilisation process and matches the experimental data within some ranges. In addition, further studies

concluded that besides the liquid properties, the fibre properties such as porosity (Ding and Liu, 2011), slip properties (Haefner et al., 2015) and shape (Xie et al., 2021), as well as geometric parameters like nozzle geometry (Sadeghpour et al., 2017), have significant impacts on altering the dynamics and defining the range of occurrence of each unstable regime. Changes to the dynamics may be related to changing the dominant wavelength, switching between different regimes, changing the spacing, velocity, shape, and coalescence of mobile beads.

In all of the studies in the literature, the fibre is concentric with the liquid column, and the initial stage of any unstable regime exhibits an axisymmetric growth of the interface undulations. The recent work of Gabbard and Bostwick (2021) addresses the evolution of asymmetric beads when the film thickness is initially non-homogeneous around the fibre. In their case, they outlined the thresholds between the three regimes of isolated beads, and regular and irregular beads trains. Yet, a full understanding of the destabilisation processes is missing for the stability of non-homogeneous film thickness in flows down a fibre. For instance, it is not clear why the formation of asymmetric beads is not prevented by capillary effects. Also, the effect of non-homogeneous film thickness on the linear instability of other non-axisymmetric modes is not known. In the present study, we focus on the effect of the fibre position with respect to the liquid column, and we investigate the stability characteristics of the flow and the subsequent geometry of the emerging patterns.

This paper is structured as follows. The methodology is first presented in §3.2. To begin with, the problem formulation and the governing equations are presented in §3.2.1, from which the base flow is deduced and discussed in §3.2.2. In §3.2.3, the stability analysis formulation and the linearised governing equations are elaborated. Corresponding numerical methods are detailed in §3.2.4. In §3.3, the results of the stability analyses are presented and discussed. First, in §3.3.1, the effect of the fibre eccentricity on the stability characteristics of the flow is given. Then a similar investigation is conducted for the other dimensionless parameters in §3.3.2, followed by sketching the extensive stability maps in §3.3.3. In addition, the physical mechanisms underlying the instability of the flow are elucidated by the method of energy analysis in §3.3.4. In §3.3.5, a comparison between the linear model and our illustrative experiments is provided. Finally, conclusions are drawn in §3.4.

3.2 Governing equations and methods

3.2.1 Problem formulation

A viscous liquid column flows under gravity along a vertical solid cylindrical fibre of radius R_f placed with an eccentricity r_{ec} from the centre of the column. The schematic of the flow and the cross-sectional view are shown in figure 3.1. The standard Cartesian coordinates (x, y, z) are considered, with the origin located at the centre of the liquid column. In-plane coordinates are (x, y) , and the positive direction of the axial/vertical coordinate z , points in the direction of the gravity acceleration g . The liquid is Newtonian, of constant dynamic

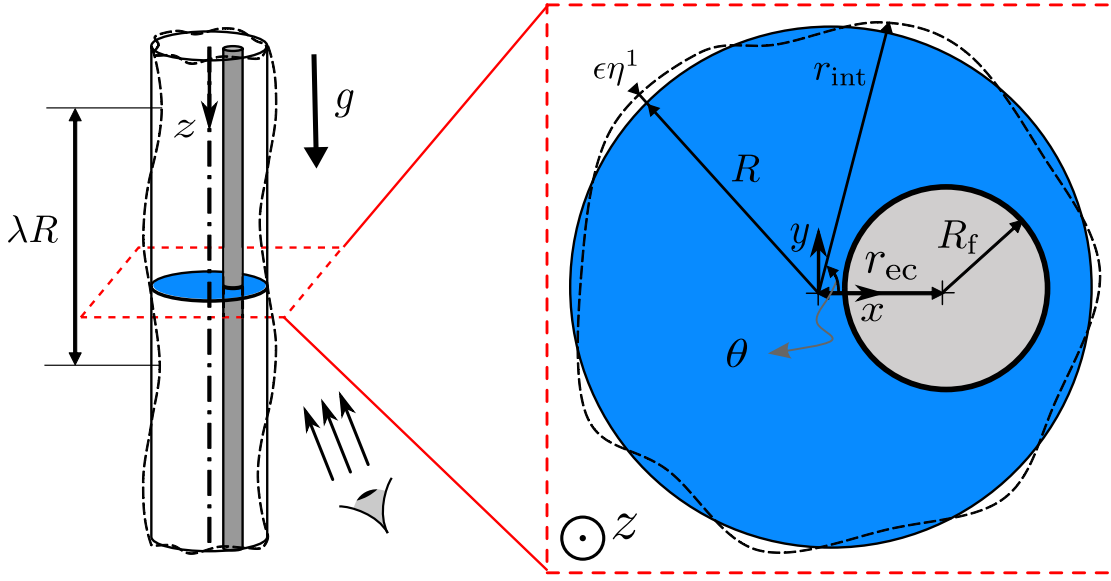


Figure 3.1: Schematic of the coating flow along an eccentric fibre and the geometrical parameters in cross-sectional view. The outer dashed black line represents the perturbed interface of local radius r_{int} and axial wavelength $R\lambda$, and outer solid black line shows the cylinder with mean radius R , which is concentric with the coordinate reference. The planar cut shows the cross-section of the liquid column and the geometrical characteristics, where the grey region shows the solid fibre.

viscosity μ , surface tension γ and density ρ , and is surrounded by an inviscid gas. Without loss of generality for sufficiently small interface deformations, the interface can be parametrised in cylindrical coordinates (r, θ, z) , as $r_{\text{int}}(t, \theta, z)$, using the same origin as the Cartesian one, and R denotes the reference value of r_{int} in the absence of any perturbation. The dimensionless state vector $\mathbf{q} = (\mathbf{u}, p, \mathcal{R}_{\text{int}})^T$ defines the flow where at time t , $\mathbf{u}(t, x, y, z) = (u_x, u_y, u_z)^T$ denotes the three-dimensional velocity field, $p(t, x, y, z)$ denotes the pressure, and $\mathcal{R}_{\text{int}} = r_{\text{int}}/R$ denotes the dimensionless interface radius. As opposed to Craster and Matar (2006), the state vector and the governing equations are rendered dimensionless by the intrinsic velocity and time scales presented by Duprat (2009), associated with the viscous axisymmetric liquid ring of uniform thickness $h_0 = R - R_f$ that coats a centred fibre. However, we choose different length and pressure scales, as follows:

$$\begin{aligned} \mathcal{L} &= R, & \mathcal{U} &= \frac{\rho g h_0^2}{\mu} = \frac{\rho g R^2}{\mu} (1 - \alpha)^2, \\ \mathcal{P} &= \rho g R, & \mathcal{T} &= \frac{\mathcal{L}}{\mathcal{U}} = \frac{\mu}{\rho g R} (1 - \alpha)^{-2}, \end{aligned} \tag{3.1}$$

where $\alpha = R_f/R$ denotes the fibre to mean radius aspect ratio. The other geometric parameter is $R_{\text{ec}} = r_{\text{ec}}/R$, which denotes the dimensionless fibre eccentricity. The flow is governed by the incompressible Navier-Stokes equations, which in dimensionless form read

$$\nabla \cdot \mathbf{u} = 0, \quad (3.2)$$

$$\frac{Bo}{Oh^2} (1 - \alpha)^4 (\partial_t + \mathbf{u} \cdot \nabla) \mathbf{u} = \nabla \cdot \underline{\underline{\tau}} + 1 \mathbf{e}_z, \quad (3.3)$$

where ∂_j denotes the partial derivative with respect to quantity j , and the stress tensor $\underline{\underline{\tau}}$ reads

$$\underline{\underline{\tau}} = -p\mathbf{I} + (1 - \alpha)^2 (\nabla \mathbf{u} + \nabla \mathbf{u}^T). \quad (3.4)$$

The two other dimensionless numbers that appear in the governing equations are the *Ohnesorge* number $Oh = \mu / \sqrt{\rho \gamma R}$, and the *Bond* number $Bo = \rho g R^2 / \gamma$. While Oh compares the viscous forces to the inertial and surface tension forces, Bo compares the gravitational and surface tension forces. Our study addresses the limit of inertialess flow where $(Bo/Oh^2)(1 - \alpha)^4 \ll 1$ without any further assumptions on α .

The no-slip boundary condition $\mathbf{u} = \mathbf{0}$ is applied on the fibre $\partial\Sigma_f$. On the shear-free fluid-gas interface, the kinematic and dynamic boundary conditions, respectively, are

$$\partial_t \mathcal{R}_{\text{int}} + \mathbf{u} \cdot \nabla \mathcal{R}_{\text{int}} = \mathbf{u} \cdot \mathbf{e}_r \quad \text{on } r = \mathcal{R}_{\text{int}}, \quad (3.5)$$

$$\underline{\underline{\tau}} \mathbf{n} = -\frac{\kappa}{Bo} \mathbf{n} \quad \text{on } r = \mathcal{R}_{\text{int}}, \quad (3.6)$$

where \mathbf{e}_r denotes the unit radial vector, $\mathbf{n} = \nabla(r - \mathcal{R}_{\text{int}}) / \|\nabla(r - \mathcal{R}_{\text{int}})\|$ denotes the unit normal vector pointing outwards from the liquid bulk, $\|\cdot\|$ denotes the Euclidean norm, and $\kappa = \nabla \cdot \mathbf{n}$ denotes the interface mean curvature.

3.2.2 Base Flow

The base flow \mathbf{q}^0 is the steady-state solution of the Navier-Stokes equations (3.2)-(3.6). We recall the solution prevailing for an eccentric fibre. In the limit of centred fibre, the analytical solution exists whose axial velocity is composed of a logarithmic term and a parabola as

$$u_z^0 = \frac{(1 - \alpha)^{-2}}{2} \left(\ln \frac{r}{\alpha} - \frac{r^2 - \alpha^2}{2} \right), \quad p^0 = \frac{1}{Bo}, \quad (3.7)$$

with a constant pressure in the liquid. This velocity field is shown in figure 3.2(a) and reveals its maximal velocity at the liquid-gas interface, and an increasing drainage flux $Q^0 = \iint_{\Omega_{xy}} u_z^0 dA_{\Omega_{xy}}$ as the aspect ratio α decreases, i.e. for a thicker liquid film (figure 3.2(b)). Inspired by the solution for the centred fibre, we seek a base flow that is parallel and fully developed in the z direction with a cylindrical interface of radius $\mathcal{R}_{\text{int}}^0 = 1$. Note that $\mathcal{R}_{\text{int}}^0 = 1$ is readily a solution to the non-linear kinematic condition (3.5). Assuming a constant pressure,

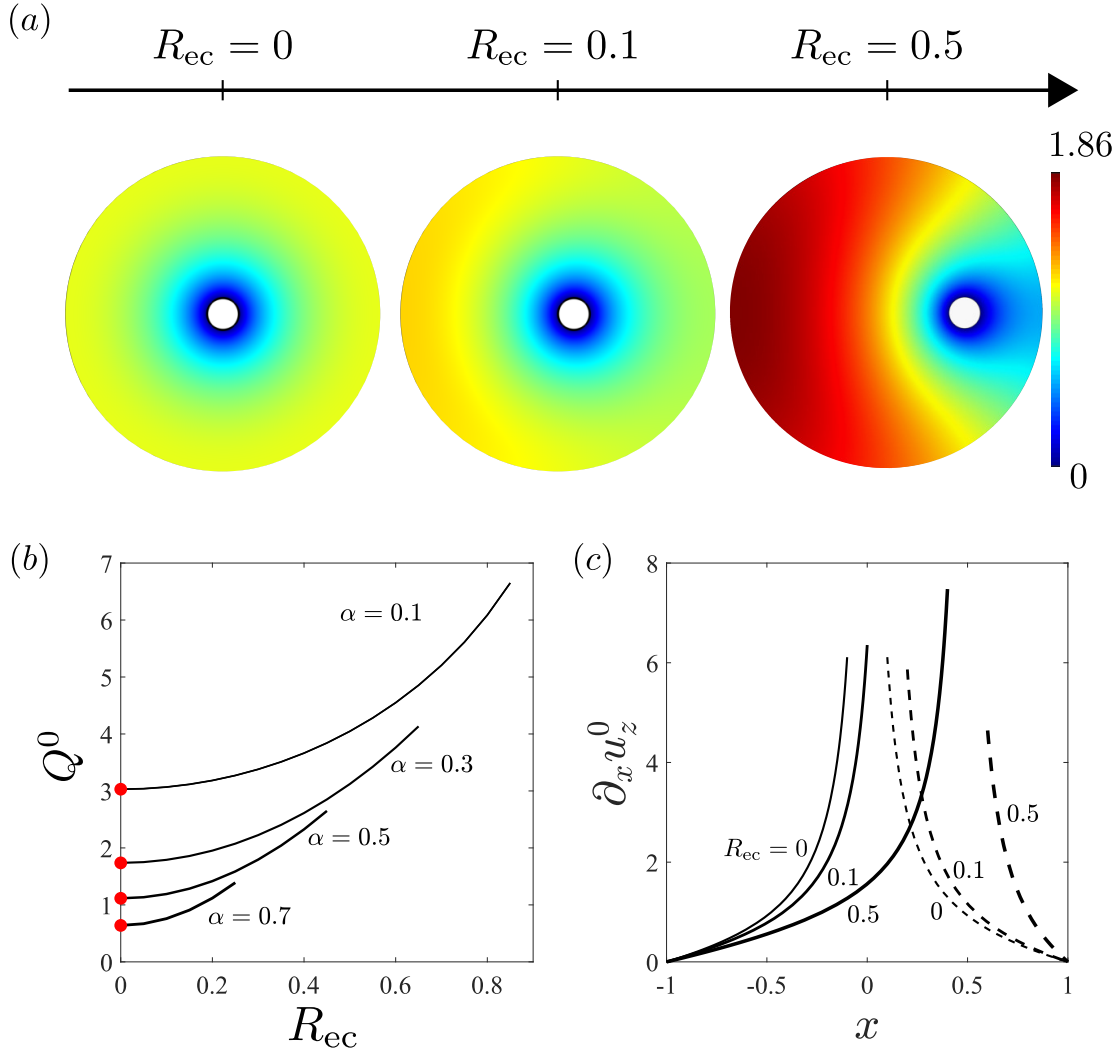


Figure 3.2: Variation of the base flow as a result of the fibre eccentricity. (a) Axial velocity u_z^0 at the cross-section for $\alpha = 0.1$ and three different values of fibre eccentricities $R_{ec} = \{0, 0.1, 0.5\}$; same colour bar applies for all plots; (b) Vertical flow rate Q^0 for different values of α and R_{ec} ; solid black lines show the results from our numerical study, and the red dots show the values computed from the analytical flow around a centred fibre, (3.7); for each value of α , the plot stops at $\alpha + R_{ec} \leq 0.95$; (c) Shear rate across the thick (continuous) and thin (dashed) sides of the liquid film along $y = 0$.

the normal component of the dynamic condition (3.6) is also satisfied. It remains to solve the Poisson equation for u_z^0 , with no-slip on the fibre and free shear on the interface, driven by gravity. The solution is computed numerically in the present study (see §3.2.4 for details) for the flow coating an eccentric fibre, although it could be interesting to try to extend to the present free-surface configuration the method proposed in Piercy et al. (1933) for a pipe flow with a solid core. The fibre eccentricity breaks the axisymmetry of the base flow, with a high-speed region on the thicker side of the liquid film, and a low-speed region on the thinner

side. On the thicker side, shear is decreased near the interface while being increased in the vicinity of the fibre (solid lines in figure 3.2(c)); on the thinner side, it evidences an increase near the interface while being decreased near the fibre (dashed lines in figure 3.2(c)). The drainage flow rate increases substantially with R_{ec} (figure 3.2(b)).

3.2.3 Linear stability analysis

In order to perform the *linear stability analysis* on the base flow, presented in §3.2.2, the state vector $\mathbf{q} = (\mathbf{u}, p, \mathcal{R}_{int})^T$ is decomposed into the sum of the steady-state base flow solution \mathbf{q}^0 , and the infinitesimal time-dependent *perturbation* $\mathbf{q}^1 = (\mathbf{u}^1, p^1, \eta^1)^T$, i.e.

$$\mathbf{q} = \mathbf{q}^0 + \epsilon \mathbf{q}^1 + \mathcal{O}(\epsilon^2), \quad \epsilon \ll 1, \quad (3.8)$$

where the amplitude ϵ is assumed to be small. We look for perturbations \mathbf{q}^1 under the normal form

$$\mathbf{q}^1 = \tilde{\mathbf{q}}(x, y) \exp[\sigma t + ikz] + \text{c.c.}, \quad (3.9)$$

with k being the longitudinal wavenumber (associated with the wavelength $\lambda = 2\pi/k$), and c.c. denoting the complex conjugate. It should be noted that the eccentricity of the fibre breaks the axisymmetry of the problem, in spite of a cylindrical base interface. Therefore, a normal mode of the form $\tilde{\mathbf{q}}(r) \exp[\sigma t + im\theta + ikz] + \text{c.c.}$ with m being the azimuthal wavenumber, is not suitable in the eccentric configuration. In the asymptotic limit of large times, a normal eigenmode perturbation with complex pulsation $\sigma = \sigma_r + i\sigma_i$ is defined as *unstable* and hence grows exponentially in time with the growth rate σ_r , if $\sigma_r > 0$, i.e. if σ is in the unstable complex half-plane. (Unless otherwise noted, the subscripts r and i denote the real and imaginary part of a complex number, respectively.) By casting the perturbed state of (3.8) into the governing equations (3.2)-(3.3), with the stationary base flow $\mathbf{q}^0 = (\mathbf{u}^0, 1/Bo, 1)^T$, and keeping the first-order terms, the linearised equations are obtained as

$$\nabla \cdot \mathbf{u}^1 = 0, \quad (3.10)$$

$$\frac{Bo}{Oh^2} (1 - \alpha)^4 \left(\partial_t \mathbf{u}^1 + (\mathbf{u}^0 \cdot \nabla) \mathbf{u}^1 + (\mathbf{u}^1 \cdot \nabla) \mathbf{u}^0 \right) = \nabla \cdot \underline{\underline{\tau}}^1. \quad (3.11)$$

The no-slip condition implies $\tilde{\mathbf{u}} = \mathbf{0}$ on the fibre. The perturbed interface boundary conditions (3.5)-(3.6) applied on the perturbed liquid interface, can be projected radially onto the base interface and ultimately linearised, a process called *flattening* (see (3.22) in appendix 3.5.1). The linearised kinematic condition can be expressed as

$$(\sigma + ik u_z^0) \tilde{\eta} = \tilde{\mathbf{u}} \cdot \mathbf{e}_r \quad \text{on } r = 1. \quad (3.12)$$

Introducing an eigenstate vector of the form (3.9) into (3.10)-(3.11), combined with (3.12) leads to a generalised eigenvalue problem for σ and $\tilde{\mathbf{q}}$:

$$\mathbf{L}\tilde{\mathbf{q}} + \text{c.c.} = \sigma \mathbf{B}\tilde{\mathbf{q}} + \text{c.c.}, \quad (3.13)$$

where the linear operators \mathbf{L} and \mathbf{B} are defined as

$$\mathbf{L} = \begin{bmatrix} (1-\alpha)^2 (\tilde{\mathbf{V}} \cdot (\tilde{\mathbf{V}} + \tilde{\mathbf{V}}^T)) & -\tilde{\mathbf{V}} & \mathbf{0} \\ \tilde{\mathbf{V}} \cdot & 0 & 0 \\ \mathbf{e}_r & 0 & -ik u_z^0 \end{bmatrix}, \quad \mathbf{B} = \begin{bmatrix} \frac{Bo}{Oh^2} (1-\alpha)^4 \mathbf{I} & \mathbf{0} & \mathbf{0} \\ \mathbf{0} & 0 & 0 \\ \mathbf{0} & 0 & 1 \end{bmatrix}, \quad (3.14)$$

and the gradient operator and the velocity gradient tensor in the Cartesian coordinates are

$$\tilde{\mathbf{V}} = (\partial_x, \partial_y, ik)^T, \quad \tilde{\mathbf{V}}\tilde{\mathbf{u}} = \begin{bmatrix} \partial_x \tilde{u}_x & \partial_y \tilde{u}_x & ik \tilde{u}_x \\ \partial_x \tilde{u}_y & \partial_y \tilde{u}_y & ik \tilde{u}_y \\ \partial_x \tilde{u}_z & \partial_y \tilde{u}_z & ik \tilde{u}_z \end{bmatrix}. \quad (3.15)$$

The operators \mathbf{L} and \mathbf{B} are then implemented and modified in the numerical model to enforce the dynamic condition, which can be expressed as

$$\begin{aligned} \tilde{\tau} \mathbf{n}^0 = & -\frac{\tilde{\kappa}}{Bo} \mathbf{e}_r \\ & + (1-\alpha)^2 \partial_\theta u_z^0 ik \tilde{\eta} \mathbf{e}_\theta \\ & + (1-\alpha)^2 (\partial_\theta u_z^0 \partial_\theta \tilde{\eta} - \partial_{rr} u_z^0 \tilde{\eta}) \mathbf{e}_z \quad \text{at } r = 1, \end{aligned} \quad (3.16)$$

where $\tilde{\kappa}$ denotes the dimensionless curvature perturbation expressed as

$$\tilde{\kappa} = (k^2 - 1) \tilde{\eta} - \frac{\partial^2 \tilde{\eta}}{\partial \theta^2}, \quad (3.17)$$

and $(\mathbf{e}_r, \mathbf{e}_\theta, \mathbf{e}_z)$ denote the unit vectors of directions in the cylindrical coordinates (r, θ, z) used for parameterising the interface; see figure 3.1. (For further details on the interface boundary conditions' derivation and implementation, see appendix 3.5.1 and §3.5.2, respectively.)

3.2.4 Numerical method

The base flow and linear stability analysis are solved numerically with the finite element method. We use the software COMSOL MultiphysicsTM. A triangular mesh of the two-dimensional domain, shown in figure 3.3, is generated with the Delaunay-Voronoi algorithm. In the following sections, the area increment in the bulk cross-section is denoted by $dA_{\Omega_{xy}}$. On the boundary j , the increment of surface area is denoted by dA_{Σ_j} , and the increment of arc length is denoted by ds . The grid size is controlled by the vertex densities on the boundaries $\partial\Sigma_f$ and $\partial\Sigma_{\text{int}}$. The variational formulation of the base flow equations (3.2)-(3.6) and the linear stability equations (3.13) are discretised spatially using quadratic (P2) Lagrange elements for \mathbf{u}^0 , $\tilde{\mathbf{u}}$ and $\tilde{\eta}$, and linear (P1) Lagrange elements for \tilde{p} , yielding approximately 200'000 and 700'000 degrees of freedom for the base flow and the linear stability analysis, respectively. The

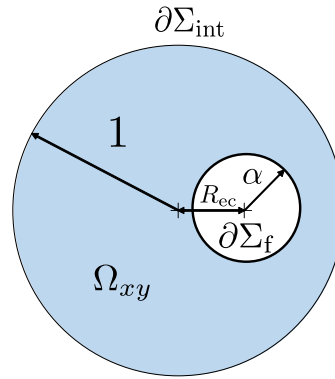


Figure 3.3: The numerical domain used for computing the base flow and linear stability analysis; the outer radius of the domain is set to unity, the same as that of the base interface. Here, Ω_{xy} denotes the liquid bulk. The boundaries of the numerical domain are denoted by $\partial\Omega_{xy} = \partial\Sigma_f \cup \partial\Sigma_{int}$. Here $\partial\Sigma_f$ represents the liquid-fibre contact boundary, and $\partial\Sigma_{int}$ represents the gas-liquid interface.

base flow, the solution of a linear Poisson equation, is computed first with a linear solver. Then this base flow is used to solve the generalised eigenvalue problem associated with the linear stability analysis using a shift-invert Arnoldi method. (See appendix 3.5.2 for details about the variational formulations, corresponding boundary conditions, and their implementation.)

The computation time associated with one given set of variables, followed by the stability analysis for ~ 20 values of k , is of the order of tens of minutes on a single Intel core at 3.6 GHz. The model is validated with the analytical solutions in the literature for the coating flow over a centred fibre. (For more details about the series of validation tests, see appendix 3.5.3.)

3.3 Results

3.3.1 Effect of the fibre eccentricity (R_{ec})

The results of the linear stability analysis are presented hereafter. Figure 3.4 shows the effect of R_{ec} on the stability of the flow. The *dispersion curve*, σ_r versus k , is plotted in figure 3.4(a) for the two least linearly stable eigenmodes, which can be characterised by the shapes of their eigeninterfaces in figure 3.4(b-c). In the limit of the concentric fibre, $R_{ec} = 0$, only one unstable mode exists in the range $0 < k \leq 1$, which undulates axisymmetrically in the axial direction. This instability is known as a variant of the Rayleigh-Plateau instability (Rayleigh, 1878). The second mode is stable over the whole range of wavenumbers, and its interface forms a single helix that whirls along the axial direction. Accordingly, hereafter, we will refer to these two modes as the *pearl* (P) and the *whirl* (W) modes, respectively. We emphasise that this instability is not to be confused with the classical whirl instability observed in liquid/gas-lubricated journal bearings, that is, a self-excited rotor whirl caused by lubricating film forces when the rotation frequency of the shaft exceeds a threshold, approaching the lowest natural

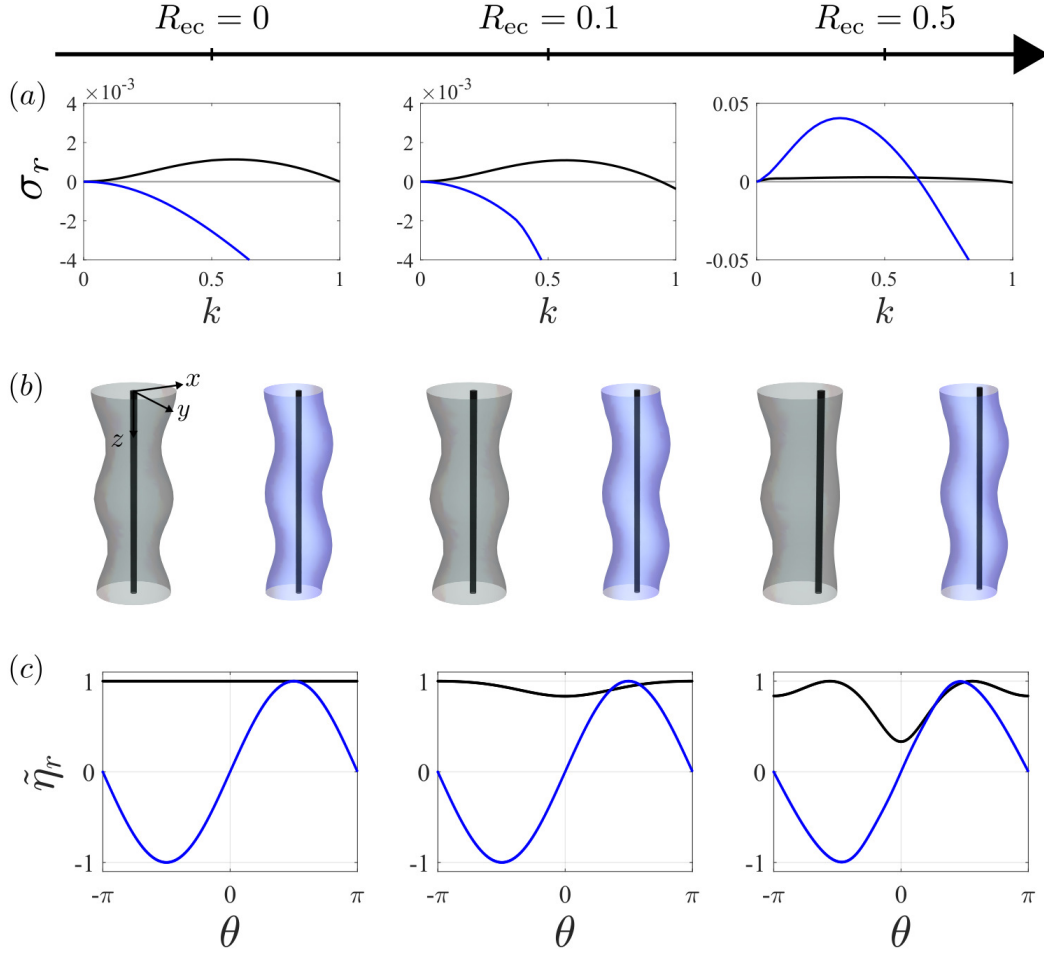


Figure 3.4: Evolution of the two least stable eigenmodes, P (black) and W (blue), with increasing the fibre eccentricity, plotted for $R_{ec} = \{0, 0.1, 0.5\}$. (a) The dispersion curve. (b) A three-dimensional render of the perturbed interface, obtained by superposition of the real part of the corresponding eigeninterfaces with amplitude 20% onto the base interface over an axial span of double wavelength $r(\theta, z) = 1 + 0.2\tilde{\eta}_r \cos(kz)$. (c) Real part of the eigeninterfaces, $\tilde{\eta}_r$, as a function of θ . All of the plots correspond to $Oh \rightarrow \infty$, $Bo = 50$ and $\alpha = 0.1$, and the eigeninterfaces are plotted at $k = 0.1$. All of the eigenstates are normalised and presented in the same complex phase, such that at the maximal positive interface perturbation, $\tilde{\eta} = 1$.

frequency of the system (Harrison, 1919; Larson and Richardson, 1962).

By increasing R_{ec} , the general trend observed in the stability of these two modes is as follows: the eigeninterfaces of both modes are deformed as the flow symmetry breaks, but their general layout remains similar to that of the concentric fibre. In addition, the P mode remains unstable, although its dispersion curve exhibits an alteration of the range of unstable wavenumbers. Moreover, increasing R_{ec} over a certain threshold destabilises the W mode, and by increasing R_{ec} further, the W mode eventually dominates over the P mode in a range of wavenumbers.

3.3.2 Bo and α effects

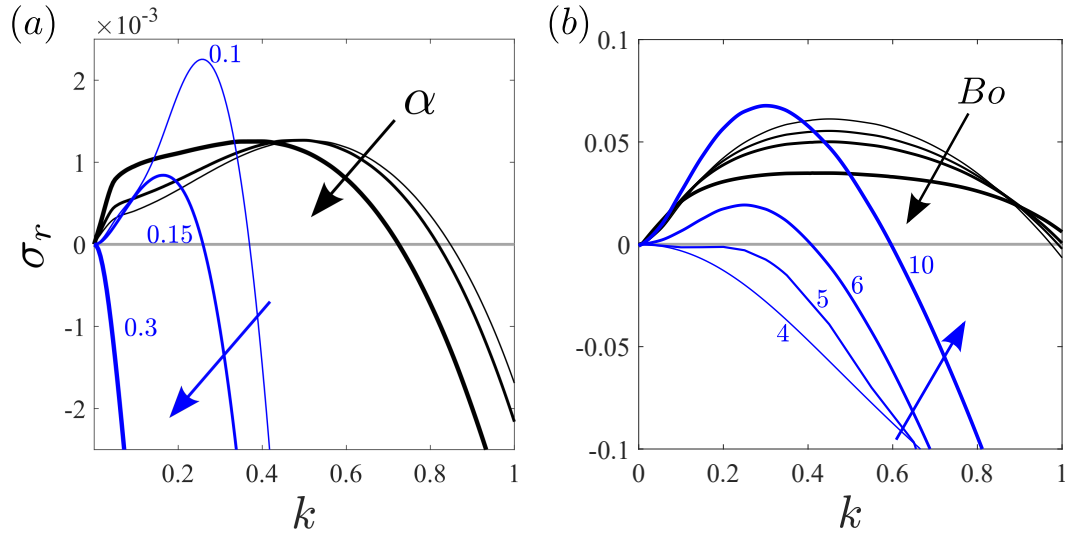


Figure 3.5: Variation of dispersion curve for the P (black) and W (blue) modes. (a) The α effect, plotted for $Oh \rightarrow \infty$, $Bo = 50$, $Re_c = 0.3$ and $\alpha = \{0.1, 0.15, 0.3\}$; each arrow shows the direction of increasing α for the P mode dispersion curve. (b) The Bo effect; plotted for $Oh \rightarrow \infty$, $Re_c = 0.7$, $\alpha = 0.1$ and $Bo = \{4, 5, 6, 10\}$; each arrow shows the direction of increasing Bo for the P mode dispersion curve.

In this subsection the effects of Bo and α on the stability characteristics of the flow are illustrated via dispersion curves. Figure 3.5(a) highlights the main changes induced by decreasing α . The instability range of the P mode extends. Additionally, although the maximal growth rate of the P mode exhibits a minor change, its *maximal wavenumber*- i.e. the wavenumber at which the maximal growth rate occurs- increases. Moreover, reducing α to less than a certain threshold destabilises the W mode. By further reducing α , the maximal wavenumber of the W mode and its growth rate increase, and eventually its growth rate dominates that of the P mode in some range of wavenumbers. Similar to decreasing α , figure 3.5(b) demonstrates the effects of increasing Bo as destabilising the W mode until its dominance over the P mode. Besides, larger Bo increases the instability range of both P and W modes. Unlike the W mode, the maximal growth rate of the P mode decreases by increasing Bo .

So far, three principal unstable regimes are identified in the parameter space: (i) only the P mode is unstable; (ii) both P and W modes are unstable, and the P mode dominates; (iii) both P and W modes are unstable, and the W mode dominates. A detailed study of the parameter space is conducted, and the results are presented in §3.3.3.

3.3.3 Phase diagrams

The $\{Bo, \alpha, Re_c\}$ space is investigated extensively to determine the threshold of the unstable regimes. Figures 3.6(a-b) present the *phase diagrams* that are obtained by holding α and Bo

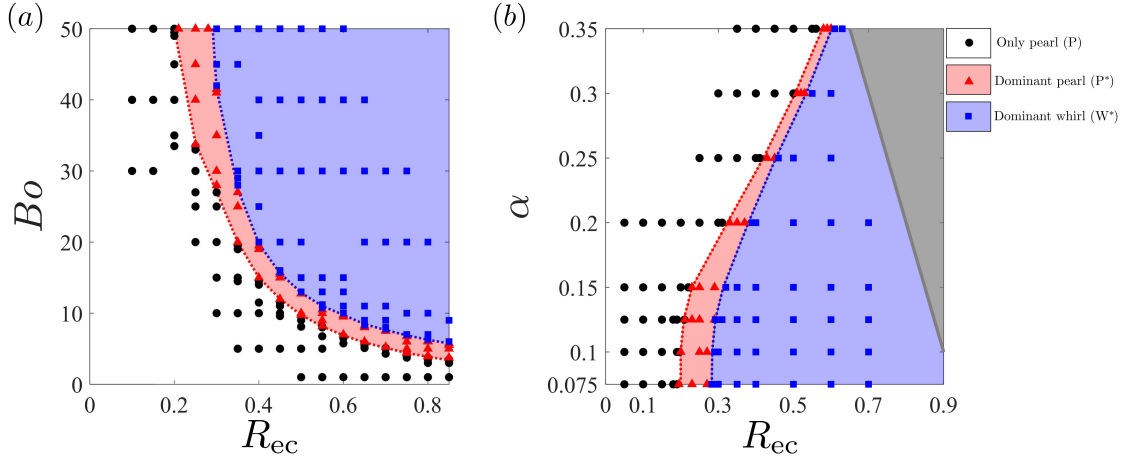


Figure 3.6: Phase diagrams of the unstable modes associated with the gravity-driven coating flow along an eccentric fibre: (a) for $\alpha = 0.1$, $Oh \rightarrow \infty$; (b) for $Bo = 50$, $Oh \rightarrow \infty$. The dotted curves mark the interpolated thresholds obtained from numerical eigenvalue calculations. The grey region in the right-hand corner excludes the infeasible geometrical limit $\alpha + R_{ec} \geq 1$ where the fibre touches the base interface. The coloured regions indicate the instabilities and dominance in terms of the growth rate as follows: white means only the P mode destabilises; red means both P and W modes destabilise and P dominates; blue means both P and W modes destabilise, and W dominates.

fixed, respectively, while varying the other parameters. For any set in the investigated range of parameters, the P mode destabilises. Furthermore, in accordance with the results presented in §3.3.1 and §3.3.2, these diagrams show that exceeding a certain threshold, increasing Bo for a fixed $\{\alpha, R_{ec}\}$, or decreasing α for a fixed $\{Bo, R_{ec}\}$, leads to the coexistence of unstable P and W modes, first with the dominance of the P mode, and later the dominance of the W mode. For instance, figure 3.6(b) reveals that at a constant $Bo = 50$, there are two cut-off values of R_{ec} : first, below $R_{ec} \approx 0.28$, the W mode never dominates the P mode for a finite fibre size; second, below $R_{ec} \approx 0.2$, only the P mode destabilises. Figure 3.6(b) is limited to $\alpha \geq 0.075$ for numerical reasons, that is, the appearance of spurious eigenmodes with discontinuities in the interface perturbation $\tilde{\eta}$ for $\alpha \leq 0.05$. Mesh refinement on the fibre boundary, on the interface boundary and inside the domain did not resolve this numerical issue.

Formerly, extensive studies addressed the shapes of the pearls in contact with a fibre (Carroll, 1984; Brochard-Wyart et al., 1990; McHale et al., 1999; Mchale et al., 2001; Duprat, 2009). However, instability of the W mode is not expected, as Rayleigh (1879) states that any non-axisymmetric perturbation should be linearly stable. The reason is that the surface energy of a liquid column is proportional to its surface area, which increases with the formation of whirling structures. Hence, such patterns are not in favour of the surface energy minimisation and should not destabilise (Cardoso and J., 2006; Duprat, 2009; Gallaire and Brun, 2017). Moreover, even though some studies have addressed the linear instability of the helical mode in the context of interfacial columnar flows, in each case an extra physical mechanism causes

helical instability. For instance, aerodynamic interactions at the interface of inertial jets (Yang, 1992), elasticity and electric stresses at the interface of electrified jets (Li et al., 2011), and the solid-liquid-gas contact line at the interface of static rivulets (Bostwick and Steen, 2018) are at play to counteract capillarity, promoting helical instabilities. In our study, i.e. in the absence of these extra triggering mechanisms, capillarity is known to stabilise non-axisymmetric interface perturbations. This apparent paradox gives the motivation to §3.3.4, where we perform an energy analysis on the flow.

3.3.4 Energy analysis

In this subsection, in an attempt to clarify the competition between capillary, potential and viscous effects, and to quantify their respective contributions to the base flow and the stability of modes P and W, we study the flow from an energy perspective. The base flow presented in §3.2.2, and the perturbed flow resulting from the linear stability analysis and presented in §3.3.1-3.3.2, are investigated by means of the *method of energy analysis* to explain the underlying physics of the flow instability. Previously, Boomkamp and Miesen (1996); Hooper and Boyd (1983); Kataoka and Troian (1997); Li et al. (2011) employed this method to determine and compare the roles of different physical mechanisms on the temporal instability of various interfacial flows.

What is commonly referred to as the energy analysis is in fact the study of the energy conservation in a flow, in different scales, from the base flow to the perturbations. More precisely, this analysis sheds light on the *rate of energy balance equation*, hereafter referred to as the *energy equation*, which for the inertialess gravity-driven flow along a fibre, can be expressed as

$$\underbrace{\iiint_{\Omega_{xy}} (1 - \alpha)^2 \operatorname{tr}((\nabla \mathbf{u} + \nabla^T \mathbf{u}) \nabla \mathbf{u})}_{\text{DIS}} + \underbrace{\iint_{\partial \Sigma_{\text{int}}} -(\underline{\tau} \mathbf{n}^0) \cdot \mathbf{u}}_{\text{BND}} + \underbrace{\iiint_{\Omega_{xy}} -u_z}_{\text{POT}} = 0, \quad (3.18)$$

where the bulk integrals are defined on the volume increment $dV = dA_{\Omega_{xy}} dz$, the surface integral is defined on the cylindrical surface with the cross-section $\partial \Sigma_{\text{int}}$ and axis in the z direction (see figure 3.3), DIS denotes the rate of viscous dissipation in the bulk fluid, BND denotes the rate of work done by the fluid through the interface, and POT denotes the rate of change of gravitational potential energy. (For more details about the derivation of the energy equation and its non-simplified and dimensional forms, see appendix 3.5.4.) The energy equation implies that the energy is released and consumed in the flow at the same rates, whereas multiple physical mechanisms may contribute to its release and consumption. In this regard, the sign of each term in (3.18) indicates whether the energy is removed from (+) or released into (−) the flow by the respective mechanism.

Energy analysis of the base flow

The energy equation for the base flow presented in §3.2.2, computed per unit length in z , can be expressed by

$$\underbrace{\iint_{\Omega_{xy}} (1-\alpha)^2 \operatorname{tr}((\nabla \mathbf{u}^0 + \nabla^T \mathbf{u}^0) \nabla \mathbf{u}^0)}_{\text{DIS}^0} + \underbrace{\iint_{\Omega_{xy}} -u_z^0}_{\text{POT}^0 = -Q^0} = 0, \quad (3.19)$$

which demonstrates that the potential energy released in the flow by drainage of the liquid is steadily dissipated in the bulk liquid. We recall that $Q^0 > 0$ (see figure 3.2) and the rate of potential energy release increases by increasing R_{ec} . Furthermore, recalling the dynamic condition (3.6), $\text{BND}^0 = 0$, which means that no energy is exchanged with the base flow from the cylindrical interface.

Energy analysis of the perturbed flow

The energy equation at the scale of the linear perturbations, i.e. ϵ^2 , computed along one wavelength, implies

$$\begin{aligned} & \left(\underbrace{\iint_{\Omega_{xy}} (1-\alpha)^2 \operatorname{tr}((\tilde{\nabla} \tilde{\mathbf{u}} + \tilde{\nabla}^T \tilde{\mathbf{u}}) \tilde{\nabla} \tilde{\mathbf{u}}^*)}_{\text{DIS}^1} \right)_r \\ & + \left(\underbrace{\int_{\partial \Sigma_{\text{int}}} \frac{\sigma^*}{Bo} \tilde{\kappa} \tilde{\eta}^*}_{\text{BND}_{c,1}^1 = \sigma^* \text{ SUR}^1} + \underbrace{\int_{\partial \Sigma_{\text{int}}} \frac{-ik u_z^0}{Bo} \tilde{\kappa} \tilde{\eta}^*}_{\text{BND}_{c,2}^1} + \underbrace{\int_{\partial \Sigma_{\text{int}}} -(\underline{\tilde{\tau}_v} \mathbf{n}^0) \cdot \tilde{\mathbf{u}}^*}_{\text{BND}_v^1} \right)_r = 0, \end{aligned} \quad (3.20)$$

where \star denotes the complex conjugate, $\text{BND}_{c,1}^1$ and $\text{BND}_{c,2}^1$ denote the capillary contributions to the rate of the work done by the fluid at the perturbed interface, SUR^1 denotes the surface energy stored in the perturbed interface, $\underline{\tilde{\tau}_v}$ denotes the viscous contribution of the stress tensor, and BND_v^1 denotes the viscous (shear) contribution to the rate of the work done by the fluid at the perturbed interface, which can be expressed as

$$\begin{aligned} \text{BND}_v^1 &= \int_{\partial \Sigma_{\text{int}}} (1-\alpha)^2 \tilde{u}_z^* \partial_{rr} u_z^0 \tilde{\eta} \\ &+ \int_{\partial \Sigma_{\text{int}}} -(1-\alpha)^2 \tilde{u}_\theta^* \partial_\theta u_z^0 ik \tilde{\eta} + \int_{\partial \Sigma_{\text{int}}} -(1-\alpha)^2 \tilde{u}_z^* \partial_\theta u_z^0 \partial_\theta \tilde{\eta}. \end{aligned} \quad (3.21)$$

We recall that the subscript r denotes the real part of a complex number. Equation (3.20) unravels that the work exchanged at the perturbed interface is partially dissipated in the bulk liquid, whereas the remainder (or deficit) is stored at (or released from) the free surface as interfacial energy. Equations (3.20)-(3.21) also evidence that the principal source of the work exchanged at the interface is the base flow itself, as the viscous contribution BND_v^1 and the

capillary contribution $\text{BND}_{c,2}^1$ are proportional to the base flow's shear and drainage velocity, respectively. Note that $\text{BND}_{c,1}^1$ also has an implicit contribution from the base flow through $\tilde{\kappa}$ and the assumption of a cylindrical interface for the base flow. (For further details on the derivation of (3.20) and its different terms, see appendix 3.5.4.)

For the P and W modes, the effect of increasing R_{ec} on each term of (3.20) is shown in table 3.1 and table 3.2, respectively. For both of these modes, the majority of energy exchange to the perturbations is due to the viscosity: energy enters the system through the shear at the interface, and it is mostly dissipated in the bulk. In the case of the P mode, $\sigma_r^* > 0$ and $(\text{SUR}^1)_r < 0$, meaning that over the course of time, by growth of the P perturbations, the surface energy is also released to the system. Recalling (3.17), for some value of $k \geq 1$, the sign of $\tilde{\kappa}$ (and subsequently the sign of $(\text{SUR}^1)_r$) changes, meaning that surface energy can be released only in small values of k , and it should be stored in large values of k , which in principle sets a cut-off wavenumber k_{cr} for the instability of the P mode. In other words, in some range $0 < k < k_{cr}$, the P mode is destabilised by both capillary and viscous mechanisms, which justifies its presence for all sets of $\{Oh \rightarrow \infty, Bo, \alpha, R_{ec}\}$. On the other hand, in the case of the W mode, $(\text{SUR}^1)_r > 0$, which indicates that with the growth of the whirling interface, a part of the energy released into the system is stored as surface energy. For small R_{ec} , the energy added to the system by the shear at the interface is not sufficient to destabilise the W mode; however, as R_{ec} increases, more energy is released to the perturbations by interfacial shear, which eventually suffices to destabilise the W mode. In other words, interfacial shear (in favour) and capillary (against) mechanisms exhibit opposite effects on the instability of the W mode; and for sufficiently large R_{ec} , the interfacial shear dominates over some range of k , thus originating the instability of the W mode.

R_{ec}	σ_r^*	$(\text{SUR}^1)_r$	$(\sigma^* \text{SUR}^1)_r$	$(\text{BND}_{c,2}^1)_r$	$(\text{BND}_v^1)_r$	$(\text{DIS}^1)_r$
0	0.0007110	-0.0079790	-0.0000057	0	-0.9999943	1
0.1	0.0007098	-0.0079499	-0.0000056	0.0000000	-0.9999943	1
0.5	0.0026527	-0.0069362	-0.0000184	0.0000064	-0.9999822	1

Table 3.1: The effect of R_{ec} on different terms in energy equation (3.20) for the perturbed flow, associated with the P mode: $Oh \rightarrow \infty$, $Bo = 50$, $\alpha = 0.1$, $k = 0.325$, $R_{ec} = \{0, 0.1, 0.5\}$. The corresponding dispersion curves and their eigeninterfaces are shown in figure 3.4. As the maximal growth rate of the W mode for $R_{ec} = 0.5$ occurs at $k = 0.325$, it is particularly chosen as the representative for demonstrating the effect of R_{ec} on the variation of each term. All of the energy terms are normalised with DIS. Recall that the sign of each term in (3.20) indicates whether the energy is removed from (+) or released into (−) the flow by the respective mechanism. Here, $(\text{SUR}^1)_r$ is also presented as its sign determines if the energy is stored in (+) or released from (−) the interface.

R_{ec}	σ_r^*	$(SUR^1)_r$	$(\sigma^* SUR^1)_r$	$(BND_{c,2}^1)_r$	$(BND_v^1)_r$	$(DIS^1)_r$
0	-0.0011307	0.0017903	-0.0000020	0	-0.9999980	1
0.1	-0.0014484	0.0016131	-0.0000023	0.0003023	-1.0003000	1
0.5	0.0406023	0.0075478	0.0003065	0.000829	-1.0011355	1

Table 3.2: Same as table 3.1 for the W mode.

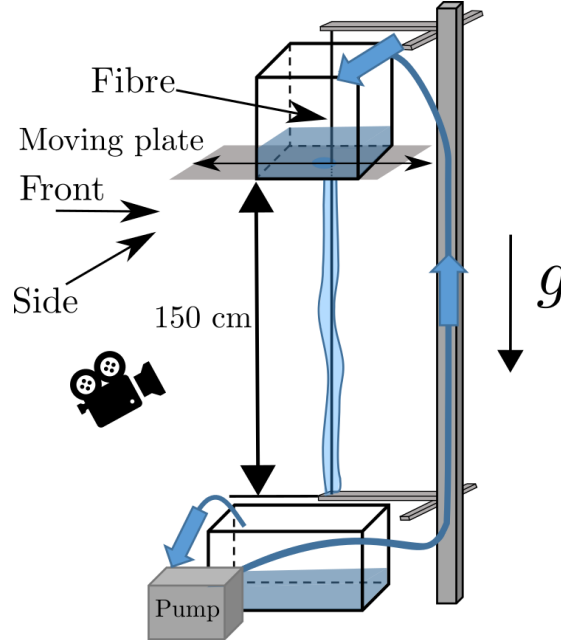


Figure 3.7: Schematic of the experimental set-up

3.3.5 Experimental observations

A set-up was designed *a posteriori* to observe experimentally the newly discovered unstable modes, as depicted in figure 3.7. Highly viscous silicone oil (47 V 100000 Bluesil™, with the following properties at 25°C: $\rho = 973 \text{ kg/m}^3$, $\mu = 89 \text{ Pa.s}$, $\gamma = 21.1 \times 10^{-3} \text{ N/m}$) is pumped by peristalsis to an upper tank with a moving bottom plate. The liquid discharges from a modular hole 8-10 mm in diameter, located on the moving plate through which a solid nylon fibre 0.7 mm in diameter passes vertically. From the upper tank, the liquid flows along the fibre over a distance $\sim 150 \text{ cm}$. The draining liquid is collected in a lower tank connected to the suction side of the pump. When the moving plate is at one extreme, the position of each fibre end is calibrated under high tension by means of two micrometric screws such that the fibre is vertical and concentric with the hole and liquid column (this step is repeated every time the moving plate is replaced to change the discharge hole diameter). Afterwards, the fibre eccentricity is varied by displacing the moving plate continuously (within $\sim 5 \text{ s}$), without touching the fibre. After displacement of the moving plate, flow takes $\sim 15 - 40 \text{ min}$ (depending on the discharge hole diameter and magnitude of the plate displacement) to redevelop along the fibre, and

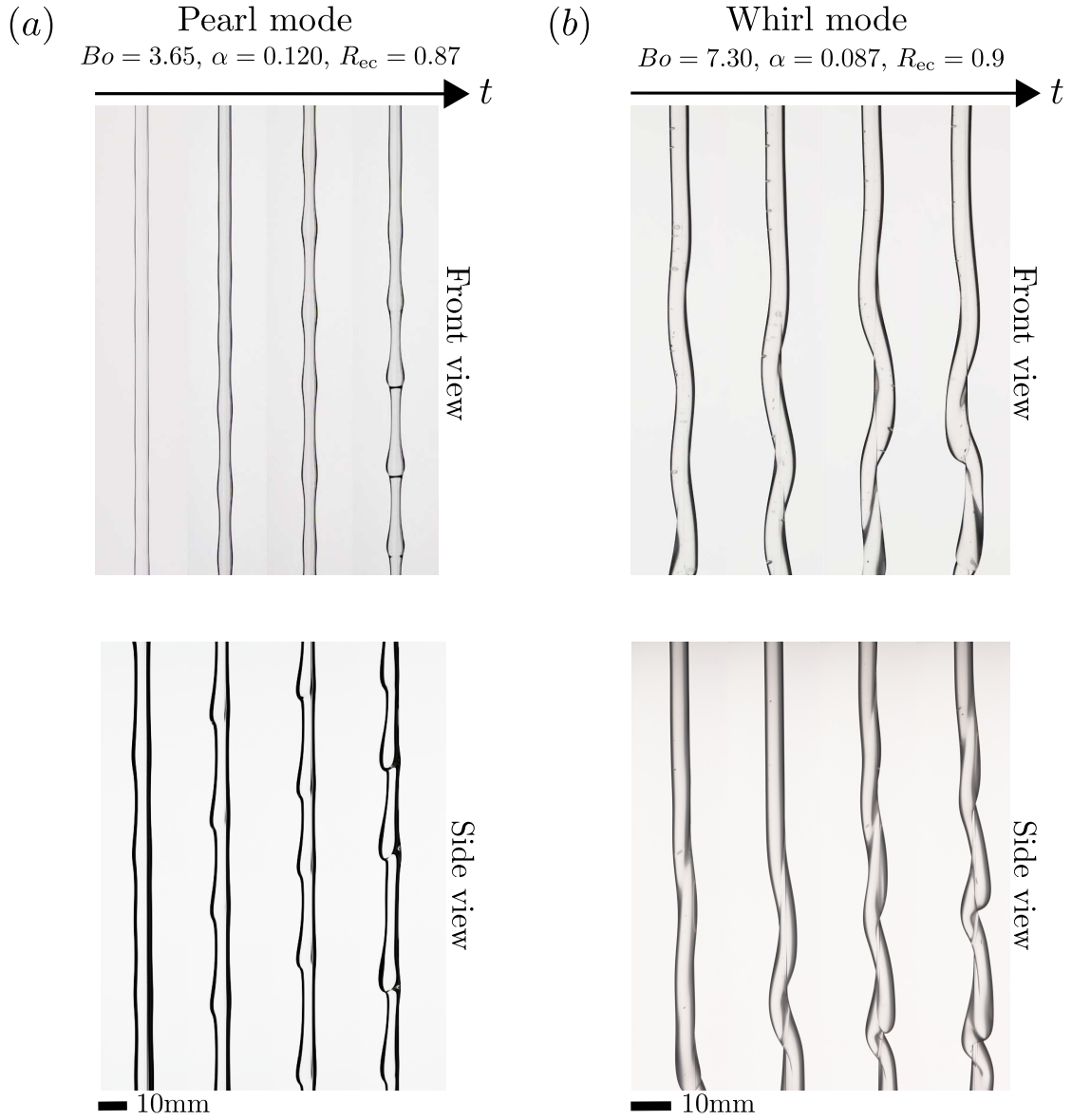


Figure 3.8: Experimental observation of the unstable modes: (a) pearls, data No. 1 in table 3.3; (b) whirling interface: data No. 7 in table 3.3. The front and side views are not synchronous.

readjusts the liquid column position and fibre eccentricity. Afterwards, it takes $\sim 5 - 10$ min for the first evidence of the instabilities to appear. Evolution of the base flow, from a concentric flow to the eccentric one, and the occurrence of the instabilities, are photographed from two orthogonal directions: in the direction of the plate displacement (hereafter front view), and orthogonal to the plate displacement (hereafter side view). After each experiment run, the moving plate is brought back to its initial position, leading to a fully developed concentric flow down the fibre. We repeat the same procedure multiple times for different values of moving plate displacement.

Data No.	Oh	Bo	α	R_{ec}	k_{exp}	k_{LSA}	Mode _{exp}	Mode _{LSA}
1	369	3.65	0.120	0.87	0.40 ± 0.06	0.44	P	P
2	344	4.83	0.107	0.64	0.43 ± 0.06	0.45	P	P
3	339	5.03	0.104	0.46	0.41 ± 0.07	0.43	P	P
4	331	5.34	0.101	0.87	0.32 ± 0.05	0.30	W	W*
5	327	5.86	0.097	0.69	0.40 ± 0.07	0.44	P	P*
6	321	6.32	0.094	0.95	0.28 ± 0.08	0.28	W	W*
7	310	7.30	0.087	0.90	0.34 ± 0.08	0.28	W	W*
8	308	7.47	0.086	0.87	0.28 ± 0.06	0.28	W	W*
9	306	7.65	0.085	0.85	0.35 ± 0.06	0.29	W	W*
10	303	7.99	0.083	0.84	0.24 ± 0.06	0.28	W	W*

Table 3.3: Dimensionless parameters associated with the experimental points, reported along with the comparison between the measured experimental wavenumber (comprising the standard deviation) k_{exp} , and the maximal wavenumber predicted by the linear stability analysis k_{LSA} . Here, Mode_{exp} indicates the mode observed experimentally, and Mode_{LSA} indicates the dominant unstable mode obtained from the stability analysis, where the superscript * indicates that both P and W modes are unstable. The linear predictions confirm the dominant modes observed in all of the experiments. Data No. 1 and 7 are illustrated in the panels (a) and (b) of figure 3.8, respectively.

Figure 3.8 presents examples of the pearling and whirling interfaces captured over time, observed from side and front views. When the fibre eccentricity is small (figure 3.8(a)), pearls start to form. While advected downwards, pearls preserve the planar symmetry of the system (front view) and grow predominantly on the thick side (side view). As they grow more, their velocity and spacing alter from the early stage of their emergence under the effect of non-linearities (see supplementary movie 1 available at <https://doi.org/10.1017/jfm.2022.876>). By increasing the fibre eccentricity far enough (figure 3.8(b)), whirling structures appear. Initially small, the perturbations grow and finally merge under non-linear effects. The merged structures are advected by the flow, and soon after, new whirling structures emerge and similar sequences repeat (see supplementary movie 2 available at <https://doi.org/10.1017/jfm.2022.876>). Table 3.3 shows, for different conditions, which mode is observed experimentally (P or W) and the unstable eigenmode(s) predicted by linear stability analysis (P only, P dominant, or W dominant). In all our experiments, the mode observed experimentally corresponds to the dominant unstable eigenmode. The wavelengths of the emerging structures were measured by means of a MathematicaTM image analysis script over multiple formation periods of the unstable structures (see appendix 3.5.5 for more details about the image analyses). Table 3.3 presents the measured wavenumbers (dimensionless) from the experimental observations, k_{exp} , and the maximal wavenumber predicted by the stability analysis, k_{LSA} . The comparison confirms a firm agreement between the experiments and the linear stability analysis. We can confirm that the flow is inertialess, as $(Bo/Oh^2)(1-\alpha)^4 \leq 6.2 \times 10^{-5}$ for all of our experiments in table 3.3.

The main difficulty of the experiments is the observation of the pearl modes at high Bo . Indeed, increasing Bo leads to faster convection, which delays the appearance of the pearls further down the liquid column. With a total length of 1.5m, pearl modes are difficult to observe above $Bo \approx 10$, and this difficulty increases as Bo is increased further (similarly when R_{ec} is decreased). Furthermore, the hole at the exit of the tank hosts a complex three-dimensional flow induced by a sudden change of boundary conditions. It leads to the selection of values for the eccentricity that are difficult to control and very sensitive to the position of the fibre within the hole.

Altogether, we believe that this is the first experimental observation of the whirling patterns in flows down a fibre. We hope that this work will foster further experimental investigations, including fluids with complex rheological properties, or non-circular sections for the liquid column.

3.4 Summary and conclusion

In this work, we studied the stability of a gravity-driven flow along an eccentric solid fibre in the absence of inertia. To begin with, the base flow was computed numerically for different values of the fibre size and eccentricity under the assumption of a fully developed parallel flow with a cylindrical interface. The results exhibit a substantial increase in the drainage, up to more than twofold, when the fibre eccentricity is increased.

Next, the stability of the base flow was investigated by means of linear stability analysis, where an extensive study was conducted on the space of dimensionless parameters $\{Oh \rightarrow \infty, Bo, \alpha, R_{ec}\}$. Two main unstable modes were identified in the parameters space. First, the pearl mode evidences the characteristics of the Rayleigh-Plateau instability, but with a distorted interface caused by the broken symmetry of the flow, due to the fibre eccentricity. This mode destabilises for any set of parameters over some range of wavenumbers $0 < k < k_{cr}$, where k_{cr} may differ from unity depending on the flow parameters. Second, we identified for the first time the instability of the whirl mode that forms a single helix whirling around the fibre along its axial direction in some region of the parameters space. While in such a flow a whirling interface is well known from the literature to be stable for defying the surface energy minimisation (the main driving force of the Rayleigh-Plateau instability), the present linear analysis depicts that a small fibre radius, large fibre eccentricity and high Bo promote instability of the whirl mode. Additionally, for a fixed Bo , a cut-off value was observed for the fibre eccentricity below which no unstable whirl mode was found, even by further decreasing the fibre radius.

In order to elucidate the origin of the whirling instability, an energy analysis was formulated to delve into the physical mechanisms underlying the flow at the scales of the base flow and linear perturbations. This analysis, at the scale of the base flow, demonstrates the drainage as the means for the liquid to release its gravitational potential energy. This released energy ultimately dissipates in the bulk fluid, which sustains a fully developed drainage. By increasing

the fibre eccentricity, drainage increases, hence the potential energy release is also boosted. In the presence of infinitesimal perturbations in the flow, a part of the dissipated energy is injected into the perturbations through the interface shear. On top of that, the energy analysis of the perturbed flow unravels the instability of the whirl mode as a direct consequence of the increased rate of shear work at the interface, which is dissipated mainly in the bulk fluid, and its remainder is stored at the liquid surface to promote the growth of the whirling structure over time. In the case of the pearl mode, both surface energy release and interface shear work support the growth of pearls for small wavenumbers. In contrast, for higher wavenumbers, surface tension acts oppositely and stabilises the perturbations, thus establishing a cut-off wavenumber k_{cr} for the instability of the pearl mode, different from that of the Rayleigh-Plateau instability (Rayleigh, 1878).

Finally, we compared the results of our stability analysis with a set of experiments carried out with a highly viscous silicone oil. We reported the experimental observation of the whirling perturbed interface in the flow down a rigid eccentric fibre. In addition, the dominant mode and the maximal wavenumbers predicted by the linear stability analysis agree very well with the experimental observations.

The formation of a liquid helix has been reported previously for the drainage of liquid jets along vertical fibres (Jambon-Puillet et al., 2019). However, those peculiar patterns have a very different origin, and emerge from an initially azimuthal flow, where surface tension keeps the liquid attached to the fibre and inertia enables it to temporarily maintain the azimuthal velocity component downstream. In our study, the shifted pearls and whirling patterns remarkably emerge from an inertialess flow, initially fully parallel to the fibre.

Possible experimental directions for future works include exploring fluids with complex rheological properties, insofar as whirling patterns emerge from a competition between interfacial shear and surface tension. In our study, the liquid column is initially cylindrical, as the hole in the bottom of the reservoir is circular. Modifications of the hole geometry (e.g. ellipsoids or polygons) are expected to lead to a rich variety of patterns. Furthermore, the flow can be studied from the absolute/convective perspective in order to better elucidate the competition between pearling and whirling modes.

Supplementary material <https://gfm.aps.org/meetings/dfd-2020/5f4e05c3199e4c091e67ba3f>

3.5 Appendix

3.5.1 Derivation of the interface boundary conditions

In this section, the derivation of the interface boundary conditions for the perturbed flow is elaborated. These conditions should be imposed on the perturbed interface, i.e. on $r = 1 + \epsilon\eta^1$, while η^1 is already a part of the problem unknowns. By using the Taylor expansion, that is, projecting radially on the base interface, i.e. on $r = 1$, any flow quantity at the perturbed interface can be readily approximated. This projection is referred to as flattening and for an arbitrary function $f(r, \theta, z)$ can be expressed as

$$f|_{(r=1+\epsilon\eta^1, \theta, z)} = f|_{(r=1, \theta, z)} + \epsilon\eta^1 \partial_r f|_{(r=1, \theta, z)} + \mathcal{O}(\epsilon^2). \quad (3.22)$$

By substituting the decomposed state vector of (3.8), into the interface conditions (3.5)-(3.6), then using the ansatz of (3.9), and applying the aforementioned flattening, we can formulate these conditions as a set of equivalent constraints on the boundary of the base interface. The linearised kinematic condition readily writes (3.12), and the linearised dynamic condition writes

$$\underline{\underline{\tau}}^0 \tilde{\mathbf{n}} + \tilde{\eta} \partial_r \underline{\underline{\tau}}^0 \mathbf{n}^0 + \tilde{\tau} \mathbf{n}^0 = -\frac{1}{Bo} (\kappa^0 \tilde{\mathbf{n}} + \tilde{\kappa} \mathbf{n}^0), \quad \text{on } r = 1, \quad (3.23)$$

where $\kappa^0 = 1$, $\mathbf{n}^0 = 1\mathbf{e}_r$ and $\tilde{\mathbf{n}} = -\partial_\theta \tilde{\eta} \mathbf{e}_\theta - ik\tilde{\eta} \mathbf{e}_z$, hence (3.16). In order to express this constraint in the Cartesian coordinates, some of its terms should be transformed by employing the Jacobian transformations as

$$\begin{aligned} \mathbf{e}_r &= \cos\theta \mathbf{e}_x + \sin\theta \mathbf{e}_y, & \mathbf{e}_\theta &= -\sin\theta \mathbf{e}_x + \cos\theta \mathbf{e}_y, \\ \partial_r &= \cos\theta \partial_x + \sin\theta \partial_y, & \partial_\theta &= \frac{\mathbf{t}^0 \cdot \nabla_s}{\mathbf{t}^0 \cdot \nabla_s \theta}, \end{aligned} \quad (3.24)$$

where \mathbf{t}^0 denotes the unit tangent vector, and $\nabla_s = \nabla - \mathbf{n}^0 (\mathbf{n}^0 \cdot \nabla)$ is the tangential derivative on the base interface. For further details concerning the numerical implementation of boundary conditions, see appendix 3.5.2.

3.5.2 Variational formulation of problem and implementation of boundary conditions

Implementation of the numerical scheme and development of the *variational formulation* associated with the governing equations presented in section 3.2 are elaborated in this appendix, recalling that the numerical domain is shown in figure 3.3.

Base flow

The stationary limit of the Navier-Stokes equations (3.2)-(3.3), for a fully developed axial flow field $\mathbf{q}^0 = (u_z^0, p^0, 1)^T$ implies

$$(1 - \alpha)^2 \nabla_{xy}^2 u_z^0 + 1 = 0, \quad p^0 = \text{const.}, \quad \text{on } \Omega_{xy}, \quad (3.25)$$

where $\nabla_{xy}^2 = \nabla_{xy} \cdot \nabla_{xy} = \partial_{xx} + \partial_{yy}$ denotes the Laplacian in the cross-section. As explained in §3.2.2, the kinematic condition (3.5) is trivial. The interface dynamic condition (3.6) readily implies

$$\nabla_{xy} u_z^0 \cdot \mathbf{n}^0 = 0, \quad p^0 = \frac{1}{Bo}, \quad \text{at } \partial\Sigma_{\text{int}}. \quad (3.26)$$

To obtain the variational form of (3.25), it should be multiplied by a *test function*, ψ_z , and be integrated on Ω_{xy} as

$$\iint_{\Omega_{xy}} \left((1 - \alpha)^2 \nabla_{xy}^2 u_z^0 + 1 \right) \psi_z \, dA_{\Omega_{xy}} = 0. \quad (3.27)$$

After integrating the first term by part, $\psi_z \nabla_{xy}^2 u_z^0 = \nabla_{xy} \cdot (\psi_z \nabla_{xy} u_z^0) - \nabla_{xy} u_z^0 \cdot \nabla_{xy} \psi_z$, and then applying the Gauss's theorem to it, $\iint_{\Omega_{xy}} \nabla_{xy} \cdot (\psi_z \nabla_{xy} u_z^0) \, dA_{\Omega_{xy}} = \int_{\partial\Omega_{xy}} (\psi_z \nabla_{xy} u_z^0) \cdot \mathbf{n}^0 \, ds$, we can impose (3.26) on $\partial\Sigma_{\text{int}}$ and no-slip condition on $\partial\Sigma_f$. The final variational form of the base flow equations writes

$$\iint_{\Omega_{xy}} \left(-(1 - \alpha)^2 \nabla_{xy} u_z^0 \cdot \nabla_{xy} \psi_z + \psi_z \right) \, dA_{\Omega_{xy}} = 0. \quad (3.28)$$

It should be noted that $\psi_z|_{\partial\Sigma_f} = 0$ due to the *Dirichlet* nature of the no-slip boundary condition. Variational equation (3.28) can be readily implemented and solved in COMSOL MultiphysicsTM.

Linear stability analysis

To develop the variational form of (3.13), the procedure is in a similar fashion as that of the base flow (see appendix 3.5.2). First, the normal mode of (3.9) is applied to the system of equations (3.10)-(3.12). Then it is internally multiplied by the vector of the test functions $\psi = (\psi_p, \psi_{\mathbf{u}}, \psi_{\eta})^T$, where $\psi_{\mathbf{u}} = (\psi_{u_x}, \psi_{u_y}, \psi_{u_z})^T$. The resulting scalar product is integrated on Ω_{xy} , which in the linear order writes

$$\begin{aligned} & \left\{ \iint_{\Omega_{xy}} \psi_p^* (\tilde{\nabla} \cdot \tilde{\mathbf{u}}) \, dA_{\Omega_{xy}} \right. \\ & + \iint_{\Omega_{xy}} \psi_{\mathbf{u}}^* \cdot \left(\frac{Bo}{Oh^2} (1 - \alpha)^4 (\sigma \tilde{\mathbf{u}} + (\mathbf{u}^0 \cdot \tilde{\nabla}) \tilde{\mathbf{u}} + (\tilde{\mathbf{u}} \cdot \nabla) \mathbf{u}^0) - \tilde{\nabla} \cdot \underline{\underline{\tilde{\tau}}}) \right) \, dA_{\Omega_{xy}} \\ & \left. + \int_{\partial\Sigma_{\text{int}}} \psi_{\eta}^* ((\sigma + ik u_z^0) \tilde{\eta} - \tilde{\mathbf{u}} \cdot \mathbf{e}_r) \, ds \right\} + \text{c.c.} = 0. \end{aligned} \quad (3.29)$$

It should be noted that in a complex system, applied scalar product is Hermitian, defined as $\langle \mathbf{a}, \mathbf{b} \rangle = \mathbf{a}^* \cdot \mathbf{b}$ where the superscript $*$ denotes the complex conjugate. In the last line of this system of equations, kinematic condition (3.12) is used to define $\tilde{\eta}$ only at $\partial\Sigma_{\text{int}}$. After integrating by part, $\psi_{\mathbf{u}}^* \cdot (\tilde{\nabla} \cdot \underline{\underline{\tilde{\tau}}}) = \tilde{\nabla} \cdot (\underline{\underline{\tilde{\tau}}} \psi_{\mathbf{u}}^*) - \text{tr} \left(\underline{\underline{\tilde{\tau}}}^T (\tilde{\nabla} \psi_{\mathbf{u}})^* \right)$, and then applying the Gauss's theorem, $\iint_{\Omega_{xy}} \tilde{\nabla} \cdot (\underline{\underline{\tilde{\tau}}} \psi_{\mathbf{u}}^*) \, dA_{\Omega_{xy}} = \int_{\partial\Omega_{xy}} (\underline{\underline{\tilde{\tau}}} \psi_{\mathbf{u}}^*) \cdot \mathbf{n}^0 \, ds$, (3.29) implies

$$\begin{aligned} & \left\{ \iint_{\Omega_{xy}} \psi_p^* (\tilde{\nabla} \cdot \tilde{\mathbf{u}}) \, dA_{\Omega_{xy}} \right. \\ & + \iint_{\Omega_{xy}} \psi_{\mathbf{u}}^* \cdot \left(\frac{Bo}{Oh^2} (1-\alpha)^4 (\sigma \tilde{\mathbf{u}} + (\mathbf{u}^0 \cdot \tilde{\nabla}) \tilde{\mathbf{u}} + (\tilde{\mathbf{u}} \cdot \nabla) \mathbf{u}^0) \right) \, dA_{\Omega_{xy}} \\ & + \iint_{\Omega_{xy}} \text{tr} \left(\underline{\underline{\tilde{\tau}}}^T (\tilde{\nabla} \psi_{\mathbf{u}})^* \right) \, dA_{\Omega_{xy}} \\ & + \int_{\partial\Omega_{xy}} -(\underline{\underline{\tilde{\tau}}} \psi_{\mathbf{u}}^*) \cdot \mathbf{n}^0 \, ds \\ & \left. + \int_{\partial\Sigma_{\text{int}}} \psi_{\eta}^* ((\sigma + iku_z^0) \tilde{\eta} - \tilde{\mathbf{u}} \cdot \mathbf{e}_r) \, ds \right\} + \text{c.c.} = 0. \end{aligned} \quad (3.30)$$

$\underline{\underline{\tilde{\tau}}}$ is symmetric, thus $(\underline{\underline{\tilde{\tau}}} \psi_{\mathbf{u}}^*) \cdot \mathbf{n}^0 = (\underline{\underline{\tilde{\tau}}} \mathbf{n}^0) \cdot \psi_{\mathbf{u}}^*$. Using the dynamic condition (3.23) and the fact that $\psi_{\mathbf{u}}|_{\partial\Sigma_f} = 0$ (because of the no-slip condition on fibre), the variational form of (3.13) implies

$$\left\{ \iint_{\Omega_{xy}} \psi_p^* (\tilde{\nabla} \cdot \tilde{\mathbf{u}}) \, dA_{\Omega_{xy}} \right. \quad (3.31)$$

$$+ \iint_{\Omega_{xy}} \psi_{\mathbf{u}}^* \cdot \left(\frac{Bo}{Oh^2} (1-\alpha)^4 \sigma \tilde{\mathbf{u}} \right) \, dA_{\Omega_{xy}} \quad (3.32)$$

$$+ \iint_{\Omega_{xy}} \psi_{\mathbf{u}}^* \cdot \left(\frac{Bo}{Oh^2} (1-\alpha)^4 ((\mathbf{u}^0 \cdot \tilde{\nabla}) \tilde{\mathbf{u}} + (\tilde{\mathbf{u}} \cdot \nabla) \mathbf{u}^0) \right) \, dA_{\Omega_{xy}} \quad (3.33)$$

$$+ \iint_{\Omega_{xy}} \text{tr} \left(\underline{\underline{\tilde{\tau}}}^T (\tilde{\nabla} \psi_{\mathbf{u}})^* \right) \, dA_{\Omega_{xy}} \quad (3.34)$$

$$+ \int_{\partial\Sigma_{\text{int}}} \left(\underline{\underline{\tau}}^0 \tilde{\mathbf{n}} + \tilde{\eta} \partial_r \underline{\underline{\tau}}^0 \mathbf{n}^0 + \frac{1}{Bo} (\kappa^0 \tilde{\mathbf{n}} + \tilde{\kappa} \mathbf{n}^0) \right) \cdot \psi_{\mathbf{u}}^* \, ds \quad (3.35)$$

$$+ \int_{\partial\Sigma_{\text{int}}} \psi_{\eta}^* (\sigma \tilde{\eta}) \, ds \quad (3.36)$$

$$+ \int_{\partial\Sigma_{\text{int}}} \psi_{\eta}^* (iku_z^0 \tilde{\eta} - \tilde{\mathbf{u}} \cdot \mathbf{e}_r) \, ds \Big\} \quad (3.37)$$

$$+ \text{c.c.} = 0. \quad (3.38)$$

This variational equation can be readily implemented and solved in COMSOL MultiphysicsTM. It is sufficient to solve the first part (in $\{\}$) and the c.c. is known consequently. The matrix representation of (3.31)-(3.38) is shown in figure 3.9.

$$\begin{array}{|c|c|c|c|c|} \hline & (3.31) & & & \\ \hline & (3.33-3.34) & & & \\ \hline & (3.31) & & & \\ \hline 0 & \mathbf{0} & 0 & \mathbf{I} & \mathbf{0} \\ \hline & (3.31) & & & \\ \hline 0 & \mathbf{0} & 0 & \mathbf{0} & (3.35) \\ \hline 0 & \mathbf{0} & 0 & \mathbf{0} & (3.37) \\ \hline \end{array}
\begin{array}{|c|} \hline \begin{bmatrix} \tilde{p} \\ \tilde{\mathbf{u}} \end{bmatrix}_{\Omega_{xy}} \\ \hline \begin{bmatrix} \tilde{p} \\ \tilde{\mathbf{u}} \end{bmatrix}_{\partial\Sigma_w} \\ \hline \begin{bmatrix} \tilde{p} \\ \tilde{\mathbf{u}} \\ \tilde{\eta} \end{bmatrix}_{\partial\Sigma_{\text{int}}} \\ \hline \end{array}
= -\sigma
\begin{array}{|c|c|c|c|c|} \hline 0 & \mathbf{0} & 0 & \mathbf{0} & \mathbf{0} \\ \hline 0 & (3.32) & 0 & \mathbf{0} & \mathbf{0} \\ \hline 0 & \mathbf{0} & 0 & \mathbf{0} & \mathbf{0} \\ \hline 0 & \mathbf{0} & 0 & \mathbf{0} & \mathbf{0} \\ \hline 0 & \mathbf{0} & 0 & \mathbf{0} & \mathbf{0} \\ \hline 0 & \mathbf{0} & 0 & \mathbf{0} & \mathbf{0} \\ \hline 0 & \mathbf{0} & 0 & \mathbf{0} & \mathbf{0} \\ \hline 0 & \mathbf{0} & 0 & \mathbf{0} & (3.36) \\ \hline \end{array}
\begin{array}{|c|} \hline \begin{bmatrix} \tilde{p} \\ \tilde{\mathbf{u}} \end{bmatrix}_{\Omega_{xy}} \\ \hline \begin{bmatrix} \tilde{p} \\ \tilde{\mathbf{u}} \end{bmatrix}_{\partial\Sigma_w} \\ \hline \begin{bmatrix} \tilde{p} \\ \tilde{\mathbf{u}} \\ \tilde{\eta} \end{bmatrix}_{\partial\Sigma_{\text{int}}} \\ \hline \end{array}$$

Figure 3.9: Matrix representation of the variational system (3.31)-(3.38), solved in COMSOL MultiphysicsTM; blue represents the implementation of (3.10)-(3.11); white represents the implementation of the no-slip boundary condition on fibre; green represents the implementation of the dynamic boundary condition (3.16); beige represents the implementation of the kinematic condition (3.12).

3.5.3 Validation of numerical model

The developed numerical scheme is validated hereafter. Several measures are taken to ensure the correspondence of the model, based on the asymptotic limits.

linear stability analysis model

Linear stability analysis is validated with the analytical solutions that Craster and Matar (2006); Duprat (2009); Gallaire and Brun (2017) presented for the coating flow over a long centred fibre. All of these references employed an approximation of the Stokes equations for long jets, referred to as the *long-wavelength approximation* (Reynolds, 1886). Craster and Matar (2006) expresses the growth rate of the linearly unstable axisymmetric modes in terms of the Bessel function of the first type for the full range of α . Duprat (2009); Gallaire and Brun (2017) employed also the *lubrication approximation* and represented the growth rate as $\sigma = \frac{1-\alpha}{3Bo}(k^2 - k^4) - ik$ in the limit of thin film, i.e. $\alpha \rightarrow 1$. Figures 3.10(a) and 3.10(b) present the validity of our model for any α , evidenced by the firm agreement between our numerical model and the analytical solutions for the arbitrary values of $\alpha = 0.6$ and $\alpha = 0.9$, representing the thick and thin liquid film limits, respectively.

Grid independency

A convergence study for the P and W modes' eigenvalues is presented in figure 3.11, for an arbitrary set of parameters as an example. Mesh convergence is already attained for $\sim 3.5k$ degrees of freedom, N_{dofs} , in this case. The threshold of mesh convergence may slightly vary with R_{ec} and Bo . In the case of large R_{ec} , fibre vicinity requires more refinement due to the large gradients of the fluid fields originated from the asymmetric base flow. Furthermore, as the capillary length scales as $l_c \propto Bo^{-1/2}$, interface mesh resolution plays a crucial role in

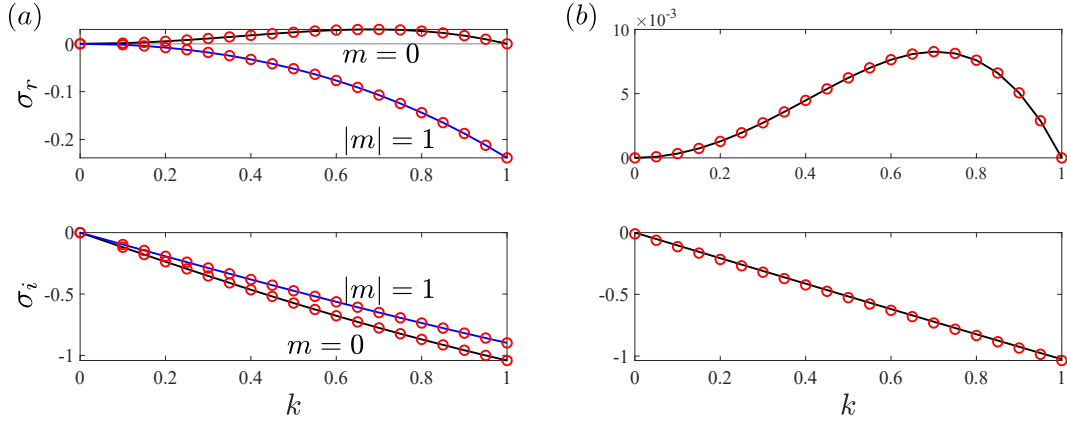


Figure 3.10: Comparison between the present numerical model (\circ) and analytical dispersion relation ($-$) for a centred fibre, $R_{ec} = 0$; (a) thick film, $\alpha = 0.6$, $|m| = \{0, 1\}$; (b) thin film, $\alpha = \{0.9\}$, $m = 0$. Both cases correspond to $Oh \rightarrow \infty$, $Bo = 1$. Black and blue colours refer to the P and W modes, respectively; Craster and Matar (2006); Duprat (2009); Gallaire and Brun (2017) considered a similar perturbation as in equation 3.8 with the Fourier ansatz exponent of $\exp[\sigma t + ikz + im\theta]$, a typical choice for the axisymmetric configurations. For a centred fibre, the P and W modes are identical to the $m = 0$ and $|m| = 1$ modes, respectively.

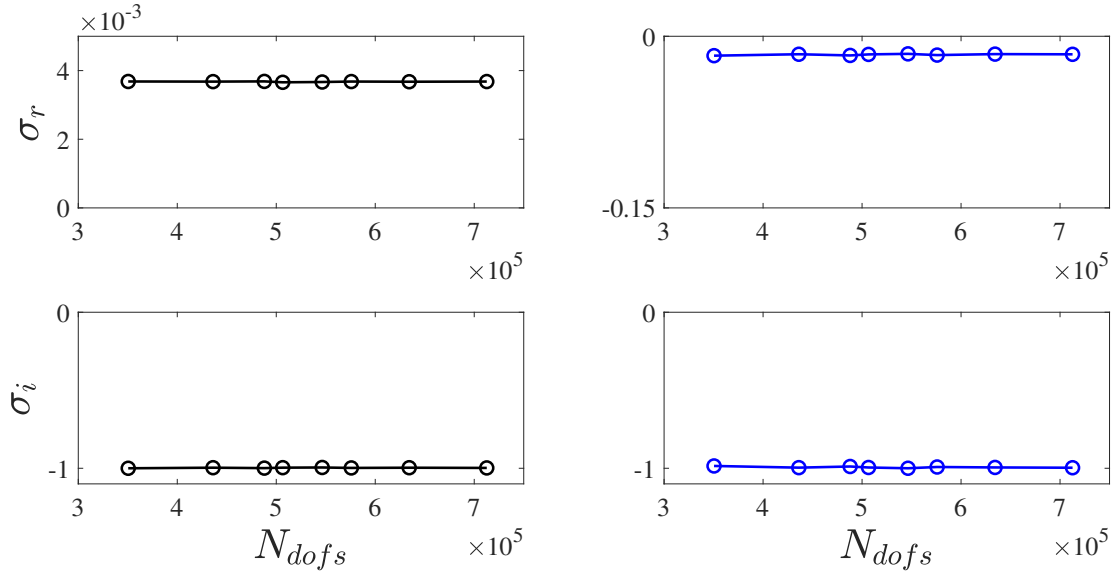


Figure 3.11: Mesh convergence proof of the P (black) and W (blue) eigenvalues as a function of N_{dofs} . Eigenvalues are rescaled with the modulus of the eigenvalue from the most refined mesh; $Oh \rightarrow \infty$, $Bo = 50$, $R_{ec} = 0.3$, $\alpha = 0.4$, $k = 0.3$.

N_{dof} required for mesh convergence. Number of divisions on the interface should be such that elements' edge stays shorter than l_c , the reason why our study is restricted up to $Bo = 50$.

3.5.4 Derivation of the energy equation

Energy equation

In this section, the derivation of the energy equation is elaborated. We recall the momentum equation (3.3), which in the dimensional form reads

$$\rho (\partial_t + (\mathbf{u}' \cdot \nabla)) \mathbf{u}' = \nabla \cdot \underline{\underline{\tau}}' + \rho \mathbf{g}, \quad (3.39)$$

where the superscript $'$ denotes dimensional quantities, and the dimensional stress tensor reads

$$\underline{\underline{\tau}}' = -p' \mathbf{I} + \mu (\nabla \mathbf{u}' + \nabla \mathbf{u}'^T). \quad (3.40)$$

To obtain the energy equation, we begin with computing the scalar product of (3.39) and the velocity vector \mathbf{u}' , then we integrate the product across the liquid bulk, which writes

$$\iiint_{\Omega_{xy}} \rho \mathbf{u}' \cdot (\partial_t \mathbf{u}' + (\mathbf{u}' \cdot \nabla) \mathbf{u}') dV = \iiint_{\Omega_{xy}} \mathbf{u}' \cdot (\nabla \cdot \underline{\underline{\tau}}' + \rho \mathbf{g}) dV. \quad (3.41)$$

Each term in this equation has the dimension of power, J/s . After integrating the first term in the right hand side (RHS) by part, that is, $\mathbf{u}' \cdot (\nabla \cdot \underline{\underline{\tau}}') = \nabla \cdot (\underline{\underline{\tau}}'^T \mathbf{u}') - tr(\underline{\underline{\tau}}' \nabla \mathbf{u}')$, and then applying the Gauss's theorem to it, $\iiint_{\Omega_{xy}} \nabla \cdot (\underline{\underline{\tau}}'^T \mathbf{u}') dV = \iint_{\partial\Omega_{xy}} (\underline{\underline{\tau}}'^T \mathbf{u}') \cdot \mathbf{n}^0 dA_{\partial\Omega_{xy}}$, (3.41) implies

$$\iiint_{\Omega_{xy}} \rho \mathbf{u}' \cdot (\partial_t \mathbf{u}' + (\mathbf{u}' \cdot \nabla) \mathbf{u}') = \iint_{\partial\Omega_{xy}} (\underline{\underline{\tau}}'^T \mathbf{u}') \cdot \mathbf{n}^0 - \iiint_{\Omega_{xy}} tr(\underline{\underline{\tau}}' \nabla \mathbf{u}') + \iiint_{\Omega_{xy}} \rho g u'_z, \quad (3.42)$$

In the aforementioned equation, and hereafter, for the ease of notation, we omit dV from volumetric integrals, $dA_{\partial\Omega_{xy}}$ from boundary surface integrals, and ds from the one-dimensional boundary integrals.

Further simplification can be made as $tr(\underline{\underline{\tau}}' \nabla \mathbf{u}') = -p' \nabla \cdot \mathbf{u}' + \mu tr((\nabla \mathbf{u}' + \nabla^T \mathbf{u}') \nabla \mathbf{u}')$, where $\nabla \cdot \mathbf{u}' = 0$ due to the incompressibility. Symmetry of the stress tensor implies $(\underline{\underline{\tau}}'^T \mathbf{u}') \cdot \mathbf{n}^0 = (\underline{\underline{\tau}}' \mathbf{n}^0) \cdot \mathbf{u}'$. Hence, the general form of the energy equation can be expressed as

$$\begin{aligned}
& \underbrace{\iiint_{\Omega_{xy}} \rho \mathbf{u}' \cdot \partial_t \mathbf{u}'}_{\text{KIN}} + \underbrace{\iiint_{\Omega_{xy}} \rho \mathbf{u}' \cdot ((\mathbf{u}' \cdot \nabla) \mathbf{u}')}_{\text{REY}} + \underbrace{\iiint_{\Omega_{xy}} \mu \operatorname{tr}((\nabla \mathbf{u}' + \nabla^T \mathbf{u}') \nabla \mathbf{u}')}_{\text{DIS}} \\
& + \underbrace{\iint_{\partial\Omega_{xy}} -(\underline{\tau}' \mathbf{n}^0) \cdot \mathbf{u}'}_{\text{BND}} + \underbrace{\iiint_{\Omega_{xy}} -\rho g u'_z}_{\text{POT}} = 0.
\end{aligned} \tag{3.43}$$

Each under-brace denotes the physical mechanism associated with the respective term, as follows:

1. KIN: the temporal rate of kinetic energy in the bulk fluid
2. REY: the rate of energy transmission between fluid layers due to the Reynolds stresses
3. DIS: the rate of viscous dissipation in the bulk fluid
4. BND: the rate of work done by the fluid through the moving boundaries
5. POT: the rate of change of gravitational potential energy

Now that the physical mechanism behind each term in the energy equation is demonstrated, following the scaling presented in §3.2, the dimensionless form of the energy equation can be expressed as

$$\begin{aligned}
& \underbrace{\iiint_{\Omega_{xy}} \frac{Bo}{Oh^2} (1-\alpha)^4 \mathbf{u} \cdot \partial_t \mathbf{u}}_{\text{KIN}} + \underbrace{\iiint_{\Omega_{xy}} \frac{Bo}{Oh^2} (1-\alpha)^4 \mathbf{u} \cdot ((\mathbf{u} \cdot \nabla) \mathbf{u})}_{\text{REY}} \\
& + \underbrace{\iiint_{\Omega_{xy}} (1-\alpha)^2 \operatorname{tr}((\nabla \mathbf{u} + \nabla^T \mathbf{u}) \nabla \mathbf{u})}_{\text{DIS}} + \underbrace{\iint_{\partial\Omega_{xy}} -(\underline{\tau} \mathbf{n}^0) \cdot \mathbf{u}}_{\text{BND}} + \underbrace{\iiint_{\Omega_{xy}} -u_z}_{\text{POT}} = 0.
\end{aligned} \tag{3.44}$$

In the limit of inertialess coating flow along a fibre, $(Bo/Oh^2)(1-\alpha)^4 \ll 1$, KIN and REY are negligible. Furthermore, $\mathbf{u} = \mathbf{0}$ at $\partial\Sigma_f$, thus yielding (3.18).

Energy equation for the perturbed flow

The energy equation for the perturbed flow is obtained by substituting the perturbed state vector (3.8) with the ansatz of (3.9), into (3.18) and integrating it over one wavelength $\Delta z = \lambda = 2\pi/k$. The resulting integral in ϵ^2 order determines the energy equation for the linear perturbations which implies

$$\frac{2\pi}{k} e^{2\sigma_r t} \left[\underbrace{\iint_{\Omega_{xy}} (1-\alpha)^2 \operatorname{tr}((\tilde{\nabla} \tilde{\mathbf{u}} + \tilde{\nabla}^T \tilde{\mathbf{u}}) \tilde{\nabla} \tilde{\mathbf{u}}^*)}_{\text{DIS}^1} + \underbrace{\int_{\partial \Sigma_{\text{int}}} -(\tilde{\underline{\mathbf{t}}} \mathbf{n}^0) \cdot \tilde{\mathbf{u}}^*}_{\text{BND}^1} \right] + \text{c.c.} = 0, \quad (3.45)$$

We remind that the ansatz of (3.9) is complex, hence the integral of terms in ϵ^1 order vanish due to the periodicity of the perturbations over λ . As $\frac{2\pi}{k} e^{2\sigma_r t} > 0$, it can be factorised and simplified. We hereafter only focus on the real part of (3.45) which writes

$$(\text{DIS}^1 + \text{BND}^1)_r = 0. \quad (3.46)$$

Recalling (3.12) and (3.16), BND can be decomposed as

$$\text{BND}^1 = \text{BND}_v^1 + \text{BND}_c^1, \quad (3.47)$$

where subscripts v and c denote the viscous and capillary contributions to the rate of work at the perturbed interface, respectively, expressed as

$$\begin{aligned} \text{BND}_v^1 = & \int_{\partial \Sigma_{\text{int}}} (1-\alpha)^2 \tilde{u}_z^* \partial_{rr} u_z^0 \tilde{\eta} \\ & + \int_{\partial \Sigma_{\text{int}}} -(1-\alpha)^2 \tilde{u}_\theta^* \partial_\theta u_z^0 i k \tilde{\eta} + \int_{\partial \Sigma_{\text{int}}} -(1-\alpha)^2 \tilde{u}_z^* \partial_\theta u_z^0 \partial_\theta \tilde{\eta}, \end{aligned} \quad (3.48)$$

$$\text{BND}_c^1 = \underbrace{\int_{\partial \Sigma_{\text{int}}} \frac{\sigma^*}{Bo} \tilde{\kappa} \tilde{\eta}^*}_{\text{BND}_{c,1}^1} + \underbrace{\int_{\partial \Sigma_{\text{int}}} \frac{-i k u_z^0}{Bo} \tilde{\kappa} \tilde{\eta}^*}_{\text{BND}_{c,2}^1}. \quad (3.49)$$

Different terms of (3.21) correspond to the rate of shear stress work on the perturbed interface. Moreover, $\text{BND}_{c,1}^1$ determines the temporal rate of surface energy release (or storage) at the perturbed interface, which can be rewritten as

$$\text{BND}_{c,1}^1 = \sigma^* \underbrace{\int_{\partial \Sigma_{\text{int}}} \frac{\tilde{\kappa} \tilde{\eta}^*}{Bo}}_{\text{SUR}^1}, \quad (3.50)$$

where SUR^1 denotes the surface energy stored in the perturbed interface, thus giving (3.20).

3.5.5 Image analysis of the experiments

In this section, we detail the step-by-step procedure to quantify our experiments by means of the image analysis of the images taken from the side and front views. All images are saved in binarised format, including only black and white pixels. This procedure is implemented in a

MathematicaTM image analyses script. The steps are as follows:

1. When the fibre is concentric with the liquid column, the edges of the liquid column are extracted from the images of the side and front views. Each edge appears as a line of black pixels and marks the extremity of the liquid column interface.
2. Angle correction is applied on the images, to obtain vertical column edges.
3. The rotation angle of each camera is saved. These angles are applied to correct all of the images from their corresponding cameras.
4. For each camera, the length scale of the images is calculated from the concentric liquid column, by counting the number of pixels per unit length of a ruler placed next to the column. These scales are saved and used for the rest of the measurements.
5. The liquid column diameter and the radial position of its mid-line axis are calculated from each camera. The mid-line axis is a vertical line, whose radial coordinate is obtained by averaging the radial position of the liquid column edges along the axis.
6. After the moving plate is displaced and flow develops, step 5 is repeated. It is important to measure the column diameter close to the nozzle, where the liquid column remains circular.
7. The in-plane displacement of the liquid column is calculated by subtracting the mid-line axis positions measured from the side view camera in steps 5 and 6. (It is verified that there is no axis displacement in the front view.)
8. The moving plate displacement is measured visually from the displacement of the ruler engraved on the plate with respect to a reference mark.
9. R_{ec} is calculated by subtracting the side view axis displacement, measured in step 7, from the moving plate displacement measured in step 8.
10. α is calculated as the ratio of the fibre-to-column diameter, calculated in step 6.
11. Dimensionless numbers $\{Oh, Bo\}$ are computed by knowing the physical properties of the working fluid, α , and the column diameter.
12. For each angle-corrected image taken from the front view, the edges of the liquid column are extracted. Each interface edge for the perturbed flow appears as a curve of black pixels (we note that at the early stage of interface destabilisation, the interface perturbations are more visible in the front view). Then the peak-to-peak and crest-to-crest axial distances on the interface are extracted.
13. The perturbation wavelength is computed by averaging the distances computed in step 12, reported along with their standard deviation during multiple formation periods of the unstable structures.

4 On the liquid film instability of an internally coated horizontal tube

Remark This chapter is largely inspired by the manuscript of the same name, submitted for publication in *Physical Review Fluids*

Shahab Eghbali[†], Y.-M. Ducimetière¹, E. Boujo¹ and F. Gallaire¹

¹ Laboratory of Fluid Mechanics and Instabilities, École Polytechnique Fédérale de Lausanne, Lausanne CH-1015, Switzerland

Authors' contributions E.G. and S.E. conceived the study. S.E. performed the stability analysis. S.E. and Y.-M.D. performed together the transient growth analysis. All authors actively participated to the theoretical developments, analysis and interpretation of the results. S.E. and Y.-M.D. wrote the manuscript and E.B. edited it, guided by E.G..

We study numerically and theoretically the gravity-driven flow of a viscous liquid film coating the inner side of a horizontal cylindrical tube and surrounding a shear-free dynamically inert gaseous core. The liquid-gas interface is prone to the Rayleigh-Plateau and Rayleigh-Taylor instabilities. Here, we focus on the limit of low and intermediate Bond numbers Bo , where the capillary and gravitational forces are comparable and the Rayleigh-Taylor instability is known to be suppressed. We first study the evolution of the axially invariant draining flow, initiating from a uniform film thickness until reaching a quasi-static regime as the bubble approaches the upper tube wall. We then investigate the flow's linear stability within two frameworks: frozen time-frame (quasi-steady) stability analysis and transient growth analysis. We explore the effect of the surface tension (Bo) and inertia (measured by the Ohnesorge number Oh) on the flow and its stability. The linear stability analysis suggests that the interface deformation at large Bo results in the suppression of the Rayleigh-Plateau instability in the asymptotic long-time limit. Furthermore, the transient growth analysis suggests that the initial flow evolution does not lead to any considerable additional amplification of initial interface perturbations, *a posteriori* rationalising the quasi-steady assumption. The present study yields a satisfactory prediction of the stabilisation threshold found experimentally by Duclaux et al. (2006).

4.1 Introduction

The gravity-driven flow of a viscous liquid film coating inside a solid cylinder has received attention by virtue of its rich dynamics and numerous applications. One major industrial application of such a flow is in two-phase heat exchangers, like in evaporators (O'Neill and Mudawar, 2020a) and vertical tube condensers (Revankar and Pollock, 2005), where the dynamics of the gas plugs and capillary blockage affect the heat transfer efficiency and pressure loss (Dobson and Chato, 1998; Teng et al., 1999). It is also relevant in the airways of the human lung where the coupling between the moving wall of the airways and the liquid film coating the wall can cause airway closure (Heil et al., 2008; Bian et al., 2010; Levy et al., 2014).

The liquid-gas interface is prone to different instabilities due to surface tension, shear, gravity, and inertia, which eventually lead to the emergence of various patterns (Eggers and Villermaux, 2008; Gallaire and Brun, 2017). For instance, the long column may break apart into distinct plugs separated axially by collars, thus minimising the surface energy. This phenomenon is classified in a large family of hydrodynamic instabilities known as the Rayleigh-Plateau instability (Plateau, 1873; Rayleigh, 1878). Flow characteristics of the viscous film coating the inner side of a tube depend also on its orientation with respect to gravity. In the case of a vertical tube, where gravity drives an axial flow, the liquid interface is mainly destabilised by the Rayleigh-Plateau instability (Goldsmith and Mason, 1963). Different stages of such instability have been investigated through a large number of numerical and experimental studies. Goren (1962) showed analytically that in the absence of inertia, the length of plugs is set by the interface radius. Frenkel et al. (1987) demonstrated that despite the growth of small disturbances, non-linear saturation of instabilities can avoid the rupture of the liquid film in a certain range of axial flow parameters. Using the long-wavelength approximation, Camassa et al. (2014, 2016) showed the existence of non-trivial axially traveling waves along the interface when the film thickness exceeds a critical value. Moreover, these studies describe how plugs form via Hopf bifurcation as the waves grow, and explore experimentally the absolute/convective properties of the traveling waves. With this general picture, further studies address the effects of flow parameters on the dynamics of the flow instability, e.g. air driven flow (Camassa et al., 2017) and multiple liquid layers (Ogrofsky, 2021a), wall porosity (Liu and Ding, 2017), Marangoni effect (Ding et al., 2018b), and the presence of surfactant (Ogrofsky, 2021b).

Alternatively, in the case of liquid film coating the inner side of long horizontal or inclined tubes, where gravity is not orthogonal to the cross-section of the tube, a second instability, the Rayleigh-Taylor instability (Rayleigh, 1882; Taylor, 1950), may arise. As a result, the heavy liquid film accelerates into the light gaseous core in the direction of the gravitational field, thus forming suspended droplets, moving lenses, or rivulets (Trinh et al., 2014; Balestra et al., 2016, 2018a), extending the case of a flat overhanging thin liquid film (Fermigier et al., 1992). Therefore, in the case of a horizontal tube, both Rayleigh-Plateau and Rayleigh-Taylor instabilities may potentially coexist depending on the film thickness (Benilov et al., 2005; Benilov, 2006). Trinh et al. (2014) investigated both experimentally and theoretically, in the absence of any axial flow, the stability of a thin viscous film that coats the underside of a

tube. Focusing on the situations where gravitational forces dominate surface tension forces, they did not evidence any manifestation of the Rayleigh-Plateau instability, highlighting that finite wall curvature and sufficiently high surface tension can suppress the Rayleigh-Taylor instability as the liquid drains. Using a similar flow configuration, and also employing the lubrication approximation, Balestra et al. (2016) showed that when gravity overcomes capillarity, the linear transient growth of the disturbances can lead to the formation of tiny spanwise homogeneous traveling waves at the top of the interface, which may pinch or decay as they travel downward. Balestra et al. (2018a) however showed that spanwise periodic (but streamwise homogeneous) structures called rivulets display significantly larger transient gains, rationalising their experimental observations.

By increasing the film thickness and/or lowering the tube curvature, liquid drainage is enhanced and the Rayleigh-Taylor instability is dampened, thus allowing the Rayleigh-Plateau instability to occur. Through an experimental investigation of a wider range of film thicknesses, Duclaux et al. (2006) evidenced that when capillary forces dominate over gravity forces, the Rayleigh-Plateau instability sets in, but when they stop to dominate, the Rayleigh-Plateau instability can be suppressed by gravity. In this case, liquid drainage is faster than capillarity-induced interface undulations and plug formation. Hence, gravity and surface tension play dual roles in interface destabilisation. While gravity promotes the Rayleigh-Taylor instability at the top of the interface, it opposes the formation of hanging droplets by enhancing drainage progressively while draining down the curved substrate. In contradistinction, surface tension promotes the Rayleigh-Plateau instability, whereas it opposes the Rayleigh-Taylor instability.

Duclaux et al. (2006) complemented their experimental measurements with a theoretical analysis based on the lubrication theory and assuming a circular interface. This analysis correctly predicted the scaling of the stability threshold in terms of film thickness and Bond number and qualitatively captured the increasing trend of the instability wavelength with the initial radius of the liquid-air interface. It did not, however, achieve a fully satisfactory quantitative agreement. In this study, we set to investigate accurately how gravity-induced drainage suppresses the Rayleigh-Plateau instability. Crucially, we consider the full Navier-Stokes equations and take into account the temporal evolution of the interface. We study the linear instability in two ways: (i) with a linear stability analysis performed at each instant taken in isolation, assuming that the base flow is "frozen"; (ii) with a transient growth analysis rigorously accounting for the temporal evolution of the base flow.

This paper is structured as follows. The methodology is presented in §4.2. The problem formulation and the dimensionless governing equations are presented in §4.2.1, from which the base flow is deduced and discussed in §4.2.2. In §4.2.3, the stability analysis formulation and the linearised governing equations are elaborated. Then, in §4.2.4 the formulation of the linear transient growth of perturbations is detailed. Corresponding numerical methods are detailed in §4.2.5. In §4.3, the results of the stability and transient growth analyses are presented and discussed. Section 4.3 summarises the effect of different dimensionless parameters on the stability of the flow: §4.3.2-4.3.3 present the effect of surface tension and inertia, respectively,

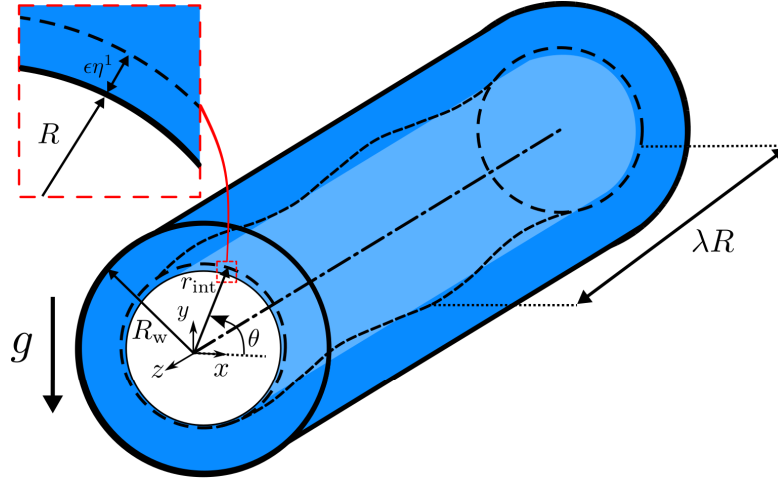


Figure 4.1: Schematic of the liquid film coating the inner side of a horizontal tube and the geometrical parameters. The thick solid black line shows the tube wall of inner radius R_w , which is concentric with the coordinate reference. Initially surrounded by a constant film thickness, the liquid-gas interface is a cylinder of radius R , concentric with the tube. The dashed black line represents the perturbed liquid-gas interface of local radius r_{int} and axial wavelength λR . The inset shows the zoomed cross-section of the initial perturbed interface. The gravitational field acts vertically, perpendicular to the tube axis.

and §4.3.4 presents the linear stability diagram. The results of the transient growth analysis are presented in §4.3.8 and finally, conclusions are drawn in §4.4 by comparing the linear stability and transient growth analyses.

4.2 Governing equations and methods

4.2.1 Problem formulation

The inner side of a cylindrical tube of radius R_w is coated with a viscous liquid film. The schematic of the flow is shown in figure 4.1. The standard Cartesian coordinates (x, y, z) are considered with the origin located at the center of the tube cross-section. In-plane coordinates are (x, y) and the gravity acceleration \mathbf{g} , points in $-y$ direction. The liquid is Newtonian, of constant dynamic viscosity μ , surface tension γ , and density ρ , and surrounds a core bubble of inviscid gas of density much smaller than that of the liquid. The bubble is initially concentric with the tube and the liquid film thickness is constant on the wall, $h_0 = R_w - R$, where R denotes the initial bubble radius. The bubble interface can be parametrised without loss of generality in cylindrical coordinates (r, θ, z) as $r_{\text{int}}(t, \theta, z)$ using the tube center as the origin. It will be shown in §4.3 that it remains radially representable at later times. The dimensionless state vector $\mathbf{q} = (\mathbf{u}, p, \mathcal{R}_{\text{int}})^T$ defines the flow at dimensionless time t , where $\mathbf{u}(t, x, y, z) = (u_x, u_y, u_z)^T$ denotes the three-dimensional velocity field, $p(t, x, y, z)$ denotes the pressure, and $\mathcal{R}_{\text{int}} = r_{\text{int}}/R$ denotes the dimensionless interface radius. The state vector and the governing

equations are rendered dimensionless by the intrinsic velocity scale associated with a viscous film of thickness h_0 falling under its weight, inspired from Duclaux et al. (2006). However, we choose differently the length, time, and pressure scales as follows:

$$\begin{aligned} \mathcal{L} = R, \quad \mathcal{U} = \frac{\rho g h_0^2}{\mu} = \frac{\rho g R^2}{\mu} (\beta - 1)^2, \\ \mathcal{P} = \frac{\gamma}{R}, \quad \mathcal{T} = \frac{\mathcal{L}}{\mathcal{U}} = \frac{\mu}{\rho g R} (\beta - 1)^{-2}, \end{aligned} \quad (4.1)$$

where $\beta = R_w/R$ denotes the dimensionless tube radius. As a result, the dimensionless value of the initial film thickness can be expressed as $\delta = h_0/R = \beta - 1$. The flow is governed by the incompressible Navier-Stokes equations which in dimensionless form read

$$\nabla \cdot \mathbf{u} = 0, \quad (4.2)$$

$$\left(\frac{Bo}{Oh} \right)^2 \delta^4 (\partial_t + \mathbf{u} \cdot \nabla) \mathbf{u} = \nabla \cdot \underline{\underline{\tau}} - Bo \mathbf{e}_y, \quad (4.3)$$

where ∂_j denotes the partial derivative with respect to quantity j , and the stress tensor $\underline{\underline{\tau}}$ reads

$$\underline{\underline{\tau}} = -p \mathbf{I} + Bo \delta^2 (\nabla \mathbf{u} + \nabla \mathbf{u}^T). \quad (4.4)$$

The two other dimensionless numbers which appear in the governing equations are the *Ohnesorge* number, $Oh = \mu / \sqrt{\rho \gamma R}$, and the *Bond* number, $Bo = \rho g R^2 / \gamma$. While Oh compares the viscous forces to the inertial and surface tension forces, Bo compares the gravitational and surface tension forces.

The no-slip boundary condition, $\mathbf{u} = \mathbf{0}$, is applied at the tube wall, $r = \beta$. At the shear-free liquid-gas interface, the dimensionless kinematic and dynamic boundary conditions write

$$\partial_t \mathcal{R}_{\text{int}} + (\mathbf{u} \cdot \nabla) \mathcal{R}_{\text{int}} = \mathbf{u} \cdot \mathbf{e}_r \quad \text{at } r = \mathcal{R}_{\text{int}}, \quad (4.5)$$

$$\underline{\underline{\tau}} \mathbf{n} = \kappa \mathbf{n} \quad \text{at } r = \mathcal{R}_{\text{int}}, \quad (4.6)$$

respectively, where \mathbf{e}_r denotes the unit radial vector, $\mathbf{n} = \nabla(r - \mathcal{R}_{\text{int}}) / \|\nabla(r - \mathcal{R}_{\text{int}})\|$ denotes the interface unit normal vector pointing from the gas to the liquid, $\|\cdot\|$ denotes the Euclidean norm, and $\kappa = \nabla \cdot \mathbf{n}$ denotes the interface mean curvature.

4.2.2 Base flow

The *base flow* denoted by $\mathbf{q}^0(t, x, y)$ is the two-dimensional time-dependent solution of the Navier-Stokes equations (4.2)-(4.6) initiated from rest at $t = 0$, with pressure $p^0(t = 0) = -1 - Bo y$, which consists of a constant contribution from the interface Laplace pressure and a linear hydrostatic term. To begin with, before even presenting the numerical tools in §4.2.5,

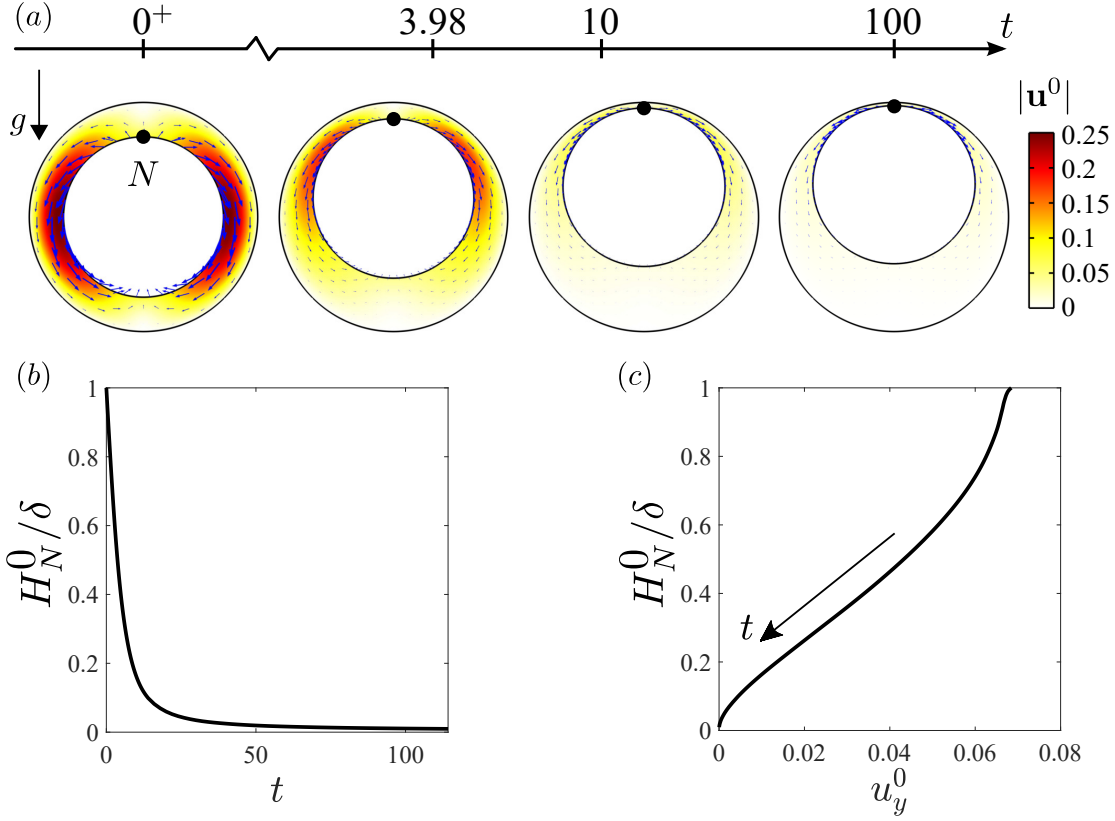


Figure 4.2: Base flow evolution: (a) Snapshots of the flow field: colour map shows the velocity magnitude, arrows show the liquid velocity field, and the point N marks the north pole of the bubble, $\theta = \pi/2$; (b) Temporal variation of the relative liquid film thickness at N ; (c) Film thickness variation as a function of the vertical velocity at N ; $Oh \rightarrow \infty$, $Bo = 0.05$, $\delta/\beta = 0.3$.

we build up the intuition about the flow by presenting an illustrative example of the base flow evolution in figure 4.2 for a case where surface tension dominates gravity, $Bo = 0.05$, and a thick initial film, $\delta/\beta = 0.3$, considering the quasi-inertialess limit when $Oh \rightarrow \infty$. The liquid drains around the core bubble under gravity, and consequently, the bubble moves upwards under the buoyancy effect. The dynamics of the base flow, presented in figure 4.2(b-c), can be characterised by quantifying the liquid film thickness and the vertical velocity at the north pole of the bubble (N , hereafter referred to as the north pole), where the strongest gravitational effects are expected (Trinh et al., 2014). In the quasi-inertialess limit, $Oh \rightarrow \infty$, drainage begins with an immediate upward drift of the bubble (denoted as $t = 0^+$ in figure 4.2(a)). Drainage and hence the rising velocity of the bubble decrease with time, as the bubble approaches the top side of the tube.

4.2.3 Linear stability analysis

Since the base flow presented in §4.2.2 is time-dependent, in order to perform the linear stability analysis, we look at the frozen frames of the unperturbed flow, from which we investigate the evolution of small *perturbations* applied to each time frame t^0 , sequentially. Here, we assume that the perturbations evolve much faster than the base flow itself, such that within their evolution, the base flow can be approximated as quasi-steady, an assumption to be verified *a posteriori* in §4.3.4. To this aim, the state vector $\mathbf{q} = (\mathbf{u}, p, \mathcal{R}_{\text{int}})^T$ is decomposed into the sum of the frozen base flow solution \mathbf{q}^0 , and the infinitesimal time-dependent *perturbation* $\mathbf{q}^1 = (\mathbf{u}^1, p^1, \eta^1)^T$ which writes

$$\mathbf{q} = \mathbf{q}^0|_{t^0} + \epsilon \mathbf{q}^1 + \mathcal{O}(\epsilon^2), \quad \epsilon \ll 1, \quad (4.7)$$

where the amplitude ϵ is assumed to be small. The ansatz of the perturbation \mathbf{q}^1 with the longitudinal wavenumber k (associated with the wavelength $\lambda = 2\pi/k$) reads

$$\mathbf{q}^1 = \tilde{\mathbf{q}}(x, y) \exp[\sigma t + ikz] + \text{c.c.}, \quad (4.8)$$

where c.c. denotes the complex conjugate. Any other function in terms of the state vector can be decomposed in the same fashion, e.g. $\underline{\tau} = \underline{\tau}^0 + \epsilon \underline{\tau}^1$, $\mathbf{n} = \mathbf{n}^0 + \epsilon \mathbf{n}^1$ and $\kappa = \kappa^0 + \epsilon \kappa^1$. For further details about the formulation of \mathbf{n}^1 and κ^1 , see appendix 4.5.3. In the asymptotic limit of large times, a normal eigenmode perturbation with complex pulsation $\sigma = \sigma_r + i\sigma_i$, is considered as *unstable* if $\sigma_r > 0$, i.e. if σ lies in the unstable complex half-plane. An unstable eigenmode grows exponentially in time with the growth rate σ_r (unless otherwise noted, the indices r and i denote the real and imaginary parts of a complex number, respectively). By casting the perturbed state (4.7) into the governing equations (4.2)-(4.3), and keeping the first-order terms, the linearised equations are obtained as

$$\nabla \cdot \mathbf{u}^1 = 0, \quad (4.9)$$

$$\left(\frac{Bo}{Oh}\right)^2 \delta^4 (\partial_t \mathbf{u}^1 + (\mathbf{u}^0 \cdot \nabla) \mathbf{u}^1 + (\mathbf{u}^1 \cdot \nabla) \mathbf{u}^0) = \nabla \cdot \underline{\tau}^1. \quad (4.10)$$

The no-slip condition implies $\tilde{\mathbf{u}} = \mathbf{0}$ on the solid wall. The interface conditions (4.5)-(4.6), applied on the perturbed liquid interface, can be projected radially onto the base interface and ultimately linearised, a process called *flattening* (see (4.25) in appendix 4.5.1). The linearised kinematic condition can be expressed as

$$\sigma \tilde{\eta} + \underbrace{\left(-\partial_r u_r^0 + \frac{\partial_r u_\theta^0 \partial_\theta \mathcal{R}_{\text{int}}^0}{\mathcal{R}_{\text{int}}^0} - \frac{u_\theta^0 \partial_\theta \mathcal{R}_{\text{int}}^0}{(\mathcal{R}_{\text{int}}^0)^2} \right) \tilde{\eta} + \frac{u_\theta^0}{\mathcal{R}_{\text{int}}^0} \partial_\theta \tilde{\eta} + \frac{\partial_\theta \mathcal{R}_{\text{int}}^0}{\mathcal{R}_{\text{int}}^0} \tilde{u}_\theta}_{-\mathbf{G}^0 \tilde{\eta}} = \tilde{u}_r \quad \text{at } r = \mathcal{R}_{\text{int}}^0, \quad (4.11)$$

where $(u_r^0, u_\theta^0)^T$ and $(\tilde{u}_r, \tilde{u}_\theta)^T$ denote the velocity vectors of the base state and perturbations, respectively, represented in the cylindrical coordinates. Introducing an eigenstate vector of the

form (4.8) into (4.9)-(4.10), combined with (4.11), leads to a generalised eigenvalue problem for σ and $\tilde{\mathbf{q}}$ that writes

$$\mathbf{L}\tilde{\mathbf{q}} + \text{c.c.} = \sigma \mathbf{B}\tilde{\mathbf{q}} + \text{c.c.}, \quad (4.12)$$

where the linear operators \mathbf{L} and \mathbf{B} are defined as

$$\begin{aligned} \mathbf{L} &= \begin{bmatrix} \left(\frac{Bo}{Oh}\right)^2 \delta^4 \mathbf{F}^0 + Bo\delta^2 (\tilde{\nabla} \cdot (\tilde{\nabla} + \tilde{\nabla}^T)) & -\tilde{\nabla} & \mathbf{0} \\ \tilde{\nabla} \cdot & 0 & 0 \\ \left(\mathbf{e}_r - \frac{\partial_\theta \mathcal{R}_{\text{int}}^0}{\mathcal{R}_{\text{int}}^0} \mathbf{e}_\theta\right) \cdot & 0 & \mathbf{G}^0 \end{bmatrix}, \\ \mathbf{B} &= \begin{bmatrix} \left(\frac{Bo}{Oh}\right)^2 \delta^4 \mathbf{I} & \mathbf{0} & \mathbf{0} \\ \mathbf{0} & 0 & 0 \\ \mathbf{0} & 0 & 1 \end{bmatrix}, \end{aligned} \quad (4.13)$$

where $\mathbf{F}^0 \tilde{\mathbf{u}} = -((\mathbf{u}^0 \cdot \tilde{\nabla}) \tilde{\mathbf{u}} + (\tilde{\mathbf{u}} \cdot \nabla) \mathbf{u}^0)$, $(\mathbf{e}_r, \mathbf{e}_\theta, \mathbf{e}_z)$ denote the vectors of unit directions in the cylindrical coordinates (r, θ, z) used for parameterising the interface, and the gradient operators and the velocity gradient tensors in the Cartesian coordinates read

$$\begin{aligned} \nabla &= (\partial_x, \partial_y, \partial_z)^T, & \nabla \mathbf{u}^0 &= \begin{bmatrix} \partial_x u_x^0 & \partial_y u_x^0 & 0 \\ \partial_x u_y^0 & \partial_y u_y^0 & 0 \\ 0 & 0 & 0 \end{bmatrix}, \\ \tilde{\nabla} &= (\partial_x, \partial_y, ik)^T, & \tilde{\nabla} \tilde{\mathbf{u}} &= \begin{bmatrix} \partial_x \tilde{u}_x & \partial_y \tilde{u}_x & ik \tilde{u}_x \\ \partial_x \tilde{u}_y & \partial_y \tilde{u}_y & ik \tilde{u}_y \\ \partial_x \tilde{u}_z & \partial_y \tilde{u}_z & ik \tilde{u}_z \end{bmatrix}. \end{aligned} \quad (4.14)$$

$$(4.15)$$

The interface dynamic condition (4.6), once linearised, can be expressed as

$$\underline{\underline{\tau}}^0 \tilde{\mathbf{n}} + \tilde{\eta} \partial_r \underline{\underline{\tau}}^0 \mathbf{n}^0 + \underline{\underline{\tau}} \mathbf{n}^0 = \kappa^0 \tilde{\mathbf{n}} + \tilde{\kappa} \mathbf{n}^0 \quad \text{at } r = \mathcal{R}_{\text{int}}^0. \quad (4.16)$$

For further details on the derivation of the interface conditions and their implementation, see appendices 4.5.1 and 4.5.2, respectively.

4.2.4 Transient growth analysis

In contrast to the linear stability analysis, the *transient growth analysis* tolerates any kind of temporal dependency for both the base flow and the perturbation and does not rely on a separation of time scales between their respective evolutions. Moreover, it accounts for the so-called "*nonmodal*" mechanisms arising from the nonnormality (non-commutativity with the adjoint) of the linear operator \mathbf{L} . Owing to these mechanisms, small-amplitude initial perturbations may experience a large transient amplification due to intricate cooperation between a possibly large number of eigenmodes; therefore, reducing the dynamics to the leading (least stable or most unstable) eigenmode might be irrelevant at finite time. If nonnormality

is often inherited from the linearization of the advective term, the operator \mathbf{L} expressed in (4.13) can be nonnormal even in the quasi-inertialess limit $Oh \rightarrow \infty$, due to the presence of the interface.

The ansatz (4.8) is generalised as

$$\mathbf{q}^1 = \bar{\mathbf{q}}(t, x, y) \exp[ikz] + \text{c.c.}, \quad (4.17)$$

where an exponential temporal behavior is not enforced. The temporal evolution of $\bar{\mathbf{q}}(t, x, y)$ is an extension of (4.12)

$$\mathbf{L}\bar{\mathbf{q}} + \text{c.c.} = \mathbf{B}\frac{\partial \bar{\mathbf{q}}}{\partial t} + \text{c.c.}, \quad (4.18)$$

We recall that \mathbf{L} is time-dependent and parameterised by k . We are interested in the initial perturbation of the interface $\bar{\mathbf{q}}(0, x, y) = [\mathbf{0}, 0, \bar{\eta}(0)]^T$ that is the most amplified by (4.18) after a temporal horizon $t = T$, where T is named a *temporal horizon*. A given initial condition might project on the optimal one, and can be amplified strongly enough to lead to a non-linear regime. We follow the methodology proposed in Del Guercio et al. (2014), and take advantage of the fact that the base flow interface is axisymmetric at $t = 0$ (see figure 4.2) to expand $\bar{\eta}(0)$ as a finite series of Fourier modes in θ

$$\bar{\eta}(0) = \sum_{m=-N}^N \alpha_m e^{im\theta} = a_0 + \sum_{m=1}^N [a_m \cos(m\theta) + b_m \sin(m\theta)] \quad (4.19)$$

with

$$\alpha_{-m} = \alpha_m^*$$

where the superscript $*$ denotes the complex conjugate, $a_0 = \alpha_0$, and for $m \geq 1$

$$a_m = \alpha_m + \alpha_m^*, \quad \text{and} \quad b_m = i(\alpha_m - \alpha_m^*).$$

Note that a_m, b_m ($m = 0, 1, 2, \dots$) and $\bar{\eta}(0)$ are real-valued. The associated first-order interfacial energy density per spanwise wavelength is proportional to

$$e_0 = \frac{k}{2\pi} \int_0^{2\pi} \int_0^{2\pi/k} \left[\bar{\eta}(0) e^{ikz} + \text{c.c.} \right]^2 dz d\theta = 2\pi \mathbf{a}^T \mathbf{a}, \quad (4.20)$$

where $\mathcal{R}_{\text{int}}^0(0) = 1$ was implied, and where we defined

$$\mathbf{a} = [a_N, a_{N-1}, \dots, a_1, \sqrt{2}a_0, b_N, b_{N-1}, \dots, b_1]. \quad (4.21)$$

Let us define $\bar{\eta}_m(t)$ as the evolution at time t of each term $\bar{\eta}_m(0) = e^{im\theta}$ of the initial condition (4.19). Thanks to the linearity of the evolution equation (4.18), the interface shape at $t = T$ reads simply

$$\bar{\eta}(T) = \sum_{m=-N}^N \alpha_m \bar{\eta}_m(T). \quad (4.22)$$

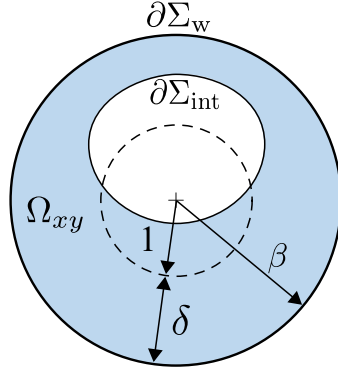


Figure 4.3: The numerical domain used for computing the base flow and the linear stability analysis. Ω_{xy} denotes the liquid bulk. The boundaries of the numerical domain are denoted by $\partial\Omega_{xy} = \partial\Sigma_w \cup \partial\Sigma_{int}$. Here, $\partial\Sigma_w$ represents the interior wall of the tube with the radius β , and $\partial\Sigma_{int}$ represents the gas-liquid interface. The cross-section of the interface is initially a circle of unit radius, concentric with the tube (sketched with dashed line).

The corresponding interfacial energy density per wavelength is proportional to

$$e(T) = \frac{k}{2\pi} \int_0^{2\pi} \int_0^{2\pi/k} |\bar{\eta}(T)e^{ikz} + c.c|^2 dz \mathcal{R}_{int}^0(T) d\theta. \quad (4.23)$$

We further show in appendix 4.5.4 that $e(T) = 2\mathbf{a}^T \mathbf{E}(T) \mathbf{a}$ where $\mathbf{E}(T)$ is a real-valued, symmetric, strictly positive definite matrix of size $(2N+1) \times (2N+1)$. In this manner, the (optimal) *transient gain* $G(T)$ defined as

$$G(T) = \max_{\mathbf{a}} \frac{e(T)}{e_0} = \pi^{-1} \frac{\mathbf{a}^T \mathbf{E}(T) \mathbf{a}}{\mathbf{a}^T \mathbf{a}} \quad (4.24)$$

is simply the largest eigenvalue of $\mathbf{E}(T)$ divided by π , and the associated eigenvector provides directly the Fourier mode coefficients of the optimal initial condition.

4.2.5 Numerical method

The base flow calculation, linear stability, and transient growth analyses are performed numerically employing the finite element package COMSOL MultiphysicsTM. A triangular mesh is generated on the two-dimensional domain shown in figure 4.3. In the following sections, the area increment in the bulk cross-section is denoted by $dA_{\Omega_{xy}}$. On the boundary j , the increment of surface area is denoted by dA_{Σ_j} , and the increment of arc length is denoted by ds . The grid size is controlled by the vertex densities on the boundaries $\partial\Sigma_w$ and $\partial\Sigma_{int}$. The variational formulations of the base flow equations (4.2)-(4.6), linear stability equations (4.12), and linearised Navier-Stokes equations (4.18) are discretised spatially using quadratic (P2) Lagrange elements for \mathbf{u}^0 , $\tilde{\mathbf{u}}$, $\bar{\mathbf{u}}$, $\tilde{\eta}$ and $\bar{\eta}$ as well as the base flow interface geometry, and linear (P1) Lagrange elements for p^0 , \tilde{p} , and \bar{p} . While the interface conditions are applied in the built-in modules of COMSOL MultiphysicsTM, the linearised condition (4.16) is applied by

means of the Lagrange multipliers of quadratic (P2) order. The employed discretisation yields approximately 500'000 degrees of freedom for the base flow, linear stability, and transient growth analyses.

The time-dependent base flow is computed using the laminar two-phase flow module coupled with the moving mesh module. The numerical time step is set by the Backward differentiation formula with maximum differentiation order of 2. The solver is initialised by the Backward Euler consistent initialization with an initial step fraction of 10^{-9} . At each time step, Newton's method is used to solve the non-linear equations, where the relative tolerance for convergence is set to 10^{-6} . Following the computed base flow, and after extracting the geometric characteristics of the base interface at each time step, the generalised eigenvalue problem (4.12) is solved using the shift-invert Arnoldi method (for more details on the development of the variational formulation, the implementation of the linear stability eigenvalue problem and their corresponding boundary conditions see appendix 4.5.2).

The computation time associated with obtaining the base flow for a given set of parameters, followed by the stability analysis for ~ 20 values of k , is of the order of a few hours on a single Intel core at 3.6 GHz. For the transient growth analysis, the computation of the propagator matrices with $-5 \leq m \leq 5$ over 10 values of k takes a few days; the calculation of the optimal transient gain for the same k values and ~ 12 values of the temporal horizon T takes approximately one hour. Both the base flow and stability analysis model are validated with the analytical solutions available in the literature for the flow of liquid coating the inside of a vertical tube (for more details about the series of validation tests see appendix 4.5.5).

4.3 Stability analysis results

In this section, we present the linear stability characteristics associated with the drainage of a liquid film coating the inside of a horizontal circular tube. The results of the frozen base flow linear stability analysis in terms of different parameters are presented hereafter. First, an overview of the stability characteristics of the flow is presented in §4.3.1. Then, the influence of Bo and Oh is demonstrated in §4.3.2-4.3.3, and the stability diagram is presented in §4.3.4. Additional comments on the effect of Bo and on the most unstable wavenumber are given in §4.3.5-4.3.6. The validity of the frozen base flow assumption is discussed in §4.3.7.

4.3.1 Stability of draining film at different instants of its evolution

Figure 4.4(a-b) shows the three least stable modes of the base flow presented in figure 4.2 at the initial time, $t = 0^+$, and figure 4.4(c) presents the corresponding *dispersion curves* (growth rate σ_r as a function of the axial wavenumber k). Only one unstable mode (mode 1) is detected, whose dispersion curves at later time instants are shown in figure 4.4(d). The characteristics of this mode are symmetry with respect to the vertical mid-plane, strong interface modulation at the bottom of the bubble, and weak interface modulation at the top of the bubble. The

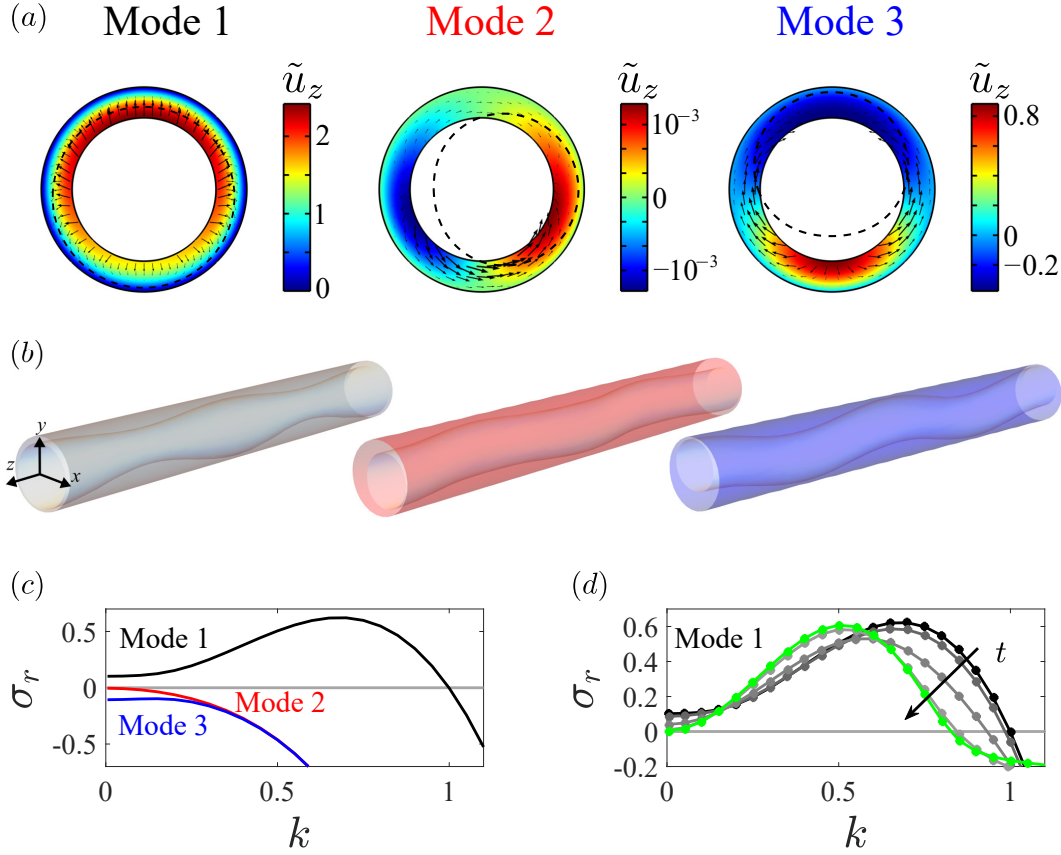


Figure 4.4: Linear stability analysis of the base flow presented in figure 4.2. (a) Three least stable eigenmodes for $t = 0^+$, $k = 0.55$. The colour map presents the axial eigenvelocity, black arrows show the in-plane eigenvelocity field, and black dashed line shows the superposition of the eigeninterface (with arbitrary amplitude) onto the base interface. (b) Three-dimensional render of the same perturbed interfaces. (c) The dispersion curve of the same three modes at $t = 0^+$. (d) Temporal variation of the dispersion curve of the unstable mode (mode 1). The green line marks the large time limit; $Oh \rightarrow \infty$, $\delta/\beta = 0.3$, $Bo = 0.05$.

fact that this mode is unstable at $k = 0$ is reminiscent of the instability properties of a purely viscous liquid thread in absence of inertia (see Eggers and Villermaux (2008)). This mode resembles the structure of the unstable interface observed in the experiments of Duclaux et al. (2006). The maximal growth rate of the unstable mode initially decreases before increasing and eventually saturating to a value inferior to the initial one (see the green line in figure 4.4(d)), as the flow evolves further. The corresponding wavenumber decreases monotonously.

4.3.2 Effect of the Bond (Bo) number

In this section, the influence of Bo on the base flow and its stability is illustrated. Figure 4.5(a-b) show for several Bo values the characteristics of the north pole evolution until $t = t_f$, when the relative thickness at the north pole H_N^0/δ diminishes below 10% for an initial thick film

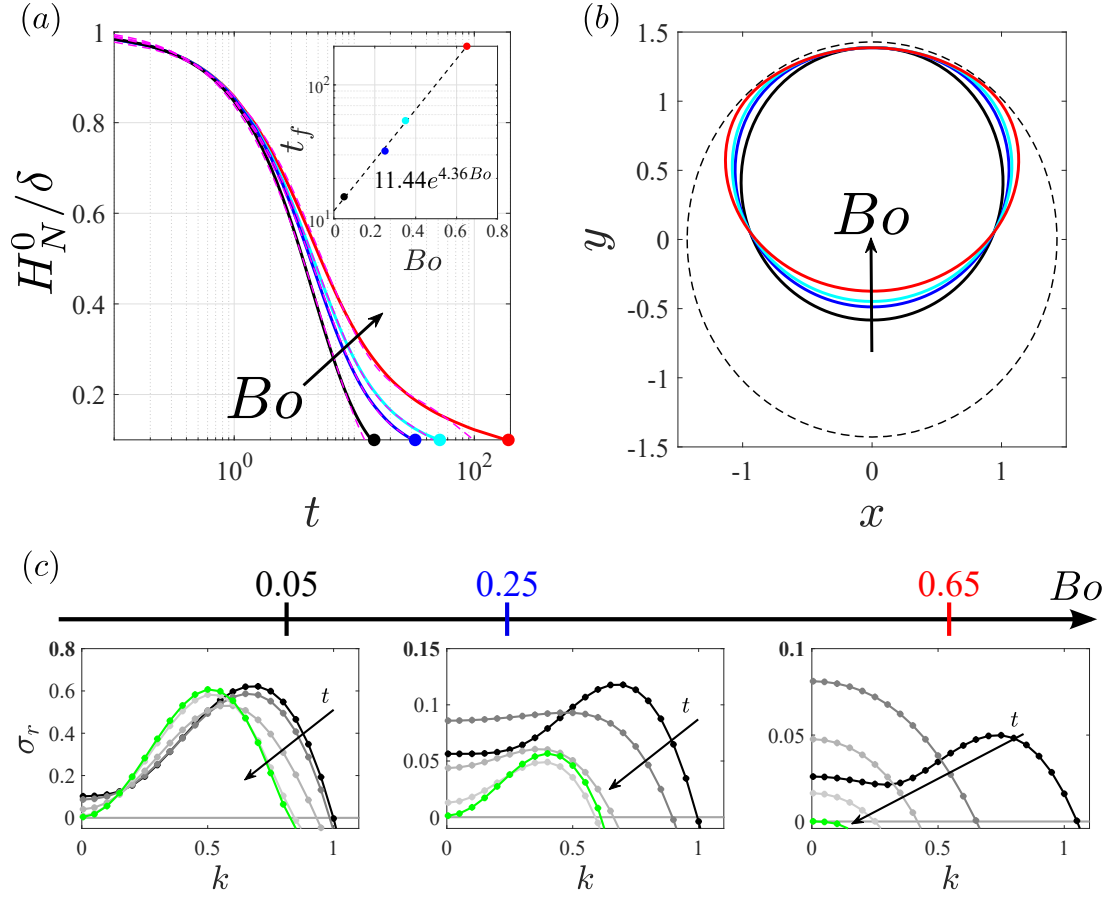


Figure 4.5: Influence of Bo on the base flow and its long-time linear stability for $Oh \rightarrow \infty$, $\delta/\beta = 0.3$, $Bo = \{0.05, 0.25, 0.35, 0.65\}$. (a) Evolution of the relative thickness at the north pole. The dashed line present the exponential fit $H_N^0/\delta = a_1 \exp[-t/T_1] + a_2 \exp[-t/T_2]$, and the values of $\{a_1, a_2, T_1, T_2\}$ are given in table 4.1. The inset shows the variation of t_f as a function of Bo . (b) Bubble interface at $t = t_f$ when the relative thickness at the north pole reaches 10%. The dashed line shows the tube wall. (c) Dispersion curve of the unstable eigenmode, mode 1, for $Bo = \{0.05, 0.25, 0.65\}$.

Bo	a_1	T_1	a_2	T_2
0.05	0.986	5.07	0.014	51.5
0.25	0.831	4.75	0.178	52.9
0.35	0.788	4.74	0.217	58.0
0.65	0.731	5.07	0.261	103

Table 4.1: Fitting parameters associated with the relative pole thickness $H_N^0/\delta = a_1 \exp[-t/T_1] + a_2 \exp[-t/T_2]$ for different values of Bo presented in figure 4.5(a).

$\delta/\beta = 0.3$. The relative pole thickness decays exponentially with two distinct time scales, presented in table 4.1. Increasing Bo results in an exponential increase of t_f (figure 4.5(a)). Figure 4.5(b) presents for the same flows the bubble interface at $t = t_f$. This figure evidences the horizontal bubble widening as it rises towards the upper wall. Low surface tension or large gravitational effects, i.e. high Bo , results in more deviation of the interface cross-section from its initial circular shape. Note that as Bo increases, the location where the gap between the interface and the tube is thinnest moves from the north pole to the sides.

The influence of Bo on the dispersion curve of mode 1 is presented in figure 4.5(d). The evolution of the dispersion curves for small Bo values (here $Bo = \{0.05, 0.25\}$) is similar to that demonstrated in §4.3.1. Increasing Bo reduces the maximal growth rate of the unstable mode and the range of unstable wavenumbers, k . Further increasing Bo results in the suppression of the instability after a finite time (see $Bo = 0.65$). In this investigation, no other unstable or marginally stable mode was detected while varying Bo .

4.3.3 Effect of the Ohnesorge (Oh) number

In the present study, all of the aforementioned results were limited to the quasi-inertialess regime, where $(Bo/Oh)^2 \delta^4 \rightarrow 0$. One can interpret $(Bo/Oh)^2 \delta^4 = Re \delta^2$ where the Reynolds number Re , is defined upon the same length scale and drainage velocity scale given in (4.1). In this section, we study the base flow and its stability in presence of inertia by decreasing Oh while keeping the rest of the flow parameters identical to those presented in §4.2.2 and §4.3.1. Figure 4.6(a-b) depict the influence of inertia on the base flow evolution from the initial time $t = 0^+$ to a terminal time $t = t_f$ identical to that presented in §4.3.2. Compared to the quasi-inertialess drainage, the inertial bubble accelerates and decelerates with some delay. Eventually, the relative film thickness at the north pole and its velocity converge to that of the quasi-inertialess flow. The delays in the bubble acceleration and deceleration increase by decreasing Oh . However, the bubble interfaces in all cases are identical at the terminal time (figure 4.6(c)).

Figure 4.6(d-e) present the effect of Oh on the dispersion curve of the unstable mode at $t = 0^+$ and $t = t_f$, respectively. Including inertia (finite Oh) affects the initial dispersion relation of the unstable mode in two ways. The first effect is associated with $k = 0$, where the immediate bubble drift in the inertialess flow was seen to induce a non-zero growth rate. The addition of inertia, no matter small, yields a zero growth rate, a regularisation by inertia also observed for the Rayleigh-Plateau instability of a liquid thread (see Eggers and Villermaux (2008)). The second effect is linked to the shape of the dispersion curve, which is similar to that of the classical thin-film Rayleigh-Plateau instability in the vicinity of a wall and in the absence of gravity, as obtained by a lubrication analysis $\sigma_r \propto k^2 - k^4$ (Camassa et al., 2014; Gallaire and Brun, 2017), for $Oh > 0.25$. In the limit of small Oh , inertia diminishes the growth rate of the perturbations without altering the instability cut-off compared to the inertialess limit.

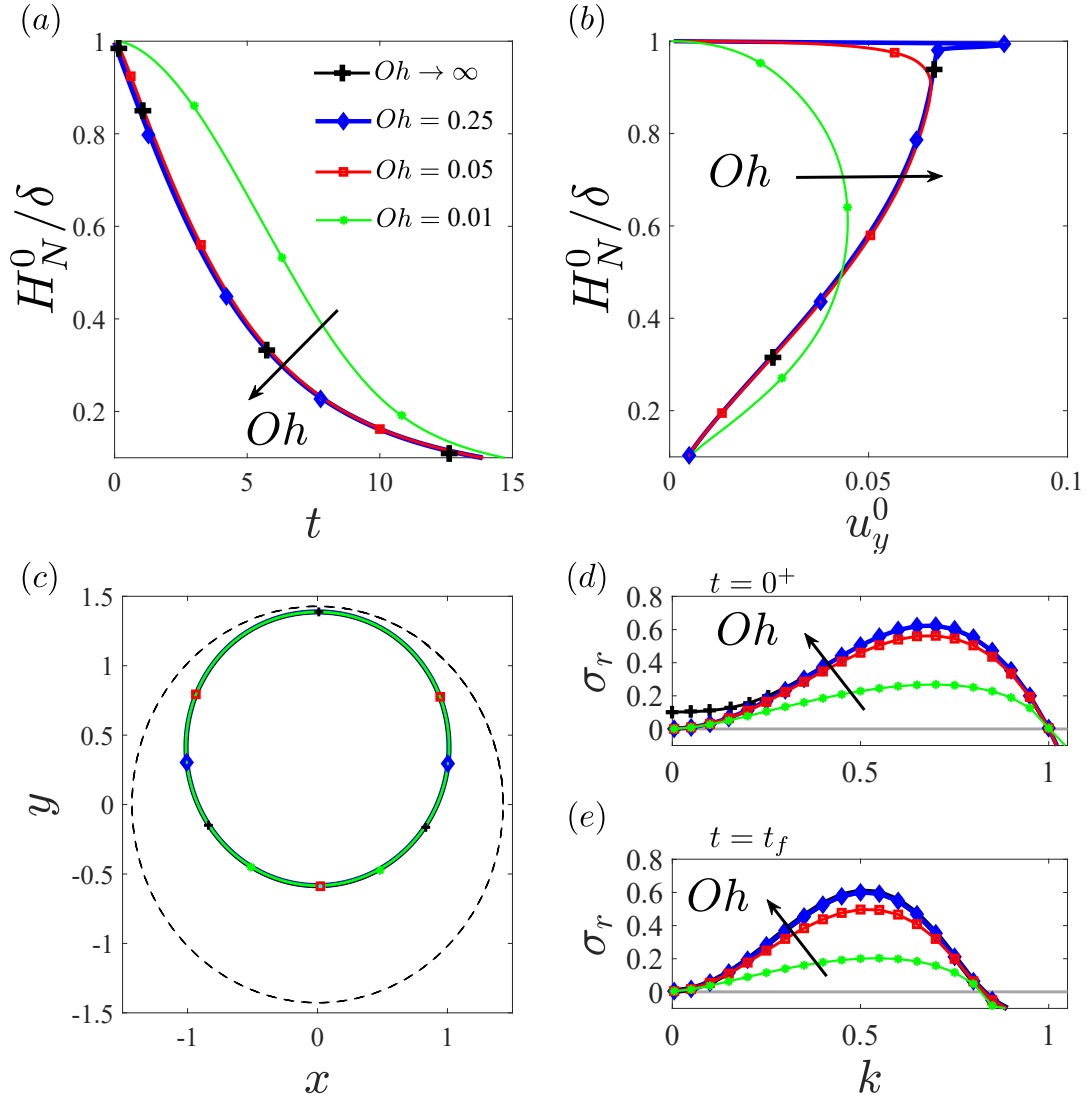


Figure 4.6: Influence of Oh : (a) Evolution of the relative thickness at the north pole. (b) The relative film thickness variation as a function of the velocity at the north pole. (c) Interface at $t = t_f$ when the relative thickness at the north pole reaches 10%; dashed line shows the tube wall. (d) Dispersion curve at $t = 0^+$. (e) Dispersion curve at $t = t_f$; $Bo = 0.05$, $\delta/\beta = 0.3$, $Oh = \{0.01, 0.05, 0.25, \infty\}$ (corresponding to $0 \leq (Bo/Oh)^2 \delta^4 \leq \mathcal{O}(1)$).

4.3.4 Asymptotic linear stability diagram

The $\{\delta, Bo\}$ space is investigated to follow the transition of the interface from unstable to stable. Figure 4.7(a) presents the *stability diagram* based on the dispersion curve of the most unstable mode obtained from the linear stability analysis at large time $t = t_f$ (it is verified that evaluation of the stability at $t = \{0.75t_f, 7t_f\}$ does not alter the obtained marginal curve). For each δ , increasing Bo results in interface stabilisation. Figure 4.7(b) presents the same linear stability phase diagram in δ vs $Bo/(1 - Bo)^2$ plane. Such an abscissa is suggested by Duclaux

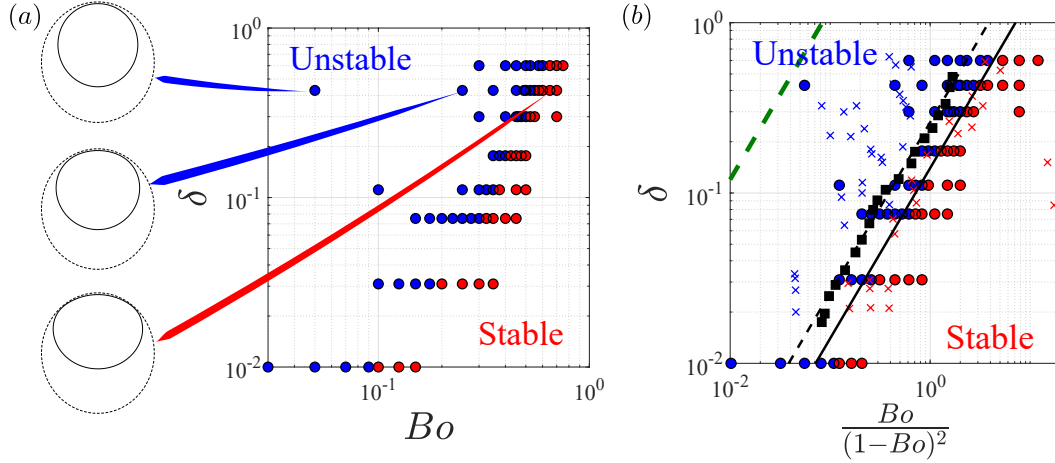


Figure 4.7: Linear stability stability diagram: (a) In $\delta - Bo$ plane; the blue and red bullets are obtained from the present numerical stability analysis. three base interfaces at $t = t_f$ are shown for $\delta/\beta = 0.3$ (corresponding to $\delta = 0.43$) and $Bo = \{0.05, 0.25, 0.65\}$. (b) the same diagram shown in $\delta - Bo/(1 - Bo)^2$ plane; the green dashed line shows the analytical stability margin predicted by Duclaux et al. (2006), the black squares and the passing dashed line show their transition experimental data and their best linear fit $\delta = 0.26Bo/(1 - Bo)^2$, respectively. The crosses show their experimental data, the continuous black line shows the best linear fit to the present linear analysis: $\delta = 0.14Bo/(1 - Bo)^2$.

et al. (2006) who proposed an analytical dispersion relation using the lubrication theory and assuming a circular base interface. Note that their definition of Bo is different from ours and the abscissa is adapted to the present study. Even though their analysis suggests the stability threshold as $\delta = 12Bo/(1 - Bo)^2$, their experiments suggest $\delta = 0.26Bo/(1 - Bo)^2$ for the stability transition. The present numerical stability analysis suggests the best fit to the separatrix as $\delta = 0.14Bo/(1 - Bo)^2$. Therefore, our stability analysis yields a significant improvement, although a discrepancy remains. Note that the definition by Duclaux et al. (2006) of the transition regime is not the appearance of growing perturbations but rather that of a visible top/down asymmetry. It is therefore reassuring to observe their transition points (black squares) fall in the unstable region predicted by our stability analysis (see figure 4.7(b)). However, for a few points, the linear analysis predicts instability while the experiments report a stable interface, resulting in a small relative error in δ .

4.3.5 Why does increasing Bond number stabilise the flow?

To shed light on the reasons for the present improvement in the prediction of the stability threshold, we recall from §4.2.2 that the present study exhibits for a high Bo a remarkable deformation of the rising bubble (also shown in figure 4.7(a)). The interface deformation is disregarded in the analysis of Duclaux et al. (2006). Yet, their analysis predicts the suppression of the instability. To elucidate the stabilising role of the Bond number, we take benefit of the linear instability formalism to decouple artificially the effect of Bo into (i) its capacity to

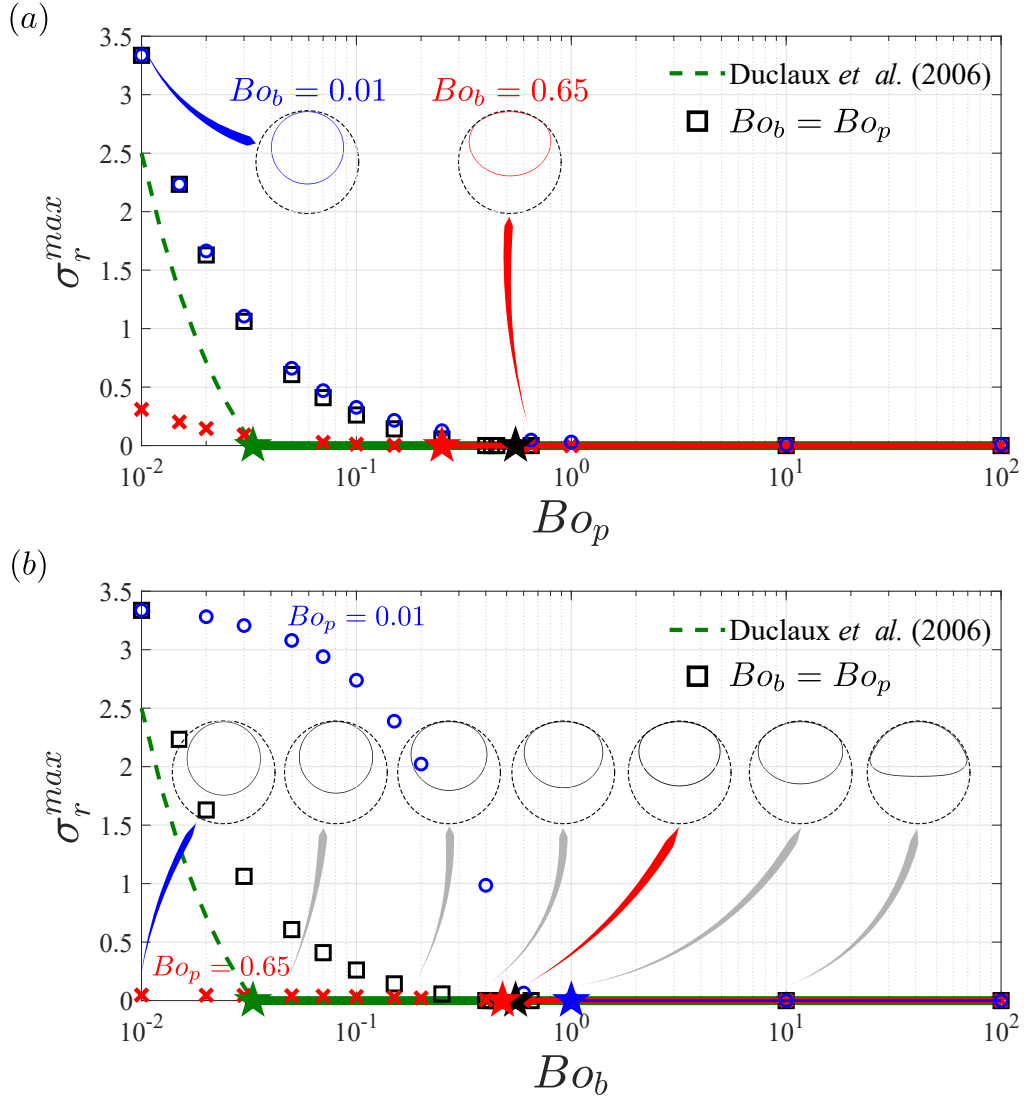


Figure 4.8: Decoupled effects of Bo on the linear stability of the flow at different scales for $\delta/\beta = 0.3$: (a) the maximal growth rate obtained by isolating Bo for the base flow ($Bo_b = \{0.01, 0.65\}$) and varying it for perturbations (Bo_p). (b) the maximal growth rate obtained by varying Bo for the base flow (Bo_b) and isolating it for the unstable perturbations ($Bo_p = \{0.01, 0.65\}$). The varying base interfaces are shown. In both panels, thin dashed lines show the tube wall and thin solid lines show the base interfaces, the thick solid lines represent a stable regime, and pentagrams mark the stabilisation thresholds, and the green colour presents the analytical prediction by Duclaux et al. (2006).

deform the base state as a result of drainage and capillary forces, and (ii) its explicit role in the perturbation equations (4.12) and (4.13). As detailed below, we will therefore distinguish the "perturbation Bond number" Bo_p and the "base Bond number" Bo_b .

1. First, we isolate the effect of the perturbation Bond Bo_p on the stability properties by

fixing the base state according to two extreme values of the base Bond number Bo_b . In other words, we artificially prevent the Bond number from deforming the base state but let it act on the perturbations. We consider the two limits of low ($Bo_b = 0.01$) and high ($Bo_b = 0.65$) base Bond numbers for $\delta/\beta = 0.3$. The former is unstable and the latter stable according to our linear analysis (figure 4.7), and the stabilisation threshold is $Bo \approx 0.575$. Fixing the bubble interface to that obtained at t_f , the effect of Bo_p is investigated by varying it over a wide range. Remember that the base flow at t_f is quasi-stagnant. The variation of the maximal growth rate, σ_r^{max} , is presented in figure 4.8(a) along with its corresponding prediction from the dispersion relation of Duclaux et al. (2006) (green) and the "matching" value obtained when $Bo_b = Bo_p$ (black squares). The results show that the growth rate for the bubble with a circular cross-section ($Bo_b = 0.01$, blue circles) diminishes with Bo_p . However, the interface does not stabilise (the growth rate does not cross zero) even for a rather large perturbation Bond number, $Bo_p = 10^2$. In contrast, the deformed interface of $Bo_b = 0.65$ (red crosses) stabilises as Bo_p exceeds a threshold (red pentagram) inferior to that of the "matching" case $Bo_b = Bo_p$ (black pentagram), and far larger than that of Duclaux et al. (2006) (green pentagram). Moreover, for small Bo_b where the bubble interface is almost circular, the isolated growth rate (blue circle) is close to the "matching" value (black square). We observe that the present linear analysis does not agree with the growth rate predicted by Duclaux et al. (2006) even in the low Bo limit, where the interface is circular. It is seen that the base bubble deformation state plays a significant role: a more deformed bubble (larger Bo_b) is less unstable so that a lower Bo_p number is needed to eventually stabilise the flow than when $Bo_p = Bo_b$. Remember that, in contrast, a quasi-cylindrical bubble (smaller Bo_b) is found more unstable than the "matching" case $Bo_p = Bo_b$, and is actually never stabilised. This demonstrates the essential role of the perturbation Bond number Bo_p .

2. Next, we artificially fix the perturbation Bond number Bo_p to the same extreme values ($Bo_p = 0.01$ and $Bo_p = 0.65$) and let the base Bond number Bo_b influence the base state. Not surprisingly, a larger perturbation Bond number ($Bo_p = 0.65$, red crosses) is more stabilising than the "matching" case (black squares), while a smaller perturbation Bond number ($Bo_p = 0.01$, blue circles) is more destabilising. The associated critical Bo_b numbers (blue and red pentagrams) bracket the "matching" critical Bond number (black pentagram). This demonstrates the role of the Bond number on the base state and, in turn, on the stability properties.

To conclude, decoupling the effects of Bo on the base flow and perturbations suggests that its influence on the base state (as revealed by the bubble deformation at t_f) is essential to stabilise the flow. Without base state deformation, the instability would persist at large Bond numbers.

This remark contrasts with what Duclaux et al. (2006) concluded, namely that the whole flow would become stable as soon as any region would become stable (in this case the north pole). The mismatch between their analytical threshold and experiments (as well as our analysis)

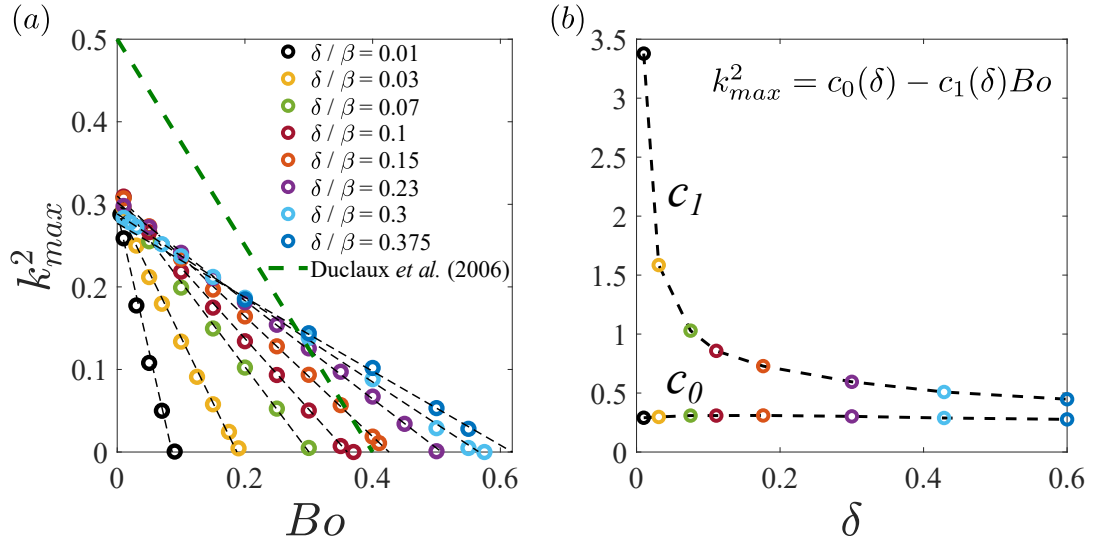


Figure 4.9: Maximal wavenumber (k_{max}) obtained from the linear stability analysis: (a) in $k_{max}^2 - Bo$ plane for different initial film thickness values; the black dashed lines show the linear fit to the present numerical data $k_{max}^2 = c_0(\delta) - c_1(\delta)Bo$, and the green dashed line shows the prediction by Duclaux et al. (2006). (b) The prefactors obtained from the fit shown in panel (a).

could therefore be possibly explained by the circular bubble cross-section assumption in their derivation of the linear stability characteristics. Another source of discrepancy may be related to their dispersion relation, where the growth rate is non-uniform in θ , whereas in principle the normal mode assumption forbids any dependency of the growth rate on the spatial coordinates.

4.3.6 Maximal unstable wavenumber

The maximal wavenumber, associated with the maximal growth rate of the unstable mode 1 is shown in figure 4.9 for a wide range of parameters. Increasing Bo decreases the optimal wavelength and $k_{max} \rightarrow 0$ on the stability boundary. While Duclaux et al. (2006) propose the fit $k_{max}^2 = 0.5 - 1.25Bo$, the present linear analysis evidences a similar trend but with different fitting parameters that depend on the initial film thickness. These fitting parameters are presented in figure 4.9(b). Note that considering the universal relation of Duclaux et al. (2006), one expects a unique stabilisation threshold of $Bo = 0.4$ for all film thickness values in contrast to their phase diagram.

4.3.7 Validity of the frozen frame assumption

We should recall from §4.2.3 that the key assumption behind the frozen frame approach for the linear stability analysis is that the perturbations evolve much faster than the base flow (Tan and

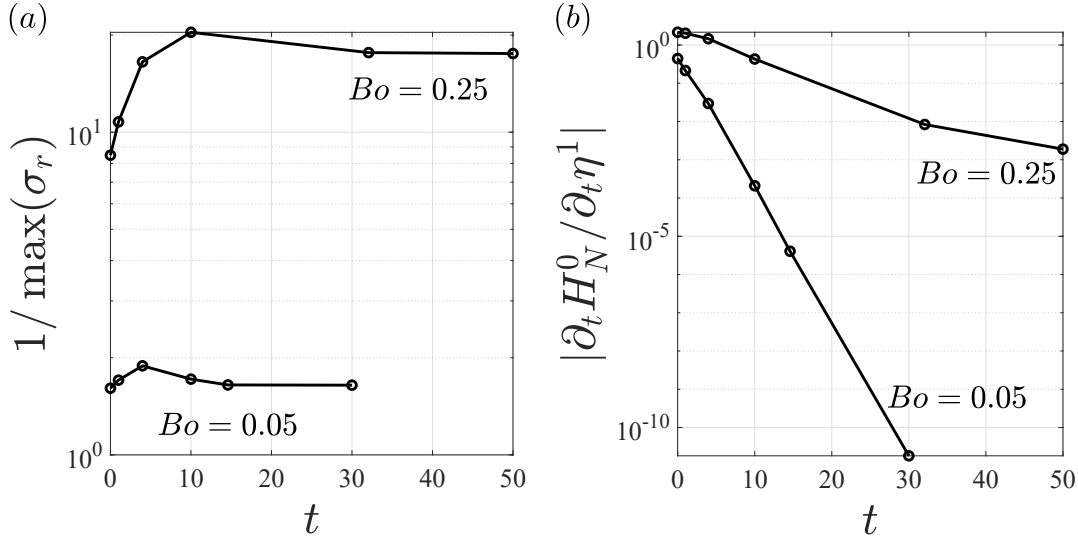


Figure 4.10: Frozen frame analysis validity check for the unstable modes presented in figure 4.5(c). (a) Temporal evolution of $1/\max(\sigma_r)$. (b) Comparison of the evolution rate between the base and perturbed flows.

Homsy, 1986). To assess the validity of this assumption, one can consider the characteristic time scales of the base flow evolution presented in table 4.1. After the initial bubble drift, the base flow decelerates mainly with two distinct time scales; a fast time scale $T_1 \sim 5$ and a slow time scale $T_2 > 50$. On the other hand, the relevant time scale for the unstable perturbation's evolution can be computed at different time steps as $1/\max(\sigma_r)$, which is presented in figure 4.10(a). To indicate how fast the base flow interface evolves compared to the unstable perturbation, $|\partial_t H_N^0 / \partial_t \eta^1| \sim \delta (a_1/T_1 \exp[-t/T_1] + a_2/T_2 \exp[-t/T_2]) / \max(\sigma_r) \exp[\max(\sigma_r)t]$ is presented in figure 4.10(b). The numerator is calculated from the double-exponent fit of the base flow, and the denominator is calculated from the temporal growth of the most unstable mode. A look at this indicator reveals that the base flow and perturbations may evolve at similar rates at small times, and even in some cases that the base flow may evolve faster than the perturbation. Nevertheless, at large times, when the drainage has decayed, the unstable perturbation grows faster than the base flow. Thus, the frozen frame assumption is only valid for large times, and loses its rigor in the early stages. We recall that the criterion to distinguish between stable and unstable modes in figure 4.7 is the growth rate of the modes at large times, sufficient for the frozen frame assumption to hold. However, it is crucial to properly take into account the base flow evolution at early times and to account for possible nonmodal mechanisms. For this reason, we carry out a transient growth analysis whose results are presented and discussed in the next section.

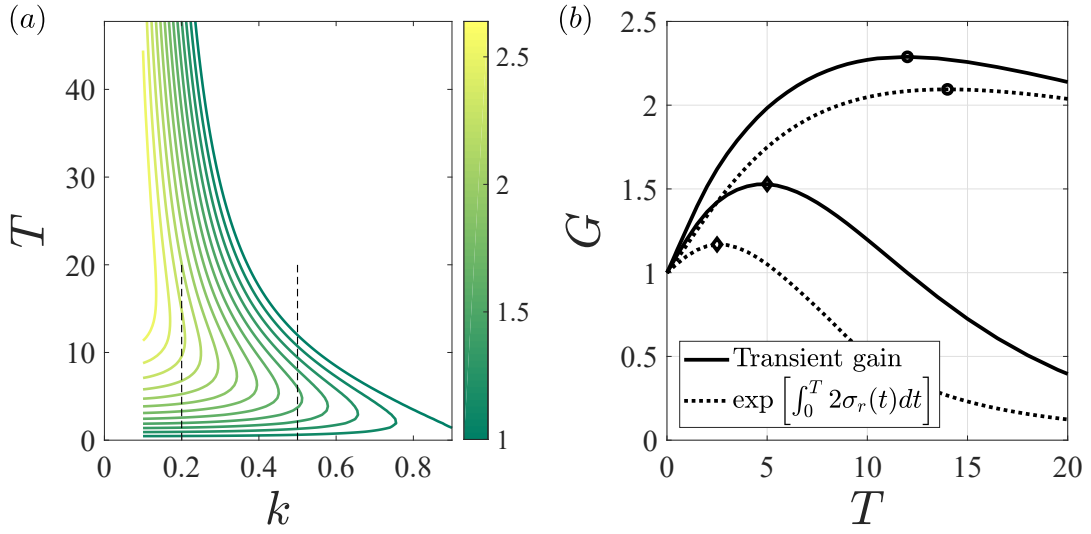


Figure 4.11: The parameters $\delta/\beta = 0.3$ and $Bo = 0.65$ have been selected. (a) Isocontours of the transient gain G defined in (4.24) in the $k - T$ plane, the temporal horizon $T \in [0, t_f]$ (only the region where $G \geq 1$ is shown). (b) Along the thin dashed lines in (a), comparison of the transient gain (full line) with its approximation using the dispersion curve only (dotted line), for $k = 0.2$ and $k = 0.5$ (maximum gain highlighted by a circle and a diamond, respectively).

4.3.8 Transient growth analysis

We present in what follows the results of the transient growth analysis, conducted mainly in the stable part of the parameter space in figure 4.7. Indeed, a flow can be linearly (asymptotically) stable but transiently amplify an initial perturbation so significantly that it is destabilised through a subcritical transition.

The transient gain for $\delta/\beta = 0.3$ and $Bo = 0.65$ is shown in figure 4.11(a) as a function of the wavenumber k and the temporal horizon T . Longer waves are subject to larger maximum transient gain but require more time before reaching it. The maximum attainable transient gain over all considered k and T is $G_{\max} = 2.64$, reached for the lowest considered k . This maximum gain value is of order unity, such that, for the considered parameters at least, a small-amplitude initial perturbation is not expected to be sufficiently amplified by the flow to trigger non-linearities.

The extent to which the transient growth is driven by nonmodal mechanisms, and may or may not be estimated directly from dispersion curves is investigated in figure 4.11(b), where the transient gains are compared with the integrated growth rate $\exp \left[\int_0^T 2\sigma_r(k, t) dt \right]$ for $k = 0.2$ and $k = 0.5$ (thin dashed lines). We recall that the growth rate $\sigma_r(k, t)$ for $\delta/\beta = 0.3$ and $Bo = 0.65$ is shown in figure 4.5(c). For $k = 0.5$ in figure 4.11(b), the curves are qualitatively similar but present some small quantitative discrepancies: the maximum transient gain reaches a slightly larger value at a larger temporal horizon, $T = 5$ against $T = 2.5$. Thus, between these two times, the energy of the perturbation can grow although the frozen base

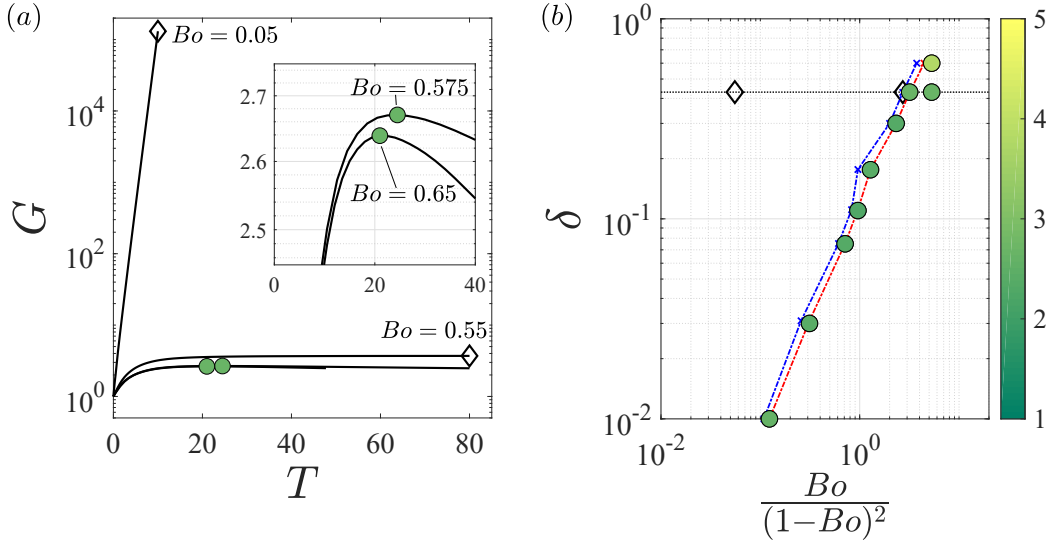


Figure 4.12: (a) Transient gains for $\delta = 0.43$ (corresponding to $\delta/\beta = 0.3$), and $Bo = 0.05$ (significantly unstable), $Bo = 0.55$ (slightly unstable), $Bo = 0.575$ (stable) and $Bo = 0.65$ (stable). Bullet (resp. diamond) markers highlight the largest gain for linearly stable (resp. unstable) parameters. Inset: zoom highlighting the largest gains for $Bo = 0.575$ and $Bo = 0.65$. The wavenumber k leading to the largest growth has been selected for all curves. (b) Phase diagram obtained from the transient growth analysis. Colours stand for $G_{\max} = \max_{k,T} G$ with $k \in [0.1, 0.9]$ and $T \in [0, t_f]$. The thin dotted line corresponds to $\delta/\beta = 0.3$. The blue (resp. red) dashed-dotted line links the last unstable (resp. first stable) points for a given δ and by increasing Bo .

flow is linearly stable. For $k = 0.2$ the transient gain is also systematically larger, however the two curves present little differences, implying this transient gain to be driven mostly by modal mechanisms.

In figure 4.12(a), the gain for $\delta/\beta = 0.3$ and $Bo = 0.65$ is compared to those of three additional Bond numbers: $Bo = 0.575$, $Bo = 0.55$ and $Bo = 0.05$, which correspond to a stable, a slightly and a strongly unstable flow, respectively. The wavenumber associated with the largest gain was selected. For $Bo = 0.05$, the maximum growth rate remains large (see figure 4.5(c)) and the gain quickly aligns on the fast exponential growth; specifically, the slope of the line marked with the black diamond is two times the maximum growth rate. For $Bo = 0.55$, the maximum growth rate rapidly converges towards very small values but does not become negative, thus the gain also grows exponentially for large times. Overall, results shown in figure 4.12(a) suggest that large gains can only be attained through instability.

To assess the generality of this conclusion, we report $G_{\max} \doteq \max_{k,T} G$ for $k \in [0.1, 0.9]$ and $T \in [0, t_f]$ in figure 4.12(b), in the same $\{\delta, Bo\}$ parameter space as in figure 4.7. The considered points were voluntarily chosen in the stable regime and the closest to the separatrix (i.e., the first red dot for a given δ in figure 4.7(b)). For all the considered parameters, G_{\max} does not exceed the small value of $G_{\max} = 3.8$. In this sense, the linear stability analysis seems to provide

a sufficiently complete description of this flow, since linear stability seems to imply small transient gains; conversely, linear instability seems to be a necessary and sufficient condition for large gains. Moreover, as we saw for $\delta/\beta = 0.3$ and $Bo = 0.65$, and we have checked these conclusions to be true for all the other points in figure 4.12(b), G_{\max} is reasonably well characterised using solely the information about the growth rate. In conclusion, nonmodal mechanisms are believed to have little influence on the flow, at least for the parameters considered in this paper.

4.4 Summary and conclusion

In this work, we have studied the draining flow of a viscous liquid film coating the inner wall of a horizontal tube. First, the temporal evolution of the axially invariant base flow with an initially stagnant film of uniform thickness was computed numerically. In the absence of inertia, the base flow exhibits an instantaneous upward drift of the core bubble, followed by an exponential decay of the flow as the interface approaches the tube upper wall.

Next, the stability of the evolving base flow was investigated by means of a linear stability analysis under the frozen frame assumption. It was verified that this assumption holds at large times. One unstable mode was observed which features the characteristics of the Rayleigh-Plateau mode: axial interface undulations, horizontal symmetry, and vertical asymmetry evidencing stronger modulation at the bottom. These features match the interface shape observed in the experiments of Duclaux et al. (2006). The maximal growth rate of this mode decreases as the bubble approaches the tube upper wall.

A parametric study was then conducted in the space of dimensionless parameters $\{Bo, Oh, \beta\}$. This study suggests that increasing Bo , equivalent to weakening surface tension in comparison with gravity, results in a horizontally wider bubble interface that rises more slowly than quasi-cylindrical bubbles observed at small Bond numbers. The bubble slowdown coincides with the displacement of the location of minimum film thickness from the north pole to the sides. With increasing Bo , the deformed interface becomes less unstable, and the Rayleigh-Plateau instability is suppressed above a critical Bo value. We also demonstrated that inertial forces, achieved at finite Oh , affect the flow mainly at the onset of the drainage such that the bubble drifts upward more smoothly, and the drainage is delayed. However, inertia does not alter the shape of the interface, nor its linear stability regime, and has a minor influence on the maximal growth rate at large times.

Finally, a stability diagram was sketched by investigating the linear stability of the deformed interface in the limit of large times for various $\{Bo, \beta\}$, confirming the stabilising effect of larger Bond numbers and thinner films. By relaxing assumptions of past studies (e.g. circular base interface), the present linear study showed an interesting improvement on existing theoretical results for the transition between stable and unstable interfaces. A slight discrepancy with the experimental data of Duclaux et al. (2006) remains, resulting in a few stable experimental conditions predicted to be unstable by our linear stability analysis. Comparing the experi-

mental protocol of Duclaux et al. (2006) with the assumptions of the present study suggests some possibilities for the observed slight mismatch. Firstly, the most unstable wavenumber diminishes with Bo , which results in the promotion of very long wavelengths. Capturing wavelengths longer than the finite length of the experimental apparatus is not possible, which may result in the stabilization of perturbations that would be unstable in an infinitely long tube. Additionally, in the experiments, the gaseous core is pushed into a wet tube by a syringe pump; any residual axial velocity, left-right asymmetry, or axial variations in the deposited film thickness (Balestra et al., 2018c) may all have some influence on the stability. Finally, we note that linear analysis cannot capture the influence of non-linearities on the final pattern. Non-linearities may quickly saturate the growth of the linear modes to a very small amplitude (Halpern and Grotberg, 2003) which may make it difficult to observe the instability experimentally.

Lastly, a transient growth analysis was conducted so as to relax the frozen base flow assumption. It conclusively demonstrated the small importance of nonmodal mechanisms, both because the transient gains were systematically of order unity in the linearly stable region of the parameter space, and because they were rather well predicted from the growth rate of the leading eigenvalue. This justifies the relevance of the linear stability analysis for this flow when compared with experimental data.

The present study, based on the full Navier-Stokes equations and capable of handling complex interface geometries, paves the way for a wealth of future investigations. For instance, it would be of interest to investigate the effect of inclining the tube: as gravity becomes non-orthogonal to the tube axis, one can expect a competition between transverse drainage and longitudinal advection, possibly resulting in a transition from absolute to convective instability. Another exciting perspective is that of a film coating the outside of an inclined tube: in addition to the aforementioned competition, this configuration offers the possibility of rich non-linear dynamics such as pinch-off. Finally we recall that the present study has focused on the regime of small and intermediate Bond numbers, where the Rayleigh-Taylor instability is suppressed (Trinh et al., 2014; Balestra et al., 2016). A natural extension of our work should explore larger Bond numbers. We conjecture the existence of an interval of stable Bond numbers, with smaller Bo unstable to the Rayleigh-Plateau instability (like in the present study) and larger Bo unstable to the Rayleigh-Taylor instability (Trinh et al., 2014; Balestra et al., 2016, 2018b).

4.5 Appendix

4.5.1 Derivation of the interface boundary conditions

In this section, the derivation of the interface boundary conditions for the perturbed flow is elaborated. These conditions should be imposed on the perturbed interface, i.e. at $r = \mathcal{R}_{\text{int}}^0 + \epsilon \eta^1$, while η^1 is already a part of the problem unknowns. By using the Taylor expansion, that is, projecting radially on the base interface, i.e. on $r = \mathcal{R}_{\text{int}}^0(\theta, t)$, any flow quantity at the perturbed interface can be readily approximated. This projection is referred to as flattening and for an arbitrary function $f(r, \theta, z, t)$ can be expressed as

$$f|_{(r=\mathcal{R}_{\text{int}}^0+\epsilon\eta^1,\theta,z,t)} = f|_{(r=\mathcal{R}_{\text{int}}^0,\theta,z,t)} + \epsilon\eta^1 \partial_r f|_{(r=\mathcal{R}_{\text{int}}^0,\theta,z,t)} + \mathcal{O}(\epsilon^2). \quad (4.25)$$

By substituting the decomposed state vector of (4.7), into the interface conditions (4.5)-(4.6), then using the ansatz of (4.8), and applying the aforementioned flattening, we can formulate these conditions as a set of equivalent constraints on the boundary of the base interface. The linearised form of the kinematic condition (4.5) writes

$$\partial_t (\mathcal{R}_{\text{int}}^0 + \epsilon \eta^1) + (\mathbf{u}^0 + \epsilon \mathbf{u}^1) \cdot \nabla (\mathcal{R}_{\text{int}}^0 + \epsilon \eta^1) = (\mathbf{u}^0 + \epsilon \mathbf{u}^1) \cdot \mathbf{e}_r, \quad \text{at } r = \mathcal{R}_{\text{int}}^0 + \epsilon \eta^1, \quad (4.26)$$

where the gradient vector in the Cylindrical coordinate can be expressed as $\nabla = (\partial_r, 1/r \partial_\theta, \partial_z)^T$. Applying (4.25) to (4.26) and using the ansatz of (4.8) readily results in (4.11).

The linearised dynamic condition (4.6) writes

$$\left(\underline{\underline{\tau}}^0 + \epsilon \underline{\underline{\tau}}^1 \right) (\mathbf{n}^0 + \epsilon \mathbf{n}^1) = (\kappa^0 + \epsilon \kappa^1) (\mathbf{n}^0 + \epsilon \mathbf{n}^1), \quad \text{at } r = \mathcal{R}_{\text{int}}^0 + \epsilon \eta^1, \quad (4.27)$$

Applying (4.25) to (4.27) and using the ansatz of (4.8) readily results in (4.16). In order to express interface conditions in the Cartesian coordinates, the terms which are expressed in the Cylindrical coordinates should be transformed by employing the Jacobian transformations as

$$\begin{aligned} \mathbf{e}_r &= \cos \theta \mathbf{e}_x + \sin \theta \mathbf{e}_y, & \mathbf{e}_\theta &= -\sin \theta \mathbf{e}_x + \cos \theta \mathbf{e}_y, \\ \partial_r &= \cos \theta \partial_x + \sin \theta \partial_y, & \partial_\theta &= \frac{\mathbf{t}^0 \cdot \nabla_s}{\mathbf{t}^0 \cdot \nabla_s \theta}, \end{aligned} \quad (4.28)$$

where \mathbf{t}^0 denotes the unit tangent vector, and $\nabla_s = \nabla - \mathbf{n}^0 (\mathbf{n}^0 \cdot \nabla)$ is the tangential derivative on the base interface. Both conditions (4.11) and (4.16) include the normal vector and the curvature of the perturbed interface whose formulation is given in appendix 4.5.3. For further details concerning the numerical implementation of the boundary conditions, see appendix 4.5.2.

4.5.2 Variational formulation of the linear stability analysis and implementation of boundary conditions

Implementation of the numerical scheme and development of the *variational formulation* associated with the governing equations presented in section 4.2 are elaborated in this appendix, recalling that the numerical domain is shown in figure 4.3. To develop the variational form of (4.12), firstly the normal mode of (4.8) is applied to the system of equations (4.9)-(4.11). Then it is internally multiplied by the vector of the test functions $\psi = [\psi_p, \psi_{\mathbf{u}}, \psi_\eta]$, where $\psi_{\mathbf{u}} = [\psi_{u_x}, \psi_{u_y}, \psi_{u_z}]$. The resulting scalar product is integrated on Ω_{xy} , which in the linear order gives

$$\begin{aligned} & \left\{ \iint_{\Omega_{xy}} \psi_p^* (\tilde{\nabla} \cdot \tilde{\mathbf{u}}) \, dA_{\Omega_{xy}} \right. \\ & + \iint_{\Omega_{xy}} \psi_{\mathbf{u}}^* \cdot \left(\left(\frac{Bo}{Oh} \right)^2 \delta^4 (\sigma \tilde{\mathbf{u}} + \mathbf{u}^0 \cdot \tilde{\nabla} \tilde{\mathbf{u}} + \tilde{\mathbf{u}} \cdot \nabla \mathbf{u}^0) - \tilde{\nabla} \cdot \underline{\underline{\tilde{\tau}}} \right) \, dA_{\Omega_{xy}} \\ & + \int_{\partial \Sigma_{\text{int}}} \psi_\eta^* \left(\sigma \tilde{\eta} + \left(-\partial_r u_r^0 + \frac{\partial_r u_\theta^0 \partial_\theta \mathcal{R}_{\text{int}}^0}{\mathcal{R}_{\text{int}}^0} - \frac{u_\theta^0 \partial_\theta \mathcal{R}_{\text{int}}^0}{(\mathcal{R}_{\text{int}}^0)^2} \right) \tilde{\eta} + \frac{u_\theta^0}{\mathcal{R}_{\text{int}}^0} \partial_\theta \tilde{\eta} + \frac{\partial_\theta \mathcal{R}_{\text{int}}^0}{\mathcal{R}_{\text{int}}^0} \tilde{u}_\theta - \tilde{u}_r \right) \, ds \Big\} \\ & + \text{c.c.} = 0. \end{aligned} \quad (4.29)$$

It should be noted that in a complex system, the applied scalar product is Hermitian, defined as $\langle \mathbf{a}, \mathbf{b} \rangle = \mathbf{a}^* \cdot \mathbf{b}$ where the superscript $*$ denotes the complex conjugate. In the last line of this system of equations, kinematic condition (4.11) is used to define $\tilde{\eta}$ only on $\partial \Sigma_{\text{int}}$. After integrating by parts, $\psi_{\mathbf{u}}^* \cdot (\tilde{\nabla} \cdot \underline{\underline{\tilde{\tau}}}) = \tilde{\nabla} \cdot (\underline{\underline{\tilde{\tau}}} \psi_{\mathbf{u}}^*) - tr \left(\underline{\underline{\tilde{\tau}}}^T (\tilde{\nabla} \psi_{\mathbf{u}})^* \right)$, and then applying the Gauss's theorem, $\iint_{\Omega_{xy}} \tilde{\nabla} \cdot (\underline{\underline{\tilde{\tau}}} \psi_{\mathbf{u}}^*) \, dA_{\Omega_{xy}} = \int_{\partial \Omega_{xy}} (\underline{\underline{\tilde{\tau}}} \psi_{\mathbf{u}}^*) \cdot \mathbf{n}^0 \, ds$, (4.29) implies

$$\begin{aligned} & \left\{ \iint_{\Omega_{xy}} \psi_p^* (\tilde{\nabla} \cdot \tilde{\mathbf{u}}) \, dA_{\Omega_{xy}} \right. \\ & + \iint_{\Omega_{xy}} \psi_{\mathbf{u}}^* \cdot \left(\left(\frac{Bo}{Oh} \right)^2 \delta^4 (\sigma \tilde{\mathbf{u}} + \mathbf{u}^0 \cdot \tilde{\nabla} \tilde{\mathbf{u}} + \tilde{\mathbf{u}} \cdot \nabla \mathbf{u}^0) \right) \, dA_{\Omega_{xy}} \\ & + \iint_{\Omega_{xy}} tr \left(\underline{\underline{\tilde{\tau}}}^T (\tilde{\nabla} \psi_{\mathbf{u}})^* \right) \, dA_{\Omega_{xy}} \\ & + \int_{\partial \Omega_{xy}} -(\underline{\underline{\tilde{\tau}}} \psi_{\mathbf{u}}^*) \cdot \mathbf{n}^0 \, ds \\ & + \int_{\partial \Sigma_{\text{int}}} \psi_\eta^* \left(\sigma \tilde{\eta} + \left(-\partial_r u_r^0 + \frac{\partial_r u_\theta^0 \partial_\theta \mathcal{R}_{\text{int}}^0}{\mathcal{R}_{\text{int}}^0} - \frac{u_\theta^0 \partial_\theta \mathcal{R}_{\text{int}}^0}{(\mathcal{R}_{\text{int}}^0)^2} \right) \tilde{\eta} + \frac{u_\theta^0}{\mathcal{R}_{\text{int}}^0} \partial_\theta \tilde{\eta} + \frac{\partial_\theta \mathcal{R}_{\text{int}}^0}{\mathcal{R}_{\text{int}}^0} \tilde{u}_\theta - \tilde{u}_r \right) \, ds \Big\} \\ & + \text{c.c.} = 0. \end{aligned} \quad (4.30)$$

The stress tensor $\underline{\underline{\tilde{\tau}}}$ is symmetric, thus $(\underline{\underline{\tilde{\tau}}} \psi_{\mathbf{u}}^*) \cdot \mathbf{n}^0 = (\underline{\underline{\tilde{\tau}}} \mathbf{n}^0) \cdot \psi_{\mathbf{u}}^*$. Using the dynamic condition (4.16) and the fact that $\psi_{\mathbf{u}}|_{\partial \Sigma_f} = 0$ (because of the no-slip condition on the solid wall), the

(4.31)					$= -\sigma$	0 0 0 0 0						0 0 0 0 0					
(4.33-4.34)						0 (4.32) 0 0 0						0 0 0 0 0					
(4.31)						0 0 0 0 0						0 0 0 0 0					
0	0	0	I	0		0	0	0	0	0		0	0	0	0	0	
(4.31)					$= -\sigma$	0 0 0 0 0						0 0 0 0 0					
(4.35)						0 0 0 0 0						0 0 0 0 0					
(4.37)						0 0 0 0 0						0 0 0 0 0					
0	0	0	0	0		0	0	0	0	0		0	0	0	0	0	

Figure 4.13: Matrix representation of the variational system (4.31)-(4.38), solved in COMSOL MultiphysicsTM; blue represents the implementation of (4.9)-(4.10), white represents the implementation of the no-slip boundary condition on the solid wall, green represents the implementation of the dynamic boundary condition (4.16), represents the implementation of the kinematic condition (4.11).

variational form of (4.12) implies

$$\left\{ \iint_{\Omega_{xy}} \psi_p^* (\tilde{\nabla} \cdot \tilde{\mathbf{u}}) \, dA_{\Omega_{xy}} \right. \quad (4.31)$$

$$+ \iint_{\Omega_{xy}} \psi_{\mathbf{u}}^* \cdot \left(\left(\frac{Bo}{Oh} \right)^2 \delta^4 \sigma \tilde{\mathbf{u}} \right) \, dA_{\Omega_{xy}} \quad (4.32)$$

$$+ \iint_{\Omega_{xy}} \psi_{\mathbf{u}}^* \cdot \left(\left(\frac{Bo}{Oh} \right)^2 \delta^4 (\mathbf{u}^0 \cdot \tilde{\nabla} \tilde{\mathbf{u}} + \tilde{\mathbf{u}} \cdot \nabla \mathbf{u}^0) \right) \, dA_{\Omega_{xy}} \quad (4.33)$$

$$+ \iint_{\Omega_{xy}} tr \left(\tilde{\tau}^T (\tilde{\nabla} \psi_{\mathbf{u}})^* \right) \, dA_{\Omega_{xy}} \quad (4.34)$$

$$+ \int_{\partial \Sigma_{\text{int}}} \left(\underline{\tau}^0 \tilde{\mathbf{n}} + \tilde{\eta} \partial_r \underline{\tau}^0 \mathbf{n}^0 - (\kappa_0 \tilde{\mathbf{n}} + \tilde{\kappa} \mathbf{n}^0) \right) \cdot \psi_{\mathbf{u}}^* \, ds \quad (4.35)$$

$$+ \int_{\partial \Sigma_{\text{int}}} \psi_{\eta}^* (\sigma \tilde{\eta}) \, ds \quad (4.36)$$

$$+ \int_{\partial \Sigma_{\text{int}}} \psi_{\eta}^* \left(\left(-\partial_r u_r^0 + \frac{\partial_r u_{\theta}^0 \partial_{\theta} \mathcal{R}_{\text{int}}^0}{\mathcal{R}_{\text{int}}^0} - \frac{u_{\theta}^0 \partial_{\theta} \mathcal{R}_{\text{int}}^0}{(\mathcal{R}_{\text{int}}^0)^2} \right) \tilde{\eta} + \frac{u_{\theta}^0}{\mathcal{R}_{\text{int}}^0} \partial_{\theta} \tilde{\eta} + \frac{\partial_{\theta} \mathcal{R}_{\text{int}}^0}{\mathcal{R}_{\text{int}}^0} \tilde{u}_{\theta} - \tilde{u}_r \right) \, ds \Big\} \quad (4.37)$$

$$+ \text{c.c.} = 0. \quad (4.38)$$

This variational equation can be readily implemented and solved in COMSOL MultiphysicsTM. It is sufficient to solve the first part (in $\{\}$) and the c.c. is known consequently. The matrix representation of (4.31)-(4.38) is shown in figure 4.13.

4.5.3 Characterization of an arbitrary interface

In this section, we present the geometrical characterization of an arbitrary interface parameterised in Cylindrical coordinates. The aim is to develop the characteristics of a three-dimensional interface, as well as the linear perturbations applied to this interface. The key

properties of interest are the normal vector and the local curvature.

Normal vector

We recall that the unit normal vector of a linearly perturbed interface can be decomposed as $\mathbf{n} = \mathbf{n}^0 + \epsilon \mathbf{n}^1$ which reads

$$\mathbf{n}^0 = \begin{pmatrix} n_r^0 \\ n_\theta^0 \\ n_z^0 \end{pmatrix} = A^{-1/2} \begin{pmatrix} 1 \\ -\frac{1}{\mathcal{R}_{\text{int}}^0} \partial_\theta \mathcal{R}_{\text{int}}^0 \\ \partial_z \mathcal{R}_{\text{int}}^0 \end{pmatrix}, \quad (4.39)$$

$$\mathbf{n}^1 = \begin{pmatrix} n_r^1 \\ n_\theta^1 \\ n_z^1 \end{pmatrix} = \begin{pmatrix} B_r \eta^1 + C_r \partial_\theta \eta^1 + D_r \partial_z \eta^1 \\ B_\theta \eta^1 + C_\theta \partial_\theta \eta^1 + D_\theta \partial_z \eta^1 \\ B_z \eta^1 + C_z \partial_\theta \eta^1 + D_z \partial_z \eta^1 \end{pmatrix}, \quad (4.40)$$

where

$$\begin{aligned} A &= 1 + \left(\frac{1}{\mathcal{R}_{\text{int}}^0} \partial_\theta \mathcal{R}_{\text{int}}^0 \right)^2 + (\partial_z \mathcal{R}_{\text{int}}^0)^2, & B_r &= \frac{A^{-3/2}}{(\mathcal{R}_{\text{int}}^0)^3} (\partial_\theta \mathcal{R}_{\text{int}}^0)^2, \\ B_\theta &= A^{-3/2} \left(-\frac{1}{(\mathcal{R}_{\text{int}}^0)^4} (\partial_\theta \mathcal{R}_{\text{int}}^0)^3 + \frac{A}{(\mathcal{R}_{\text{int}}^0)^2} \partial_\theta \mathcal{R}_{\text{int}}^0 \right), & B_z &= -\frac{A^{-3/2}}{(\mathcal{R}_{\text{int}}^0)^3} (\partial_\theta \mathcal{R}_{\text{int}}^0)^2 \partial_z \mathcal{R}_{\text{int}}^0, \\ C_r &= -\frac{A^{-3/2}}{(\mathcal{R}_{\text{int}}^0)^2} \partial_\theta \mathcal{R}_{\text{int}}^0, & C_\theta &= -\frac{A^{-3/2}}{\mathcal{R}_{\text{int}}^0} \left(1 + (\partial_z \mathcal{R}_{\text{int}}^0)^2 \right), & C_z &= \frac{A^{-3/2}}{(\mathcal{R}_{\text{int}}^0)^2} \partial_\theta \mathcal{R}_{\text{int}}^0 \partial_z \mathcal{R}_{\text{int}}^0, \\ D_r &= -A^{-3/2} \partial_z \mathcal{R}_{\text{int}}^0, & D_\theta &= \frac{A^{-3/2}}{\mathcal{R}_{\text{int}}^0} \partial_z \mathcal{R}_{\text{int}}^0 \partial_\theta \mathcal{R}_{\text{int}}^0, & D_z &= A^{-3/2} \left((\partial_z \mathcal{R}_{\text{int}}^0)^2 - A \right). \end{aligned} \quad (4.41)$$

For a base interface of the form $r = \mathcal{R}_{\text{int}}^0(t, \theta)$ and a perturbation ansatz (4.8), the normal vector of the base interface can be further simplified as

$$\mathbf{n}^0 = \begin{pmatrix} n_r^0 \\ n_\theta^0 \\ n_z^0 \end{pmatrix} = A^{-1/2} \begin{pmatrix} 1 \\ -\frac{1}{\mathcal{R}_{\text{int}}^0} \partial_\theta \mathcal{R}_{\text{int}}^0 \\ 0 \end{pmatrix}, \quad (4.42)$$

and simplification of the linearised perturbation of the normal vector (4.40)-(4.41) implies

$$\tilde{\mathbf{n}} = \begin{pmatrix} \tilde{n}_r \\ \tilde{n}_\theta \\ \tilde{n}_z \end{pmatrix} = \begin{pmatrix} B_r \tilde{\eta} + C_r \partial_\theta \tilde{\eta} \\ B_\theta \tilde{\eta} + C_\theta \partial_\theta \tilde{\eta} \\ ik D_z \tilde{\eta} \end{pmatrix}, \quad (4.43)$$

where

$$\begin{aligned}
A &= 1 + \left(\frac{1}{\mathcal{R}_{\text{int}}^0} \partial_\theta \mathcal{R}_{\text{int}}^0 \right)^2, & B_r &= \frac{A^{-3/2}}{(\mathcal{R}_{\text{int}}^0)^3} (\partial_\theta \mathcal{R}_{\text{int}}^0)^2, \\
B_\theta &= A^{-3/2} \left(-\frac{1}{(\mathcal{R}_{\text{int}}^0)^4} (\partial_\theta \mathcal{R}_{\text{int}}^0)^3 + \frac{A}{(\mathcal{R}_{\text{int}}^0)^2} \partial_\theta \mathcal{R}_{\text{int}}^0 \right), & C_r &= -\frac{A^{-3/2}}{(\mathcal{R}_{\text{int}}^0)^2} \partial_\theta \mathcal{R}_{\text{int}}^0, \\
C_\theta &= -\frac{A^{-3/2}}{\mathcal{R}_{\text{int}}^0}, & D_z &= -A^{-1/2}.
\end{aligned} \tag{4.44}$$

Curvature

We recall that the local curvature of a linearly perturbed interface can be decomposed as $\kappa = \kappa^0 + \epsilon \kappa^1$ which reads

$$\kappa^0 = \frac{1}{\mathcal{R}_{\text{int}}^0} (n_r^0 + \partial_\theta n_\theta^0) + \partial_z n_z^0, \tag{4.45}$$

$$\begin{aligned}
\kappa^1 &= -\frac{\eta^1}{(\mathcal{R}_{\text{int}}^0)^2} (n_r^0 + \partial_\theta n_\theta^0) + \frac{1}{\mathcal{R}_{\text{int}}^0} (n_r^1 + \partial_\theta n_\theta^1) + \partial_z n_z^1 \\
&= E\eta^1 + F\partial_\theta \eta^1 + G\partial_z \eta^1 + D_z \partial_{zz}^2 \eta^1 + \frac{C_\theta}{\mathcal{R}_{\text{int}}^0} \partial_{\theta\theta}^2 \eta^1,
\end{aligned} \tag{4.46}$$

where

$$\begin{aligned}
E &= \frac{1}{\mathcal{R}_{\text{int}}^0} (B_r + \partial_\theta B_\theta) - \frac{1}{(\mathcal{R}_{\text{int}}^0)^2} (n_r^0 + \partial_\theta n_\theta^0) + \partial_z B_z, \\
F &= \frac{1}{\mathcal{R}_{\text{int}}^0} (C_r + \partial_\theta C_\theta + B_\theta + D_\theta \partial_z) + \partial_z C_z + C_z \partial_z, \\
G &= B_z + \partial_z D_z.
\end{aligned} \tag{4.47}$$

Note that the subscript r in (4.39)-(4.47) does not imply the real part. For a base interface of the form $r = \mathcal{R}_{\text{int}}^0(t, \theta)$ and a perturbation ansatz (4.8), the curvature of the base interface can be further simplified as

$$\kappa^0 = \frac{1}{\mathcal{R}_{\text{int}}^0} (n_r^0 + \partial_\theta n_\theta^0), \tag{4.48}$$

and simplification of the linearised perturbation of the curvature (4.46)-(4.47) implies

$$\begin{aligned}
\tilde{\kappa} &= -\frac{\tilde{\eta}}{(\mathcal{R}_{\text{int}}^0)^2} (n_r^0 + \partial_\theta n_\theta^0) + \frac{1}{\mathcal{R}_{\text{int}}^0} (\tilde{n}_r + \partial_\theta \tilde{n}_\theta) + ik\tilde{n}_z \\
&= E\tilde{\eta} + F\partial_\theta \tilde{\eta} - k^2 D_z \tilde{\eta} + \frac{C_\theta}{\mathcal{R}_{\text{int}}^0} \partial_{\theta\theta}^2 \tilde{\eta},
\end{aligned} \tag{4.49}$$

where

$$E = \frac{1}{\mathcal{R}_{\text{int}}^0} (B_r + \partial_\theta B_\theta) - \frac{1}{(\mathcal{R}_{\text{int}}^0)^2} (n_r^0 + \partial_\theta n_\theta^0),$$

$$F = \frac{1}{\mathcal{R}_{\text{int}}^0} (C_r + \partial_\theta C_\theta + B_\theta).$$

4.5.4 Derivation of a simplified expression for the energy density of the transient response.

The interfacial energy density per wavelength is proportional to

$$\begin{aligned} e(T) &= \frac{k}{2\pi} \int_0^{2\pi} \int_0^{2\pi/k} |\tilde{\eta}(T) e^{ikz} + c.c|^2 dz \mathcal{R}_{\text{int}}^0(T) d\theta \\ &= 2 \int_0^{2\pi} |\tilde{\eta}(T)|^2 \mathcal{R}_{\text{int}}^0(T) d\theta \\ &= 2 \sum_{m=-N}^N \sum_{n=-N}^N \alpha_m^* \alpha_n \int_0^{2\pi} \tilde{\eta}_m(T)^* \tilde{\eta}_n(T) \mathcal{R}_{\text{int}}^0(T) d\theta \\ &= 2 \boldsymbol{\alpha}^H \mathbf{A}(T) \boldsymbol{\alpha} \end{aligned} \tag{4.50}$$

where the strictly positive definite and Hermitian matrix $\mathbf{A}(T)$ is such that

$$[\mathbf{A}(T)]_{mn} = \int_0^{2\pi} \tilde{\eta}_m(T)^* \tilde{\eta}_n(T) \mathcal{R}_{\text{int}}^0(T) d\theta, \tag{4.51}$$

for $-N \leq m \leq N$ and $-N \leq n \leq N$, and where we defined

$$\boldsymbol{\alpha} = [\alpha_N^*, \alpha_{N-1}^*, \dots, \alpha_1^*, \alpha_0, \alpha_1, \dots, \alpha_{N-1}, \alpha_N]^T. \tag{4.52}$$

The leading eigenvector of $\mathbf{A}(T)$ has no particular reason to have its N first elements equal to the complex conjugate of its last N . Thus, it cannot correspond directly to the optimal set of $\boldsymbol{\alpha}$, that should satisfy this last constraint. For this reason we introduce the matrix

$$\mathbf{M}^{-1} = \begin{bmatrix} \mathbf{I} & \mathbf{O} & \mathbf{P} \\ \mathbf{O}^T & \sqrt{2} & \mathbf{O}^T \\ -i\mathbf{I} & \mathbf{O} & i\mathbf{P} \end{bmatrix}, \quad \text{with } \mathbf{I}_{ij} = \delta_{ij}, \quad \mathbf{P}_{ij} = \delta_{N-i+1,j}, \quad \text{and } \mathbf{O}_i = 0. \tag{4.53}$$

for $1 \leq i, j \leq N$. Namely, \mathbf{I} is the identity matrix of size $N \times N$, \mathbf{P} is the identity matrix mirrored around its vertical axis (it contains ones on the diagonal from the bottom-left to the top-right and zeros everywhere else) and \mathbf{O} is a vectors of zeros of size $N \times 1$. In this manner, we have directly $\mathbf{a} = \mathbf{M}^{-1} \boldsymbol{\alpha}$, such that :

$$e(T) = 2 \boldsymbol{\alpha}^H \mathbf{A}(T) \boldsymbol{\alpha} = 2 \mathbf{a}^T \mathbf{M}^H \mathbf{A}(T) \mathbf{M} \mathbf{a} = 2 \mathbf{a}^T \Re[\mathbf{M}^H \mathbf{A}(T) \mathbf{M}] \mathbf{a} \tag{4.54}$$

where we used that \mathbf{a} and $e(T)$ are a real-valued. Therefore, defining $\mathbf{E}(T) = \Re[\mathbf{M}^H \mathbf{A}(T) \mathbf{M}]$ leads to the desired result.

4.5.5 Validation of the numerical model

The developed numerical scheme is validated hereafter. Several measures are taken to ensure the correspondence of the model, based on the asymptotic limits where an analytical solution may exist.

Base flow model

The present base flow model is validated with Balestra et al. (2016) who studied a similar base flow in the limit of thin film, $\delta \ll 1$, and small surface tension, $Bo \gg 1$, by employing lubrication equations (Oron et al., 1997). Figure 4.14(a) shows that the present model gives a solution of the base flow in full agreement with the solution of Balestra et al. (2016).

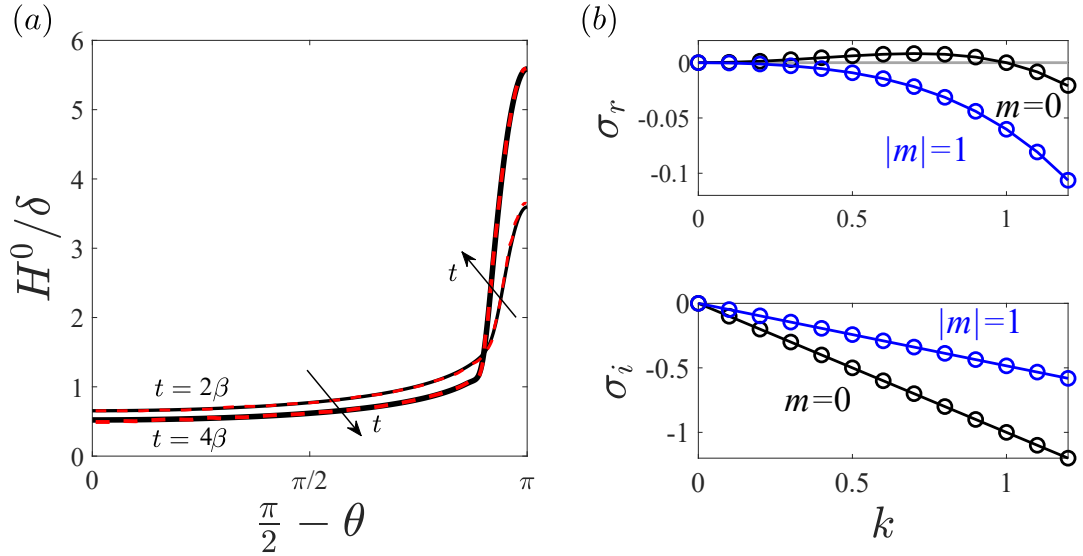


Figure 4.14: Numerical model validation. (a) Base flow: two snapshots of the liquid film thickness $H^0 = \beta - \mathcal{R}_{\text{int}}^0$, in the right half-plane, at time $t = \{2\beta, 4\beta\}$. Solid lines present the solution from the present study, and the dashed lines present the solution obtained by Balestra et al. (2016); $Oh = 10.05$, $Bo = 1960.2$, $\delta/\beta = 0.01$. (b) Stability analysis: dispersion curves of the two least stable modes associated with the viscous film coating inside a vertical tube, namely $|m| = \{0, 1\}$. The continuous lines present the analytical solution obtained from the Stokes equations, and the circle represents the results from the present model; $Oh \rightarrow \infty$, $Bo = 1$, $\delta = 0.1$.

Linear stability analysis model

The present linear stability model is validated with the analytical solution that Camassa et al. (2014) presented for the gravity-driven flow of a viscous film that coats the interior side of a vertical tube (where gravity points in z direction in figure 4.1). The corresponding base flow is parallel and can be expressed in cylindrical coordinates as

$$u_z^0 = \frac{\delta^{-2}}{2} \left(\frac{\beta^2 - r^2}{2} + \ln \frac{r}{\beta} \right), \quad p^0 = -1, \quad \mathcal{R}_{\text{int}}^0 = 1. \quad (4.55)$$

For the linear stability analysis, Camassa et al. (2014) employed an approximation of the Stokes equations for long jets, referred to as the *long-wavelength approximation* (Reynolds, 1886) and compared the results with the analytical solution, in terms of Bessel functions, obtained by solving the full Stokes equations (Goren, 1962). Thanks to the axisymmetry of the base flow, Camassa et al. (2014) considered a perturbation as in (4.8) with the Fourier ansatz exponent of $\exp[\sigma t + ikz + im\theta]$ where m denotes the azimuthal wavenumber. Both of the aforementioned equations match in the limit of thin liquid film, $\beta \rightarrow 1$, where the long-wavelength approximation gives a dispersion relation of $\sigma = S(k^2 - k^4) - ik$ with $S = S(Bo, \delta)$ being constant for the axisymmetric perturbation $m = 0$. All of the helical perturbations, $|m| > 0$, are known to be linearly stable for such a flow (Rayleigh, 1878). Figure 4.14(b) presents the full agreement between the present linear stability model and the analytical solution for a relatively thin film thickness $\delta = 0.1$. It should be noted that despite the axisymmetric nature of the validated case, this presented validation holds also for an arbitrary interface. For this aim, the geometrical symmetry in the numerical reference frame is broken by setting the origin of the coordinates system at an arbitrary location inside the bubble, $(x, y) = (0.2, 0.7)$.

Grid independency

A convergence study for the base flow evolution and the linear stability of the unstable eigenvalue is presented in figure 4.15, for $\{Oh \rightarrow \infty, Bo = 0.05, \delta/\beta = 0.3\}$. Mesh resolution is controlled by setting the number of divisions on the solid wall and interface boundaries. Mesh convergence is already attained for the presented grids. All of the presented results in the manuscript are obtained employing M3.

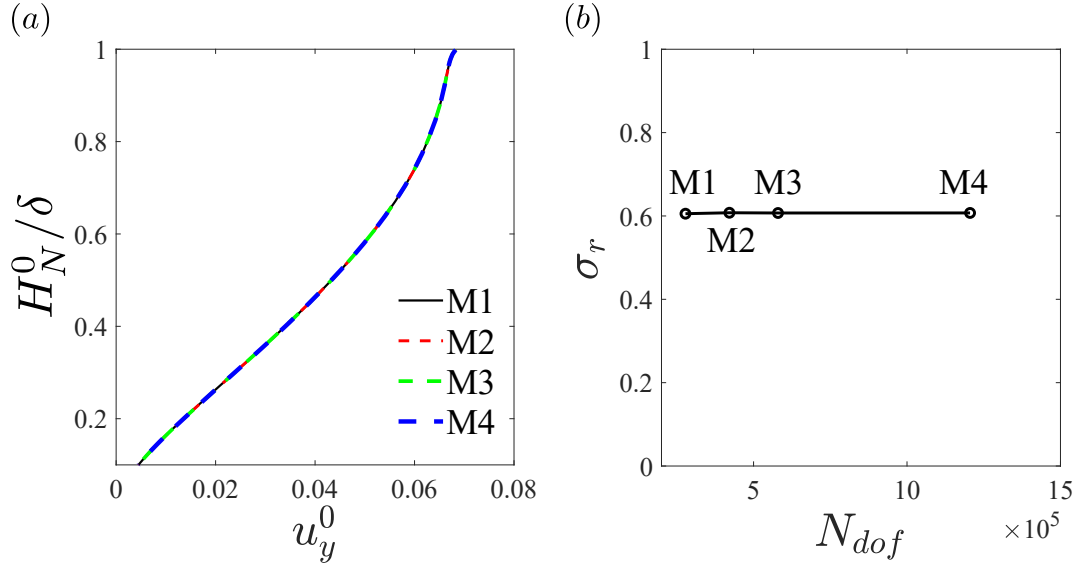


Figure 4.15: Mesh convergence proof for $Oh \rightarrow \infty$, $Bo = 0.05$, $\delta/\beta = 0.3$: (a) base flow; H_N^0/δ vs u_y^0 ; (b) linear stability analysis; σ_r^{max} vs N_{dof} . All of the results presented in this manuscript are obtained for M3.

5 Stability of liquid film coating a horizontal cylinder: capillary and potential interplay

Shahab Eghbali[†], S. Djambov¹ and F. Gallaire¹

¹ Laboratory of Fluid Mechanics and Instabilities, École Polytechnique Fédérale de Lausanne, Lausanne CH-1015, Switzerland

In preparation

Authors' contributions S.E. and F.G. conceived the project. S.E. performed the stability analysis. S. D. and S.E. performed together the transient growth analysis. All authors actively participated to the theoretical developments, analysis and interpretation of the results. S.E. and S.D. wrote the manuscript, guided by F.G..

In this chapter, we study the drainage of a viscous liquid film coating the outside of a solid horizontal cylinder, where gravity acts vertically. We focus on the limit of large Ohnesorge numbers Oh , where inertia is negligible compared to viscous effects. We first study the evolution of the axially invariant draining flow, initiated at rest with uniform film thickness δ . Non-linear simulations indicate that for each δ , there is a threshold in the Bond number (Bo , which compares the gravitational effects with surface tension) above which the draining liquid bulk ruptures. This critical Bo is found to scale inversely with δ , below which a quasi-stationary pendant liquid curtain is sustained below the cylinder by surface tension. The interface of the pendant curtain is unconditionally linearly unstable and is prone to Rayleigh-Plateau-like, capillarity-driven, and Rayleigh-Taylor, gravity-driven, instabilities. The linear stability of the quasi-static state along with an energy analysis of the unstable mode illustrates that while the Rayleigh-Taylor instability is always present, capillary effects dominate the instability at small Bo , which promotes the formation of pearls enveloping the cylinder. In contrast, at large Bo , capillarity acts in a stabilising way and the instability is purely gravity-driven, forming vertical fingers. We present the asymptotic energy repartition representing the different physical mechanisms at play in the instability of the saturated curtains for a wide range of $\{Bo, \delta\}$. The results of the linear analysis confirm the pre-existing non-linear simulations of Weidner et al. (1997) in the limit of a thin film and extend the results for thick films. Additionally, based

on the volume made available for droplet growth by the development of the most linearly amplified wavelength, we build a phase diagram that predicts the final patterns emerging from the pendant curtain, namely an array of saturated pearls or pendant drops or the onset of three-dimensional droplet pinch-off. Furthermore, a transient growth analysis accounting for the time-evolution of the base state towards a saturated curtain conclusively demonstrates that the initial flow evolution does not result in altering the most amplified wavelength, thus rationalising *a posteriori* the asymptotic analysis to predict the fate of the three-dimensional patterns.

Keywords: coating, Rayleigh-Taylor instability, Rayleigh-Plateau instability, surface tension, linear stability analysis, interface, transient growth

5.1 Introduction

Gravity-driven liquid films coating the outer side of a solid surface are ubiquitous in nature. Some daily-life examples are dew covering the strings of spider silk (Elettro et al., 2016), raindrop spread and accumulation around tree branches (Herwitz, 1987), and lava flow on volcanoes (Kilburn, 2000), to name a few. Such a flow is also of interest for several practical applications, for instance in coating industries (Quééré, 1999; Shen et al., 2002; Duprat et al., 2007), painting (Blair, 1969; Zenit, 2019), vapor absorption (Chinju et al., 2000; Grünig et al., 2012; Hosseini et al., 2014; Ding et al., 2018a) and desalination (Sadeghpour et al., 2019), shell fabrication (Lee et al., 2016) and heat exchangers (Zeng et al., 2017, 2018). The motion of the coating liquid film may be influenced by several factors, most chiefly, the solid surface geometry, and gravitational, capillary, and viscous forces. The dynamics of coating film flows, their instabilities, and subsequent pattern formation have gained attention in the last decades (Eggers and Villermaux, 2008; Gallaire and Brun, 2017).

A particular coating flow configuration is the gravity-driven flow around a horizontal solid cylinder. The interface of this draining film is prone to several instabilities which have been studied extensively, both numerically and experimentally. A vast majority of the numerical analyses have focused on the thin film limit and exploited the lubrication approximation (Oron et al., 1997). Balestra et al. (2019) for instance investigated the conditions for fingering instability to occur during the spreading of a thin film over a partially wetting horizontal cylinder. Several other studies addressed the liquid motion, film thickness, and the centrifugal instability of a liquid-coated cylinder rotating around its axis (Hansen and Kelmanson, 1994; Peterson et al., 2001; Ashmore et al., 2003; Evans et al., 2004; Li and Kumar, 2018). However, surprisingly, the coating flow around a fully wetting horizontal cylinder, in absence of rotation, has received little attention. Reisfeld and Bankoff (1992) investigated the two-dimensional isothermal and non-isothermal evolution of a thin liquid film of initially uniform thickness around a stationary horizontal cylinder. Their study describes the flow as the drainage of the liquid film around the cylinder that leads to the formation of a pendant liquid curtain at the bottom of the cylinder. They also investigated the shape variation of the pendant interface as a function of the thermal properties of the flow. Later, using non-linear simulations of a similar

isothermal flow configuration, Weidner et al. (1997) demonstrated the three-dimensional temporal evolution of the flow. Initially perturbed by a low-level white noise, they depicted the flow evolution in four phases: First, the axially invariant liquid bulk is pulled off without any evidence of instabilities. After a while past the establishment of a pendant curtain, the second phase starts with the appearance of growing small-amplitude longitudinal wavy perturbations at the bottom of the interface. The third phase evidences non-linearities that affect the growth of these wavy patterns and lead to the formation of large drops separated axially by very thin liquid ridges, as well as possible smaller satellite drops. In the fourth phase, the satellite drops coalesce into bigger drops and the interaction between single drops ceases. Weidner et al. (1997) highlighted that in the limit of small cylinder diameter with respect to the capillary length, where surface tension is important, perturbations lead to an upward motion of the flow that results in pierced droplets surrounding the cylinder, hereafter *pearls*. Later, Weidner (2013) reported a similar reversal of drop formation due to surface tension modification in the presence of surfactants.

While these studies are limited to a thin film layer, where the lubrication approximation holds, the formation of a collected liquid bulk underneath the cylinder may violate the thin-film assumption. Weidner et al. (1997) reasoned in analogy with a static pendant drop solution, where except for highly curved regions of the interface, a thin-film approximation results in a fair prediction of the curtain interface. remarkably, at the south pole of the cylinder that is the thickest region, exhibits a good accordance. Furthermore, despite their effort to apply an initial white noise to the film, the amplification of perturbations during the first phase (liquid pull-off), and its potential influence on the final droplet size are not well understood. Characteristics of the emerging patterns and their shape strongly resemble those of the classical Rayleigh-Taylor instability (Rayleigh, 1882; Taylor, 1950) and capillary instability, which can be considered as an extension of the Rayleigh-Plateau instability (Plateau, 1873; Rayleigh, 1878) on a fibre (Quéré, 1999).

The present study revisits the flow configuration as in Weidner et al. (1997) from an arbitrary thick-film viewpoint and aims at linking the pattern formation in such a flow with the linear interplay between the capillary-driven and gravity-driven instabilities. This aim is pursued by means of the linear stability analysis of the quasi-static pendant liquid curtain for a wide range of parameters. Additionally, we examine the amplification of the initial perturbations during the liquid drainage around the cylinder by means of transient growth analysis and address its effects on the pattern formation.

This paper is structured as follows. The methodology is detailed in §5.2. The problem formulation and governing equations are presented in §5.2.1, from which the base flow is deduced and discussed in §5.2.2. In §5.2.3, the formulation for the stability analysis and the linearised governing equations are elaborated. In §5.2.4 the formulation of the transient growth analysis is detailed. The numerical methods are presented in §5.2.5. In §5.3, the results of the stability and transient growth analyses are presented. In §5.3.1 the influence of the Bond number on the characteristics of the flow stability is summarised. In §5.3.2, the flow is investigated

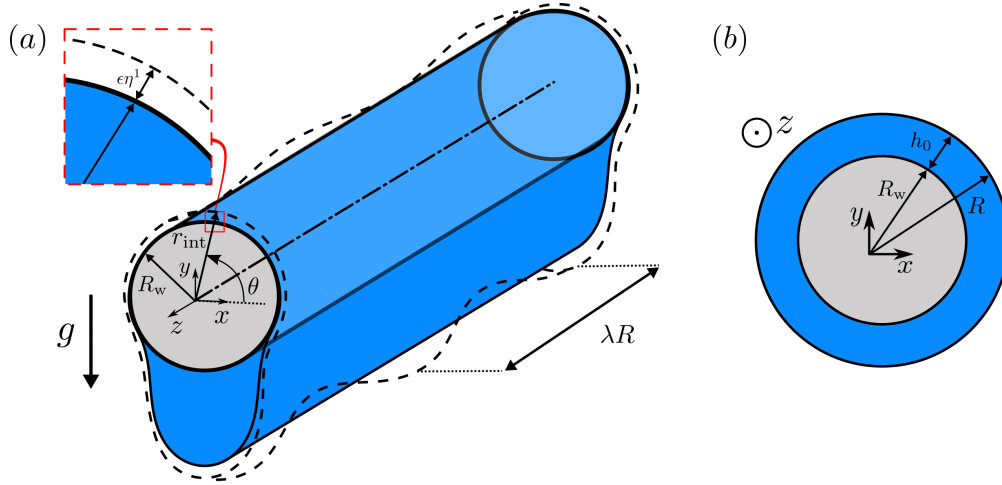


Figure 5.1: (a) Schematic of the liquid film coating the outside of a horizontal cylinder and the geometrical parameters. The thick solid black line shows the cylinder wall of the radius R_w , centred at $(0, 0, 0)$. The liquid-gas interface is shown in the thin solid black line. Grey colour marks the interior cross-section of the solid cylinder. The dashed black line represents the perturbed liquid-gas interface of the local radius r_{int} and axial wavelength λR . The inset shows the zoomed cross-section of the perturbed interface. Gravity acts vertically, perpendicular to the tube axis; (b) The initial $x - y$ cross-section of the liquid column.

from an energy perspective, and the base flow and the perturbed flow's energy balance are detailed in §5.3.2 and §5.3.2, respectively, followed by the obtention of an asymptotic energy diagram in §5.3.2. The linear stability phase diagram and the large-time pattern formation are discussed in §5.3.3. Finally, the results of the transient growth analysis are presented in §5.3.4 where conclusions are drawn by contrasting the transient and the stability around the saturated pendant curtain analyses.

5.2 Governing equations and methods

5.2.1 Problem formulation

The outer wall of a rigid and immobile solid circular cylinder of radius R_w is coated with a viscous liquid film. The schematic of the flow is presented in figure 5.1(a). The standard Cartesian coordinates (x, y, z) are considered with the origin concentric with the solid cylinder. In-plane coordinates are (x, y) , and the gravity acceleration \mathbf{g} , points in the $-y$ direction. We consider a Newtonian liquid of constant dynamic viscosity μ , surface tension γ , and density ρ , surrounded by an inviscid immobile gas. The interface radius r_{int} is parametrised in cylindrical coordinates (r, θ, z) as $\mathcal{F} = r - r_{\text{int}}(t, \theta, z) = 0$, using the same origin as the Cartesian one. The liquid-gas interface is initially concentric with the cylinder and the liquid film thickness is constant around the periphery of the wall, $h_0 = R - R_w$, where R denotes the initial interface radius (figure 5.1(b)). At dimensionless time $t = 0$, the initial condition writes $r_{\text{int}}(0, \theta, z) = R$.

The dimensionless state vector $\mathbf{q} = (\mathbf{u}, p, \mathcal{R}_{\text{int}})^T$ describes the liquid motion at any instance t , where $\mathbf{u}(t, x, y, z) = (u_x, u_y, u_z)^T$ denotes the three-dimensional velocity field, $p(t, x, y, z)$ denotes the pressure, and $\mathcal{R}_{\text{int}} = r_{\text{int}}/R$ denotes the dimensionless interface radius. We choose the initial interface radius R as the length scale and its static pressure jump as the pressure scale. The intrinsic velocity scale associated with a viscous liquid film of thickness h_0 falling under its weight, presented by Duclaux et al. (2006), is chosen to make the state vector and the governing equations dimensionless. Additionally, the advecting time scale is constructed based on the aforementioned velocity and length scales as:

$$\begin{aligned} \mathcal{L} = R, \quad \mathcal{U} &= \frac{\rho g h_0^2}{\mu} = \frac{\rho g R^2}{\mu} (1 - \beta)^2, \\ \mathcal{P} &= \frac{\gamma}{R}, \quad \mathcal{T} = \frac{\mathcal{L}}{\mathcal{U}} = \frac{\mu}{\rho g R} (1 - \beta)^{-2}, \end{aligned} \quad (5.1)$$

where $\beta = R_w/R$ denotes the dimensionless wall radius. Consequently, the dimensionless value of the initial film thickness is expressed as $\delta = h_0/R = 1 - \beta$. The flow is governed by the conservation of mass and momentum equations which in dimensionless form read

$$\nabla \cdot \mathbf{u} = 0, \quad (5.2)$$

$$\left(\frac{Bo}{Oh} \right)^2 \delta^4 (\partial_t + \mathbf{u} \cdot \nabla) \mathbf{u} = \nabla \cdot \underline{\underline{\tau}} - Bo \mathbf{e}_y, \quad (5.3)$$

respectively, where ∂_j denotes the partial derivative with respect to quantity j , and the stress tensor $\underline{\underline{\tau}}$ is expressed as

$$\underline{\underline{\tau}} = -p\mathbf{I} + Bo \delta^2 (\nabla \mathbf{u} + \nabla \mathbf{u}^T). \quad (5.4)$$

Two other dimensionless numbers appear in the governing equations: *Ohnesorge* number, $Oh = \mu / \sqrt{\rho \gamma R}$, compares the viscous and inertial forces. *Bond* number, $Bo = \rho g R^2 / \gamma$, compares the gravitational and surface tension forces. Our study addresses the limit of inertialess flow where $(Bo/Oh)^2 \delta^4 \ll 1$. One can re-express $(Bo/Oh)^2 \delta^4$ as $Re \delta^2$ where the *Reynolds* number, $Re = \rho \mathcal{U} \mathcal{L} / \mu$, is constructed upon the same scales presented in (5.1).

The no-slip boundary condition, $\mathbf{u} = \mathbf{0}$, is applied on the solid wall, at $r = \beta$. On the shear-free fluid-gas interface, the kinematic and dynamic boundary conditions write

$$\partial_t \mathcal{R}_{\text{int}} + \mathbf{u} \cdot \nabla \mathcal{R}_{\text{int}} = \mathbf{u} \cdot \mathbf{e}_r \quad \text{at } r = \mathcal{R}_{\text{int}}, \quad (5.5)$$

$$\underline{\underline{\tau}} \mathbf{n} = -\kappa \mathbf{n} \quad \text{at } r = \mathcal{R}_{\text{int}}, \quad (5.6)$$

respectively, where \mathbf{e}_r denotes the unit radial vector, $\mathbf{n} = \nabla(r - \mathcal{R}_{\text{int}}) / \|\nabla(r - \mathcal{R}_{\text{int}})\|$, denotes the interface unit normal vector pointing outward from the origin of the coordinate system,

$\|\cdot\|$ denotes the Euclidean norm, and $\kappa = \nabla \cdot \mathbf{n}$ denotes the mean curvature of the interface. To build intuition about the flow characteristics and before detailing the stability analysis and numerical method, we illustrate the reference flow in §5.2.2.

5.2.2 Base flow

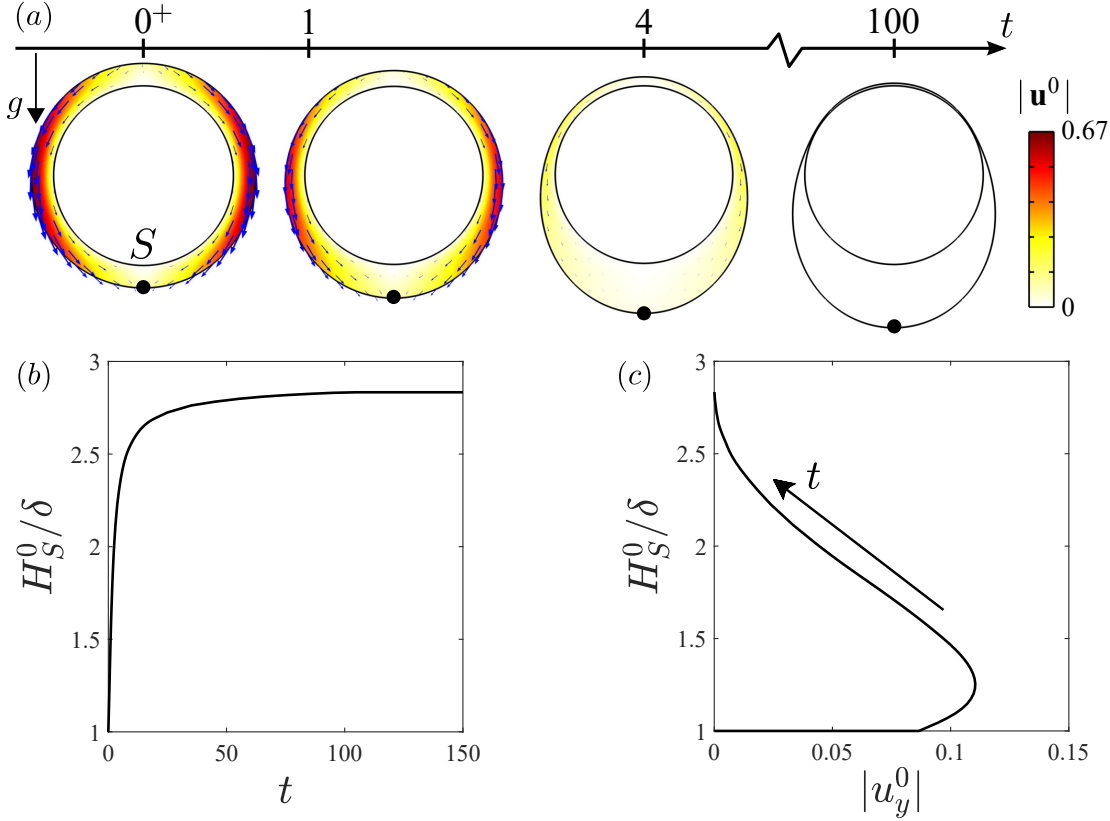


Figure 5.2: Base flow evolution for $Oh \rightarrow \infty$, $Bo = 0.4$, $\delta = 0.2$. (a) Snapshots of the flow field: colour map shows the in velocity magnitude, arrows show the liquid velocity field, and the point S marks the south pole of the bubble, $\theta_S = 3\pi/2$. (b) Temporal variation of the relative liquid film thickness at the pole $H_S^0/\delta = (\mathcal{R}_{\text{int}}^0(\theta_S) - \beta)/\delta$. (c) Film thickness variation as a function of the vertical velocity at the pole.

The *base flow*, denoted by \mathbf{q}^0 , is the transient solution of the non-linear conservation equations (5.2)-(5.6) where the fluid is initially assumed at rest with constant initial pressure $p^0(t=0) = 1$ and $\mathcal{R}_{\text{int}}^0 = 1$. Due to the non-linear nature of the interface conditions, finding an analytical solution for such a flow is challenging. Hence, the temporal evolution of the flow is computed numerically (see §5.2.5 for details). Some snapshots from the base flow evolution are shown in figure 5.2 for an exemplary case of $\delta = 0.2$, and an intermediate Bond number $Bo = 0.4$. The dynamics of the base flow, presented in figure 5.2(b-c), can be characterised by quantifying the relative liquid film thickness $H^0/\delta = (\mathcal{R}_{\text{int}}^0 - \beta)/\delta$ at the south pole cylinder, $\theta = 3\pi/2$, and its vertical velocity. This point is hereafter referred to as the pole, where the

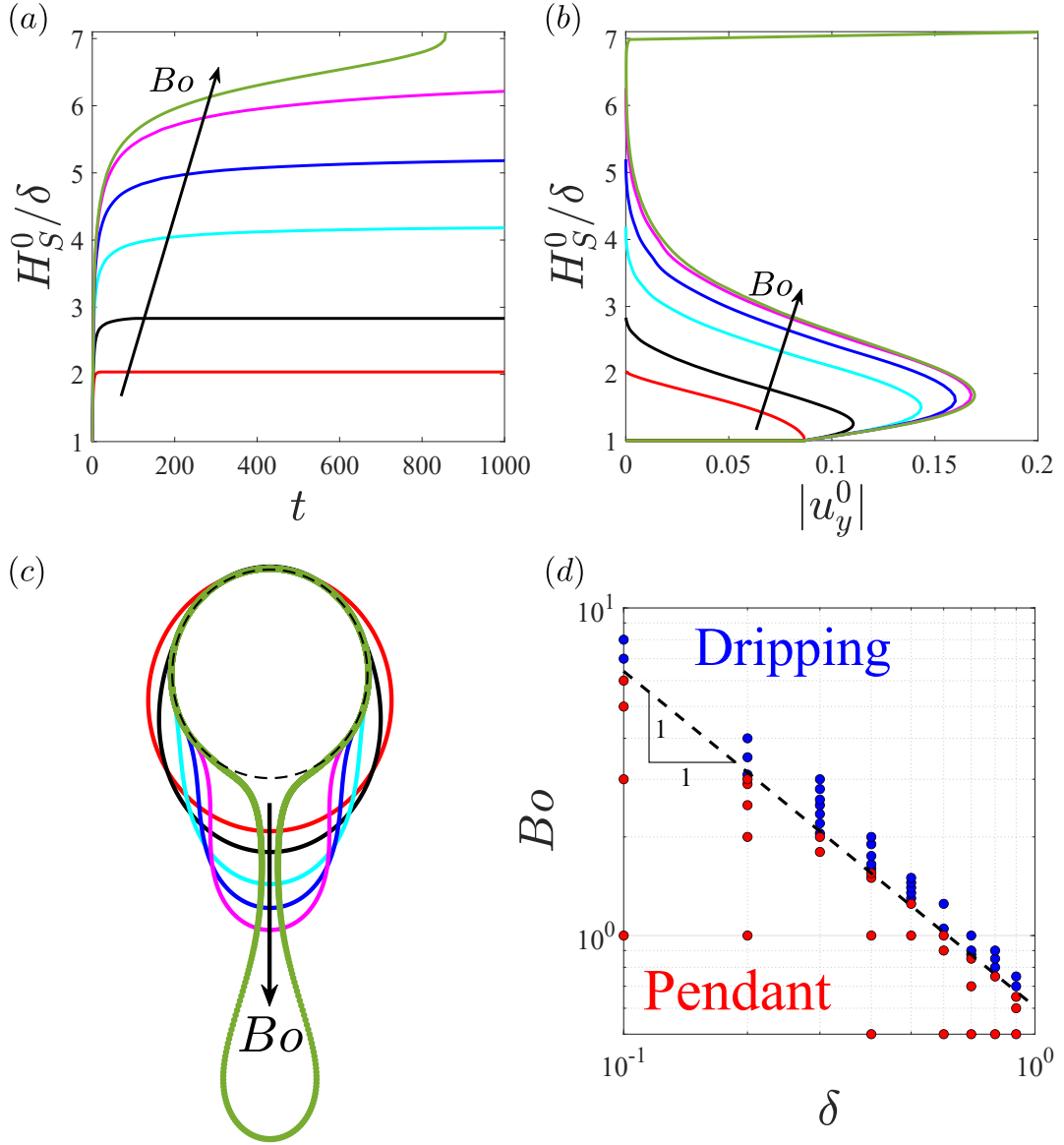


Figure 5.3: Influence of the surface tension. The base flow dynamics for $Oh \rightarrow \infty, \delta = 0.2, Bo = \{0.01, 0.4, 1.6, 2.5, 3, 3.1\}$: (a) Temporal variation of the relative liquid film thickness at the pole. (b) Film thickness variation as a function of the vertical velocity at the pole. (c) Large-time interface of the pendant curtain at $Bo = \{0.01, 0.4, 1.6, 2.5, 3\}$, and the dripping curtain at $Bo = 3.1$ (green) for the same flows presented in panels (a-b). The black dashed circle shows the cylinder. (d) Two-dimensional pendant vs dripping diagram in the $\delta - Bo$ plane: the black dashed line corresponds to the best fit to the two-dimensional pendant to dripping transition: $Bo = 0.61\delta^{-1}$.

strongest gravitational effects are expected. Drainage begins with an immediate liquid pull-off around the solid cylinder that decays with time. The liquid body forms a two-dimensional quasi-static pendant curtain as $t \rightarrow \infty$.

Drainage dynamics are significantly influenced by surface tension and gravity effects, i.e. by Bo . Figure 5.3 presents the influence of the Bond number. By increasing Bo , i.e. weakening the effect of surface tension against gravity, flow initially accelerates before decaying and the formation of the quasi-static curtain delays (figure 5.3(a)). Exceeding a critical Bo value, the interface cannot sustain the liquid weight anymore and the pole accelerates downward sharply (green line in figure 5.3(a-b)), thus causing a two-dimensional rupture. Figure 5.3(c) shows the interface of the quasi-static pendant curtain for several Bo values as well as one example of dripping bulk after re-accelerating. While small Bo numbers sustain the quasi-circular cross-section of the curtain, increasing Bo results in a stretched interface in the direction of gravity. The green line in figure 5.3(c) depicts the falling liquid interface right after the pole acceleration (at $t = 855.8$). Figure 5.3(d) presents the region of saturation towards a static pendant curtain in the $\delta - Bo$ plane. This phase diagram is obtained by following the non-linear drainage simulations until the maximal flow velocity magnitude drops below 10^{-5} (pendant) or the occurrence of the large-time pole acceleration (dripping). It was verified for some marginal sub-critical pairs of $\{Bo, \delta\}$ that lowering the velocity threshold down to 10^{-7} does not affect the critical parameters at the transition between these two behaviours. The dripping occurs if $Bo > 0.61\delta^{-1}$, suggested by the best fit to the data from our simulations.

We now follow a scaling argument to rationalise the obtained threshold. In the case of a pendant curtain, the capillary force per unit axial length $\propto 2\gamma$ overcomes the bulk weight, $\pi\rho g R^2\delta(1 + \beta)$. This comparison implies the dripping threshold as $Bo > (2/\pi)\delta^{-1}(1 + \beta)^{-1}$ where $2/\pi \approx 0.64$. In the thick-film limit, $\beta \ll 1$ (remember that $\delta = 1 - \beta$), the dripping threshold approaches $0.64\delta^{-1}$ which is in good agreement with our numerics. Following this scaling argument, by approaching the thin-film limit, $\beta \rightarrow 1$, the dripping threshold should approach $Bo > 0.32\delta^{-1}$. However, this scaling contradicts the numerical observation. One might propose a correction to this scaling argument by taking into account the tangential direction at which the minimum capillary force is applied. However, such a correction was found unsuccessful, too. Note that rupture occurs through the pole acceleration, and necking takes place at some distance below the cylinder, where surface tension fails to withstand merely the portion of the liquid weight that accelerates underneath the neck (see the green interface in figure 5.3(c)).

5.2.3 Linear stability analysis of the pendant curtain

To conduct the *linear stability analysis* of the quasi-static pendant curtain, presented in §5.2.2, the state vector $\mathbf{q} = (\mathbf{u}, p, \mathcal{R}_{\text{int}})^T$ is decomposed into the sum of the steady saturated base flow solution \mathbf{q}_{∞}^0 (subscript ∞ denotes large-time evaluation), and the infinitesimal time-dependent *perturbation* $\mathbf{q}^1 = (\mathbf{u}^1, p^1, \eta^1)^T$, i.e.

$$\mathbf{q} = \mathbf{q}_{\infty}^0 + \epsilon \mathbf{q}^1 + \mathcal{O}(\epsilon^2), \quad \epsilon \ll 1, \quad (5.7)$$

where the amplitude ϵ is small. The normal mode of the perturbation \mathbf{q}^1 with the longitudinal wavenumber k (associated with the wavelength $\lambda = 2\pi/k$) reads

$$\mathbf{q}^1 = \bar{\mathbf{q}}(x, y) \exp[\sigma t + ikz] + \text{c.c.}, \quad (5.8)$$

where c.c. denotes the complex conjugate. All other functions in terms of the state vector can be decomposed in a similar fashion. Namely, $\underline{\tau} = \underline{\tau}^0 + \epsilon \underline{\tau}^1$, $\mathbf{n} = \mathbf{n}^0 + \epsilon \mathbf{n}^1$ and $\kappa = \kappa^0 + \epsilon \kappa^1$. (For further details about the formulation of \mathbf{n}^1 and κ^1 , see §4.5.3 in **chapter 4**.) In the asymptotic limit of large times, a normal eigenmode perturbation with complex pulsation factor $\sigma = \sigma_r + i\sigma_i$, is *unstable* if $\sigma_r > 0$. An unstable eigenmode grows exponentially in time with the growth rate σ_r . (Unless otherwise noted, the indices r and i denote the real and imaginary parts of a complex number, respectively.) After casting the perturbed state of (5.7) into the governing equations (5.2)-(5.3), with the static pendant curtain base state $\mathbf{q}_\infty^0 = (\mathbf{u}^0, p^0, \mathcal{R}_{\text{int}}^0)^T$, and neglecting the higher orders in ϵ , the linearised equations can be expressed as

$$\nabla \cdot \mathbf{u}^1 = 0, \quad (5.9)$$

$$\left(\frac{Bo}{Oh}\right)^2 \delta^4 (\partial_t \mathbf{u}^1 + (\mathbf{u}^0 \cdot \nabla) \mathbf{u}^1 + (\mathbf{u}^1 \cdot \nabla) \mathbf{u}^0) = \nabla \cdot \underline{\tau}^1. \quad (5.10)$$

The corresponding boundary conditions are as follows. On the solid cylinder boundary, $r = \beta$, the no-slip condition implies $\tilde{\mathbf{u}} = \mathbf{0}$. As the geometry of the perturbed flow is unknown, the interface conditions (5.5)-(5.6), applied on the perturbed liquid interface $r = \mathcal{R}_{\text{int}}^0 + \epsilon \eta^1$, should be projected radially onto the base interface, $r = \mathcal{R}_{\text{int}}^0$, and ultimately linearised; a process called *flattening* (see (5.29) in appendix 5.5.1). The kinematic condition, once linearised implies

$$\sigma \tilde{\eta} + \underbrace{\left(-\partial_r u_r^0 + \frac{\partial_r u_\theta^0 \partial_\theta \mathcal{R}_{\text{int}}^0}{\mathcal{R}_{\text{int}}^0} - \frac{u_\theta^0 \partial_\theta \mathcal{R}_{\text{int}}^0}{(\mathcal{R}_{\text{int}}^0)^2} \right) \tilde{\eta} + \frac{u_\theta^0}{\mathcal{R}_{\text{int}}^0} \partial_\theta \tilde{\eta} + \frac{\partial_\theta \mathcal{R}_{\text{int}}^0}{\mathcal{R}_{\text{int}}^0} \tilde{u}_\theta}_{-\mathbf{G}^0 \tilde{\eta}} = \tilde{u}_r, \quad \text{at } r = \mathcal{R}_{\text{int}}^0, \quad (5.11)$$

where $(u_r^0, u_\theta^0)^T$ and $(\tilde{u}_r, \tilde{u}_\theta)^T$ denote the velocity vectors of the base state and perturbations, respectively, represented in the cylindrical coordinates. Even though in the case of a quasi-static pendant curtain, $\mathbf{u}^0 \approx \mathbf{0}$, we keep the corresponding terms in the linearised equations (5.11) and the following equations, since they will be needed in the transient growth analysis, to be presented in §5.2.4. Introducing a normal eigenmode of the form (5.8) into (5.9)-(5.10), combined with (5.11), leads to a generalised eigenvalue problem for σ and $\bar{\mathbf{q}}$ as

$$\mathbf{L} \bar{\mathbf{q}} + \text{c.c.} = \sigma \mathbf{B} \bar{\mathbf{q}} + \text{c.c.}, \quad (5.12)$$

where the linear operators \mathbf{L} and \mathbf{B} can be expressed as

$$\begin{aligned} \mathbf{L} &= \begin{bmatrix} \left(\frac{Bo}{Oh}\right)^2 \delta^4 \mathbf{F}^0 + Bo \delta^2 (\tilde{\nabla} \cdot (\tilde{\nabla} + \tilde{\nabla}^T)) & -\tilde{\nabla} & \mathbf{0} \\ \tilde{\nabla} \cdot & 0 & 0 \\ \left(\mathbf{e}_r - \frac{\partial_\theta \mathcal{R}_{\text{int}}^0}{\mathcal{R}_{\text{int}}^0} \mathbf{e}_\theta\right) \cdot & 0 & \mathbf{G}^0 \end{bmatrix}, \\ \mathbf{B} &= \begin{bmatrix} \left(\frac{Bo}{Oh}\right)^2 \delta^4 \mathbf{I} & \mathbf{0} & \mathbf{0} \\ \mathbf{0} & 0 & 0 \\ \mathbf{0} & 0 & 1 \end{bmatrix}, \end{aligned} \quad (5.13)$$

where $\mathbf{F}^0 \tilde{\mathbf{u}} = -((\mathbf{u}^0 \cdot \tilde{\nabla}) \tilde{\mathbf{u}} + (\tilde{\mathbf{u}} \cdot \nabla) \mathbf{u}^0)$. Here, $(\mathbf{e}_r, \mathbf{e}_\theta, \mathbf{e}_z)$ denote the unit direction vectors in the cylindrical coordinates (r, θ, z) used for parameterising the interface, and the gradient operators and the velocity gradient tensors in the Cartesian coordinates read

$$\begin{aligned} \nabla &= (\partial_x, \partial_y, \partial_z)^T, & \nabla \mathbf{u}^0 &= \begin{bmatrix} \partial_x u_x^0 & \partial_y u_x^0 & 0 \\ \partial_x u_y^0 & \partial_y u_y^0 & 0 \\ 0 & 0 & 0 \end{bmatrix}, \\ \tilde{\nabla} &= (\partial_x, \partial_y, ik)^T, & \tilde{\nabla} \tilde{\mathbf{u}} &= \begin{bmatrix} \partial_x \tilde{u}_x & \partial_y \tilde{u}_x & ik \tilde{u}_x \\ \partial_x \tilde{u}_y & \partial_y \tilde{u}_y & ik \tilde{u}_y \\ \partial_x \tilde{u}_z & \partial_y \tilde{u}_z & ik \tilde{u}_z \end{bmatrix}. \end{aligned} \quad (5.14)$$

The interface dynamic condition (5.6), once linearised, reads

$$\underline{\underline{\tau}}^0 \tilde{\mathbf{n}} + \tilde{\eta} \partial_r \underline{\underline{\tau}}^0 \mathbf{n}^0 + \underline{\underline{\tau}} \mathbf{n}^0 = -(\kappa^0 \tilde{\mathbf{n}} + \tilde{\kappa} \mathbf{n}^0), \quad \text{at } r = \mathcal{R}_{\text{int}}^0. \quad (5.15)$$

(For further details on the derivation of the interface conditions and their implementation, see appendices 5.5.1 and 5.5.2, respectively.)

5.2.4 Transient growth analysis

As the base flow presented in §5.2.2 evolves temporally, we perform a *transient growth analysis* to study the evolution of the perturbations from the initial state until the formation of the pendant curtain. In contrast with the linear stability analysis, the transient growth analysis accounts for the temporal dependency of both the base flow and the perturbation.

We follow a similar procedure as in **chapter 4**; the perturbation is now written without imposing its exponential temporal evolution

$$\mathbf{q}^1 = \bar{\mathbf{q}}(t, x, y) \exp[ikz] + \text{c.c.}, \quad (5.16)$$

which is instead a straightforward extension of (5.12):

$$\mathbf{L}(t)\bar{\mathbf{q}} + \text{c.c.} = \mathbf{B}\frac{\partial \bar{\mathbf{q}}}{\partial t} + \text{c.c.}, \quad (5.17)$$

recalling that \mathbf{L} is parametrised by k . We seek an initial perturbation of the interface $\bar{\mathbf{q}}(0, x, y) = [\mathbf{0}, 0, \bar{\eta}(0)]^T$ that is the most amplified by (5.17) after a time $t = T$, where T is named the *temporal horizon*. Imperfect initial flow structure or experimental artifacts might project on this optimal one and might be greatly amplified, possibly triggering a non-linear regime and/or being directly comparable with the experimentally observed patterns, thus making the linear stability analysis results irrelevant. To this aim, we pursue the methodology proposed by Del Guercio et al. (2014), and take advantage of the fact that the base flow interface is axisymmetric at $t = 0$ (see figure 5.2) to expand $\bar{\eta}(0)$ as Fourier modes in θ as

$$\bar{\eta}(0) = \sum_{m=-N}^N \alpha_m e^{im\theta} = a_0 + \sum_{m=1}^N [a_m \cos(m\theta) + b_m \sin(m\theta)], \quad (5.18)$$

with $\alpha_{-m} = \alpha_m^*$, $a_0 = \alpha_0$, and for $m \geq 1$: $a_m = \alpha_m + \alpha_m^*$ and $b_m = i(\alpha_m - \alpha_m^*)$. Note that a_m, b_m (where $m = 0, 1, 2, \dots$) and $\bar{\eta}(0)$ are real-valued.

We then define $\bar{\eta}_m(t)$ as the evolved state at time t of the specific initial condition $\bar{\eta}_m(0) = e^{im\theta}$ for the interface. Thanks to the linearity of the evolution equation (5.17), the interface shape at $t = T$ simply reads

$$\bar{\eta}(T) = \sum_{m=-N}^N \alpha_m \bar{\eta}_m(T). \quad (5.19)$$

The associated interfacial energy density per spanwise wavelength is proportional to

$$e(T) = \frac{k}{2\pi} \oint_{S(T)} \int_0^{2\pi/k} |\bar{\eta}(T) e^{ikz} + \text{c.c.}|^2 dz ds = 2\mathbf{a}^T \mathbf{E}(T) \mathbf{a}, \quad (5.20)$$

where $\oint_{S(T)} ds$ represents the closed line integration along the time-dependent base state interface, $\mathbf{E}(T)$ is a real-valued, symmetric, strictly positive definite $(2N+1) \times (2N+1)$ matrix, derived in appendix 5.5.3, and

$$\mathbf{a} = [a_N, a_{N-1}, \dots, a_1, \sqrt{2}a_0, b_N, b_{N-1}, \dots, b_1]. \quad (5.21)$$

In this manner, the *optimal transient gain* $G(T)$, defined as

$$G(T) = \max_{\mathbf{a}} \frac{e(T)}{e(0)} = \pi^{-1} \frac{\mathbf{a}^T \mathbf{E}(T) \mathbf{a}}{\mathbf{a}^T \mathbf{a}}, \quad (5.22)$$

is simply the largest eigenvalue of $\mathbf{E}(T)$ divided by π , and the associated eigenvector provides directly the Fourier mode coefficients of the optimal initial condition, where we used that $\mathbf{E}(0) = \pi \mathbf{I}$.

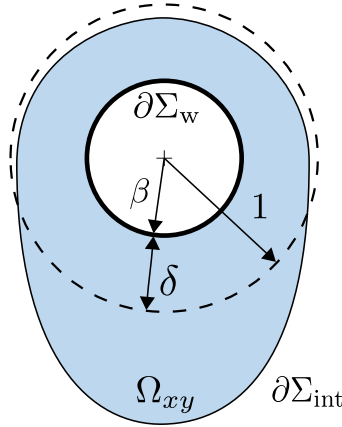


Figure 5.4: The numerical domain for computing the base flow, transient growth study, and linear stability analysis. Here, Ω_{xy} denotes the liquid bulk. The boundaries of the numerical domain are denoted by $\partial\Omega_{xy} = \partial\Sigma_w \cup \partial\Sigma_{int}$, where $\partial\Sigma_w$ represents the exterior wall of the cylinder with the radius of β , and $\partial\Sigma_{int}$ represents the gas-liquid interface. The cross-section of the interface is initially a circle of unit radius, concentric with the cylinder (sketched in black dashed line).

5.2.5 Numerical method

The base flow, transient growth, and linear stability analyses are carried out numerically by the finite element software COMSOL MultiphysicsTM. A triangular moving mesh is generated on the two-dimensional domain shown in figure 5.4. The grid size is controlled by the vertex densities on the boundaries $\partial\Sigma_w$ and $\partial\Sigma_{int}$. The variational formulation of the base flow equations (5.2)-(5.6), linear stability equations (5.12), and linearised Navier-Stokes equations (5.17) are discretised spatially using quadratic (P2) Lagrange elements for the geometrical shape function, \mathbf{u}^0 , $\tilde{\mathbf{u}}$, $\tilde{\eta}$ and $\tilde{\eta}$, and linear (P1) Lagrange elements for p^0 , \tilde{p} , and \bar{p} . This discretisation results in approximately 400'000 degrees of freedom, N_{dof} , for each step of the base flow, linear stability, and transient growth analyses.

First, the base flow is computed using the laminar two-phase flow module incorporated with the moving mesh module. The numerical time step is determined by the Backward differentiation formula with maximum differentiation order of 2. The solver is initialised by the Backward Euler consistent initialisation with an initial step fraction of 10^{-9} . At each time step, Newton's method is used to solve the non-linear equations, where the relative tolerance for the iterative solver convergence is set to 10^{-6} . In order for the base flow solver to capture the rupture, the kinematic condition (5.5) is replaced by its equivalent form readily implemented in the built-in fluidic module of COMSOL MultiphysicsTM. It enforces instead $\mathbf{u} \cdot \mathbf{n} = \mathbf{u}_{mesh} \cdot \mathbf{n}$, at $\partial\Sigma_{int}$, where \mathbf{u}_{mesh} denotes the moving mesh velocity. Following the computed base flow, the first solution after the maximal velocity falls below 10^{-5} is considered as the static pendant curtain. After extracting the flow field and geometrical characteristics of the base interface, linear perturbation analyses are conducted. For the linear stability analysis, the generalised eigenvalue problem (5.12) is solved for the static pendant curtain using the shift-invert Arnoldi

method. For the transient growth analysis, the linearised conservation equations (5.17) are solved over the corresponding time horizon with a dimensionless time step of 0.1. Then, the resulting propagator matrices are computed and imported to MatlabTM, where the optimal transient gain (5.22) is computed. (For more details on the development of the variational formulation, implementation of the linearised Navier-Stokes and linear stability eigenvalue problem, and their corresponding boundary conditions see appendix 5.5.2.)

The computation time for obtaining the base flow for a given set of parameters, followed by the stability analysis for ~ 20 values of k , is of the order of an hour on a single Intel core at 3.6 GHz. For the transient growth analysis, the computation of the propagator matrices with $-5 \leq m \leq 5$ over 10 values of k and dimensionless temporal horizon of dozen units, and the maximal gain calculation take place in the order of a few days in total. Both the base flow and stability analysis model are validated with the existing solutions in the literature. (For more details about the series of validation tests see appendix 5.5.4.)

5.3 Results

The results of the linear stability analysis and transient growth analysis are presented hereafter. To begin with, an overview of the stability of the pendant curtain and the influence of Bo are presented in §5.3.1. Then both the base flow and the perturbations feeding on the pendant curtain are further discussed from an energy viewpoint in §5.3.2, enabling us to investigate the contributions of different physical mechanisms in the formation of the pendant curtain and its instability, and to complement the stability diagram by identifying regions where either the Rayleigh-Plateau or the Rayleigh-Taylor instabilities dominate. In §5.3.3, the most asymptotically amplified linear modes and the consequent pattern formation are discussed, followed by sketching the phase diagram of the pendant curtain predicted by the linear analysis. The transient growth of the perturbations before reaching the quasi-static state is detailed in §5.3.4 where the influence of the optimal perturbation amplification on the ultimate pattern formation is discussed.

5.3.1 Linear stability of the pendant curtain

In this section, we present the linear stability characteristics associated with the quasi-static pendant curtain coating the outside of a horizontal cylinder. We follow the same exemplary cases of $\delta = 0.2$ the base flows of which are presented in §5.2.2. Each set of parameters exhibits only a single unstable mode whose *dispersion curve*, representing the growth rate $\sigma_r(k)$, is presented in figure 5.5(a). This mode is unstable within a range of wavenumbers $0 \leq k \leq k_c$, where k_c denotes the cut-off wavenumber, and exhibits a peak in its growth rate, σ_r^{max} , at an associated maximal wavenumber k_{max} . Starting from large surface tension compared to gravity, $Bo = 0.01$, increasing Bo results first in a decrease in σ_r^{max} (from $Bo = 0.01$ to $Bo = 0.4$) followed by a rebound for large Bo (for $Bo > 0.4$). The cut-off wavenumber k_c increases monotonously, whereas k_{max} increases up to a saturated value $k \approx 1.05$.

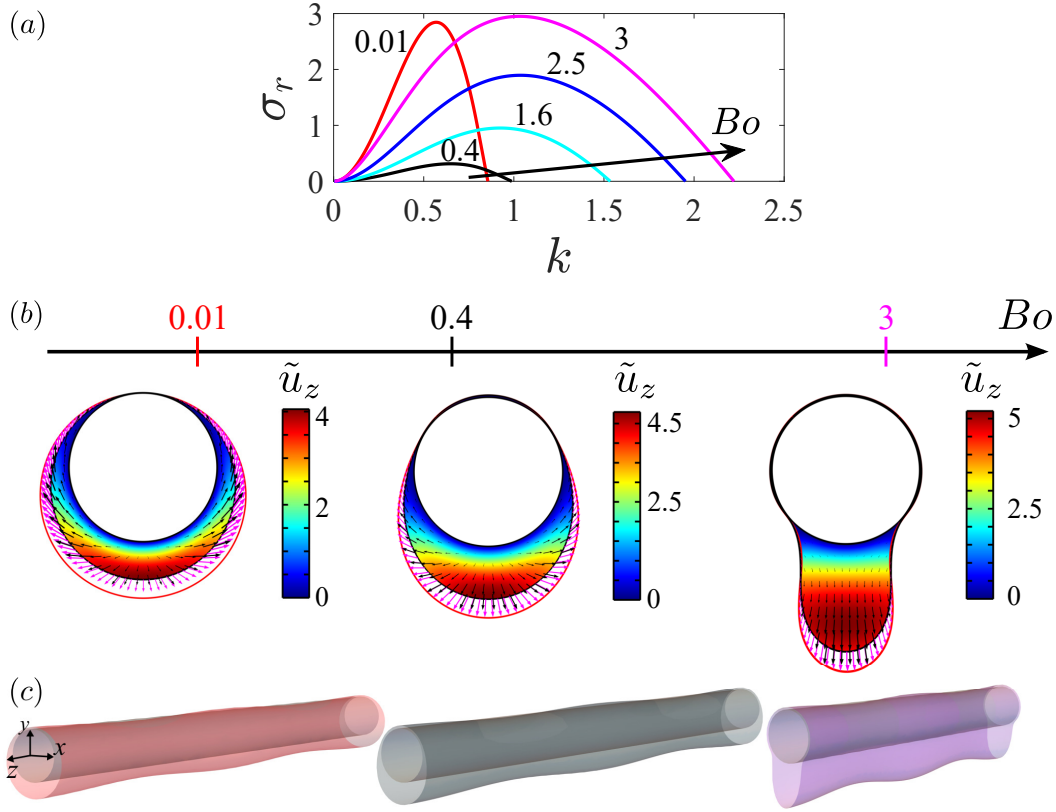


Figure 5.5: The influence of Bo on the linear stability of the pendant curtains whose base flows are presented in figure 5.3: (a) Dispersion curve of the unstable eigenmode; (b) Eigenvelocity fields and eigeninterfaces of the same unstable modes at k_{max} , corresponding to σ_r^{max} ; the color map presents the axial eigenvelocity, black arrows show the in-plane eigenvelocity field; magenta arrows show the eigenvelocity at the base interface, and the red line renders the base interface perturbed by an arbitrary amplitude; (c) The three-dimensional rendering of the asymptotically most amplified perturbed interfaces, shown in panel (b); $Oh \rightarrow \infty$, $\delta = 0.2$.

The perturbation eigenvelocity fields at k_{max} and three-dimensional rendering of the perturbed interface with an arbitrary amplitude are presented for $Bo = \{0.01, 0.4, 3\}$ in figure 5.5(b-c), respectively. Each eigenstate \tilde{q} is normalised with its RMS value, and its phase is corrected such that the axial velocity of the pole, $\tilde{u}_z(\theta = -\pi/2)$, becomes real-valued. The unstable mode features left/right symmetry, strong interface modulation at the bottom of the pendant curtain, and an immobile interface at the top of the cylinder, $\theta = \pi/2$. While intermediate and strong surface tension to gravity ratios, $Bo = \{0.01, 0.4\}$, evidence the flow reversal towards the top side of the cylinder, when gravity dominates at $Bo = 3$, interface perturbations take place only at the bottom of the pendant curtain, promoting vertical fingers underneath the cylinder. Similar patterns were reported through the non-linear simulations of Weidner et al. (1997) in the thin film limit with large surface tension. For one particular case of liquid roll-up, they observed that the non-linear evolution of the perturbations results in lower surface energy

at the cost of increasing the potential energy of the liquid. On the contrary, for one case of gravity dominance, the non-linear perturbation evolution was reported in favour of the potential energy reduction despite increasing the surface energy. These arguments give us the motivation to further study the base flow and linear perturbations from an energy perspective to quantify the effect of different physical mechanisms at play in the flow.

5.3.2 Energy analysis

In this section, we study the flow from an energy point of view in order to clarify the interactions between capillary, viscous, and gravitational effects, and to quantify their respective contributions to the formation and linear instability of a pendant curtain. Formerly, Hooper and Boyd (1983); Boomkamp and Miesen (1996); Kataoka and Troian (1997); Li et al. (2011) employed this method to evaluate and compare the role of different physical mechanisms on the temporal instability of various interfacial flows. Hereafter, the area increment in the bulk cross-section is denoted by $dA_{\Omega_{xy}}$. On the boundary j , the increment of the surface area is denoted by dA_{Σ_j} , and the increment of the arc length is denoted by ds .

Here, we study energy conservation in the flow, on different scales, from the base flow to the perturbations. We focus on the base flow presented in §5.2.2 and the unstable modes presented in §5.3.1. More precisely, the energy analysis sheds light on the balance of the energy rate, hereafter referred to as the *energy equation*, which for the inertialess gravity-driven flow down a horizontal cylinder can be expressed as

$$\underbrace{\iiint_{\Omega_{xy}} Bo \delta^2 \operatorname{tr}((\nabla \mathbf{u} + \nabla^T \mathbf{u}) \nabla \mathbf{u}) dV}_{\text{DIS}} + \underbrace{\iint_{\partial \Sigma_{\text{int}}} -(\underline{\tau} \mathbf{n}^0) \cdot \mathbf{u} dA_{\Sigma_{\text{int}}}}_{\text{BND}} + \underbrace{\iiint_{\Omega_{xy}} -Bo u_y dV}_{\text{POT}} = 0, \quad (5.23)$$

where the bulk integral is defined on the volume increment $dV = dA_{\Omega_{xy}} dz$, the surface integral is defined on the columnar surface with the cross-section $\partial \Sigma_{\text{int}}$ and axis in z direction (see figure 5.4), DIS denotes the rate of viscous dissipation in the bulk fluid, BND denotes the rate of interfacial work conducted by the fluid, and POT denotes the rate of change of gravitational potential energy. (For more details about the derivation of the energy equation, see appendix 5.5.5. Hereafter, for the ease of notation, we omit dV from volumetric integrals, $dA_{\Sigma_{\text{int}}}$ from boundary surface integrals, and ds from the one-dimensional boundary integrals.) The energy equation implies that the net rate of energy exchange in the flow is zero, where multiple physical mechanisms may contribute to energy release and consumption. The sign of each term in (5.23) indicates whether the energy is removed from (+) or released into (−) the flow by the respective mechanism.

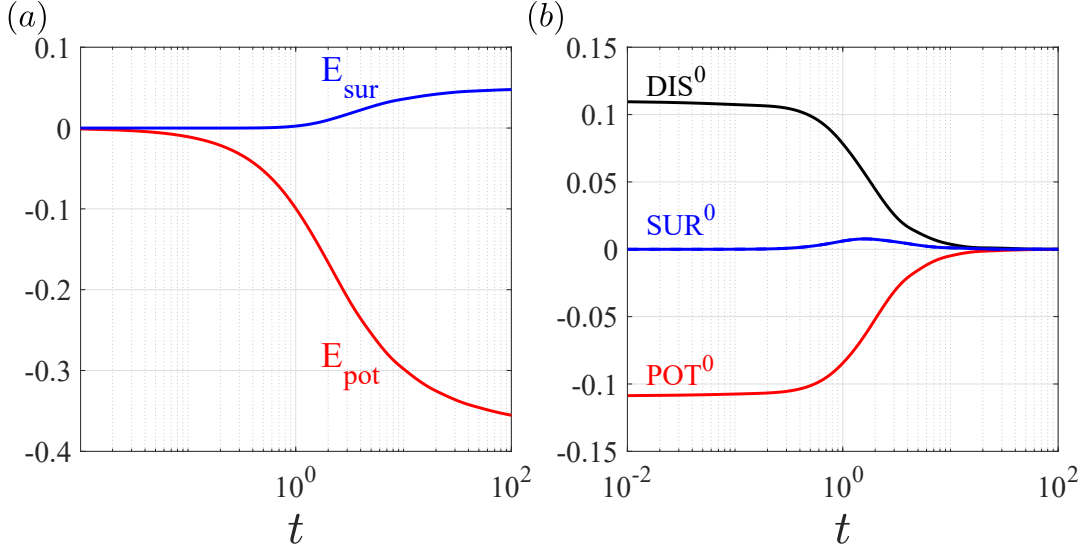


Figure 5.6: Energy analysis of the base flow presented in figure 5.2. (a) Evolution of the surface energy E_{sur} , and potential energy E_{pot} , per unit length. (b) The rate of viscous dissipation DIS^0 , surface energy SUR^0 , and potential energy POT^0 .

Energy analysis of the base flow

The energy equation for the base flow presented in §5.2.2, computed per unit length in z , can be expressed as

$$\underbrace{\iint_{\Omega_{xy}} Bo \delta^2 \text{tr}((\nabla \mathbf{u}^0 + \nabla^T \mathbf{u}^0) \nabla \mathbf{u}^0)}_{\text{DIS}^0} + \underbrace{\int_{\partial \Sigma_{\text{int}}} \kappa^0 \mathbf{n}^0 \cdot \mathbf{u}^0}_{\text{SUR}^0} + \underbrace{\iint_{\Omega_{xy}} -Bo u_y^0}_{\text{POT}^0} = 0. \quad (5.24)$$

In the case of the base flow, the dimensionless bulk potential energy (made dimensionless by γR^2), evaluated with respect to the initial state, can be expressed as

$$E_{\text{pot}} = \iint_{\Omega_{xy}} Bo y, \quad (5.25)$$

and the dimensionless surface energy evaluated with respect to the initial state can be expressed as

$$E_{\text{sur}} = -2\pi + \int_{\partial \Sigma_{\text{int}}} 1. \quad (5.26)$$

Figure 5.6(a) shows the temporal evolution of the potential and surface energies until reaching a quasi-static pendant drop for $\{\delta, Bo\} = \{0.2, 0.4\}$ whose base flow is presented in figure 5.2. As the liquid is pulled off the cylinder, the bulk potential energy is released. Being partially stored as surface energy, the potential energy allows the interface to deform. This energy transfer slows down and saturates later when the pendant curtain stagnates. The rates at which the energy is transferred are presented in figure 5.6(b) which demonstrates that the

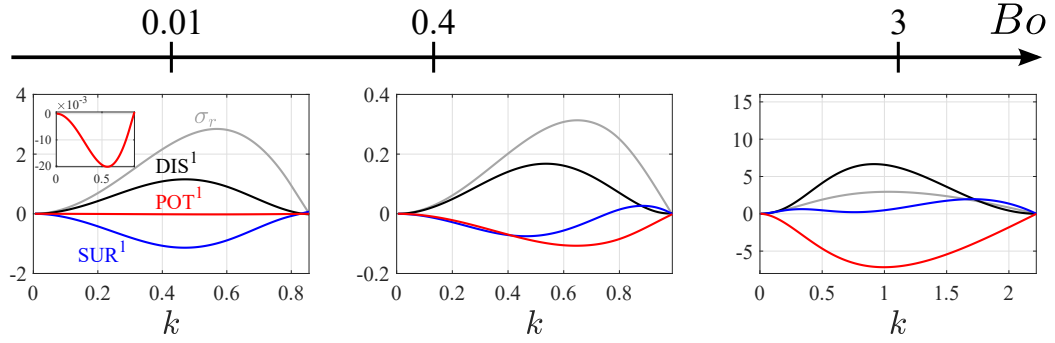


Figure 5.7: Energy analysis of the perturbations and the influence of Bo . The presented modes are the same as in figure 5.5. Energy terms are given in (5.27), and the grey curve shows the dispersion curve of the mode. The inset of the left panel shows POT^1 . All of the rate of energy terms are normalised by $\iint_{\partial\Sigma_{\text{int}}} |\tilde{\eta}|^2$.

excess potential energy is dissipated in the bulk liquid.

Energy analysis of the perturbed flow

The energy equation at the scale of linear perturbations computed along one wavelength results in terms with an order of ϵ^2 , giving

$$\left(\underbrace{\iint_{\Omega_{xy}} Bo \delta^2 \text{tr}((\tilde{\nabla} \tilde{\mathbf{u}} + \tilde{\nabla}^T \tilde{\mathbf{u}}) \tilde{\nabla} \tilde{\mathbf{u}}^*)}_{DIS^1} \right)_r + \left(\underbrace{\int_{\partial\Sigma_{\text{int}}} \tilde{\kappa} \mathbf{n}^0 \cdot \tilde{\mathbf{u}}^*}_{SUR^1} + \underbrace{\int_{\partial\Sigma_{\text{int}}} (\tilde{\eta} \partial_r \underline{\underline{\tau}}^0 \mathbf{n}^0) \cdot \tilde{\mathbf{u}}^*}_{POT^1} \right)_r = 0, \quad (5.27)$$

where \star denotes the complex conjugate, DIS^1 denotes the bulk viscous dissipation rate, and SUR^1 and POT^1 denote the contributions of capillarity and gravity to the rate of the work done by the fluid at the perturbed interface, respectively. (For further details on the derivation of (5.27) and its different terms see appendix 5.5.5.) We recall that the subscript r here denotes the real part of a complex number. As for the base flow, equation (5.27) unravels that the work exchanged at the perturbed interface is partially dissipated in the bulk liquid, and the remainder (or deficit) is stored at (or released from) the free surface in the form of surface energy.

Figure 5.7 shows the results of the energy analysis on the unstable mode for $\delta = 0.2$ and $Bo = \{0.01, 0.4, 3\}$. We remind the reader that the linear stability characteristics of this mode are presented in figure 5.5. In the case of large surface tension to gravity ratios, typically $Bo = 0.01$,

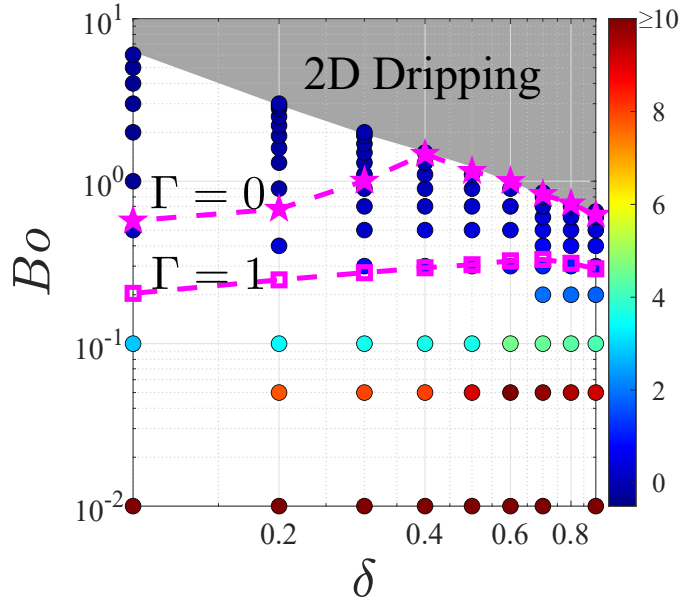


Figure 5.8: (a) Linear stability energy diagram of the pendant curtain: the color bar indicates the energy ratio Γ , magenta dashed lines with the pentagram and square markers show $\Gamma = 0$ and $\Gamma = 1$ iso-values, respectively, obtained by data interpolation. The sub-region above the pentagrams is purely gravity-driven Rayleigh-Taylor instability, and $Bo < 0.05$ indicates capillarity-dominant instability.

where the base interface is quasi-circular, both potential and capillary mechanisms drive the instability. However, the instability is dominated by capillarity, as the majority of the energy exchange to the perturbations is provided by capillarity ($|\text{SUR}^1| \gg |\text{POT}^1|$). By increasing Bo which results in a vertically outstretched pendant curtain, the instability becomes less favourable for the surface energy minimisation. Ultimately, exceeding a threshold for Bo , the instability is merely induced by the potential energy release, and capillarity acts to stabilise the flow ($\text{SUR}^1 > 0$ for $Bo = 3$, see figure 5.7).

Asymptotic energy diagram of the static pendant curtain

The $\{\delta, Bo\}$ space is investigated to follow the linear stability of the pendant curtain. The pendant state is found unconditionally unstable for a single unstable mode for which the gravitational effect is always destabilising. Here, the maximal wavenumber k_{max} , and the contribution of the involving mechanisms are studied merely for this unstable mode. To compare the role of gravity and capillarity in the flow destabilisation, following the results presented in §5.3.2, we can define the capillary-to-potential rate of energy ratio, hereafter referred to as the *energy ratio*, as

$$\Gamma = \frac{\text{SUR}^1}{\text{POT}^1} \bigg|_{k_{max}}. \quad (5.28)$$

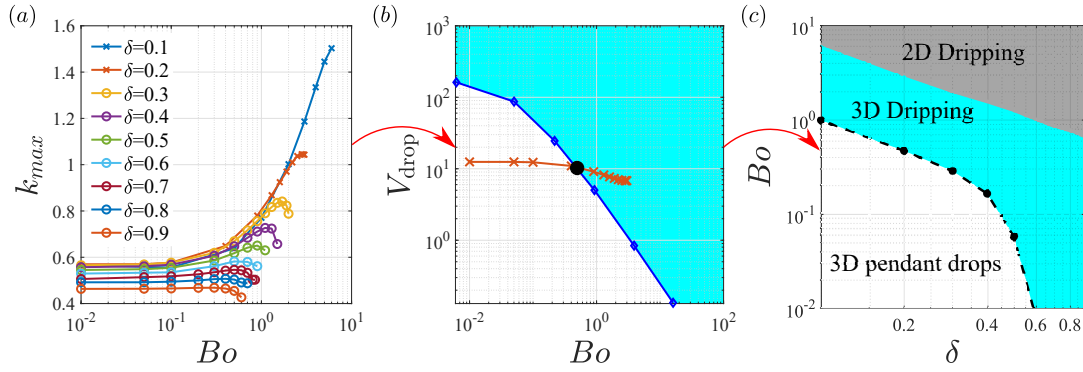


Figure 5.9: (a) k_{max} vs Bo for different values of δ obtained from the linear analysis of the pendant curtain. (b) An exemplary evaluation of the drop pinching criteria for $\delta = 0.2$: diamonds represent the maximum plausible volume of a static three-dimensional droplet (Weidner et al., 1997), crosses represent the volume of a droplet based on the most linearly amplified wavenumber, $V_{drop} = 2\pi^2(1 - \beta^2)/k_{max}$, solid lines here show interpolation between discrete data, and the black circle indicates the critical value for pinching; the cyan region highlights the drip parameters, and the white region highlight the pendant state. (c) Stability diagram based on the encapsulated volume within the most linearly amplified perturbation, following the same sample calculation as in panel (b): the grey region shows the two-dimensional curtain dripping in absence of perturbations; the circles, cyan and white regions indicate the post-instability state, the same as in panel (b); the black dashed line shows the logarithmic interpolation between critical values.

The energy ratio includes two pieces of information at the most linearly amplified wavenumber k_{max} ; firstly, as $POT^1 < 0$ always, the sign of Γ indicates if the capillarity acts as a stabilising mechanism (−) or a destabilising (+) one. Secondly, the magnitude of Γ indicates if the instability is gravity-dominated ($|\Gamma| \ll 1$), capillarity-dominated ($|\Gamma| \gg 1$). When $|\Gamma| = \mathcal{O}(1)$, both mechanisms contribute to the curtain instability. Figure 5.8 presents the energy diagram coloured by the energy ratio. When surface tension dominates gravity, $Bo \leq 0.05$, the instability is capillarity-dominated (warm colours). Although $\Gamma > 45$ for all of the data with $Bo = 0.01$, the color bar is limited to 10 for better visibility of the energy diagram. Increasing Bo for a fixed δ reduces the capillary contribution. Exceeding some threshold in Bo (marked by the magenta pentagrams), capillarity becomes stabilising and the instability turns purely gravity-driven. The sub-region of the purely gravity-driven instability narrows down by increasing δ , and for $\delta \geq 0.4$ this threshold is very close and slightly inferior to the critical Bo for two-dimensional curtain dripping. (The grey shaded area is the two-dimensional dripping presented in figure 5.3(d).)

5.3.3 Linear prediction: pattern formation and three-dimensional pinch-off

Figure 5.9(a) presents the variation of k_{max} for different values of $\{\delta, Bo\}$. For $Bo \leq 0.1$ and fix δ , where the instability is surface tension dominated, k_{max} is set by capillarity and does not

exhibit a significant variation, whereas further increasing Bo towards where capillarity and gravity become comparable, k_{max} is affected. For $\delta > 0.4$, k_{max} diminishes slightly with Bo , whereas for $\delta < 0.4$, increasing Bo over the pure gravity-driven instability threshold (above pentagrams in figure 5.8) leads to an increase of k_{max} , reaching up to three-fold for $\delta = 0.1$.

Further growth of linearly unstable modes is expected to form a single array of drops, either as pearls wrapping around the cylinder, or pendants underneath the cylinder. The volume of the biggest static three-dimensional droplet that can suspend on/under a cylinder was calculated previously by Weidner et al. (1997). In the thin-film limit, their non-linear simulations evidenced that even though the amplification rate of perturbation varies with time due to non-linear effects, the fundamental wavelength of the perturbed interface does not change significantly. They also noticed that in the case of a small Bond number, the final size of the pearl was comparable to that predicted by the linear theory for a coating film on a fibre in the absence of gravity. Inspired by this observation, our linear analysis suggests a prediction of the final state of the pendant curtain after instability, deduced from $\{\delta, Bo\}$ and k_{max} as follows. Mass conservation implies that the volume contained within the most linearly amplified wavelength $\lambda_{max} = 2\pi/k_{max}$ is given by $V_{drop} = \pi(1 - \beta^2)\lambda_{max}$. Therefore, comparing this value with the one calculated by Weidner et al. (1997) can indicate whether or not the patterns emerging from a pendant curtain ultimately drip. (See an exemplary investigation for $\delta = 0.2$ in figure 5.9(b).)

Figure 5.9(c) sketches a phase diagram obtained by following a similar calculation for a wide range of $\{\delta, Bo\}$: the grey shade indicates the parameters' range for which a two-dimensional rupture occurs, the same as presented in figure 5.3(d). The cyan designates the region where the most linearly amplified mode results in a volume larger than what surface tension can withstand, thus a three-dimensional pinch-off leading to dripping. For parameter combinations in the white region however, the pendant curtain transforms into an array of static pearls/pendants. This phase diagram demonstrates that the parameters in the vicinity of the two-dimensional dripping result in a three-dimensional rupture, irrespective of δ . Furthermore, a thick film of $\delta > 0.6$ will always pinch-off even when surface tension largely dominates gravity, i.e. at small Bo .

We recall that the phase diagram presented in figure 5.9(c) is attained from the asymptotic analysis of the quasi-static pendant curtain. In other words, the aforementioned linear analysis does not account for the possible amplification of the perturbations before reaching a two-dimensional pendant equilibrium, nor for the possible nonnormality in the system. As a piece of evidence, the non-linear simulations of Weidner et al. (1997) did not report for any of their simulations the appearance of any measurable interface disturbances before reaching a pendant state. Later simulations of Weidner (2013) in presence of surfactants led to a similar observation. In both studies, an initial low-level white noise of dimensionless amplitude 10^{-6} was applied at the interface of a liquid column at rest and concentric with the solid cylinder. Nevertheless, performing a rigorous transient growth analysis is insightful toward comprehension of the short-term perturbations' amplification.

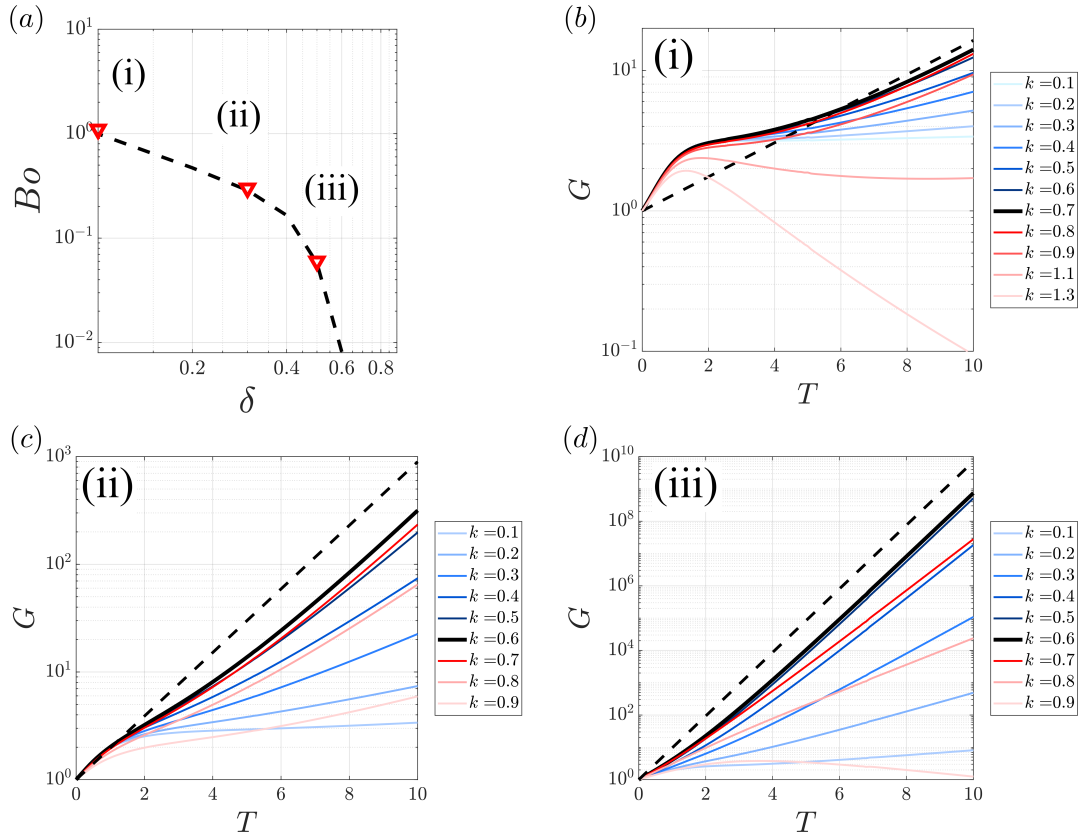


Figure 5.10: Transient growth analysis: (a) Three pinching pairs of $\{Bo, \delta\}$ analysed in the vicinity of the critical pinch-off separatrix (dashed line): (b) Point (i): $\{Bo, \delta\} = \{1.1, 0.1\}$; (c) Point (ii): $\{Bo, \delta\} = \{0.3, 0.3\}$ (d) Point (iii): $\{Bo, \delta\} = \{0.06, 0.5\}$. Panels (b-d) present the optimal transient gain G , as a function of the temporal horizon T , for different wave numbers k . The exponential evolution of the asymptotically predicted most unstable wave number k_{max} , is shown in a black dashed line, and the thick black line represents the transient gain of k_{max} .

5.3.4 Transient growth analysis

In the following, we present the results of the transient growth analysis for three pairs of parameters $\{Bo, \delta\}$, shown in figure 5.10(a), at the vicinity of the three-dimensional pinch-off separatrix, obtained in §5.3.3. As it is constructed using the drop volumes, corresponding to the asymptotically most unstable wavelengths, predicted by the linear analysis of the pendant state, it is especially important to evaluate the transient effects, which might amplify potentially different wavelengths before the formation of the pendant curtain, thus possibly modifying the end-fate of the drops.

Figures 5.10(b-d) present the optimal transient gains as a function of the time horizon, for different wave numbers k . We observe no appreciable transient growth, which is consistent with the lack of measurable interface disturbances before the saturation of the pendant curtain in the non-linear simulations of Weidner et al. (1997). Moreover, the wavelength

selection appears to be unaffected. The gain of the asymptotically most unstable wave number, predicted by linear stability analysis (black dashed line), largely coincides with that of the envelope, i.e. it is as amplified as the transiently most amplified wave number. Therefore, we can safely conclude that the criterion for three-dimensional pinch-off is unaltered by the transient nature of the drainage, and is instead well captured, at least in the linear regime, by the asymptotic quasi-stationary modal stability analysis.

5.4 Summary and conclusion

In this work, we studied the gravity-driven flow of a viscous liquid film coating the outer wall of a horizontal cylinder in the inertialess regime. A numerical solution was first computed for the temporal evolution of an axially invariant base flow, starting from rest and of a uniform thickness. The base flow exhibits an instantaneous liquid pull-off. For a fixed mean thickness, but depending on the Bond number, two trends were observed at large times: either the draining film reaches a quasi-static axially invariant pendant curtain (at small Bond numbers), or the liquid pull-off continues and results in a two-dimensional pinch-off under the cylinder (at large Bond numbers). While at small Bond numbers, surface tension sustains a quasi-circular interface shape, increasing the Bond number results in further deformation of the interface, stretching out vertically underneath the cylinder. A similar effect of the Bond number on the deformation of the interface was observed in **chapter 4** for a liquid film coating the inside of a tube. However, inside a tube, the surrounding solid wall prohibits any two-dimensional rupture. The critical two-dimensional pinch-off Bond number is found to scale as the inverse of the mean film thickness around the cylinder. This scaling and its numerically obtained prefactor agree firmly with the critical value obtained by a scaling analysis that equates the weight of the whole liquid bulk with the surface tension in the thick-film limit. The scaling analysis however fails to give an accurate prediction for the thick film, as the dripping occurs following an interface necking at some distance below the cylinder. As a result, the surface tension fails to retain a fraction of the liquid bulk which accelerates below the neck.

Next, the stability of the quasi-stationary pendant curtain was investigated through a linear stability analysis. The curtain was found unconditionally linearly unstable. The sole unstable mode features a left/right symmetry, strong interface modulations at the bottom, and an immobile interface at the top of the cylinder for all parameter ranges. A similar top/bottom asymmetry in the unstable mode was found in **chapter 4**. In both flows, the small film thickness in the vicinity of a solid wall at the top of the interface forbids the interface from being perturbed. The unstable eigenmode varies strongly with the Bond number; at small Bond numbers, where surface tension dominates over gravity, the instability causes a flow reversal towards the top of the cylinder, resembling the capillary-driven Rayleigh-Plateau instability. By increasing the Bond number, the flow reversal weakens and ultimately vanishes, and the instability promotes the formation of vertical fingers under the cylinder, resembling the Rayleigh-Plateau instability. This observation is in accordance with the non-linear simulations

of Weidner et al. (1997); Weidner (2013) in the thin film limit.

A parametric study was then conducted on the space of the dimensionless parameters $\{Bo, \delta\}$, along with the energy analysis of the base flow and unstable mode. The energy analysis helped interpreting the formation of a pendant curtain as a process to minimise the gravitational potential energy of the bulk flow, subject to a surface energy barrier. It furthermore demonstrates that gravity is unconditionally destabilising, whereas the role of surface tension varies with the Bond number. At small Bond numbers, surface tension is destabilising and dominates the instability. The eigenflow reduces the surface energy, confirming the characteristics of the Rayleigh-Plateau instability. In contrast, increasing the Bond number reduces the capillarity contribution to the instability, and exceeding a threshold, surface tension turns stabilising as the eigenmode reduces only the gravitational potential energy, in analogy with the purely gravity-driven Rayleigh-Taylor instability. Both limits are in accordance with the former description given by Weidner et al. (1997) in the early stages of the appearance of disturbances to the flow in the thin film limit. Nevertheless, their analysis addressed a stabilising effect of gravity at a low Bond number when the perturbations amplify beyond the linear range.

The present linear analysis also illustrates that the wavenumber of the most amplified mode is selected through a compromise between surface energy and potential energy reduction, and varies non-monotonously as a function of the mean film thickness and Bond number. Moreover, a phase diagram was sketched for the viscous liquid films draining down the outer wall of a horizontal cylinder, based on the asymptotic linear analysis of a quasi-static pendant curtain, postulating that the non-linearity does not affect selection of the most amplified wavelength. This assumption is aligned with the non-linear simulations of Weidner et al. (1997). This diagram proposes a regime boundary as a function of the Bond number and mean film thickness to predict if the emerging pattern leads into a three-dimensional pinch-off or forms a static array of wrapping pearls or pendant drops. Lastly, a transient growth analysis revealed that the most amplified wavenumber is correctly predicted by the leading eigenvalue associated to the stability of the saturated pendant curtain, and concluded that the nonmodal mechanisms are too weak to alter the fate of the pendant curtain instability.

Finger (Takagi and Huppert, 2010; Balestra et al., 2019) and pearl (Carroll, 1984; Brochard-Wyart et al., 1990; McHale et al., 1999) formation in the viscous flow on top of a cylindrical substrate have been addressed extensively. However, one should note that the contact-line plays an essential role in those cases, hence they differ in nature from the instabilities reported in our analysis. The linear stability of a liquid column covering the entire periphery of a horizontal cylinder at rest in the presence of gravity has not been well addressed experimentally in the literature. One possible reason may be the practical challenge of initiating a long liquid column of desired thickness around the cylinder. Yet it will be of interest to explore this flow experimentally and compare the real-life pattern formations with those predicted by our study.

Note that the threshold of three-dimensional droplet rupture by Weidner et al. (1997) was obtained using the thin film equations. This prediction states that a pearl of large mean

thickness eventually pinches even at a very low Bond number; an intuitively reasonable prediction. Yet, the critical pinch-off volume may feature a thick film for which the thin-film equations may suffer from a lack of accuracy. Therefore, a direct numerical simulation of a three-dimensional static drop may verify the accuracy of the analysis of Weidner et al. (1997), and consequently the droplet pinch-off boundary in the phase diagram of the present study. Additionally, a key assumption behind the presented phase diagram in §5.3.3 is that the most amplified wavelength remains unchanged throughout different instability stages. It is worth therefore verifying this assumption by means of direct numerical simulations. Such an analysis will be insightful for verifying whether or not the droplet rupture will be affected by the meniscus connecting the droplet to the thin film that remains on the cylinder or by coalescing with possible neighbouring tiny satellite pearls (Weidner et al., 1997). It would further be pertinent to perform a transient growth analysis in the two-dimensional dripping regime. Under the effect of finite-time amplification of perturbations, the draining bulk could arguably split into an array of droplets, small enough to remain suspended on the fibre, before the rupture of the curtain. Another direction for future investigations is to evaluate the flow instability when the cylinder is inclined so that a longitudinal component of gravity creates axial flow motion, forming a single rivulet under the cylinder (Aktershev et al., 2021).

5.5 Appendix

5.5.1 Derivation of the interface boundary conditions

In this section, the derivation of the interface boundary conditions is elaborated for the perturbed flow. These conditions are imposed at the perturbed interface, i.e. at $r = \mathcal{R}_{\text{int}}^0 + \epsilon\eta^1$, while η^1 is already an unknown of the problem. By using the Taylor expansion, that is, projecting radially at the base interface, i.e. at $r = \mathcal{R}_{\text{int}}^0(\theta, t)$, any flow quantity at the perturbed interface can be readily approximated. This projection is referred to as flattening and for an arbitrary function $f(r, \theta, z, t)$ can be expressed as

$$f|_{(r=\mathcal{R}_{\text{int}}^0+\epsilon\eta^1, \theta, z, t)} = f|_{(r=\mathcal{R}_{\text{int}}^0, \theta, z, t)} + \epsilon\eta^1 \partial_r f|_{(r=\mathcal{R}_{\text{int}}^0, \theta, z, t)} + \mathcal{O}(\epsilon^2). \quad (5.29)$$

By substituting the decomposed state vector of (5.7), into the interface conditions (5.5)-(5.6), then using the normal mode (5.8), and applying the aforementioned flattening, we can formulate these conditions as a set of equivalent constraints at the boundary of the base interface. The linearised form of the kinematic condition (5.5) writes

$$\partial_t (\mathcal{R}_{\text{int}}^0 + \epsilon\eta^1) + (\mathbf{u}^0 + \epsilon\mathbf{u}^1) \cdot \nabla (\mathcal{R}_{\text{int}}^0 + \epsilon\eta^1) = (\mathbf{u}^0 + \epsilon\mathbf{u}^1) \cdot \mathbf{e}_r \quad \text{at } r = \mathcal{R}_{\text{int}}^0 + \epsilon\eta^1, \quad (5.30)$$

where the gradient vector in the Cylindrical coordinates can be expressed as $\nabla = (\partial_r, 1/r \partial_\theta, \partial_z)^T$. Applying (5.29) to (5.30) and using the normal mode (5.8) readily results in (5.11).

The linearised dynamic condition (5.6) writes

$$\left(\underline{\underline{\tau}}^0 + \epsilon \underline{\underline{\tau}}^1 \right) (\mathbf{n}^0 + \epsilon \mathbf{n}^1) = -(\kappa^0 + \epsilon \kappa^1) (\mathbf{n}^0 + \epsilon \mathbf{n}^1) \quad \text{at } r = \mathcal{R}_{\text{int}}^0 + \epsilon\eta^1, \quad (5.31)$$

Applying (5.29) to (5.31) and using the normal mode (5.8) readily results in (5.15). In order to express interface conditions in the Cartesian coordinates, the terms which are expressed in the Cylindrical coordinates should be transformed by employing the Jacobian transformations as

$$\begin{aligned} \mathbf{e}_r &= \cos \theta \mathbf{e}_x + \sin \theta \mathbf{e}_y, & \mathbf{e}_\theta &= -\sin \theta \mathbf{e}_x + \cos \theta \mathbf{e}_y, \\ \partial_r &= \cos \theta \partial_x + \sin \theta \partial_y, & \partial_\theta &= \frac{\mathbf{t}^0 \cdot \nabla_s}{\mathbf{t}^0 \cdot \nabla_s \theta}, \end{aligned} \quad (5.32)$$

where \mathbf{t}^0 denotes the unit tangent vector, and $\nabla_s = \nabla - \mathbf{n}^0 (\mathbf{n}^0 \cdot \nabla)$ is the tangential derivative at the base interface. Both conditions (5.11) and (5.15) include the normal vector and the curvature of the perturbed interface whose formulation is given in §4.5.3 in **chapter 4**. For further details concerning the numerical implementation of the boundary conditions, see appendix 5.5.2.

5.5.2 Variational formulation of the linear stability analysis and implementation of its boundary conditions

Implementation of the numerical scheme and development of the variational formulation associated with the governing equations presented in section 5.2 are elaborated in this appendix, recalling that the numerical domain is shown in figure 5.4. To develop the variational form of (5.12), firstly the normal mode of (5.8) is applied to the system of equations (5.9)-(5.11). Then it is internally multiplied by the vector of the test functions $\psi = [\psi_p, \psi_{\mathbf{u}}, \psi_\eta]$, where $\psi_{\mathbf{u}} = [\psi_{u_x}, \psi_{u_y}, \psi_{u_z}]$. The resulting scalar product is integrated at Ω_{xy} , which in the linear order writes

$$\left\{ \iint_{\Omega_{xy}} \psi_p^* (\tilde{\nabla} \cdot \tilde{\mathbf{u}}) dA_{\Omega_{xy}} \right. \quad (5.33)$$

$$+ \iint_{\Omega_{xy}} \psi_{\mathbf{u}}^* \cdot \left(\left(\frac{Bo}{Oh} \right)^2 \delta^4 \sigma \tilde{\mathbf{u}} \right) dA_{\Omega_{xy}} \quad (5.34)$$

$$+ \iint_{\Omega_{xy}} \psi_{\mathbf{u}}^* \cdot \left(\left(\frac{Bo}{Oh} \right)^2 \delta^4 (\mathbf{u}^0 \cdot \tilde{\nabla} \tilde{\mathbf{u}} + \tilde{\mathbf{u}} \cdot \nabla \mathbf{u}^0) \right) dA_{\Omega_{xy}} \quad (5.35)$$

$$+ \iint_{\Omega_{xy}} tr \left(\tilde{\underline{\underline{\tau}}}^T (\tilde{\nabla} \psi_{\mathbf{u}})^* \right) dA_{\Omega_{xy}} \quad (5.36)$$

$$+ \int_{\partial \Sigma_{\text{int}}} \left(\tilde{\underline{\underline{\tau}}}^0 \tilde{\mathbf{n}} + \tilde{\eta} \partial_r \tilde{\underline{\underline{\tau}}}^0 \mathbf{n}^0 + (\kappa_0 \tilde{\mathbf{n}} + \tilde{\kappa} \mathbf{n}^0) \right) \cdot \psi_{\mathbf{u}}^* ds \quad (5.37)$$

$$+ \int_{\partial \Sigma_{\text{int}}} \psi_\eta^* (\sigma \tilde{\eta}) ds \quad (5.38)$$

$$+ \int_{\partial \Sigma_{\text{int}}} \psi_\eta^* \left(\left(-\partial_r u_r^0 + \frac{\partial_r u_\theta^0 \partial_\theta \mathcal{R}_{\text{int}}^0}{\mathcal{R}_{\text{int}}^0} - \frac{u_\theta^0 \partial_\theta \mathcal{R}_{\text{int}}^0}{(\mathcal{R}_{\text{int}}^0)^2} \right) \tilde{\eta} + \frac{u_\theta^0}{\mathcal{R}_{\text{int}}^0} \partial_\theta \tilde{\eta} + \frac{\partial_\theta \mathcal{R}_{\text{int}}^0}{\mathcal{R}_{\text{int}}^0} \tilde{u}_\theta - \tilde{u}_r \right) ds \Big\} \quad (5.39)$$

$$+ \text{c.c.} = 0. \quad (5.40)$$

It should be noted that in a complex system, the applied scalar product is Hermitian, defined as $\langle \mathbf{a}, \mathbf{b} \rangle = \mathbf{a}^* \cdot \mathbf{b}$ where the superscript \star denotes the complex conjugate. This variational equation can be readily implemented and solved in COMSOL MultiphysicsTM. It is sufficient to solve the first part (in $\{\}$) and the c.c. is known consequently. Step-by-step derivation of this equation is presented in §4.5.2. The matrix representation of (5.33)-(5.40) is also similar to that shown in figure 4.13.

5.5.3 Derivation of a simplified expression for the energy density of the transient response.

The interfacial energy density per wavelength is proportional to

$$\begin{aligned}
e(T) &= \frac{k}{2\pi} \oint_{S(T)} \int_0^{2\pi/k} |\bar{\eta}(T) e^{ikz} + c.c|^2 dz ds = 2 \oint_{S(T)} |\bar{\eta}(T)|^2 ds \\
&= 2 \sum_{m=-N}^N \sum_{n=-N}^N \alpha_m^* \alpha_n \oint_{S(T)} \bar{\eta}_m(T)^* \bar{\eta}_n(T) ds \\
&= 2 \boldsymbol{\alpha}^H \mathbf{A}(T) \boldsymbol{\alpha},
\end{aligned} \tag{5.41}$$

where the strictly positive definite and Hermitian matrix $\mathbf{A}(T)$ is such that

$$[\mathbf{A}(T)]_{mn} = \oint_{S(T)} \bar{\eta}_m(T)^* \bar{\eta}_n(T) ds, \tag{5.42}$$

for $-N \leq m \leq N$ and $-N \leq n \leq N$, and where we defined

$$\boldsymbol{\alpha} = [\alpha_N^*, \alpha_{N-1}^*, \dots, \alpha_1^*, \alpha_0, \alpha_1, \dots, \alpha_{N-1}, \alpha_N]^T. \tag{5.43}$$

The leading eigenvector of $\mathbf{A}(T)$ has no particular reason to have its N first elements equal to the complex conjugate of its last N . Thus, it cannot correspond directly to the optimal set of $\boldsymbol{\alpha}$, that should satisfy this last constraint. For this reason we introduce the matrix

$$\mathbf{M}^{-1} = \begin{bmatrix} \mathbf{I} & \mathbf{O} & \mathbf{P} \\ \mathbf{O}^T & \sqrt{2} & \mathbf{O}^T \\ -i\mathbf{I} & \mathbf{O} & i\mathbf{P} \end{bmatrix}, \quad \text{with } \mathbf{I}_{ij} = \delta_{ij}, \quad \mathbf{P}_{ij} = \delta_{N-i+1,j}, \quad \text{and } \mathbf{O}_i = 0. \tag{5.44}$$

for $1 \leq i, j \leq N$. Namely, \mathbf{I} is the identity matrix of size $N \times N$, \mathbf{P} is the identity matrix mirrored around its vertical axis (it contains ones on the diagonal from the bottom-left to the top-right and zeros everywhere else) and \mathbf{O} is a vector of zeros of size $N \times 1$. In this manner, we have directly $\mathbf{a} = \mathbf{M}^{-1} \boldsymbol{\alpha}$, such that

$$e(T) = 2 \boldsymbol{\alpha}^H \mathbf{A}(T) \boldsymbol{\alpha} = 2 \mathbf{a}^T \mathbf{M}^H \mathbf{A}(T) \mathbf{M} \mathbf{a} = 2 \mathbf{a}^T \Re[\mathbf{M}^H \mathbf{A}(T) \mathbf{M}] \mathbf{a}, \tag{5.45}$$

where we used that \mathbf{a} and $e(T)$ are real-valued. Therefore, defining $\mathbf{E}(T) = \Re[\mathbf{M}^H \mathbf{A}(T) \mathbf{M}]$ leads to the desired result.

Finally, the orthogonality of the Fourier modes ensures that $\mathbf{A}(0) = 2\pi \mathbf{I}$. It is further straightforward to show that $\mathbf{M}^H \mathbf{M} = \frac{1}{2} \mathbf{I}$, resulting in $\mathbf{E}(0) = \pi \mathbf{I}$ and $e(0) = 2\pi \mathbf{a}^T \mathbf{a}$.

5.5.4 Validation of the numerical model

The present numerical scheme is validated hereafter. Several measures are taken to ensure the correspondence of the model, based on the asymptotic limits and analytical solutions if any.

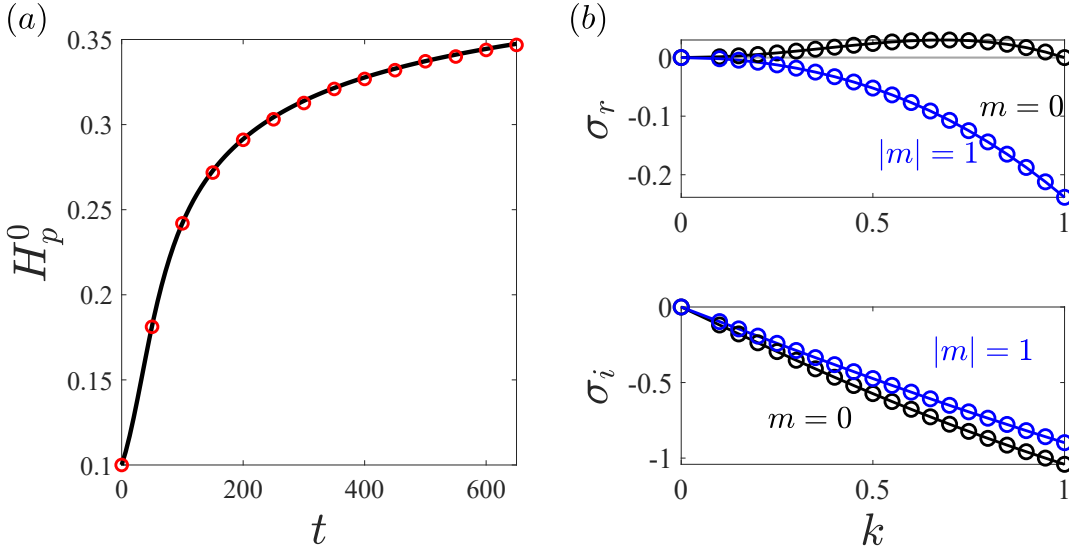


Figure 5.11: Numerical model validation; (a) base flow: temporal evolution of the south pole thickness; solid line presents the solution from the present numerical study, and the red circles present the solution obtained by Weidner et al. (1997); $Oh \rightarrow \infty, Bo = 1.21, \beta = 10/9$; (b) linear stability analysis: dispersion curves of the two least stable modes associated with the gravity-driven viscous film flow down a centered cylinder, namely $|m| = \{0, 1\}$. The continuous lines present the analytical solution obtained from the Stokes equations, and the circles represent the results from the present numerical model; Craster and Matar (2006) considered a similar perturbation as in equation 5.7 with the normal mode of $\exp[\sigma t + ikz + im\theta]$, a typical choice for the axisymmetric configurations. Note that the present model, in the Cartesian coordinates, does not expand in the azimuthal wavenumber m ; $Oh \rightarrow \infty, Bo = 1, \delta = 0.4$.

Base flow model

The present base flow model is validated with Weidner et al. (1997) who employed the lubrication approximation (Oron et al., 1997) to simulate the non-linear gravity-driven evolution of a thin film around a solid horizontal cylinder. Figure 5.11(a) shows the temporal evolution at the south pole of the cylinder for $\{Oh \rightarrow \infty, Bo = 1.21, \beta = 10/9\}$. The present model results in a solution of the base flow in firm agreement with the solution of Weidner et al. (1997).

Linear stability analysis model

The present linear stability model is validated with the analytical solutions that Craster and Matar (2006) presented for the gravity-driven coating flow down a vertical centered cylinder (where gravity points in z direction in figure 5.1). The corresponding base flow is parallel and

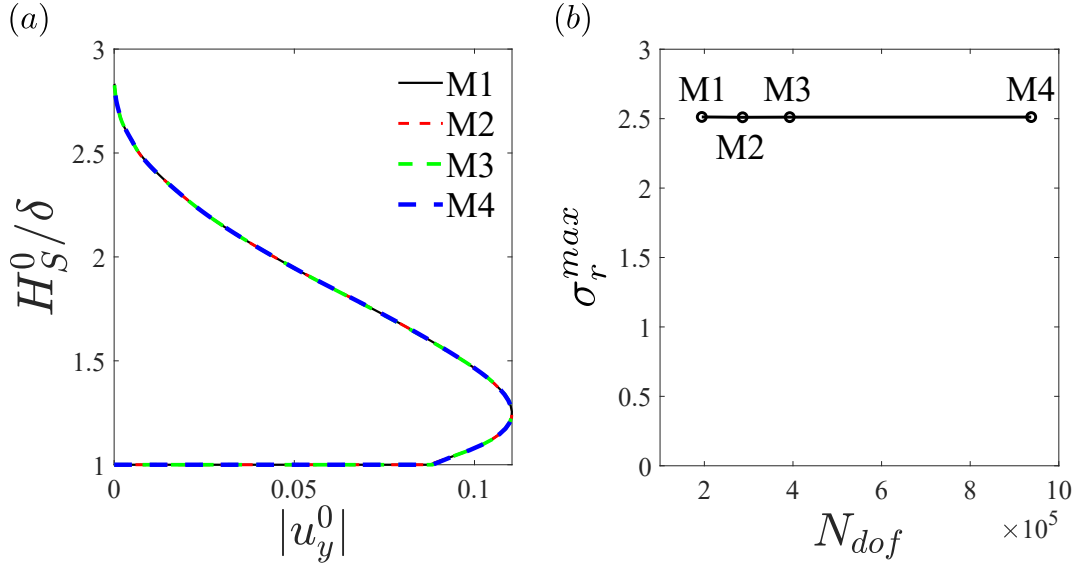


Figure 5.12: Mesh convergence proof for $Oh \rightarrow \infty$, $Bo = 0.4$, $\delta = 0.2$: (a) base flow; H_S^0/δ vs $|u_y^0|$; (b) linear stability analysis; σ_r^{max} vs N_{dof} . All of the results presented in this manuscript are obtained from M3.

can be expressed in cylindrical coordinates as

$$u_z^0 = \frac{\delta^{-2}}{2} \left(\ln \frac{r}{\beta} - \frac{r^2 - \beta^2}{2} \right), \quad p^0 = 1, \quad \mathcal{R}_{\text{int}}^0 = 1. \quad (5.46)$$

For the linear stability analysis, Craster and Matar (2006) employed the long-wavelength approximation (Reynolds, 1886) and compared the results with the analytical solution, in terms of Bessel functions, obtained by solving the full Stokes equations (Goren, 1962). Unlike the present study that is formulated in the Cartesian coordinates, Craster and Matar (2006) used the axisymmetry of the flow and considered a perturbation as in (5.8) with the normal mode exponent of $\exp[\sigma t + ikz + im\theta]$ where m denotes the azimuthal wavenumber. Figure 5.11(b) presents the agreement between the present linear stability model and the analytical solution for a thick film $\delta = 0.4$. It should be noted that despite the axisymmetric nature of the validated case, this presented validation holds also for an arbitrary interface. For this aim, the geometrical symmetry in the numerical reference frame is broken by setting the origin of the coordinates system at an arbitrary location inside the liquid film, $(x, y) = (0.2, 0.7)$.

Grid independency

A convergence study for the base flow evolution and the linear stability of the most unstable eigenvalue is presented in figure 5.12, for $\{Oh \rightarrow \infty, Bo = 0.4, \delta = 0.2\}$. Mesh resolution is controlled by setting a prefactor multiplied by the number of divisions at the solid wall and interface boundaries. Mesh convergence is obtained for the presented grids. All of the

presented results in the manuscript are obtained employing M3.

5.5.5 Derivation of the energy equation

In this section, the derivation of the energy equation is elaborated. Dimensional form of the momentum equation (5.3) in the inertialess limit is given in **chapter 3**. Following the same formalism, the dimensionless form of the energy equation, obtained under the scaling presented in §5.2, can be expressed as

$$\underbrace{\iiint_{\Omega_{xy}} Bo \delta^2 \text{tr}((\nabla \mathbf{u} + \nabla^T \mathbf{u}) \nabla \mathbf{u})}_{\text{DIS}} + \underbrace{\iint_{\partial\Omega_{xy}} -(\underline{\underline{\tau}} \mathbf{n}^0) \cdot \mathbf{u}}_{\text{BND}} + \underbrace{\iiint_{\Omega_{xy}} -Bo u_y}_{\text{POT}} = 0. \quad (5.47)$$

Each under-brace denotes the physical mechanism associated with the respective term, as follows:

1. DIS: the rate of viscous dissipation in the bulk fluid
2. BND: the rate of work done by the fluid through the moving boundaries
3. POT: the rate of change of gravitational potential energy

No-slip condition implies $\mathbf{u} = \mathbf{0}$ at $\partial\Sigma_w$, thus yielding (5.23).

Energy equation for the perturbed flow

The energy equation for the perturbed flow is obtained by substituting the perturbed state vector (5.7) with the normal mode (5.8), into (5.23) and integrating it over one wavelength $\Delta z = \lambda = 2\pi/k$. The resulting integral is of the order ϵ^2 and determines the energy equation for the linear perturbations which implies

$$\frac{2\pi}{k} e^{2\sigma_r t} \left[\underbrace{\iint_{\Omega_{xy}} Bo \delta^2 \text{tr}((\tilde{\nabla} \tilde{\mathbf{u}} + \tilde{\nabla}^T \tilde{\mathbf{u}}) \tilde{\nabla} \tilde{\mathbf{u}}^*)}_{\text{DIS}^1} + \underbrace{\int_{\partial\Sigma_{\text{int}}} -(\underline{\underline{\tau}} \mathbf{n}^0) \cdot \tilde{\mathbf{u}}^*}_{\text{BND}^1} \right] + \text{c.c.} = 0, \quad (5.48)$$

We remind that the normal mode (5.8) is complex, hence the integral of terms in ϵ^1 order vanish due to the periodicity of the perturbations over λ . As $(2\pi/k) e^{2\sigma_r t} > 0$, it can be factorised and simplified. We hereafter only focus on the real part of (5.48) which writes

$$(\text{DIS}^1 + \text{BND}^1)_r = 0. \quad (5.49)$$

Let us recall (5.15), and that for a quasi-static pendant drop where $\mathbf{u}^0 \approx \mathbf{0}$, $\underline{\underline{\tau}}^0 = -p^0 \mathbf{I}$. Except for the thin film covering the upper side of the cylinder, where $\tilde{\eta} \approx 0$ and pressure follows the lu-

brication pressure, bulk pressure is hydrostatic, $p^0 \approx -Bo \, y$. Thus, BND^1 can be decomposed as

$$BND^1 = SUR^1 + POT^1, \quad (5.50)$$

where SUR^1 denotes the capillary contribution to the rate of work at the perturbed interface, and POT^1 denotes the rate at which the fluid works against the hydrostatic pressure to perturb the interface. These terms can be expressed as

$$SUR^1 = \int_{\partial\Sigma_{\text{int}}} \tilde{\kappa} \mathbf{n}^0 \cdot \tilde{\mathbf{u}}^*, \quad (5.51)$$

$$POT^1 = \int_{\partial\Sigma_{\text{int}}} \left(\tilde{\eta} \, \partial_r \underline{\underline{\tau}}^0 \mathbf{n}^0 \right) \cdot \tilde{\mathbf{u}}^*, \quad (5.52)$$

thus giving (5.27).

6 Modeling melt electrowriting beam

Remark This chapter is largely inspired by the master thesis of Cédric Scherz, of the same title

Cédric Scherz¹, Shahab Eghbali[†] and F. Gallaire¹

¹ Laboratory of Fluid Mechanics and Instabilities, École Polytechnique Fédérale de Lausanne, Lausanne CH-1015, Switzerland

Authors' contributions F.G. conceived the project, funded by SFA Advanced Manufacturing. S.E. prepared the preliminary multiphysics numerical model and developed the theoretical framework. C.S provided further developments on the model. S.E. supervised C.S. during his master thesis, and wrote the manuscript with input from C.S..

6.1 Introduction

The flow of an electrically induced liquid jet has received attention since the early studies of Zeleny (1914). When the bulk of two immiscible fluids of finite conductivity in contact with each other is exposed to an intense electric field, the free ions carried by the fluids are attracted in the direction of the applied field due to additional stress, known as Maxwell stress. Since the interface halts the transport of charged particles from one fluid to another, ions accumulate at the interface and form a strong local electric field. The difference in the polarisability of the media in contact, measured by their permittivity, induces a stress jump at the interface that can cause vigorous interfacial motions. In such a case, the superposition of hydrodynamic and electrical stresses modifies the shape of the interface. Most notably, the interface forms a conical shape when the applied electrical field is intense enough.

Electrified flows have a vast number of applications in biomedical or soft robotics, micro/-nanofluidics, ink-jet and 3D printing, fine material production and processing, combined electrical and mechanical flow focusing, and pharmaceutical processes (Gañán-Calvo et al., 2006; Gañán-Calvo and Montanero, 2009; Gomez and Deng, 2011; Schröder, 2012; Cruz-Mazo

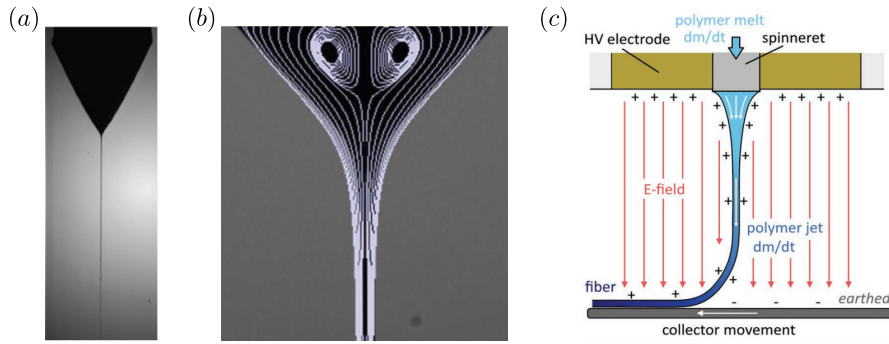


Figure 6.1: (a) Cone-jet with the well visible cone apex and emitting thin jet from the tip, reprinted from Rosell-Llompart et al. (2018); (b) Cone-jet with a smooth meniscus connecting to the thin jet; white lines show the numerically computed streamlines, reprinted from Herrada et al. (2012); (c) Illustration of the melt electrowriting process, reprinted from Robinson et al. (2019).

et al., 2016; Boda et al., 2018; Gañán-Calvo et al., 2018b). In a pioneering theoretical study, Taylor (1964) neglected the fluid motion and considered the conical deformation of an inviscid drop for which he computed the angle that satisfies the balance of stresses between the surface tension and the one induced by the electric field. The equilibrium suggests a cone half-angle value equal to 49.3° , known as the Taylor cone. Analogously, in the case of a liquid jet in an intense electric field, the interface thins along the flow and forms a similar conical shape with an emerging jet from its apex (cf. figure 6.1(a)), a configuration referred to hereafter as *cone-jet*. The emerging jet from the cone is prone to the instabilities caused by the capillary effects in the presence of electrical charge transportation, leading to the jet break up and formation of droplets; single ones, or spraying clusters downstream of the thin jet (Zeleny, 1914; Cloupeau and Prunet-Foch, 1989). Numerous studies have addressed electrified liquid jets surrounded by air from two perspectives: (i) based on the scaling analysis, and (ii) theoretical electrohydrodynamic models. Studying the underlying mechanisms by means of scaling laws is mainly based on Gañán-Calvo et al. (1994); Gañán-Calvo (1999) where the intrinsic scales of length, time, and electric current were proposed to analyse the universal properties of the cone-jet. Such arguments have suggested scalings for the jet size, electric current, and the droplet size (De La Mora and Loscertales, 1994; Gañán-Calvo et al., 1994; Gañán-Calvo, 1999; Gañán-Calvo and Montanero, 2009) based on the hydrodynamic and electrical properties of the liquid and the ambient air. These scales are in agreement with numerous experimental measurements (see Gañán-Calvo et al. (2018b) for the review).

On the other hand, the Taylor-Melcher leaky dielectric model (Melcher and Taylor, 1969; Saville, 1997) is the backbone of the theoretical studies of electrified liquids. Gañán Calvo (1997) employed this model and described the static cone-jet using the slender-jet description. Later, López-Herrera et al. (2013) showed the accuracy of the slender-jet assumption for the quasi-cylindrical jets in the high Ohnesorge limit. Gamero-Castaño and Magnani (2019b) simulated static cone-jet of a smooth conical meniscus by solving the Navier-Stokes equations

coupled with the electric field equation, in favourable agreement with the experiments (cf. figure 6.1(b)). These studies, among all, distinguished three main sub-regions in the cone-jet: (i) the upstream meniscus attached to the capillary, where the charge transport is dominated by ohmic conduction; (ii) the cone neck, which is the intermediate transition region between the conduction-dominant meniscus and the convection-dominated jet; and (iii) the downstream jet, where the surface convection leads the charge transport.

In this chapter, we investigate numerically the cone-jet formation from the perspective of the melt electrowriting, that is, an additive manufacturing technique that gained a growing interest over the last ten years (see Robinson et al. (2019) for detailed review). In this process, a liquid thread of dozens nl/s volumetric flow rate falls on a moving collector, while an electric field acts on the thread, schematised in figure 6.1(c). The electric field, created by a potential difference of kV order between the metallic nozzle and a ground electrode located at the collector level reduces the liquid beam size. Common thread diameters measure dozens of micrometers, while the smallest values can reach around $2 \mu\text{m}$ (Bober and Chen, 2011; Hrynevich et al., 2018). Neglecting what happens when the thread reaches the collector plate, we focus on the interface shape and flow characteristics near the nozzle outlet, and on the dependence of the jet thinning and cone half-angle on the electrical and hydrodynamic parameters. To this aim, we extend the methodology of Herrada et al. (2012) to a time-dependent laminar jet flow in two-dimensional axisymmetric configuration.

This chapter is organised as follows. In § 6.2, the problem formulation and numerical method are detailed. The governing equations and underlying assumptions are presented in § 6.2.1, and the numerical procedure is detailed in § 6.2.2. The results are presented and discussed in § 6.3. The influence of the applied electric field on the flow field is discussed in § 6.3.1. Moreover, the variation of the jet interface under the applied electric field is quantified in § 6.3.2, whereas the influence of gravity on the electrified field is discussed in § 6.3.3. Lastly, a summary and the future perspectives are outlined in § 6.4.

6.2 Governing equations and methods

6.2.1 Problem formulation

An axisymmetric liquid jet is considered to discharge into the air with a volumetric flow rate of Q from a nozzle of radius R . The schematic of the flow is shown in figure 6.2. The standard axisymmetric coordinates (r, z) are considered with the origin $(r = 0, z = 0)$ located at the center of the nozzle outlet, and the gravity acceleration, \mathbf{g} , points in the positive z direction. A potential difference V_0 is applied between the nozzle and a ground plate located at a distance H . Both liquid and air are assumed incompressible and Newtonian. The liquid is of density ρ , viscosity μ and surface tension γ , while the surrounding air is of density $\rho_{air} \ll \rho$ and viscosity $\mu_{air} \ll \mu$. The electrical permittivity of air is ϵ_0 , the liquid-to-air electrical permittivity ratio is β , the liquid conductivity is K , and the conductivity of air is neglected. The

interface can be parametrised with its radial position in cylindrical coordinates as $r_{\text{int}}(t, z)$. The

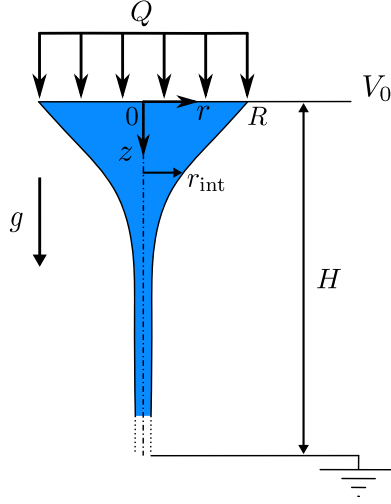


Figure 6.2: Schematic of an electrified jet; the blue area shows the liquid jet surrounded by air, the thin solid line shows the liquid-air interface, and the substrate of zero potential is located at a far distance H downstream the nozzle. The volumetric flow rate of the nozzle is denoted by Q .

dimensionless state vector $\mathbf{q} = (\mathbf{u}^{i,o}, p^{i,o}, \mathcal{R}_{\text{int}}, V^{i,o})^T$ defines the flow at dimensionless time t , where $\mathbf{u}^{i,o}(t, r, z) = (u_r^{i,o}, u_z^{i,o})^T$ denotes the two-dimensional velocity field, $p^{i,o}(t, r, z)$ denotes the pressure, $\mathcal{R}_{\text{int}} = r_{\text{int}}/R$ denotes the dimensionless interface radius, and $V^{i,o}$ denotes the electrical potential. Superscripts i and o denote hereafter the inner liquid domain and the outer air domain, respectively. The equations governing the system are the Navier-Stokes equations for the pressure and velocity fields and the Laplace equation for the potential of the electric field. The state vector and the governing equations are rendered dimensionless using the nozzle radius as characteristic length $\mathcal{L} = R$, viscous time scale $\mathcal{T} = \rho R^2/\mu$, viscous velocity scale $\mathcal{U} = R/T = \mu/\rho R$, viscous stress $\mathcal{P} = \mu^2/\rho R^2$, and the nozzle voltage V_0 .

The dimensionless Navier-Stokes equations in the liquid and air domains, respectively, write

$$\nabla \cdot \mathbf{u}^i = 0, \quad (6.1a)$$

$$\left(\partial_t + \mathbf{u}^i \cdot \nabla \right) \mathbf{u}^i = -\nabla p^i + \nabla^2 \mathbf{u}^i + \frac{Bo}{Oh^2} \mathbf{e}_z, \quad (6.1b)$$

$$\nabla \cdot \mathbf{u}^o = 0, \quad (6.2a)$$

$$\frac{\rho_{\text{air}}}{\rho} \left(\partial_t + \mathbf{u}^o \cdot \nabla \right) \mathbf{u}^o = -\nabla p^o + \frac{\mu_{\text{air}}}{\mu} \nabla^2 \mathbf{u}^o + \frac{\rho_{\text{air}}}{\rho} \frac{Bo}{Oh^2} \mathbf{e}_z, \quad (6.2b)$$

where ∂_j denotes the partial derivative with respect to quantity j , $Oh = \mu/\sqrt{\rho R \gamma}$ is the *Ohnesorge* number and $Bo = \rho g R^2/\gamma$ is the hydrodynamic *Bond* number computed for the liquid.

While Oh compares the viscous forces to the inertial and surface tension forces, Bo compares the gravitational and surface tension forces. We recall that $\rho_{air} \ll \rho$ and $\mu_{air} \ll \mu$.

The dimensionless Laplace equations for the electric potential in the liquid and air write

$$\nabla^2 V^{i,o} = 0. \quad (6.3)$$

From the potentials, the electric fields in the liquid and air domains can be deduced as $\mathbf{E}^{i,o} = -\nabla V^{i,o}$. The motion of charged species is modeled using the leaky dielectric model, assuming that the electric relaxation time is much smaller than the hydrodynamic time scale (Yan et al., 2003; Rosell-Llompart et al., 2018; Herrada et al., 2012). Thus, the charge density in the liquid bulk vanishes and all of the electric charges accumulate at the jet interface (Melcher and Taylor, 1969), where the coupling between the fluid and the electric field occurs through the balance of the electrical (Maxwell) stress and the mechanical stress, which implies

$$\left(\underline{\tau}_m^o - \underline{\tau}_m^i\right) \mathbf{n} + \frac{\chi}{Oh^2} \left(\underline{\tau}_e^o - \beta \underline{\tau}_e^i\right) \mathbf{n} = \frac{1}{Oh^2} (\nabla_s \cdot \mathbf{n}) \mathbf{n}, \quad \text{at } r = \mathcal{R}_{\text{int}}, \quad (6.4)$$

where the mechanical stress tensor reads

$$\underline{\tau}_m^{i,o} = -p^{i,o} \mathbf{I} + \frac{\mu^{i,o}}{\mu} \left(\nabla \mathbf{u}^{i,o} + \nabla^T \mathbf{u}^{i,o} \right), \quad (6.5)$$

$\chi = \epsilon_0 V_0^2 / \gamma R$ denotes the electrical Bond number that compares the electrical forces and capillary ones, $\nabla_s \cdot \mathbf{n}$ is the interface curvature, $\nabla_s = (\mathbf{I} - \mathbf{n} \mathbf{n}^T) \nabla$ denotes the surface gradient operator (see appendix 6.5.1 for further detail), and Maxwell stress reads

$$\underline{\tau}_e^{i,o} = \mathbf{E}^{i,o} \otimes \mathbf{E}^{i,o} - \frac{1}{2} \|\mathbf{E}^{i,o}\|^2 \mathbf{I}, \quad (6.6)$$

where \otimes denotes the tensor product of two vectors and $\|\cdot\|$ denotes the Euclidean norm of a vector. The conservation of surface charge at the interface reads

$$\partial_t \sigma + \nabla_s \cdot (\sigma \mathbf{u}^i) = \alpha \mathbf{E}^i \cdot \mathbf{n}, \quad \text{at } r = \mathcal{R}_{\text{int}}, \quad (6.7)$$

where $\sigma = (\mathbf{E}^o - \beta \mathbf{E}^i)|_{r=\mathcal{R}_{\text{int}}} \cdot \mathbf{n}$ denotes the surface charge density, and $\alpha = K \rho R^2 / \mu \epsilon_0$ denotes the dimensionless electrical conductivity. The boundary conditions to complement the system of governing equations are presented in § 6.2.2.

6.2.2 Numerical method

In this section, the numerical procedure to simulate the melt electrowriting beam is detailed. The state vector is obtained by solving the governing equations (6.1)-(6.7) numerically employing the finite element package COMSOL MultiphysicsTM. The numerical domain is sketched in figure 6.3. The flow behaviour in the vicinity of the nozzle is of the utmost interest, thus the numerical domain is truncated before the flow reaches the collector plate, where the jet

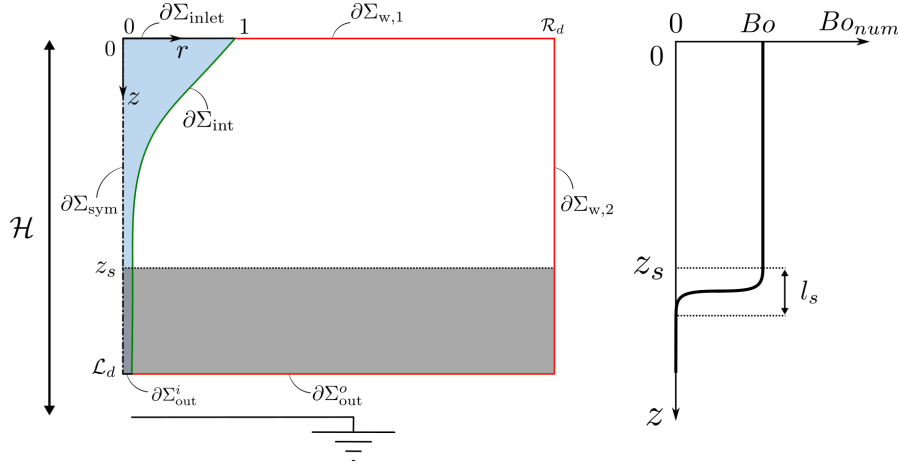


Figure 6.3: Numerical domain; the liquid domain is indicated in blue, the air domain is indicated in white, the red lines indicate the boundaries of the air domain, and the liquid-air interface is indicated by the green continuous line, $\partial\Sigma_{\text{int}}$. Nozzle outlet (domain inlet) is marked as $\partial\Sigma_{\text{inlet}}$, axis is marked as $\partial\Sigma_{\text{sym}}$, top wall is marked as $\partial\Sigma_{w,1}$, side wall is marked as $\partial\Sigma_{w,2}$, liquid outlet is marked as $\partial\Sigma_{\text{out}}^i$ and air outlet is marked as $\partial\Sigma_{\text{out}}^o$. The numerical sponge region is shaded in grey. The right panel shows the numerical variation of the Bond number, Bo_{num} , along the domain and numerical sponge, upstream of the outlet.

has a dimensionless length of \mathcal{L}_d , referred to hereafter as the jet length. The dimensionless distance of the nozzle from the ground potential is denoted by $\mathcal{H} = H/\mathcal{L}$. The shear-free air surrounding the jet is considered up to a far-field radius \mathcal{R}_d from the axis, referred to hereafter as the domain width. Inspired by Ponce-Torres et al. (2018), the dimensions of the computational domain are set to $\{\mathcal{L}_d, \mathcal{R}_d, \mathcal{H}\} = \{20, 40, 40\}$. (Dependence of the solutions on the domain dimensions is presented in appendix 6.5.2.)

The computational domain is discretized using triangular mesh elements, where the grid size is controlled by the vertex densities on the boundaries. The Navier-Stokes equations (6.1)-(6.2) are discretised using the linear Lagrange shape function (P1) for the velocity and the pressure with streamline diffusion stabilization. The Laplace equations (6.3) and the conservation of surface charge equation (6.7) are discretised with the quadratic Lagrange shape function (P2). Such a discretisation results in $\sim 160'000$ degrees of freedom, verified to attain a grid-independent solution (see appendix 6.5.2 for more details).

Numerical boundary conditions

The boundary conditions are as follows:

- **Nozzle:**

The inlet volumetric flow rate is applied as

$$\mathcal{Q} = 2\pi \int_{r=0}^1 u_z^i r \, dr, \quad \text{at } \partial\Sigma_{\text{inlet}}, \quad (6.8)$$

where $\mathcal{Q} = \rho Q / \mu R$ denotes the dimensionless flow rate and the constant voltage is imposed as

$$V^i = 1, \quad \text{at } \partial\Sigma_{\text{inlet}}. \quad (6.9)$$

- **Axis:**

The symmetry condition is applied as

$$u_r^i = \partial_r u_z^i = \partial_r V^i = 0, \quad \text{at } \partial\Sigma_{\text{sym}}. \quad (6.10)$$

- **Walls:**

No slip condition is applied as $\mathbf{u}^{i,o} = \mathbf{0}$ on $\partial\Sigma_{w,1} \cup \partial\Sigma_{w,2}$. On the top wall, the logarithmic drop of potential is applied (Ponce-Torres et al., 2018) that implies

$$V^o = 1 - (1 - \phi(r = \mathcal{R}_d, z = 0)) \frac{\log r}{\log \mathcal{R}_d}, \quad \text{at } \partial\Sigma_{w,1}, \quad (6.11)$$

where $\phi(r, z)$ is the analytical solution for a far-field potential given as

$$\phi(r, z) = -\frac{K_v}{\log(4\mathcal{H})} \log \left(\frac{\sqrt{r^2 + (z/\mathcal{H})^2} + z/\mathcal{H}}{\sqrt{r^2 + (2 - z/\mathcal{H})^2} + (2 - z/\mathcal{H})} \right), \quad (6.12)$$

where $K_v(H)$ is a dimensionless constant given by Gañán-Calvo et al. (1994). Furthermore, the far-field potential at the right-side boundary implies

$$V^o = \phi(r = \mathcal{R}_d, z), \quad \text{at } \partial\Sigma_{w,2}. \quad (6.13)$$

- **Interface:**

The kinematic boundary condition and continuity of the electric potential are imposed as

$$\mathbf{u}^i \cdot \mathbf{n} = \mathbf{u}^o \cdot \mathbf{n}, \quad \text{at } \partial\Sigma_{\text{int}}, \quad (6.14)$$

$$V^i = V^o, \quad \text{at } \partial\Sigma_{\text{int}}, \quad (6.15)$$

respectively, where \mathbf{n} denotes the normal vector to the interface that points from the liquid to the air. The dynamic condition (6.4) is applied using the Lagrange multipliers of quadratic shape function (P2).

- **Outlet:**

Setting the outlet hydrodynamic condition requires further numerical treatments as the liquid jet in presence of gravity varies continuously along the axial direction. A numerical

sponge region is considered to neutralise gravity numerically before the jet reaches the outlet. The Bond number in the numerics is set as $Bo_{num} = Bo(1 - \text{step}(z, z_s, l_s))$. In the domain, for $z < z_s = 15$, this value is set by the hydrodynamic Bond number, and in the sponge region, for $z \geq z_s$, a smooth step function with continuous second derivative, is used to reduce the Bond number to null over a vertical distance of $l_s = 2$ (for further details about the independency of the solution from sponge parameters, see appendix 6.5.2). As a result, the stress-free condition at the jet outlet can be imposed as

$$\underline{\tau}_m^i \mathbf{e}_z = \mathbf{0}, \quad \text{at } \partial \Sigma_{\text{out}}^i. \quad (6.16)$$

Also, the outlet pressure in the air implies

$$\underline{\tau}_m^o \mathbf{e}_z = -p_0 \mathbf{e}_z, \quad \text{at } \partial \Sigma_{\text{out}}^o. \quad (6.17)$$

Additionally, the constant surface charge at the interface is applied (Ponce-Torres et al., 2018) that gives

$$\partial_z \sigma(z = \mathcal{L}_d) = 0, \quad \text{at } \partial \Sigma_{\text{int}}, \quad (6.18)$$

and the far-field potential at the outlet of both fluids implies

$$\partial_z V^{i,o} = \partial_z \phi = -\frac{K_v}{\mathcal{H} \log(4\mathcal{H})} \left(\frac{1}{\sqrt{r^2 + (\mathcal{L}_d/\mathcal{H})^2}} + \frac{1}{\sqrt{r^2 + (2 - \mathcal{L}_d/\mathcal{H})^2}} \right), \quad \text{at } \partial \Sigma_{\text{out}}^{i,o}. \quad (6.19)$$

Numerical solver settings

The time-dependent flow is computed using the laminar two-phase flow module coupled with the moving mesh module and the equation-based PDE solver for the electrical potential in two domains and surface charge density at the interface. An automatic remeshing order is activated if the mesh quality, defined as the volume-to-circumradius ratio (COMSOL MultiphysicsTM, 2020), falls under 0.2. The parallel sparse direct solver (PARDISO) is used for the iterations with a backward differentiation formula that sets the time step automatically with a second-order scheme. In order to avoid the singularity while solving the shear-free interface, we set $\mu^o/\mu^i = \rho^o/\rho^i = 10^{-6}$.

The time-dependent solver was found to be very sensitive to flow initialisation. Several trials to initialise the flow with a cylindrical interface and stagnant air failed at the very first time step. These trials consist of setting various combinations of initialising the flow with electrified or non-electrified fluids, a stagnant or Poiseuille velocity profile, constant or hydrostatic pressure in the liquid body, and a Stokes flow field with a cylindrical interface (obtained by removing the inertia terms from (6.1) and (6.2)). Therefore, the following numerical procedure with three main steps is proposed in order to reduce the solver sensitivity step by step.

1. In the initialisation step, the Navier-Stokes equations are solved with unitary $\{Q, Oh, Bo\}$.

Due to the sensitivity of the solver to the initialisation, this step is divided into two sub-steps as follows.

- First, in the absence of nozzle voltage, the interface is initialised with an arbitrary analytical shape. The velocity and pressure fields are then initialised by solving a steady solver in which the interface is considered a solid slip wall. Several initial shapes of the initial interface are tested, all resulting in the same solution (for more details see appendix 6.5.2).
 - Second, the liquid-air interface conditions are imposed at the interface. The time-dependent computation is pursued until reaching the steady state. With the present initialisation, several tests suggest that the solution reaches saturation within 100 dimensionless time units.
2. Next, the volumetric flow rate \mathcal{Q} is increased to 15 with a smooth step function over the time interval $\Delta t = 10$. Several trials suggest that a time span of 1000 dimensionless units is sufficient for the flow to saturate.
 3. Finally, the fully coupled system of equations is solved for $\{\alpha, \beta\} = \{10, 10\}$. The nozzle voltage is increased by a smooth step function from 0 to 1 over the time interval $\Delta t = 20$, where the maximal time step and relative tolerance of the solver are set to 0.5 and 10^{-6} , respectively. Variation of the flow as a function of the electrical Bond number χ is then pursued through a continuation in this step from 0 to 10^4 until reaching saturation for each χ .

6.3 Results

This section presents the results of the electrified jet simulations. The space of variables $\{Oh, Bo, \mathcal{Q}, \mathcal{H}, \alpha, \beta, \chi\}$ is vast and can be explored following various formalisms. However, in favour of time, only the effect of the electrical Bond number χ is studied in detail where we shed light on the flow after the steady state is achieved.

6.3.1 Influence of the electrical Bond number (χ)

The effect of increasing the electrical Bond number on the flow is depicted in figure 6.4 for $\{Oh, Bo, \mathcal{Q}, \mathcal{H}, \alpha, \beta\} = \{1, 1, 15, 40, 10, 10\}$. In absence of any electrical field, $\chi = 0$, the liquid bulk accelerates as it falls under the effect of gravity, leading to a continuous reduction in the cross-sectional area of the jet (cf. figure 6.4(a)). Increasing χ to 10^4 results in a gradual formation of a stretched meniscus, reminiscent of the Taylor cone, in the vicinity of the nozzle with a high-speed jet emitting downstream, up to 18 times faster than the non-charged jet. A closer look at the meniscus reveals that at the nozzle tip, streamlines fold and for a sufficiently large χ , a recirculation cell appears which grows with increasing χ (cf. figure 6.4(b)). Existence of such a recirculating cell was reported in some previous studies (Herrada et al., 2012; Gupta et al., 2021). At the interface, the liquid velocity is enhanced the most, and the velocity accelerates

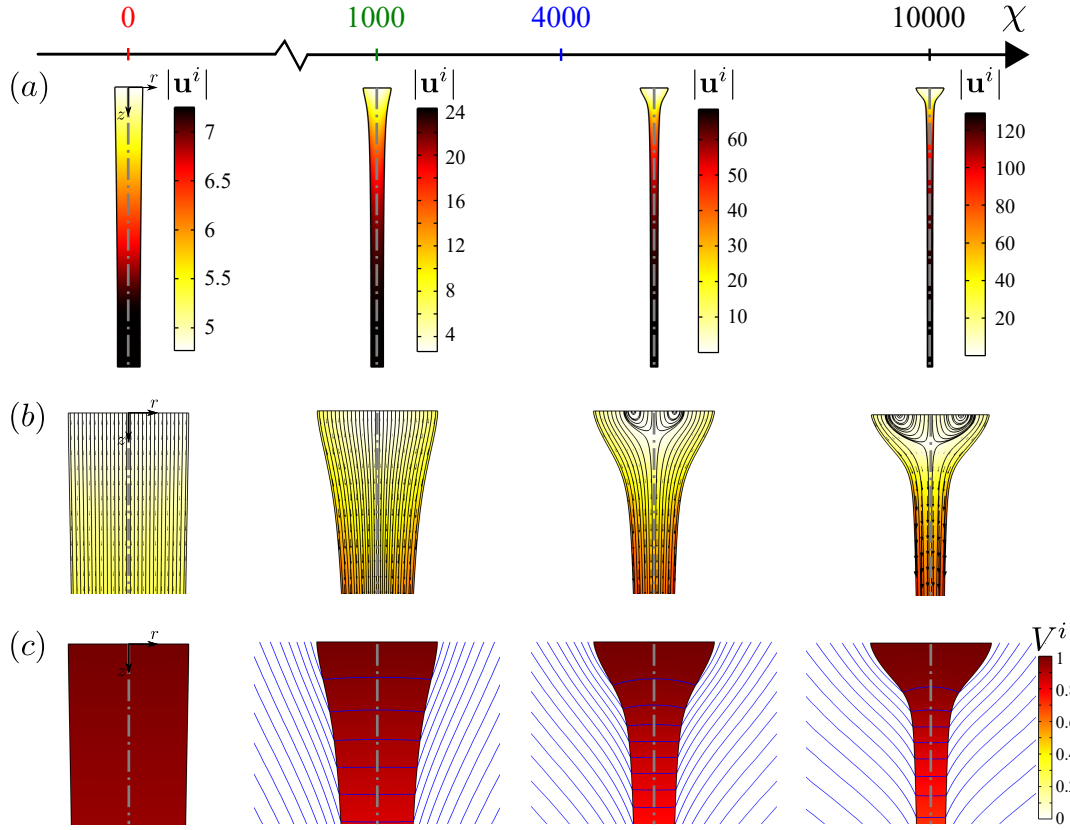


Figure 6.4: Variation of the saturated flow as a function of electrical Bond χ ; (a) Liquid velocity and interface shape; (b) The same field zoomed in the vicinity of the nozzle tip; the black continuous lines show the streamlines and the vectors show the velocity field; (c) Electrical potential in the liquid jet; the blue continuous lines show the contours of electrical potential in the liquid and air.

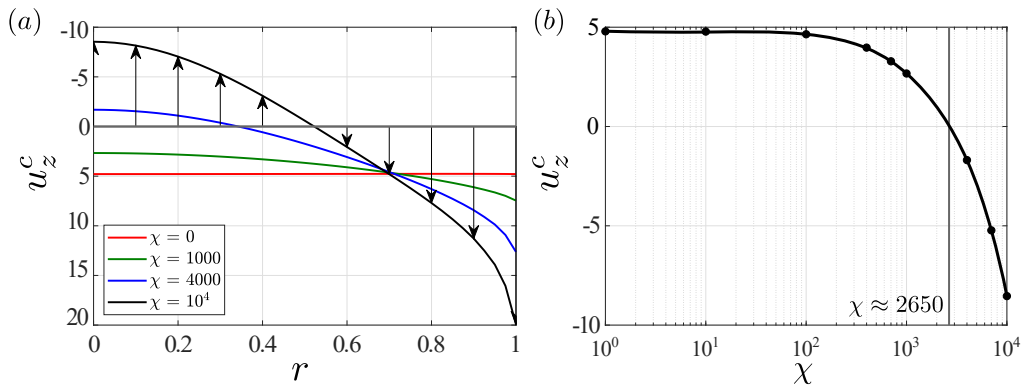


Figure 6.5: (a) Axial velocity profile at the nozzle tip for different χ values for $\{Oh, Bo, Q, \mathcal{H}, \alpha, \beta\} = \{1, 1, 15, 40, 10, 10, 40\}$; the black arrows represent the velocity vectors along the velocity profile for $\chi = 10^4$; upward arrows indicate backflow; (b) Axial velocity at the center of the nozzle outlet, at $(r, z) = (0, 0)$.

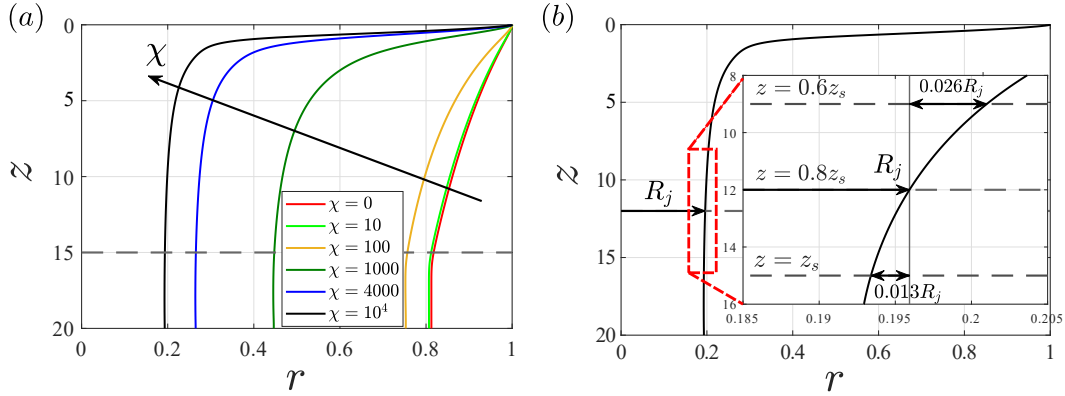


Figure 6.6: (a) Jet interface for various electrical Bond numbers; for $\{Oh, Bo, Q, \mathcal{H}, \alpha, \beta\} = \{1, 1, 15, 40, 10, 10\}$; the dashed gray line marks the beginning of the sponge region, z_s ; (b) Jet interface revisited for $\chi = 10^4$; the inset zooms on the same interface in the vicinity of the sponge, $z_s = 15$.

further along the meniscus. Figure 6.4(c) exhibits a strong discontinuity in the electric field (potential gradient) at the two sides of the interface along the meniscus. We recall from the dynamic condition (6.4) that the influence of the maxwell stress increases proportionally with increasing χ , implying that this strong liquid acceleration is induced by the strong tangential stress applied at the meniscus. The formation of a recirculating cell is therefore a natural response of the flow to conserve the mass flow rate at the nozzle tip. Away from the meniscus, figure 6.4(c) evidences that the electrical potential becomes constant at the cross-section of the jet and merely varies along the axial direction. The air electrical potential, in contrast, varies in both (r, z) directions.

One can distinguish a recirculation cell simply through the backflow at the nozzle tip. Figure 6.5(a) shows that the strongest backflow occurs at the center of the nozzle, $(r, z) = (0, 0)$. Before the recirculation cells form, the nozzle center evidences the least axial velocity. Figure 6.5(b) presents the variation of the liquid axial velocity at the center of the nozzle, $u_z^c = u_z^i(r = 0, z = 0)$, as a function of χ . This minimum velocity remains invariant for $\chi \leq 100$, followed by a decrease as χ increases. The occurrence of the backflow, sign change from positive to negative, takes place for $\chi \approx 2650$, obtained from a logarithmic interpolation of the numerical simulations. Note that this value corresponds only to the present set of parameters, that is $\{Oh, Bo, Q, \mathcal{H}, \alpha, \beta\} = \{1, 1, 15, 40, 10, 10\}$.

6.3.2 Jet interface

The liquid-air interface is depicted in figure 6.6 for several values of χ . The interface can be further investigated from two perspectives: (i) the thin jet radius emitting from the meniscus, and (ii) the cone half-angle. Figure 6.6(a) evidences that higher electrical Bond results in a more

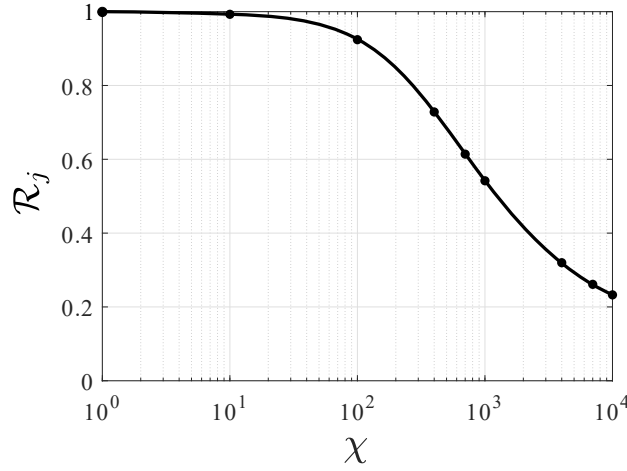


Figure 6.7: (a) Jet radius ratio as a function of the electrical Bond number for $\{Oh, Bo, Q, \mathcal{H}, \alpha, \beta\} = \{1, 1, 15, 40, 10, 10\}$; the black dots show the obtained values for the present simulations, and the continuous line shows the interpolated values. (b) The cone half-angle as a function of the electrical Bond number for the same parameters; the black dashed line shows the theoretical angle obtained from the analysis of Taylor (1964).

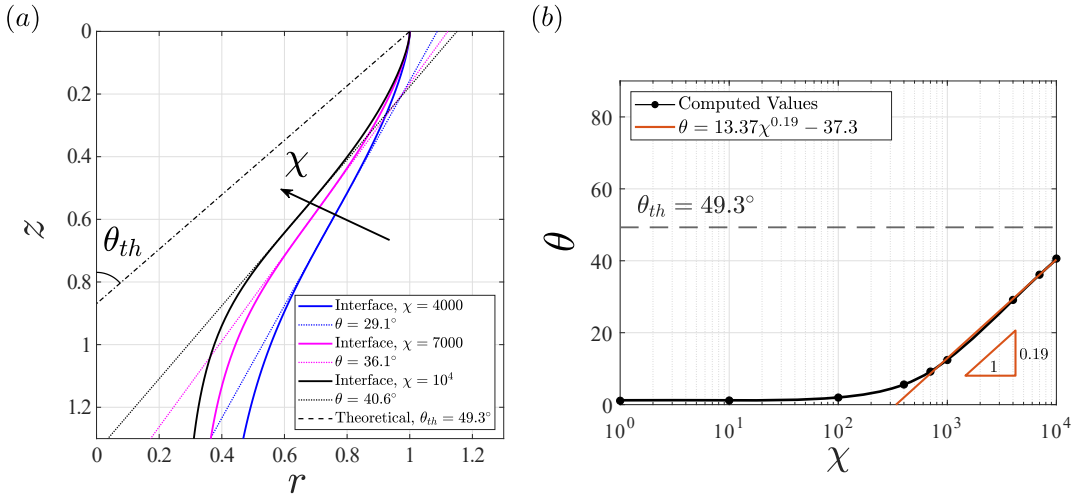


Figure 6.8: (a) The cone half-angle for large χ values; the solids line shows the meniscus; the dotted line shows the tangent line at the inflection point; the black dash-dotted line presents the Taylor cone with the theoretical angle; (b) The cone half-angle as a function of the electrical Bond number for the same parameters as in figure 6.7; the black dashed line shows the theoretical angle obtained from the analysis of Taylor (1964).

distinct conical meniscus of shorter length. The jet thinning almost plateaus downstream of the cone with a variation of only 3.9% for $\chi = 10^4$ over a distance $0.6z_s \leq z \leq z_s$, corresponding to a distance of about 30 times larger than the local jet radius, as shown in figure 6.6(b). Therefore, we set a metric, hereafter referred to as radius ratio, to measure the emerging jet

radius before the numerical sponge, at a distance of $0.8z_s$ downstream of the nozzle, to that of the non-electrified jet at the same flow parameters, i.e. $\mathcal{R}_j = \mathcal{R}_{\text{int}}(z = 0.8z_s, \chi) / \mathcal{R}_{\text{int}}(z = 0.8z_s, \chi = 0)$. This metric represents the downstream jet thinning due to the electric potential. Figure 6.7 presents the radius ratio as a function of χ . The decrease in \mathcal{R}_j takes place for $\chi > 10$ and continues for larger χ in the present study.

Another important characteristic of the interface is the cone half-angle. Note that even though highly electrified menisci in the present study resemble the Taylor cone at intermediate and large χ , they do not exhibit a perfectly straight side as for a cone (cf. figure 6.8(a)). Still, it is insightful to measure the half-angle of the electrified menisci. To do so, the angle between the axis and the tangent line at the inflection point of the meniscus (dotted lines in figure 6.8(a)) is measured as the cone half-angle θ . Figure 6.8(b) presents the variation of θ for several values of χ . This angle begins to vary for $\chi > 100$ coinciding with the flow deceleration at the nozzle center (cf. figure 6.5(a)). Within $700 \leq \chi \leq 10^4$, the variation exhibits a power law, best fitted by $\theta = 13.37\chi^{0.19} - 37.3$. The largest θ found in the present study is $\theta(\chi = 10^4) = 40.6^\circ$ which differs from that calculated in Taylor (1964), $\theta_{th} = 49.3^\circ$. For $\chi > 10^4$, the numerical solver slows down, resulting in very long simulations with tiny time steps of the order of 10^{-8} . Several settings were examined to accelerate the simulation time; increasing the mesh resolution at the nozzle tip, reducing the mesh quality threshold for remeshing, applying the mesh distortion as the remeshing criteria, increasing the solver tolerance, and varying the iterative solver and time stepping settings, to name a few. Yet, no tangible improvement was achieved. Thus, the present study is limited to $0 \leq \chi \leq 10^4$. Considering the same trend observed for θ , it is not impossible that this angle approaches the theoretical one. Nevertheless, it is not clear if the same power law sustains for all ranges of larger χ , in which case it exceeds the theoretical 49.3° . We note that the cone half-angles lower or higher than that of Taylor's calculation have been reported experimentally in the literature (De La Mora, 1992; Pantano et al., 1994).

6.3.3 Effect of the gravity

One of the above-mentioned observations is that the jet radius plateaus upstream of the sponge (cf. figure 6.6(b)). Such an observation is contrary to the typical jet thinning due to gravity. Thus we investigate the effect of gravity on the interface of the electrified jet. Figure 6.9 compares the interface for $Bo = \{0, 1\}$ at the highest electrical Bond in the present study, $\chi = 10^4$. In the absence of gravity, the interface does not alter for the presented electrified jet. This result suggests that the behaviour of the electrified jet is ruled by the electrical Bond number and not the hydrodynamic one. Such an observation is consistent with those of Ponce-Torres et al. (2018); Gamero-Castaño and Magnani (2019a,b); Saville (1997) who neglected the gravity in their computations.

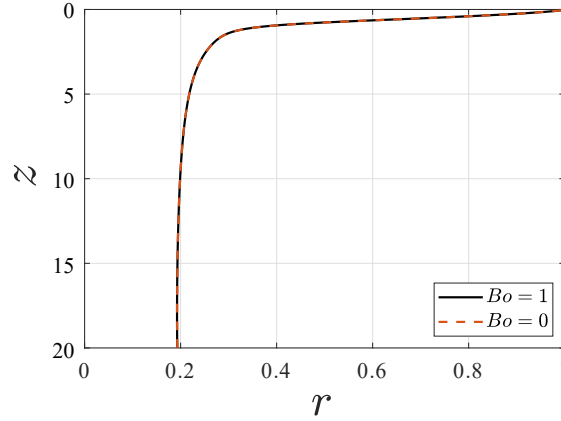


Figure 6.9: Effect of gravity on the jet interface $\{Oh, Q, \mathcal{H}, \alpha, \beta\} = \{1, 15, 40, 10, 10\}$ and $Bo = \{0, 1\}$.

6.4 Summary and perspective

In this chapter, the behaviour of a liquid jet under the action of an electric field was studied. In particular, we investigated the jet thinning and formation of the conical meniscus as electrical stresses increase, by increasing the electrical Bond number. The steady electrified was obtained numerically by solving the time-dependent Navier-Stokes equations until large times in both liquid and surrounding shear-free air in the axisymmetric configuration, coupled with the electric field equations under the leaky-dielectric assumption.

The interface transition was successfully captured from a falling nozzle outlet to the conical meniscus with a fine jet emerging from its tip. For low and intermediate electrical Bond, the flow is mainly governed by the hydrodynamic parameters. On the contrary, it was shown that increasing the electrical Bond results in a strong jump in the electric field at the liquid-air interface. As a result, the liquid flow accelerates tangentially at the interface and the streamlines fold in the vicinity of the nozzle. Exceeding the electrical Bond over a threshold results in the formation of a recirculating cell and backflow at the nozzle tip to preserve the mass flow rate. By increasing the electrical Bond further, this recirculation cell grows while the length of the meniscus shrinks; approaching a cone-like shape. Furthermore, the far downstream jet radius and cone half-angle were measured as a function of the electrical Bond. A strong jet thinning occurs as the electrical Bond increases, resulting in a downstream jet 5 times smaller in radius for the highest electrical Bond studied. The present study reveals that for a sufficiently large electrical Bond, the emitting thin jet reaches a parallel profile downstream of the meniscus where the jet thinning saturates. It was also shown that gravity does not affect the interface at large electrical Bond numbers, whereas the meniscus half-angle increases by increasing the voltage, exhibiting a power law trend with the electrical Bond.

Despite depicting the cone-jet formation, the present study remains a preliminary parametric

study that was restricted to one set of hydrodynamic parameters due to the time constraint. Investigating the full space of dimensionless numbers $\{Oh, Bo, Q, \mathcal{H}, \alpha, \beta, \chi\}$ requires considerable time and computation power. Nevertheless, from a practical perspective, such an investigation can be beneficial to provide the operation maps for electrified jets, as well as correlations for the jet radius, cone half-angle, and charge transport along the meniscus and emitting jet. In the present case, it was observed that exceeding an electrical Bond of 10^4 prohibitively increases the computation time, thus the presented results are limited to this value. Furthermore, the present hydrodynamic parameter set does not correspond to any of the studies in the literature. In spite of several measures taken to reassure the robustness of the developed numerical scheme, it is essential to extend the range of parameters in order to compare and validate the present model with the existing numerical solutions and experimental observations in the literature. Moreover, the present model takes into account the temporal evolution of the flow and opens the door to further investigating the spatio-temporal stability characteristics of the electrified jet.

6.5 Appendix

6.5.1 Surface divergence in the cylindrical coordinates

The surface divergence of a vector \mathbf{u} is defined as the trace of its surface gradient, that is $\nabla_s \cdot \mathbf{u} = \text{tr}(\nabla_s \mathbf{u})$ (Gurtin and Ian Murdoch, 1975; Buscaglia and Ausas, 2011), where $\nabla_s = (\mathbf{I} - \mathbf{n}\mathbf{n}^T)\nabla$ is the surface gradient operator, with \mathbf{n} being the vector normal to the surface and \mathbf{I} denoting the identity tensor. Thus, the surface divergence can be written as

$$\nabla_s \cdot \mathbf{u} = \text{tr}((\mathbf{I} - \mathbf{n}\mathbf{n}^T)\nabla \mathbf{u}). \quad (6.20)$$

Considering the cylindrical coordinates, $\mathbf{u} = u\mathbf{e}_r + v\mathbf{e}_\theta + w\mathbf{e}_z$, $\mathbf{n} = n_r\mathbf{e}_r + n_\theta\mathbf{e}_\theta + n_z\mathbf{e}_z$ and the gradient of a vector writes

$$\nabla \mathbf{u} = \begin{pmatrix} \partial_r u & \frac{1}{r}\partial_\theta u - \frac{v}{r} & \partial_z u \\ \partial_r v & \frac{1}{r}\partial_\theta v + \frac{u}{r} & \partial_z v \\ \partial_r w & \frac{1}{r}\partial_\theta w & \partial_z w \end{pmatrix} \quad (6.21)$$

Hence, the surface divergence in cylindrical coordinates implies

$$\begin{aligned} \nabla_s \cdot \mathbf{u} &= \text{tr} \left(\begin{pmatrix} 1 - n_r^2 & -n_r n_\theta & -n_r n_z \\ -n_\theta n_r & 1 - n_\theta^2 & -n_\theta n_z \\ -n_z n_r & -n_z n_\theta & 1 - n_z^2 \end{pmatrix} \begin{pmatrix} \partial_r u & \frac{1}{r}\partial_\theta u - \frac{v}{r} & \partial_z u \\ \partial_r v & \frac{1}{r}\partial_\theta v + \frac{u}{r} & \partial_z v \\ \partial_r w & \frac{1}{r}\partial_\theta w & \partial_z w \end{pmatrix} \right) \\ &= (1 - n_r^2)\partial_r u - \frac{n_r n_\theta}{r}\partial_\theta u - n_r n_z \partial_z u + \frac{1 - n_\theta^2}{r}u \\ &\quad - n_\theta n_r \partial_r v + \frac{1 - n_\theta^2}{r}\partial_\theta v - n_\theta n_z \partial_z v + \frac{n_\theta n_r}{r}v \\ &\quad - n_z n_r \partial_r w - \frac{n_z n_\theta}{r}\partial_\theta w + (1 - n_z^2)\partial_z w \end{aligned} \quad (6.22)$$

6.5.2 Validation of the numerical model

Influence of the domain dimensions

The size of the computational domain is set with two parameters, namely the jet length \mathcal{L}_d and the domain width \mathcal{R}_d . Their influence on the results is investigated here. The jet interface is shown in figure 6.10(a) for $\mathcal{L}_d = \{20, 22.5, 25\}$, evidencing that the interface is identical for these cases.

Next, the influence of the domain width \mathcal{R}_d on the flow is investigated. Figure 6.10(b) shows the variation of the jet interface is not negligible in terms of \mathcal{R}_d . An explanation for this dependence is how the potential on the upper boundary of the air domain is set through the boundary condition (6.11). The applied potential is plotted in figure 6.10(c) for $\mathcal{R}_d = \{20, 40, 60\}$. The potential decrease from the nozzle to the far field depends on \mathcal{R}_d with the

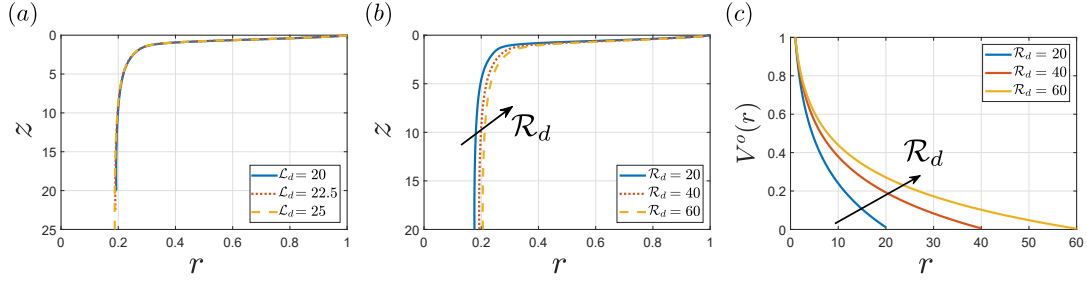


Figure 6.10: Influence of the computational domain dimensions on the jet interface for $\{Oh, Bo, Q, \mathcal{H}, \alpha, \beta, \chi\} = \{1, 1, 15, 40, 10, 10, 10^4\}$; (a) Effect of jet length \mathcal{L}_d ; (b) Effect of the domain width \mathcal{R}_d ; (c) Applied potential on $\partial\Sigma_{w,1}$.

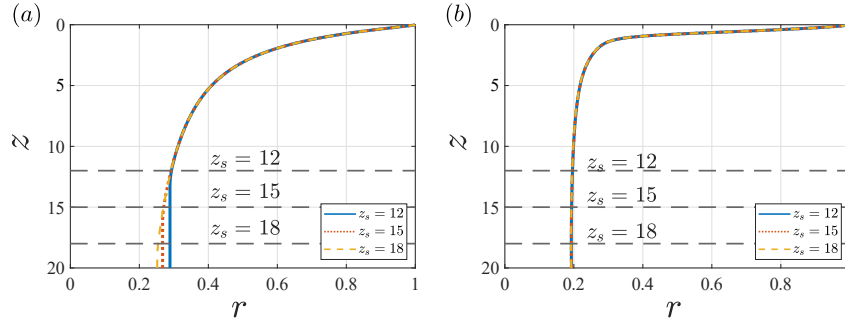


Figure 6.11: Effect of the sponge location on the jet interface for $\{Oh, Bo, \mathcal{H}, \alpha, \beta\} = \{1, 1, 40, 10, 10\}$; (a) Non-electrified jet of small flow rate; $\{Q, \chi\} = \{1, 0\}$; (b) Highly electrified jet; $\{Q, \chi\} = \{15, 10^4\}$.

imposed condition. Therefore, it is essential to replace the employed condition with another choice, converging with increasing \mathcal{R}_d in the far field.

Dependence of the solution on the numerical sponge location

The influence of sponge location, z_s , on the jet interface is investigated here. To this end, the jet interfaces for $\chi = \{0, 10^4\}$ are plotted in figure 6.11 for $z_s = \{12, 15, 18\}$. In both cases of the non-electrified jet with low flow rate (figure 6.11(a)) and electrified jet (figure 6.11(b)), the interface upstream of the sponge region remains identical for these choices of z_s . Thus, the choice of the z_s is sufficiently large to not affect the flow upstream of the sponge.

Mesh dependency of the results

Figure 6.12 presents the mesh dependency of the obtained results. We recall that the number of degrees of freedom N_{dof} is controlled by changing the number of divisions on each boundary. Figure 6.12(a) depicts the jet interface is independent of the mesh for $N_{dof} \geq 93'325$.

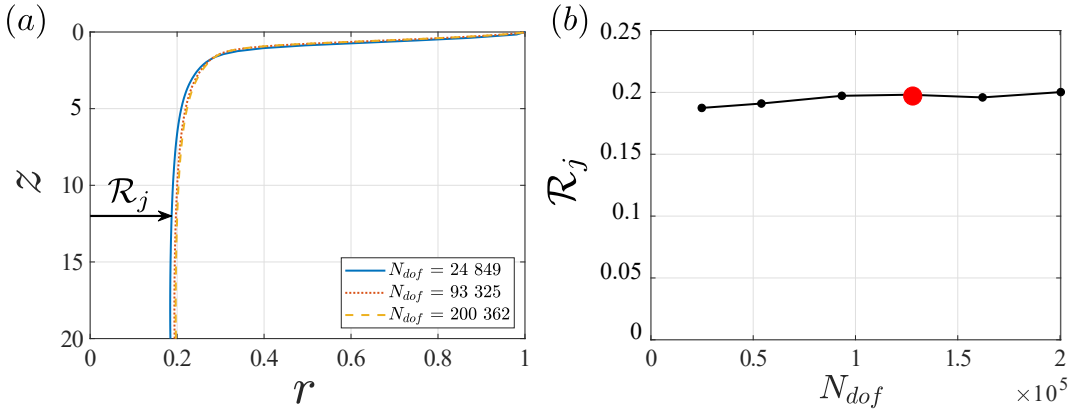


Figure 6.12: Mesh convergence of the obtained results for $\{Oh, Bo, Q, \mathcal{H}, \alpha, \beta, \chi\} = \{1, 1, 15, 40, 10, 10, 10^4\}$ assessed for different mesh refinements; (a) Jet interface; (b) radius ratio; the red point corresponds to the mesh used for the presented results in § 6.3.

Additionally, figure 6.12(b) shows that the radius ratio converges above the same value. In the present study, the results are associated with the grid with $N_{dof} = 162\,125$.

Sensitivity of the flow to the initialised interface

As mentioned in § 6.2.2, in order to ensure the independence of the obtained results on the flow initialisation, three different initial interfaces are examined. The initialised interfaces are as follows.

$$\text{Initial Shape A: } r = \frac{1}{\sqrt{1+z}}$$

$$\text{Initial Shape B: } z = \mathcal{L}_d \left[1 - \log_{10} \left(\frac{1+9r-10r_{end}}{1-r_{end}} \right) \right], \quad r_{end} = 0.3$$

$$\text{Initial Shape C: } z = \mathcal{L}_d \left[1 - \mathcal{L}_d \left(\frac{r-r_{end}}{1-r_{end}} \right)^{1/4} \right], \quad r_{end} = 0.2$$

Figure 6.13 presents the initial interfaces and obtained steady jet interface. The steady interfaces remain identical under the examined initialisations. As the electric potential is applied to this steady interface, the electrified interface is also expected to remain independent from the initialised interface geometry.

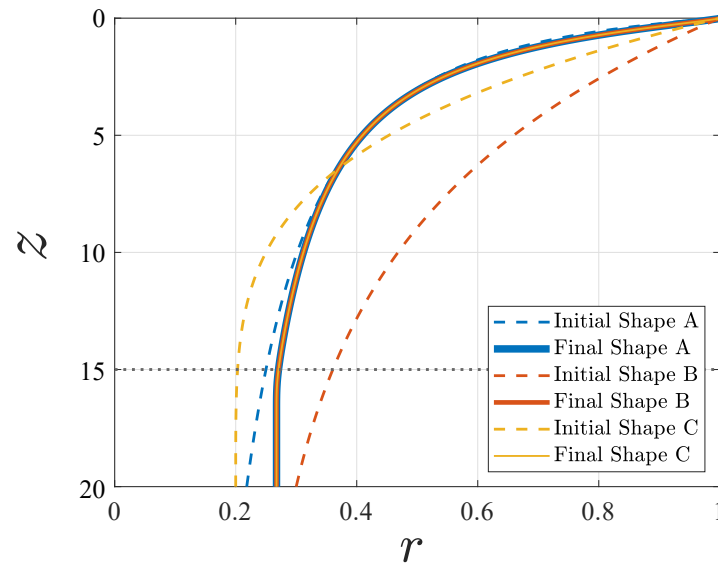


Figure 6.13: Dependence of the obtained non-electrified interface on the interface initialisation; the dashed lines show different initial interfaces and the solid lines show the corresponding steady interface; the black dotted line shows the onset of the sponge region.

7 Conclusions and perspectives

The circumstantial conclusions were drawn at the end of each chapter, so we provide here only a brief summary of each chapter with some future perspectives.

7.1 Conclusions

The principal objective of this thesis was to investigate fully-described laminar flows of column-like free interfaces whose symmetry of the base state is broken and to relate the patterns emerging from these flows to the dynamics of the small perturbations applied to them. **Chapter 2** laid the foundation by developing a parametrisation based on domain perturbation in order to describe hydrodynamic boundary conditions at generic perturbed columnlike interfaces incorporating possible symmetry breaking and time variations. Furthermore, some canonical geometries are highlighted along with their simplified interface conditions. The following chapters employed the representation of **chapter 2** for linear stability analyses of some exemplary interfacial flows of broken symmetry.

In **chapter 3** we studied the gravity-driven cylindrical viscous liquid column flowing down an eccentric vertical fibre. Even though the base interface is axisymmetric, the draining flow is not axisymmetric as a result of the non-homogeneous film thickness surrounding the fibre. We highlighted the influence of fibre eccentricity on the linear stability of the flow. We observed that the Rayleigh-Plateau mode of asymmetric interface destabilises for all eccentricities, forming pearls that are fatter on the thicker film side, whereas the combination of a large eccentricity, large Bond number, and small fibre radius can trigger a whirling mode which forms a single helical pattern along the fibre. While the pearl mode is driven by surface tension and shear according to a perturbative energy analysis, the whirl mode is shear-driven and in spite of increasing surface energy, it can dominate the pearl mode for a large enough eccentricity. Both pearl and whirl modes were observed in experiments using highly viscous silicone oil, exhibiting favourable agreement with the linear theory in both interface shape and wavelength.

In **chapter 4** we investigated the linear stability of the frozen frames of the draining liquid film coating the interior wall of a long horizontal cylinder whose axis is orthogonal to gravity. We accounted in this chapter for the time-varying non-linear distortion of the unperturbed domain as well as non-axisymmetric flow. It was shown that the drainage slows down as the gaseous core approaches the upper side of the wall under the effect of buoyancy. While at small Bond numbers, the interface remains quasi-cylindrical, it flattens horizontally as the Bond number is increased. Linear stability analysis at large times (when the flow is quasi-stationary) demonstrated the symmetry breaking of the Rayleigh-Plateau modes featuring larger modulations at the bottom of the interface which ultimately stabilise at sufficiently large Bond numbers. The critical stabilising Bond number increases for thicker films. Furthermore, we demonstrated that the interface deformation is mandatory for the suppression of instability. The linear analysis exhibits satisfactory quantitative agreement with the experiments of Duclaux et al. (2006) in terms of the stabilisation threshold and the emerging wavelengths. Formerly, their linear analysis using the thin-film equation had failed in predicting the stabilisation threshold and wavelength of the most unstable mode quantitatively. Additionally, it was concluded that flow inertia and transient amplification of perturbations are not significant to alter the stabilisation threshold obtained from the linear analysis.

Following the linear analyses of the previous chapters, we looked in **chapter 5** at a draining viscous liquid film coating the exterior wall of a long horizontal cylinder whose axis is orthogonal to gravity as another example of interface-deforming base flow. Unlike the drainage inside a horizontal tube, the unperturbed draining liquid around a cylinder does not always reach an equilibrium state. The parameter ranges to outstretch toward a steady pendant curtain were sought in terms of the Bond number and mean film thickness, outside of which the pendant curtain goes through a two-dimensional pinch-off. There is a sole unconditional linearly unstable mode that destabilises the quasi-static pendant curtain displaying two distinct behaviours: (i) drainage reversal at small Bond numbers which eventually forms pearls wrapping around the entire circumference of the cylinder, (ii) strong undulations at the bottom of the curtain for large Bond numbers that ultimately forms droplets. In the former, the Rayleigh-Plateau instability dominates the instability, whereas the latter is purely driven by the Rayleigh-Taylor instability. Moderate Bond numbers have a comparable contribution from both instability mechanisms. In consequence, the most linearly unstable wavenumber is selected upon a trade-off between these two instabilities. Generally, surface energy minimisation promotes a smaller wavenumber than potential energy minimisation for the majority of the range of the studied parameters. The results of the linear analysis complement the vision achieved by the non-linear analysis of Weidner et al. (1997) in the thin-film limit. A prediction for the three-dimensional dripping is proposed accordingly by extrapolating the recruitable fluid volume from the most linearly unstable wavelength. Transient growth of the most amplified mode happens to cause no alternation in the droplet dripping prediction.

Lastly, in **chapter 6** we humbly revisited numerically the non-linear evolution of an electrified liquid jet and its smooth transition from a falling filament to the formation of a conical meniscus connected to the nozzle tip that emits a fine downstream jet from its apex.

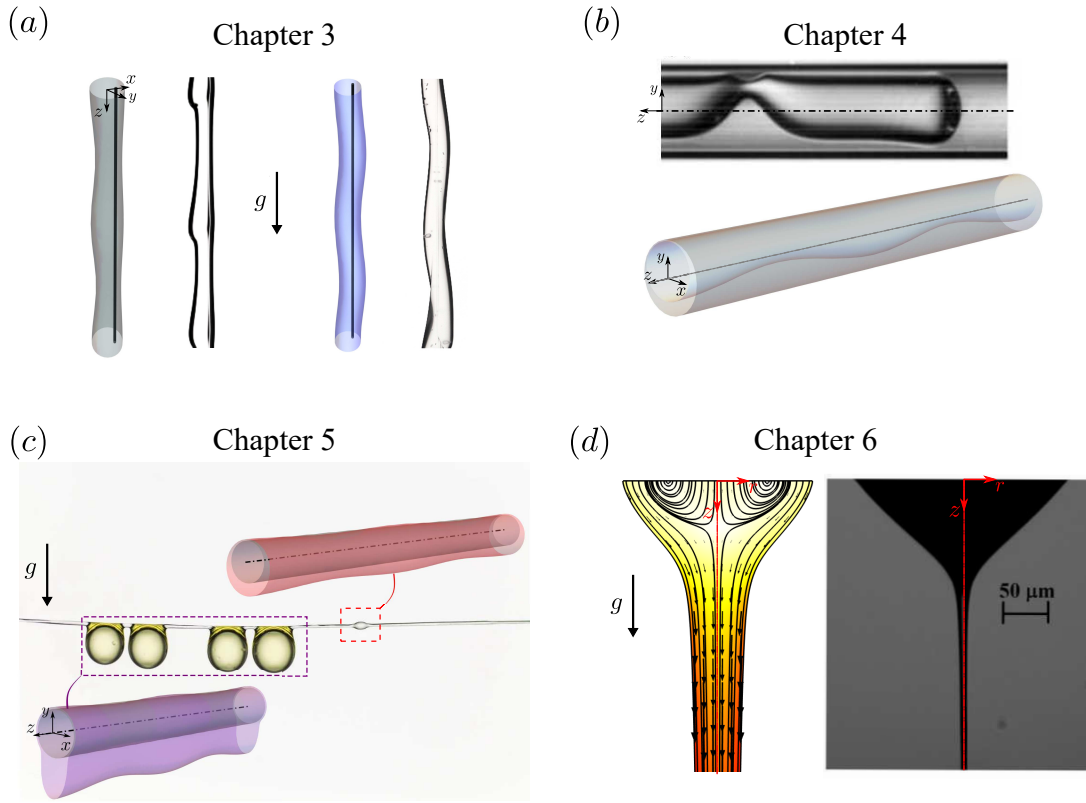


Figure 7.1: Graphical summary of the physical problems addressed in the present thesis (qualitative comparison in all panels): (a) **Chapter 3**: numerical and experimental visualisations of the pearl (left pair) and whirl (right pair) modes; (b) **Chapter 4**: (top) experimental visualisation of the unstable liquid film coating inside a horizontal tube, reprinted from Duclaux et al. (2006); (bottom) numerical visualisation of the perturbed interface obtained from the present linear analysis; (c) **Chapter 5**: an observation of the two distinct patterns emerging from olive oil coating a horizontal fibre along with the visualisation of the modes from the present linear study: a small pearl wrapping around the fibre formed under the Rayleigh-Plateau instability (red numerical interface), four bigger pendant drops formed under Rayleigh-Taylor instability (purple numerical interface), Credit: Hervé Elettro, reprinted from <https://royalsociety.org/journals/publishing-activities/photo-competition/2017-winners-runners-up/micro-imaging/>; (d) **Chapter 6**: (left) numerical and (right) experimental visualisation of the cone-jet under electrical excitation, experiment reprinted from (Herrada et al., 2012).

Figure 7.1 sketches a graphical summary of the flows studied in the present thesis. To conclude, we recall that neither of the flow instabilities addressed in the present thesis could have been comprehensively quantified over a wide range of parameters by using depth-averaging and reduced-order flow equations.

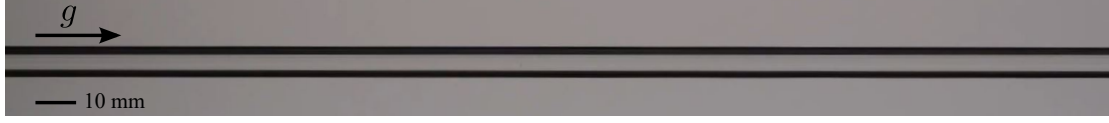


Figure 7.2: Experimentally stable eccentric column; the fibre, located at the vicinity of the interface, is not visible as a result of the highly shifted liquid column.

7.2 Perspectives

In this section, we outline the future directions of the present work. According to the findings of this thesis, two main directions can be appraised: (i) methodological perspectives to extend the present method beyond its restrictions, (ii) numerical and experimental perspectives that use the present work's method for further problems.

7.2.1 Methodological perspectives

The interface parametrisation presented in **chapter 2** evidenced remarkable versatility in enabling the application of the linear stability analysis to the non-symmetric and non-axisymmetric base flows. Despite the large number of problems that can be addressed by the present method, there exist certain failure limits which are already pointed to in **chapter 2**. We recall that the three main origins of the aforementioned limitations root in (i) the necessity of the base interface manifold to be an explicit radially representable surface in a suitably-chosen cylindrical coordinate system, (ii) the prohibition of a vanishing interface radius at any polar cross-section, (iii) the prohibition of the base interface whose polar cross-section is an open curve whose normal vectors at the two endpoints are parallel to each other.

To address some of the restrictions of the present method, one can pursue a generic interface parametrisation for the explicit expressible manifolds in other coordinate systems, i.e. in Cartesian coordinates, spherical coordinates, toroidal coordinates, etc. Eventually, the only remedy to resolve all of the above-mentioned limitations is the development of a local interface parametrisation that relies on the local differential geometry representation of the linearly perturbed manifolds. (See § 2.3 for a detailed discussion.)

7.2.2 Theoretical, numerical and experimental perspectives

Flow down an eccentric vertical fibre

We showed in **chapter 3** the existence of two linearly unstable modes in the gravity-driven flow down an eccentric fibre, namely the pearl and the whirl modes. As the base flow has an axial velocity component, a natural direction to explore is the absolute/convective behaviour of these two modes (Huerre and Monkewitz, 1990; Carriere and Monkewitz, 1999). Such an analysis has been carried out theoretically for a fibre coated with a concentric draining column of small film thickness (Duprat et al., 2007; Gallaire and Brun, 2017), exhibiting good

agreement with the experiments (Duprat et al., 2009). Our experiments on the eccentric fibre evidenced, in the case of the pearl dominance, that for some sets of the drainage hole diameters and fibre eccentricities the appearance of pearls at the very bottom of the experimental apparatus. Decreasing the eccentricity resulted in the pearls being washed down the fibre and sustaining the columnar shape of the interface eccentric with the fibre along the apparatus (cf. figure 7.2); suggesting a convective instability. (For a descriptive movie about these effects, see <https://gfm.aps.org/meetings/dfd-2020/5f4e05c3199e4c091e67ba3f>) We also noted that for the hole diameters with which we could observe pearls and whirls, the concentric column-fibre configuration was always stable, too. Experiments of Gabbard and Bostwick (2021) also indicated an absolute/convective transition in their observed pearls, despite the possibility of the existing contact-line effects on the flow due to the flow feeding mechanism in the set-up. In contrast, when the whirl mode was observed, increasing the eccentricity resulted in a self-sustained unstable interface that periodically deteriorated under the non-linear evolution of the perturbations followed by the reformation of the whirling structures, resembling absolute instability.

Our numerical model can readily examine the spatio-temporal characteristics of the flow for a wide range of fibre aspect ratios, Bond numbers, and fibre eccentricities. Furthermore, we focused only on the inertialess limit in our analysis. Formerly, Ruyer-Quil et al. (2008) demonstrated the wave dynamics and inertia-driven Kapitza instability of the flow down a centred fibre. Including finite inertia in the linear stability analysis of the eccentric fibre would also shed light on its influences on the temporal and spatio-temporal dynamics of the perturbations. Additionally, further investigations are proposed for probing the flows down an eccentric vertical fibre for Non-Newtonian fluids, and in the presence of surfactants and thermally-driven Marangoni effects. Such a study can be of interest in vertical fibre heat exchangers (Zeng et al., 2019), for instance.

From an experimental viewpoint, the present set-up detailed in **chapter 3** can be modified and adapted to probe the absolute/convective nature of both pearl and whirl modes, as well as using less viscous working fluids in order to investigate the effects of inertia on the appearance and characteristics of the whirl mode.

Flow down an inclined fibre

Another direction to pursue is bridging between the findings of **chapter 3** and **chapter 5** by conducting in the linear stability framework both temporal and spatio-temporal analyses of a gravity-driven flow down an inclined cylinder (cf. figure 7.3). For an inclined fiber, tilted with an angle ϕ_g measured between the gravity and fiber axis, the dimensionless conservation of mass and momentum equations can be expressed as

$$\nabla \cdot \mathbf{u} = 0, \quad (7.1)$$

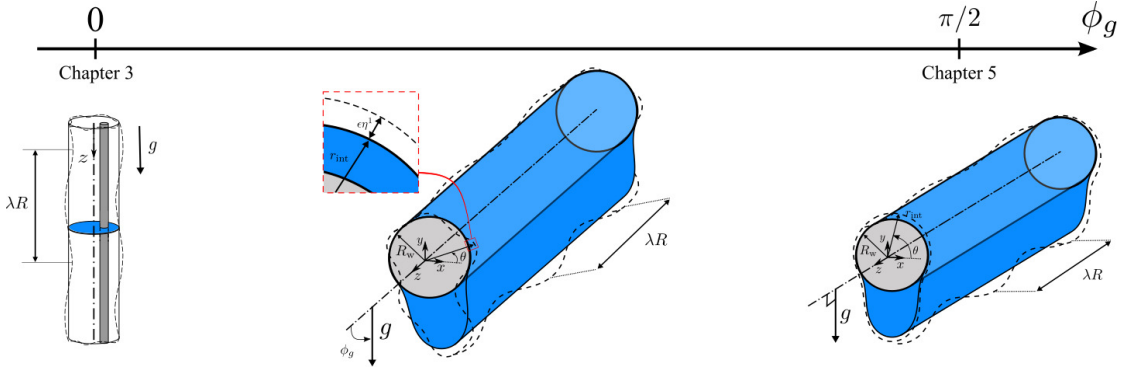


Figure 7.3: Schematic of a the effect of fibre inclination: Stability of a rivulet flowing down an inclined cylinder proposed for future study.

$$\left(\frac{Bo}{Oh}\right)^2 \delta^4 (\partial_t + \mathbf{u} \cdot \nabla) \mathbf{u} = \nabla \cdot \underline{\underline{\tau}} + Bo \cos \phi_g \mathbf{e}_z - Bo \sin \phi_g \mathbf{e}_y, \quad (7.2)$$

under the same dimensional scaling, dimensionless parameters, and boundary conditions presented in **chapter 5**, where \mathbf{e}_y and \mathbf{e}_z denote the unit directions in the positive y and z directions. Studies of **chapter 3** and **chapter 5** are the two limits of $\phi_g = 0$ and $\phi_g = \pi/2$ of this configuration, respectively (cf. figure 7.3). In spite of the non-linear nature of the interface kinematic condition, we can postulate, inspired by the pendant curtain solutions obtained in **chapter 5**, a steady-state parallel base flow with a pendant interface whose velocity field is merely axial, i.e. a single rivulet flowing under the cylinder and parallel to it. Hence, the z -momentum equation is decoupled from the other directions, and the axial velocity can be obtained from the Poisson equation solved in **chapter 3**. Interestingly, such a decoupling results in the pressure field and cross-sectional geometry of the pendant curtain invariant as long as $Bo \sin \phi_g$ is fixed. To put it differently, the interface around a titled cylinder of inclination ϕ_g and the pressure in the cross-section are identical to those of a horizontal cylinder with a Bond number of $Bo \sin \phi_g$. Such a solution satisfies the governing equations and their respective boundary conditions, i.e. no-slip on the cylinder and shear-free interface. Recently Aktershev et al. (2021) investigated the dynamics of the waves traveling along the similar rivulet flow in the thin-film limit by means of Integral Boundary Layer model (Demekhin and Shkadov, 1984) and long-wave approximation (Eggers and Dupont, 1994). The domain of existence of the whirl mode is to be investigated in the range of $0 < \phi_g < \pi/2$, as well as the detailed influence of the inclination on the temporal stability and absolute/convective characteristics of both pearl and whirl modes.

Some preliminary results: Figure 7.4 presents the results obtained from the linear spatio-temporal analysis of a draining rivulet down a cylinder of inclination $\phi_g = \pi/4$, $Bo = 0.0354$ and $\beta = 0.8$. Figure 7.4(a) shows the base flow where the colour code measures the axial velocity field (remembering that the in-plane velocity is null). Figure 7.4(b) presents the leading eigenmode, corresponding to $k = 0.5$ in the dispersion relation of figure 7.4(c). Figure 7.4(d)

presents the saddle point analysis of this eigenmode, evidencing a saddle point (red dot) of positive growth rate, indicating an absolute instability (Huerre and Monkewitz, 1990; Gallaire and Brun, 2017).

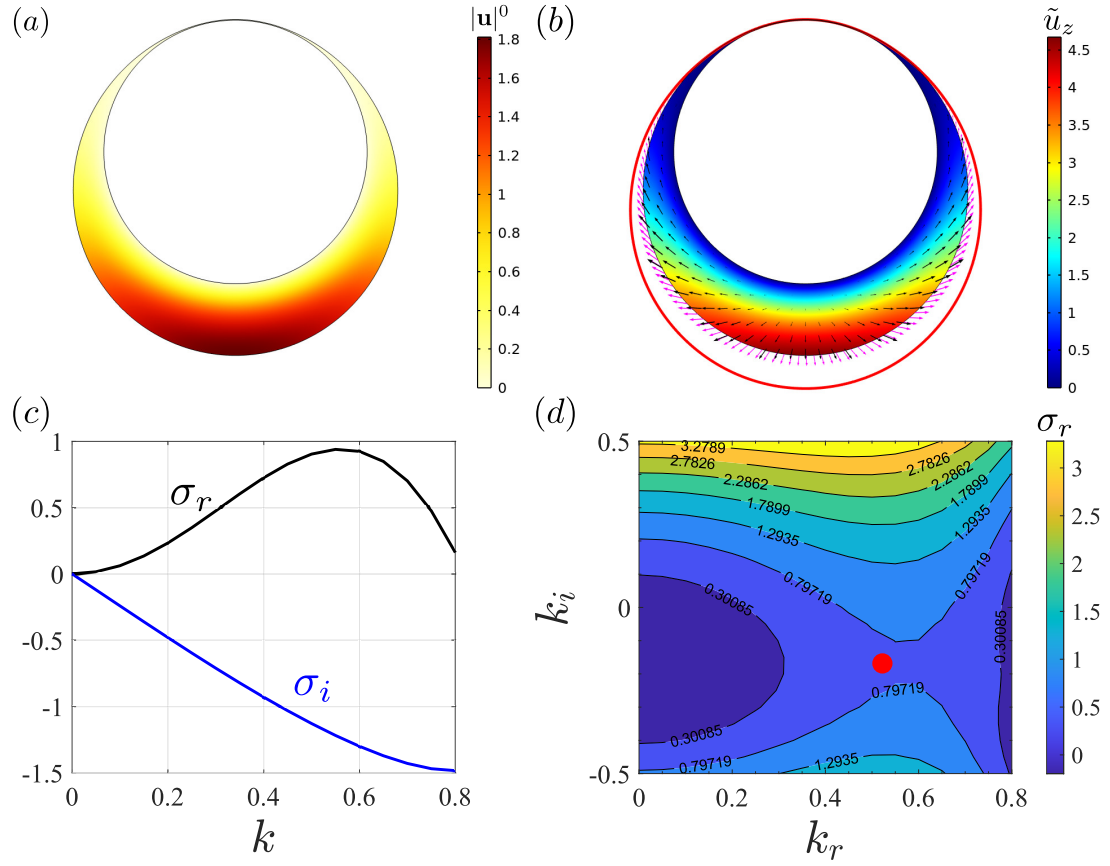


Figure 7.4: Linear stability analysis of a pendant rivulet down an inclined cylinder at $Oh \rightarrow \infty$, $\{Bo, \beta, \phi_g\} = \{0.0354, 0.8, \pi/4\}$. (a) Base flow; the colour map indicates the axial velocity (in-plane velocity is null). (b) The leading eigenmode of $k = 0.5$: colour map indicates the axial eigenvelocity, black vectors present the in-plane eigenflow field, purple arrows show the velocity at the interface, and red line presents the perturbed interface of an arbitrary amplitude. (c) Dispersion curve: growth rate (black) and eigenfrequency (blue) of the unstable mode. (d) Saddle point analysis of the same mode; colour map indicates the growth rate for the space of imaginary wavenumbers; red point presents the saddle point.

Buckling of a viscous sheet or filament

The buckling of a liquid filament falling from a sufficiently high distance on a substrate was first addressed by Taylor (1969). This instability, referred to as the *viscous buckling instability* or *coiling instability* in the case of cylindrical liquid ropes, is present in nature in different length scales, and is important in engineering applications. A few examples are shown in figure 7.5(a). Many studies have addressed for decades the viscous buckling

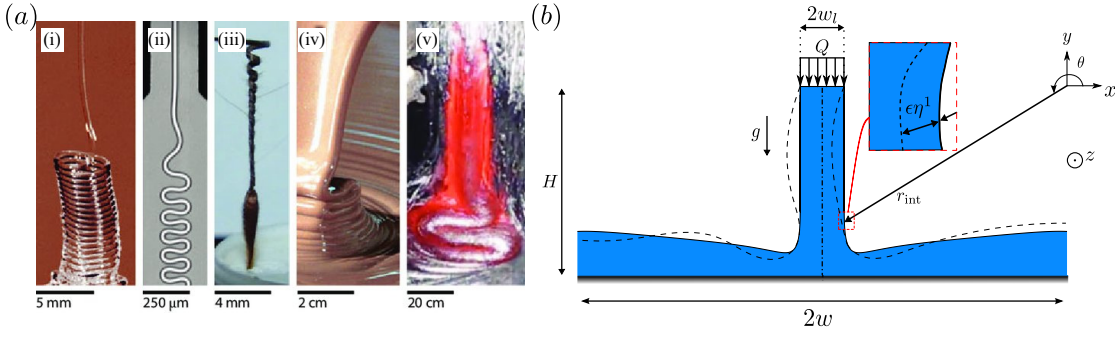


Figure 7.5: Viscous buckling; (a) Examples taken from Ribe (2017): (i) Coiling of silicone oil (Mahadevan et al., 1998); (ii) Folding silicone oil rope in a microchannel; photo by T. Cubaud; (iii) Desiccation-induced coiling of *Erodium cicutarium* seed; (iv) A falling molten chocolate sheet folding; photo by Mars Inc; (v) A falling lava stream folding; photo from the U.S. Geological Survey; (b) Schematic of a viscous sheet falling on a solid substrate proposed for future study.

instability theoretically (Skorobogatiy and Mahadevan, 2000; Ribe, 2003; Jawed et al., 2015), numerically (Tome and McKee, 1999; Batty and Bridson, 2008; de Souza Andrade et al., 2015), and experimentally (Cruickshank and Munson, 1981; Cubaud and Mason, 2006; Le Merrer et al., 2012; Lisicki et al., 2022). A large number of the numerical and theoretical studies employed reduced-order one-dimensional equations for thin viscous sheets under some loading or slender liquid ropes for viscous liquid filaments and sought the threshold and characteristics of the liquid rope coiling (Ribe, 2002, 2004; Ribe et al., 2012). These equations apply the force and torque balance over the midsurface of the viscous sheets and the centreline of the liquid filaments.

On the other hand, Brun et al. (2015) introduced a quasistatic geometrical model for a viscous filament that falls on a moving belt. Their model counted for the radial deflection, the orientation, and the curvature of the path of the filament's contact point with the moving belt, and captured the coiling patterns. The filament buckling does not occur only for falling liquids. Le Merrer et al. (2012) observed experimentally that a non-oscillating (steady) buckling takes place while a fast compression of a liquid column that is pinned to solid walls at its two ends. In a recent study, Tian et al. (2020) highlighted the importance of the capillary effects for the coiling of liquid ropes in certain jet regimes and applied a linear stability analysis on the slender-jet equations (Ribe, 2004). They reported a steady unstable buckling mode, however, their quantified characteristics differ substantially from the experimental observations of Le Merrer et al. (2012). Their study suggests that the nonuniformity along the shape of the liquid rope and the gravity may be the reason for such a mismatch.

We recall that the slender-jet and thin-sheet equations are both long wavelength approximations exploiting a separation of scales in the flow. Even though they impose the natural essence of the velocity profile in the cross-section, they may not be able to fully capture the flow resolution within the falling liquid bulk; analogous to the long-wavelength approximation

(to capture whirls in **chapter 3**) and thin-film model (to analyse the problems in **chapter 4,5**) in presence of strong symmetry breaking. Furthermore, these methods cannot account for the meniscus at the bottom of the liquid sheet/rope where the liquid bulk reaches either a substrate or a liquid bath.

Therefore, we propose the numerical investigation of the viscous coiling via linear stability analysis of the primitive flow equations. To begin with, we suggest a planar configuration to examine the linear stability of a viscous liquid sheet falling from a slot on a liquid bath covering a solid substrate (cf. figure 7.5(b)). The flow symmetry with respect to the vertical midplane (dash-dotted line) allows us to perform a numerical simulation of the flow in the half domain by applying the symmetry condition at the midplane. The base flow can be obtained by following the numerical method we pursued in **chapter 6**, that is, running a time-dependent simulation until reaching a steady-state solution. Then, we seek possible anti-symmetric two-dimensional global unstable modes that correspond to the buckling of the liquid falling sheet. Considering the limitations of our present parametrisation method, discussed in **chapter 2**, we note here that the cross-section of the interface does not form a closed path. Hence, to utilise the present formulation, the origin of the coordinates system should uniquely be located at the intersection of the normal directions of the two endpoints of the interface, as shown in figure 7.5(b). Additionally, such a flow may be prone to the formation of a hydraulic jump. The present formulation can bear hydraulic jumps as long as the base interface remains explicitly radially representable in the selected coordinates reference, i.e. no interface overturning is viewed from the coordinates' origin.

An extension of the proposed study is to carry out numerically the linear stability and transient growth analyses of a round (axisymmetric) liquid filament; either a steady-state rope falling on a liquid bath, or a compressing filament replicating the experiments of Le Merrer et al. (2012). In the axisymmetric configuration, no hydraulic jump can be tolerated with the present interface parametrisation. Nevertheless, several experimental observations reassure us that a hydraulic jump does not occur for a wide range of active buckling regimes (cf. supplementary video of Tian et al. (2020)), therefore, maintaining our motivation to capture the buckling instability using the present numerical model.

Some preliminary results: Figure 7.6 presents some preliminary results of the linear stability analysis of a viscous sheet of aspect ratio $H/w_l = 14$, falling on a flat substrate.

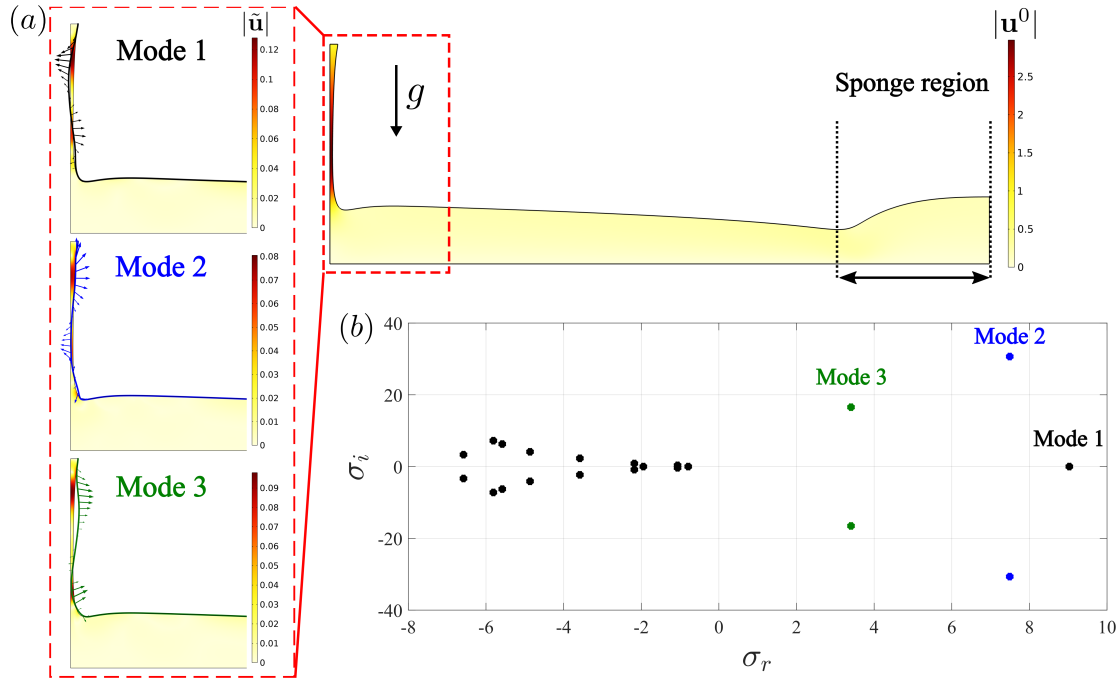


Figure 7.6: Preliminary results of the linear stability analysis of a planar viscous sheet. (a) Base flow in half domain; colour map indicates the base flow velocity magnitude. Inset: three antisymmetric unstable modes; the colour map in the inset indicates the in-plane eigenvelocity magnitude, the solid line represents the perturbed interface of an arbitrary amplitude, and vectors represent the eigenvelocity field at interface. (b) Eigenvalue spectrum.

Bibliography

- Aktershev, S., Alekseenko, S., and Bobylev, A. (2021). Waves in a rivulet falling down an inclined cylinder. *AIChE Journal*, 67(1):e17002.
- Amaouche, M., Mehidi, N., and Amatousse, N. (2007). Linear stability of a two-layer film flow down an inclined channel: a second-order weighted residual approach. *Physics of Fluids*, 19(8):084106.
- Ashmore, J., Hosoi, A. E., and Stone, H. A. (2003). The effect of surface tension on rimming flows in a partially filled rotating cylinder. *Journal of Fluid mechanics*, 479:65–98.
- Augello, L. (2015). *Instability of two-phase co-axial jets at small Reynolds number*. PhD thesis, EPFL.
- Balestra, G. (2018). *Pattern formation in thin liquid films: from coating-flow instabilities to microfluidic droplets*. PhD thesis, EPFL.
- Balestra, G., Badaoui, M., Ducimetière, Y.-M., and Gallaire, F. (2019). Fingering instability on curved substrates: optimal initial film and substrate perturbations. *Journal of Fluid Mechanics*, 868:726–761.
- Balestra, G., Brun, P.-T., and Gallaire, F. (2016). Rayleigh-taylor instability under curved substrates: An optimal transient growth analysis. *Phys. Rev. Fluids*, 1(8):083902.
- Balestra, G., Kofman, N., Brun, P.-T., Scheid, B., and Gallaire, F. (2018a). Three-dimensional rayleigh–taylor instability under a unidirectional curved substrate. *J. Fluid Mech.*, 837:19–47.
- Balestra, G., Nguyen, D. M.-P., and Gallaire, F. (2018b). Rayleigh-taylor instability under a spherical substrate. *Phys. Rev. Fluids*, 3(8):084005.
- Balestra, G., Zhu, L., and Gallaire, F. (2018c). Viscous taylor droplets in axisymmetric and planar tubes: from bretherton’s theory to empirical models. *Microfluidics and Nanofluidics*, 22(6):1–27.
- Barbosa, J. r. and Jader, R. (2018). Fluid flow and thermal phenomena in emerging cooling technologies. In *THMT-18. Turbulence Heat and Mass Transfer 9 Proceedings of the Ninth International Symposium On Turbulence Heat and Mass Transfer*. Begel House Inc.

Bibliography

- Batchelor, G. K. (2000). *An introduction to fluid dynamics*. Cambridge university press.
- Batty, C. and Bridson, R. (2008). Accurate viscous free surfaces for buckling, coiling, and rotating liquids. *Proc. ACM SIGGRAPH/Eurographics Symp. Comput. Animation*.
- Bender, C. M., Orszag, S., and Orszag, S. A. (1999). *Advanced mathematical methods for scientists and engineers I: Asymptotic methods and perturbation theory*, volume 1. Springer Science & Business Media.
- Benilov, E. S. (2006). Does surface tension stabilize liquid films inside a rotating horizontal cylinder? part 2: Multidimensional disturbances. *Studies in Applied Mathematics*, 116(1):1–20.
- Benilov, E. S., Kopteva, N., and O’Brien, S. B. G. (2005). Does surface tension stabilize liquid films inside a rotating horizontal cylinder? *Quarterly Journal of Mechanics and Applied Mathematics*, 58(2):185–200.
- Bertozzi, A. L. and Brenner, M. P. (1997). Linear stability and transient growth in driven contact lines. *Physics of Fluids*, 9(3):530–539.
- Bian, S., Tai, C. F., Halpern, D., Zheng, Y., and Grotberg, J. B. (2010). Experimental study of flow fields in an airway closure model. *Journal of fluid mechanics*, 647:391–402.
- Blair, G. W. S. (1969). Rheology and painting. *Leonardo*, pages 51–53.
- Bober, D. B. and Chen, C.-H. (2011). Pulsating electrohydrodynamic cone-jets: from choked jet to oscillating cone. *Journal of Fluid Mechanics*, 689:552–563.
- Boda, S. K., Li, X., and Xie, J. (2018). Electrospraying an enabling technology for pharmaceutical and biomedical applications: A review. *Journal of Aerosol Science*.
- Boomkamp, P. A. M. and Miesen, R. H. M. (1996). Classification of instabilities in parallel two-phase flow. *International Journal of Multiphase Flow*, 22:67–88.
- Bostwick, J. B. and Steen, P. H. (2018). Static rivulet instabilities: varicose and sinuous modes. *Journal of Fluid Mechanics*, 837:819–838.
- Brochard-Wyart, F., Di Meglio, J. M., and Quéré, D. (1990). Theory of the dynamics of spreading of liquids on fibers. *Journal de Physique*, 51(4):293–306.
- Brun, P. T., Audoly, B., Ribe, N. M., Eaves, T. S., and Lister, J. R. (2015). Liquid ropes: a geometrical model for thin viscous jet instabilities. *Physical review letters*, 114(17):174501.
- Buerkin, C. K., de Vries, I., Raupp, S. M., Scharfer, P., Schabel, W., and Groen, P. (2017). Investigation of interfacial instabilities with a two-layer slide coating process. *Journal of Coatings Technology and Research*, 14(5):991–1001.

- Buscaglia, G. C. and Ausas, R. F. (2011). Variational formulations for surface tension, capillarity and wetting. *Computer Methods in Applied Mechanics and Engineering*, 200(45-46):3011–3025.
- Camassa, R., Marzuola, J., Ogrosky, H. R., and Vaughn, N. (2016). Traveling waves for a model of gravity-driven film flows in cylindrical domains. *Physica D: Nonlinear Phenomena*, 333:254–265.
- Camassa, R., Ogrosky, H. R., and J., O. (2017). Viscous film-flow coating the interior of a vertical tube. part 2. air-driven flow. *Journal of Fluid Mechanics*, 825:1056–1090.
- Camassa, R., Ogrosky, H. R., and Olander, J. (2014). Viscous film flow coating the interior of a vertical tube. part 1. gravity-driven flow. *Journal of fluid mechanics*, 745:682–715.
- Cardoso, V. and J., D. O. (2006). Rayleigh-plateau and gregory-laflamme instabilities of black strings. *Physical review letters*, 96(18):181601.
- Carriere, P. and Monkewitz, P. A. (1999). Convective versus absolute instability in mixed rayleigh-bénard-poiseuille convection. *Journal of Fluid Mechanics*, 384:243–262.
- Carroll, B. J. (1984). The equilibrium of liquid drops on smooth and rough circular cylinders. *Journal of Colloid and Interface Science*, 97(1):195–200.
- Chandrasekhar, S. (2013). *Hydrodynamic and hydromagnetic stability*. Courier Corporation.
- Chang, H.-C. and Demekhin, E. A. (1999). Mechanism for drop formation on a coated vertical fibre. *Journal of Fluid Mechanics*, 380:233–255.
- Charogiannis, A., Denner, F., van Wachem, B. G. M., Kalliadasis, S., Scheid, B., and Markides, C. N. (2018). Experimental investigations of liquid falling films flowing under an inclined planar substrate. *Physical Review Fluids*, 3(11):114002.
- Charru, F. (2011). *Hydrodynamic instabilities*, volume 37. Cambridge University Press.
- Chen, H., Wang, W., Liang, H., and Zhao, Z. (2021). Patterns of interfacial flow around a lubricated rolling point contact region. *Physics of Fluids*, 33(10):102118.
- Chen, T., Buckley, M., Cohen, I., Bonassar, L., and Awad, H. A. (2012). Insights into interstitial flow, shear stress, and mass transport effects on ecm heterogeneity in bioreactor-cultivated engineered cartilage hydrogels. *Biomechanics and modeling in mechanobiology*, 11(5):689–702.
- Chinju, H., Uchiyama, K., and Mori, Y. H. (2000). “string-of-beads” flow of liquids on vertical wires for gas absorption. *AIChE journal*, 46(5):937–945.
- Cloupeau, M. and Prunet-Foch, B. (1989). Electrostatic spraying of liquids in cone-jet mode. *Journal of Electrostatics*, 22(2):135–159.
- COMSOL MultiphysicsTM (2020). COMSOL Multiphysics Reference Manual.

Bibliography

- Cordero, M. L., Gallaire, F., and Baroud, C. N. (2011). Quantitative analysis of the dripping and jetting regimes in co-flowing capillary jets. *Physics of Fluids*, 23(9):094111.
- Craster, R. V. and Matar, O. K. (2006). On viscous beads flowing down a vertical fibre. *Journal of Fluid Mechanics*, 553:85–105.
- Cruickshank, J. and Munson, B. R. (1981). Viscous fluid buckling of plane and axisymmetric jets. *Journal of Fluid Mechanics*, 113:221–239.
- Cruz-Mazo, F., Montanero, J. M., and Gañán Calvo, A. M. (2016). Monosized dripping mode of axisymmetric flow focusing. *Phys. Rev. E*, 94:053122.
- Cubaud, T. and Mason, T. G. (2006). Folding of viscous threads in diverging microchannels. *Physical review letters*, 96(11):114501.
- Daners, D. (2008). Domain perturbation for linear and semi-linear boundary value problems. In *Handbook of differential equations: stationary partial differential equations*, volume 6, pages 1–81. Elsevier.
- De La Mora, J. F. (1992). The effect of charge emission from electrified liquid cones. *Journal of Fluid Mechanics*, 243:561–574.
- De La Mora, J. F. and Loscertales, I. G. (1994). The current emitted by highly conducting taylor cones. *Journal of Fluid Mechanics*, 260:155–184.
- De Meijer, M. (2004). A review of interfacial aspects in wood coatings: wetting, surface energy, substrate penetration and adhesion. In *COST E18 Final Seminar*, pages 26–27.
- de Souza Andrade, L. F., Sandim, M., Petronetto, F., Pagliosa, P., and Paiva, A. (2015). Particle-based fluids for viscous jet buckling. *Computers & Graphics*, 52:106–115.
- Del Guercio, G., Cossu, C., and Pujals, G. (2014). Optimal streaks in the circular cylinder wake and suppression of the global instability. *Journal of fluid mechanics*, 752:572–588.
- Demekhin, E. A. and Shkadov, V. Y. (1984). Three-dimensional waves in a liquid flowing down a wall. *Fluid Dynamics*, 19(5):689–695.
- Ding, H., Xie, P., Ingham, D., Ma, L., and Pourkashanian, M. (2018a). Flow behaviour of drop and jet modes of a laminar falling film on horizontal tubes. *International Journal of Heat and Mass Transfer*, 124:929–942.
- Ding, Z. and Liu, Q. (2011). Stability of liquid films on a porous vertical cylinder. *Physical Review E*, 84(4):046307.
- Ding, Z., Liu, R., Wong, T. N., and Yang, C. (2018b). Absolute instability induced by marangoni effect in thin liquid film flows on vertical cylindrical surfaces. *Chemical Engineering Science*, 177:261–269.

- Dobson, M. K. and Chato, J. C. (1998). Condensation in smooth horizontal tubes. *ASME. J. Heat Transfer*, 120(1):193—213.
- Drazin, P. G. (2002). *Introduction to hydrodynamic stability*, volume 32. Cambridge university press.
- Duclaux, V., Clanet, C., and Quéré, D. (2006). The effects of gravity on the capillary instability in tubes. *Journal of Fluid Mechanics*, 556:217–226.
- Duprat, C. (2009). *Instabilités d'un film liquide en écoulement sur une fibre verticale [physics.flu-dyn]*. PhD thesis, Université Pierre et Marie Curie-Paris VI.
- Duprat, C., Ruyer-Quil, C., and Giorgiutti-Dauphiné, F. (2009). Experimental study of the instability of a film flowing down a vertical fiber. *The European Physical Journal Special Topics*, 166(1):63–66.
- Duprat, C., Ruyer-Quil, C., Kalliadasis, S., and Giorgiutti-Dauphiné, F. (2007). Absolute and convective instabilities of a viscous film flowing down a vertical fiber. *Physical review letters*, 98(24):244502.
- Eames, I. and Flor, J.-B. (2011). New developments in understanding interfacial processes in turbulent flows.
- Eggers, J. and Dupont, T. F. (1994). Drop formation in a one-dimensional approximation of the navier–stokes equation. *Journal of fluid mechanics*, 262:205–221.
- Eggers, J. and Villiermaux, E. (2008). Physics of liquid jets. *Reports on progress in physics*, 71(3):036601.
- Eletto, H., Neukirch, S., Vollrath, F., and Antkowiak, A. (2016). In-drop capillary spooling of spider capture thread inspires hybrid fibers with mixed solid–liquid mechanical properties. *Proceedings of the National Academy of Sciences*, 113(22):6143–6147.
- Evans, P. L., Schwartz, L. W., and Roy, R. V. (2004). Steady and unsteady solutions for coating flow on a rotating horizontal cylinder: Two-dimensional theoretical and numerical modeling. *Physics of Fluids*, 16(8):2742–2756.
- Fermigier, M., Limat, L., Wesfreid, J. E., Boudinet, P., and Quilliet, C. (1992). Two-dimensional patterns in rayleigh-taylor instability of a thin layer. *Journal of Fluid Mechanics*, 236:349–383.
- Frenkel, A. L. (1992). Nonlinear theory of strongly undulating thin films flowing down vertical cylinders. *EPL (Europhysics Letters)*, 18(7):583.
- Frenkel, A. L., Babchin, A. J., Levich, B. G., Shlang, T., and Sivashinsky, G. I. (1987). Annular flows can keep unstable films from breakup: nonlinear saturation of capillary instability. *Journal of colloid and interface science*, 115(1):225–233.

Bibliography

- Gañán Calvo, A. M. (1997). Cone-jet analytical extension of Taylor's electrostatic solution and the asymptotic universal scaling laws in electrospraying. *Phys. Rev. Lett.*, 79:217–220.
- Gabbard, C. T. and Bostwick, J. B. (2021). Asymmetric instability in thin-film flow down a fiber. *Physical Review Fluids*, 6(3):034005.
- Gallaire, F. and Brun, P.-T. (2017). Fluid dynamic instabilities: theory and application to pattern forming in complex media. *Philosophical Transactions of the Royal Society A: Mathematical, Physical and Engineering Sciences*, 375(2093):20160155.
- Gallino, G. (2018). *When droplets deform, break up and propel microswimmers*. PhD thesis, EPFL.
- Gallino, G., Zhu, L., and Gallaire, F. (2016). The stability of a rising droplet: an inertialess non-modal growth mechanism. *Journal of Fluid Mechanics*, 786.
- Gamero-Castaño, M. and Magnani, M. (2019a). The minimum flow rate of electrosprays in the cone-jet mode. *Journal of Fluid Mechanics*, 876:553–572.
- Gamero-Castaño, M. and Magnani, M. (2019b). Numerical simulation of electrospraying in the cone-jet mode. *Journal of Fluid Mechanics*, 859:247–267.
- Gañán-Calvo, A. M. (1999). The surface charge in electrospraying: its nature and its universal scaling laws. *Journal of Aerosol Science*, 30(7):863–872.
- Gañán-Calvo, A. M., Lasheras, J. C., Dávila, J., and Barrero, A. (1994). The electrostatic spray emitted from an electrified conical meniscus. *Journal of Aerosol Science*, 25(6):1121–1142.
- Gañán-Calvo, A. M., López-Herrera, J., and Riesco-Chueca, P. (2006). The combination of electrospray and flow focusing. *Journal of Fluid Mechanics*, 566:421–445.
- Gañán-Calvo, A. M., López-Herrera, J. M., Herrada, M. A., Ramos, A., and Montanero, J. M. (2018a). Review on the physics electrospray: from electrokinetics to the operating conditions of single and coaxial Taylor cone-jets, and ac electrospray. *Journal of Aerosol Science*.
- Gañán-Calvo, A. M., López-Herrera, J. M., Herrada, M. A., Ramos, A., and Montanero, J. M. (2018b). Review on the physics of electrospray: from electrokinetics to the operating conditions of single and coaxial Taylor cone-jets, and AC electrospray. *Journal of Aerosol Science*, 125:32–56.
- Gañán-Calvo, A. M. and Montanero, J. (2009). Revision of capillary cone-jet physics: Electrospray and flow focusing. *Physical Review E*, 79(6):066305.
- Garvine, R. W. (1974). Dynamics of small-scale oceanic fronts. *Journal of Physical Oceanography*, 4(4):557–569.
- Gilet, T., Terwagne, D., and Vandewalle, N. (2009). Digital microfluidics on a wire. *Applied physics letters*, 95(1):014106.

- Goldsmith, H. L. and Mason, S. G. (1963). The flow of suspensions through tubes. ii. single large bubbles. *Journal of Colloid Science*, 18(3):237–261.
- Gomez, A. and Deng, W. (2011). Fundamentals of cone-jet electrospray. *Aerosol Measurement: Principles, Techniques, and Applications*, pages 435–448.
- Goren, S. L. (1962). The instability of an annular thread of fluid. *Journal of Fluid Mechanics*, 12(2):309–319.
- Grünig, J., Lyagin, E., Horn, S., Skale, T., and Kraume, M. (2012). Mass transfer characteristics of liquid films flowing down a vertical wire in a counter current gas flow. *Chemical engineering science*, 69(1):329–339.
- Gupta, A., Mishra, B. K., and Panigrahi, P. (2021). Internal and external hydrodynamics of Taylor cone under constant and alternating voltage actuation. *Physics of Fluids*, 33(11):117118.
- Gurtin, M. E. and Ian Murdoch, A. (1975). A continuum theory of elastic material surfaces. *Archive for Rational Mechanics and Analysis*, 57(4):291–323.
- Haefner, S., Benzaquen, M., Bäümchen, O., Salez, T., Peters, R., McGraw, J. D., Jacobs, K., Raphaël, E., and Dalnoki-Veress, K. (2015). Influence of slip on the plateau-rayleigh instability on a fibre. *Nature communications*, 6(1):1–6.
- Halpern, D. and Grotberg, J. B. (2003). Nonlinear saturation of the rayleigh instability due to oscillatory flow in a liquid-lined tube. *Journal of Fluid Mechanics*, 492:251–270.
- Hansen, E. B. and Kelmanson, M. A. (1994). Steady, viscous, free-surface flow on a rotating cylinder. *Journal of Fluid mechanics*, 272:91–108.
- Harrison, W. J. (1919). The hydrodynamical theory of the lubrication of a cylindrical bearing under variable load and of a pivot bearing. *Transactions of the Cambridge Philosophical Society*, 22(18):373–388.
- Heil, M., Hazel, A. L., and Smith, J. A. (2008). The mechanics of airway closure. *Respiratory physiology & neurobiology*, 163(1-3):214–221.
- Herrada, M. A., López-Herrera, J. M., Gañán-Calvo, A. M., Vega, E. J., Montanero, J. M., and Popinet, S. (2012). Numerical simulation of electrospray in the cone-jet mode. *Physical Review E*, 86(2):026305.
- Herwitz, S. R. (1987). Raindrop impact and water flow on the vegetative surfaces of trees and the effects on stemflow and throughfall generation. *Earth surface processes and landforms*, 12(4):425–432.
- Hester, J. J. (2008). The crab nebula: an astrophysical chimera. *Annu. Rev. Astron. Astrophys.*, 46:127–155.

Bibliography

- Hibara, A., Fukuyama, M., Chung, M., Priest, C., and Proskurnin, M. A. (2016). Interfacial phenomena and fluid control in micro/nanofluidics. *Analytical Sciences*, 32(1):11–21.
- Hoffmann, P. (2017). Powder focusing for beam induced laser 3d printing. Technical report, Strategic Focus Area (SFA) Advanced Manufacturing.
- Hooper, A. P. and Boyd, W. G. C. (1983). Shear-flow instability at the interface between two viscous fluids. *Journal of Fluid Mechanics*, 128:507–528.
- Hosseini, S. M., Alizadeh, R., Fatehifar, E., and Alizadehdakhl, A. (2014). Simulation of gas absorption into string-of-beads liquid flow with chemical reaction. *Heat and Mass Transfer*, 50(10):1393–1403.
- Hrynevich, A., Elçi, B., Haigh, J. N., McMaster, R., Youssef, A., Blum, C., Blunk, T., Hochleitner, G., Groll, J., and Dalton, P. D. (2018). Dimension-based design of melt electrowritten scaffolds. *Small*, 14(22):1800232.
- Huerre, P. and Monkewitz, P. A. (1990). Local and global instabilities in spatially developing flows. *Annual review of fluid mechanics*, 22(1):473–537.
- Jambon-Puillet, E., Bouwhuis, W., Snoeijer, J. H., and Bonn, D. (2019). Liquid helix: how capillary jets adhere to vertical cylinders. *Physical review letters*, 122(18):184501.
- Jambon-Puillet, E., Ledda, P. G., Gallaire, F., and Brun, P.-T. (2021). Drops on the underside of a slightly inclined wet substrate move too fast to grow. *Physical review letters*, 127(4):044503.
- Jawed, M. K., Brun, P. T., and Reis, P. M. (2015). A geometric model for the coiling of an elastic rod deployed onto a moving substrate. *Journal of Applied Mechanics*, 82(12):121007.
- Joseph, D. D., Bai, R., Chen, K. P., Renardy, Y. Y., et al. (1997). Core-annular flows. *Annual Review of Fluid Mechanics*, 29(1):65–90.
- Joseph, D. D. and Renardy, Y. Y. (2013a). *Fundamentals of two-fluid dynamics: Part i: Mathematical theory and applications*, volume 3. Springer Science & Business Media.
- Joseph, D. D. and Renardy, Y. Y. (2013b). *Fundamentals of two-fluid dynamics: part II: lubricated transport, drops and miscible liquids*, volume 4. Springer Science & Business Media.
- Kaita, R., Berzak, L., Boyle, D., Gray, T., Granstedt, E., Hammett, G., Jacobson, C. M., Jones, A., Kozub, T., Kugel, H., et al. (2010). Experiments with liquid metal walls: Status of the lithium tokamak experiment. *Fusion Engineering and Design*, 85(6):874–881.
- Kapitza, P. L. (1949). Wave flow of thin viscous liquid films. iii. experimental study of wave regime of a flow. *J. Exp. Theor. Phys.*, 19(2):105–120.
- Kataoka, D. E. and Troian, S. M. (1997). A theoretical study of instabilities at the advancing front of thermally driven coating films. *Journal of colloid and interface science*, 192(2):350–362.
- Kilburn, C. R. J. (2000). Lava flows and flow fields. *Encyclopedia of volcanoes*, pages 291–305.

- Kliakhandler, I. L., Davis, S. H., and Bankoff, S. G. (2001). Viscous beads on vertical fibre. *Journal of Fluid Mechanics*, 429:381–390.
- Kneller, B., Nasr-Azadani, M. M., Radhakrishnan, S., and Meiburg, E. (2016). Long-range sediment transport in the world’s oceans by stably stratified turbidity currents. *Journal of Geophysical Research: Oceans*, 121(12):8608–8620.
- Kreyszig, E. (2013). *Differential geometry*. Courier Corporation.
- Larson, R. H. and Richardson, H. H. (1962). A preliminary study of whirl instability for pressurized gas bearings. *ASME. J. Basic Eng.*, 84(4):511—518.
- Le Merrer, M., Quéré, D., and Clanet, C. (2012). Buckling of viscous filaments of a fluid under compression stresses. *Physical review letters*, 109(6):064502.
- Ledda, P. G. (2022). *From coating flow patterns to porous body wake dynamics via multiscale models*. PhD thesis, EPFL.
- Ledda, P. G. and Galleire, F. (2021). Secondary instability in thin film flows under an inclined plane: growth of lenses on spatially developing rivulets. *Proceedings of the Royal Society A*, 477(2251):20210291.
- Ledda, P. G., Pezzulla, M., Jambon-Puillet, E., Brun, P. T., and Galleire, F. (2022). Gravity-driven coatings on curved substrates: a differential geometry approach. *Journal of Fluid Mechanics*.
- Lee, A., Brun, P. T., Marthelot, J., Balestra, G., Galleire, F., and Reis, P. M. (2016). Fabrication of slender elastic shells by the coating of curved surfaces. *Nature communications*, 7(1):1–7.
- Lerisson, G., Ledda, P. G., Balestra, G., and Galleire, F. (2019). Dripping down the rivulet. *Physical Review Fluids*, 4(10):100504.
- Levy, R., Hill, D. B., Forest, M. G., and Grotberg, J. B. (2014). Pulmonary fluid flow challenges for experimental and mathematical modeling.
- Lewis, D. J. (1950). The instability of liquid surfaces when accelerated in a direction perpendicular to their planes. ii. *Proceedings of the Royal Society of London. Series A. Mathematical and Physical Sciences*, 202(1068):81–96.
- Li, F., Yin, X.-Y., and Yin, X.-Z. (2011). Axisymmetric and non-axisymmetric instability of an electrically charged viscoelastic liquid jet. *Journal of non-newtonian fluid mechanics*, 166(17-18):1024–1032.
- Li, W. and Kumar, S. (2018). Three-dimensional surfactant-covered flows of thin liquid films on rotating cylinders. *Journal of Fluid Mechanics*, 844:61–91.
- Limat, L. (1993). Instabilité d’un liquide suspendu sous un surplomb solide: influence de l’épaisseur de la couche. *Comptes rendus de l’Académie des sciences. Série 2, Mécanique, Physique, Chimie, Sciences de l’univers, Sciences de la Terre*, 317(5):563–568.

Bibliography

- Limat, L., Jenffer, P., Dagens, B., Touron, E., Fermigier, M., and Wesfreid, J. E. (1992). Gravitational instabilities of thin liquid layers: dynamics of pattern selection. *Physica D: Nonlinear Phenomena*, 61(1-4):166–182.
- Lisicki, M., Adamowicz, L., Herczyński, A., and Moffatt, H. K. (2022). Viscous thread falling on a spinning surface. *Symmetry*, 14(8):1550.
- Liu, R. and Ding, Z. (2017). Stability of viscous film flow coating the interior of a vertical tube with a porous wall. *Physical Review E*, 95(5):053101.
- Liu, R. and Ding, Z. (2021). Coating flows down a vertical fibre: towards the full navier–stokes problem. *Journal of Fluid Mechanics*, 914.
- López-Herrera, J., M.A., H., J.M., M., N., R.-M., and Gañán-Calvo, A. M. (2013). On the validity and applicability of the one-dimensional approximation in cone-jet electrospray. *Journal of Aerosol Science*, 61:60–69.
- Mahadevan, L., Ryu, W. S., and Samuel, A. D. T. (1998). Fluid ‘rope trick’investigated. *Nature*, 392(6672):140–140.
- Majeski, R., Kugel, H., Kaita, R., Avasarala, S., Bell, M. G., Bell, R. E., Berzak, L., Beiersdorfer, P., Gerhardt, S. P., Granstedt, E., et al. (2010). The impact of lithium wall coatings on nstx discharges and the engineering of the lithium tokamak experiment (ltx). *Fusion engineering and design*, 85(7-9):1283–1289.
- Mchale, G., Newton, M. I., and Carroll, B. J. (2001). The shape and stability of small liquid drops on fibers. *Oil & Gas science and technology*, 56(1):47–54.
- McHale, G., Rowan, S. M., Newton, M. I., and Käß, N. A. (1999). Estimation of contact angles on fibers. *Journal of adhesion science and technology*, 13(12):1457–1469.
- Melcher, J. R. and Taylor, G. I. (1969). Electrohydrodynamics: a review of the role of interfacial shear stresses. *Annual Review of Fluid Mechanics*, 1(1):111–146.
- Mohammad Karim, A. (2022). A review of physics of moving contact line dynamics models and its applications in interfacial science. *Journal of Applied Physics*, 132(8):080701.
- Mousavi Shaegh, S. A., Nguyen, N. T., and Chan, S. H. (2011). A review on membraneless laminar flow-based fuel cells. *International Journal of Hydrogen Energy*, 36(9):5675–5694.
- Ogrofsky, H. R. (2021a). Impact of viscosity ratio on falling two-layer viscous film flow inside a tube. *Physical Review Fluids*, 6(10):104005.
- Ogrofsky, H. R. (2021b). Linear stability and nonlinear dynamics in a long-wave model of film flows inside a tube in the presence of surfactant. *Journal of Fluid Mechanics*, 908.
- O’Neill, L. and Mudawar, I. (2020a). Review of two-phase flow instabilities in macro-and micro-channel systems. *International Journal of Heat and Mass Transfer*, 157:119738.

- O'Neill, L. E. and Mudawar, I. (2020b). Review of two-phase flow instabilities in macro-and micro-channel systems. *International Journal of Heat and Mass Transfer*, 157:119738.
- Oron, A., Davis, S. H., and Bankoff, S. G. (1997). Long-scale evolution of thin liquid films. *Reviews of modern physics*, 69(3):931.
- Pantano, C., Gañán-Calvo, A. M., and Barrero, A. (1994). Zeroth-order, electrohydrostatic solution for electrospraying in cone-jet mode. *Journal of Aerosol Science*, 25(6):1065–1077.
- Pekker, L. (2018). On plateau-rayleigh instability of a cylinder of viscous liquid. *Journal of Imaging Science and Technology*, 62(4):40405–1.
- Peterson, R. C., Jimack, P. K., and Kelmanson, M. A. (2001). On the stability of viscous free-surface flow supported by a rotating cylinder. *Proceedings of the Royal Society of London. Series A: Mathematical, Physical and Engineering Sciences*, 457(2010):1427–1445.
- Piercy, N. A. V., Hooper, M. S., and Winny, H. F. (1933). Liii. viscous flow through pipes with cores. *The London, Edinburgh, and Dublin Philosophical Magazine and Journal of Science*, 15(99):647–676.
- Pitts, E. (1973). The stability of pendent liquid drops. part 1. drops formed in a narrow gap. *Journal of Fluid Mechanics*, 59(4):753–767.
- Plateau, J. A. F. (1873). *Statique expérimentale et théorique des liquides soumis aux seules forces moléculaires*, volume 2. Gauthier-Villars.
- Ponce-Torres, A., Rebollo-Muñoz, N., Herrada, M. A., Gañán-Calvo, A. M., and Montanero, J. M. (2018). The steady cone-jet mode of electrospraying close to the minimum volume stability limit. *Journal of Fluid Mechanics*, 857:142–172.
- Quéré, D. (1999). Fluid coating on a fiber. *Annual Review of Fluid Mechanics*, 31(1):347–384.
- Rayleigh, L. (1878). On the instability of jets. *Proceedings of the London mathematical society*, 1(1):4–13.
- Rayleigh, L. (1879). Vi. on the capillary phenomena of jets. *Proceedings of the Royal Society of London*, 29(196-199):71–97.
- Rayleigh, L. (1882). Investigation of the character of the equilibrium of an incompressible heavy fluid of variable density. *Proceedings of the London mathematical society*, 1(1):170–177.
- Rayleigh, L. (1892). Xvi. on the instability of a cylinder of viscous liquid under capillary force. *The London, Edinburgh, and Dublin Philosophical Magazine and Journal of Science*, 34(207):145–154.
- Reisfeld, B. and Bankoff, S. G. (1992). Non-isothermal flow of a liquid film on a horizontal cylinder. *Journal of Fluid Mechanics*, 236:167–196.

Bibliography

- Revankar, S. and Pollock, D. (2005). Laminar film condensation in a vertical tube in the presence of noncondensable gas. *Applied mathematical modelling*, 29(4):341–359.
- Reynolds, O. (1886). Iv. on the theory of lubrication and its application to mr. beauchamp tower's experiments, including an experimental determination of the viscosity of olive oil. *Philosophical transactions of the Royal Society of London*, 177:157–234.
- Ribe, N. M. (2002). A general theory for the dynamics of thin viscous sheets. *Journal of Fluid Mechanics*, 457:255–283.
- Ribe, N. M. (2003). Periodic folding of viscous sheets. *Physical Review E*, 68(3):036305.
- Ribe, N. M. (2004). Coiling of viscous jets. *Proceedings of the Royal Society of London. Series A: Mathematical, Physical and Engineering Sciences*, 460(2051):3223–3239.
- Ribe, N. M. (2017). Liquid rope coiling: a synoptic view. *Journal of Fluid Mechanics*, 812.
- Ribe, N. M., Habibi, M., and Bonn, D. (2012). Liquid rope coiling. *Annual review of fluid mechanics*, 44(1):249–266.
- Rietz, M., Scheid, B., Gallaire, F., Kofman, N., Kneer, R., and Rohlf, W. (2017). Dynamics of falling films on the outside of a vertical rotating cylinder: waves, rivulets and dripping transitions. *Journal of fluid mechanics*, 832:189–211.
- Robinson, T. M., Hutmacher, D. W., and Dalton, P. D. (2019). The next frontier in melt electrospinning: taming the jet. *Advanced Functional Materials*, 29(44):1904664.
- Rodriguez-Rodriguez, J., Sevilla, A., Martínez-Bazán, C., and Gordillo, J. M. (2015). Generation of microbubbles with applications to industry and medicine. *Annu. rev. Fluid Mech.*, 47:405–429.
- Rosell-Llompart, J., Grifoll, J., and Loscertales, I. G. (2018). Electrosprays in the cone-jet mode: From Taylor cone formation to spray development. *Journal of Aerosol Science*, 125:2–31.
- Ruyer-Quil, C. and Kalliadasis, S. (2012). Wavy regimes of film flow down a fiber. *Physical Review E*, 85(4):046302.
- Ruyer-Quil, C. and Manneville, P. (2000). Improved modeling of flows down inclined planes. *The European Physical Journal B-Condensed Matter and Complex Systems*, 15(2):357–369.
- Ruyer-Quil, C., Trevelyan, P., Giorgiutti-Dauphiné, F., Duprat, C., and Kalliadasis, S. (2008). Modelling film flows down a fibre. *Journal of Fluid Mechanics*, 603:431–462.
- Sadeghpour, A., Zeng, Z., Ji, H., Dehdari Ebrahimi, N., Bertozzi, A. L., and Ju, Y. S. (2019). Water vapor capturing using an array of traveling liquid beads for desalination and water treatment. *Science advances*, 5(4):eaav7662.

- Sadeghpour, A., Zeng, Z., and Ju, Y. S. (2017). Effects of nozzle geometry on the fluid dynamics of thin liquid films flowing down vertical strings in the rayleigh–plateau regime. *Langmuir*, 33(25):6292–6299.
- Santos, C. A., Quaresma, J. M. V., and Garcia, A. (2001). Determination of transient interfacial heat transfer coefficients in chill mold castings. *Journal of Alloys and Compounds*, 319(1-2):174–186.
- Savart, F. (1833). Wemoire sur la constitution des veines liquids lancees par des orifices circulaires en mince paroi. *Ann. de chim.*, 53:337–386.
- Saville, D. A. (1997). Electrohydrodynamics: the Taylor-Melcher leaky dielectric model. *Annual Review of Fluid Mechanics*, 29(1):27–64.
- Scheid, B. (2013). Rivulet structures in falling liquid films. In *Without Bounds: A Scientific Canvas of Nonlinearity and Complex Dynamics*, pages 435–441. Springer.
- Scherz, C. (2022). Modeling melt electrowriting beam. Technical report, EPFL semester project.
- Schmid, P. J. (2007). Nonmodal stability theory. *Annu. Rev. Fluid Mech.*, 39:129–162.
- Schmid, P. J. and Henningson, D. S. (2001). The viscous initial value problem. In *Stability and Transition in Shear Flows*, pages 99–151. Springer.
- Schmid, P. J., Henningson, D. S., and Jankowski, D. F. (2002). Stability and transition in shear flows. applied mathematical sciences, vol. 142. *Appl. Mech. Rev.*, 55(3):B57–B59.
- Schmidt, W. (2006). From tea kettles to exploding stars. *Nature Physics*, 2(8):505–506.
- Schrauf, G. (2005). Status and perspectives of laminar flow. *The aeronautical journal*, 109(1102):639–644.
- Schröder, D. (2012). Applications of electrospray ionization mass spectrometry in mechanistic studies and catalysis research. *Accounts of chemical research*, 45(9):1521–1532.
- Séro-Guillaume, O. and Er-Riani, M. (1999). Domain perturbation method and shape of a bubble in a uniform flow of an inviscid liquid. *European Journal of Mechanics-B/Fluids*, 18(6):991–1003.
- Shah, D. O. (2012). *Improved oil recovery by surfactant and polymer flooding*. Elsevier.
- Sharp, D. H. (1984). An overview of rayleigh-taylor instability. *Physica D: Nonlinear Phenomena*, 12(1-3):3–18.
- Shen, A. Q., Gleason, B., McKinley, G. H., and Stone, H. A. (2002). Fiber coating with surfactant solutions. *Physics of Fluids*, 14(11):4055–4068.

Bibliography

- Shukla, I. (2019). *Response of noise-amplifier flows: From linear control to nonlinear jet breakup*. PhD thesis, EPFL.
- Skorobogatiy, M. and Mahadevan, L. (2000). Folding of viscous sheets and filaments. *EPL (Europhysics Letters)*, 52(5):532.
- Smith, F. T. (1982). On the high reynolds number theory of laminar flows. *IMA Journal of Applied Mathematics*, 28(3):207–281.
- Takagi, D. and Huppert, H. E. (2010). Flow and instability of thin films on a cylinder and sphere. *Journal of Fluid Mechanics*, 647:221–238.
- Tan, C. T. and Homsy, G. (1986). Stability of miscible displacements in porous media: Rectilinear flow. *Phys. Fluids*, 29(11):3549–3556.
- Taylor, G. I. (1950). The instability of liquid surfaces when accelerated in a direction perpendicular to their planes. i. *Proceedings of the Royal Society of London. Series A. Mathematical and Physical Sciences*, 201(1065):192–196.
- Taylor, G. I. (1964). Disintegration of water drops in an electric field. *Proceedings of the Royal Society of London. Series A. Mathematical and Physical Sciences*, 280(1382):383–397.
- Taylor, G. I. (1969). Instability of jets, threads, and sheets of viscous fluid. In *Applied mechanics*, pages 382–388. Springer.
- Teng, H., Cheng, P., and Zhao, T. S. (1999). Instability of condensate film and capillary blocking in small-diameter-thermosyphon condensers. *International journal of heat and mass transfer*, 42(16):3071–3083.
- Tian, J., Ribe, N. M., Wu, X., and Shum, H. C. (2020). Steady and unsteady buckling of viscous capillary jets and liquid bridges. *Physical Review Letters*, 125(10):104502.
- Tome, M. F. and McKee, S. (1999). Numerical simulation of viscous flow: buckling of planar jets. *International journal for numerical methods in fluids*, 29(6):705–718.
- Trefethen, L. N., Trefethen, A. E., Reddy, S. C., and Driscoll, T. A. (1993). Hydrodynamic stability without eigenvalues. *Science*, 261(5121):578–584.
- Trinh, P. H., Kim, H., Hammoud, N., Howell, P. D., Chapman, S. J., and Stone, H. A. (2014). Curvature suppresses the rayleigh-taylor instability. *Phys. Fluids*, 26(5):051704.
- Weidner, D. E. (2013). Suppression and reversal of drop formation on horizontal cylinders due to surfactant convection. *Physics of Fluids*, 25(8):082110.
- Weidner, D. E., Schwartz, L. W., and Eres, M. H. (1997). Simulation of coating layer evolution and drop formation on horizontal cylinders. *Journal of Colloid and interface science*, 187(1):243–258.

- Xie, Q., Liu, R., Wang, X., and Chen, X. (2021). Investigation of flow dynamics of thin viscous films down differently shaped fibers. *Applied Physics Letters*, 119(20):201601.
- Yan, F., Farouk, B., and Ko, F. (2003). Numerical modeling of an electrostatically driven liquid meniscus in the cone-jet mode. *Journal of Aerosol Science*, 34(1):99–116.
- Yang, H. Q. (1992). Asymmetric instability of a liquid jet. *Physics of Fluids A: Fluid Dynamics*, 4(4):681–689.
- Yiantsios, S. G. and Higgins, B. G. (1989). Rayleigh–Taylor instability in thin viscous films. *Physics of Fluids A: Fluid Dynamics*, 1(9):1484–1501.
- Yu, L. and Hinch, J. (2013). The velocity of ‘large’ viscous drops falling on a coated vertical fibre. *Journal of fluid mechanics*, 737:232–248.
- Zeleny, J. (1914). The electrical discharge from liquid points, and a hydrostatic method of measuring the electric intensity at their surfaces. *Phys. Rev.*, 3:69–91.
- Zeng, Z., Sadeghpour, A., and Ju, Y. S. (2018). Thermohydraulic characteristics of a multi-string direct-contact heat exchanger. *International Journal of Heat and Mass Transfer*, 126:536–544.
- Zeng, Z., Sadeghpour, A., and Ju, Y. S. (2019). A highly effective multi-string humidifier with a low gas stream pressure drop for desalination. *Desalination*, 449:92–100.
- Zeng, Z., Sadeghpour, A., Warriar, G., and Ju, Y. S. (2017). Experimental study of heat transfer between thin liquid films flowing down a vertical string in the rayleigh-plateau instability regime and a counterflowing gas stream. *International Journal of Heat and Mass Transfer*, 108:830–840.
- Zenit, R. (2019). Some fluid mechanical aspects of artistic painting. *Physical Review Fluids*, 4(11):110507.
- Zhang, K., Jia, N., Li, S., and Liu, L. (2019). Rapid determination of interfacial tensions in nanopores: Experimental nanofluidics and theoretical models. *Langmuir*, 35(27):8943–8949.
- Zhou, L.-Y., Fu, J., and He, Y. (2020). A review of 3d printing technologies for soft polymer materials. *Advanced Functional Materials*, 30(28):2000187.
- Zhu, L., Gallaire, F., Reigh, S. Y., and Lauga, E. J.-M. (2017a). Swimming with a cage: low-reynolds-number locomotion inside a droplet. *Soft Matter*.
- Zhu, L.-K., Song, B. Y., Wang, Z. L., Monteil, D. T., Shen, X., Hacker, D. L., De Jesus, M., and Wurm, F. M. (2017b). Studies on fluid dynamics of the flow field and gas transfer in orbitally shaken tubes. *Biotechnology progress*, 33(1):192–200.



SHAHAB EGHBALI

+41-78-821 25 92
shahab.eghbali@epfl.ch
Shahab Eghbali

shahabeghbali
Rte de la Pierre 20A, 1024 Ecublens, Switzerland
Work permit B, avec activité (see Art. 21 para. 3)

LANGUAGES

English: C1/C2
French: B2/C1
Persian: Native

EDUCATION

PhD, Mechanics | EPFL, Switzerland 2018–2022

- Laboratory of Fluid Mechanics and Instabilities
- Thesis title:** *Columnlike free-interface flows: symmetry breaking and linear instability*, under the supervision of Prof. François Gallaire

MSc, Mechanical engineering | EPFL, Switzerland 2014–2017

- Specialization:** Aero-and Hydrodynamics, Institute of Mechanical Engineering
- Thesis title:** *Linear stability analysis of spiral vortex breakdown in presence of a spherical object in constricted pipe*, under the supervision of Dr. Simon Pasche & Prof. François Gallaire
- GPA: 5.32/6

BSc, Mechanical engineering | University of Tehran, Iran 2010–2014

- GPA: 18.26/20

SKILLS

Multiphysics analysis
Numerical modeling CFD
Electro-thermofluidic analysis
Heat & mass transfer
Machine learning
Project management
Negotiation
Presentation

PUBLICATIONS & CONFERENCES

Publications

- S. Eghbali, L. Keiser, E. Boujo, F. Gallaire, *Whirling instability of an eccentric coated fibre*, *Journal of Fluid Mechanics*, 2022
- S. Eghbali, Y.-M. Ducimetière, E. Boujo, F. Gallaire, *On the liquid film instability of an internally coated horizontal tube*, submitted
- S. Eghbali, S. Djambov, F. Gallaire, *Stability of liquid film coating a horizontal cylinder: capillary and potential interplay*, in preparation

Conferences

- 14th European Fluid Mechanics Conference (EFMC)**, Athens, Greece, 2022, S. Eghbali, L. Keiser, E. Boujo, F. Gallaire, *Whirling instability of an eccentric coated fibre*
- APS Division of Fluid Mechanics Meeting**, Chicago, USA, 2020, S. Eghbali, L. Keiser, E. Boujo, F. Gallaire, *Helical Instability of an Eccentric Coated Fiber*,

INTERESTS

Fluid Mechanics
Flow Instabilities
Coating Flows
Interfacial Flows

PROFESSIONAL EXPERIENCE

Numerical modeling analyst (PhD collaboration) | SFA Advanced Manufacturing, Switzerland 2018–2022

- Conducted electrohydrodynamic simulations of powder focusing for beam induced laser 3D printing (COMSOL)

Service & Rehab Trainee | ANDRITZ HYDRO R&D, Switzerland 17th Spring 2016

- Established experimental protocol** for measurement of material erosion (4 months)
- Modified the test rig** resulted in +40% faster erosion in cavitating venturi

IT SKILLS

Multiphysics:
COMSOL, ANSYS, FreeFem++,
OpenFOAM, CFTurbo, NU-
MECA

Machine learning:
Scikit-learn, PyTorch, Deep
learning

Programming:
C, C++, Python, MATLAB,
Mathematica, Maple

Thermal:
Wosemose, EES, CyclePad

CAD:
AutoCAD, SolidWorks

Data Visualization:
Paraview, Adobe, Tecplot

General:
MS Windows, MS Office,
Wordpress, Prezi, L^AT_EX

HOBBIES

Music (12 years):
Instruction, giving concerts,
organizing venues

Sports:
Fitness, football, hiking

Volunteering (10 years):
Charity fund raising,
voluntary education

Socializing:
Event & competition organiz-
ing (10 years)

Travelling:
Tourism & professional

TEACHING EXPERIENCE

Project supervision EPFL, Switzerland  2018–2022

- Supervised master's and semester projects (5x)

Teaching assistant EPFL, Switzerland  2014–2022

- Hydrodynamics (M.Sc. course)
- Two-phase flow and heat transfer (M.Sc. course)
- Numerical flow simulation (M.Sc. course)
- Finite element method (B.Sc. course)
- Thermodynamics (B.Sc. course)
- Analysis I & II (B.Sc. courses)
- General physics I, II & III (B.Sc. courses)

ORGANIZATION EXPERIENCE

President | Iranian Students Association at EPFL, Switzerland  2020–2021

- Other roles:** Director of communications (from 2021), Vice president (2016–2017)
- Organized** cultural events, exhibitions and festivities to promote Persian culture
- Supported** Persian scholars of Switzerland in networking, integration and administrations: **Organized** pedagogical webinars and extracurricular debate/discussion sessions; **Initiated** legal and job search consulting panel for non-EU scholars
- Executed project planning**, led an effective know-how documentation and budgeting; **Awarded** 6 grants in total 15 kCHF (**12x increase**), organized 24 events (**2x increase**)

REFERNECS

Prof. François Gallaire | LFMI-EPFL, Switzerland

- PhD & MSc advisor @ francois.gallaire@epfl.ch  +41-21-693 33 65

Dr. Mohamed Farhat | MF-EPFL, Switzerland

- MSc & internship co-advisor @ mohamed.farhat@epfl.ch  +41-21-693 50 86

Dr. Edouard Boujo | LFMI-EPFL, Switzerland

- MSc thesis referee & coauthor @ edouard.boujo@epfl.ch  +41-21-693 53 48